



HAL
open science

Image Processing Systems and Algorithms for estimating Deformations of Aircraft Structures in Flight

Quentin Demoulin

► **To cite this version:**

Quentin Demoulin. Image Processing Systems and Algorithms for estimating Deformations of Aircraft Structures in Flight. Other [cs.OH]. Institut National Polytechnique de Toulouse - INPT, 2021. English. NNT : 2021INPT0045 . tel-04170677

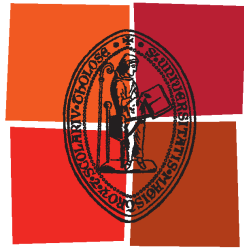
HAL Id: tel-04170677

<https://theses.hal.science/tel-04170677>

Submitted on 25 Jul 2023

HAL is a multi-disciplinary open access archive for the deposit and dissemination of scientific research documents, whether they are published or not. The documents may come from teaching and research institutions in France or abroad, or from public or private research centers.

L'archive ouverte pluridisciplinaire **HAL**, est destinée au dépôt et à la diffusion de documents scientifiques de niveau recherche, publiés ou non, émanant des établissements d'enseignement et de recherche français ou étrangers, des laboratoires publics ou privés.



Université
de Toulouse

THÈSE

En vue de l'obtention du

DOCTORAT DE L'UNIVERSITÉ DE TOULOUSE

Délivré par :

Institut National Polytechnique de Toulouse (Toulouse INP)

Discipline ou spécialité :

Informatique et Télécommunication

Présentée et soutenue par :

M. QUENTIN DEMOULIN

le vendredi 30 avril 2021

Titre :

Image Processing Systems and Algorithms for estimating Deformations of Aircraft Structures in Flight.

Ecole doctorale :

Mathématiques, Informatique, Télécommunications de Toulouse (MITT)

Unité de recherche :

Institut de Recherche en Informatique de Toulouse (IRIT)

Directeur(s) de Thèse :

M. JEAN-YVES TOURNERET

M. DENIS KOUAME

BASARAB ADRIAN

Rapporteurs :

M. OLIVIER LEZORAY, UNIVERSITE DE CAEN

M. YANNICK BERTHOUMIEU, CNRS

Membre(s) du jury :

MME CHRISTINE FERNANDEZ-MALOIGNE, UNIVERSITE DE POITIERS, Président

M. ADRIAN BASARAB, UNIVERSITE PAUL SABATIER, Membre

M. DENIS KOUAME, UNIVERSITE PAUL SABATIER, Membre

M. FRANÇOIS LEFEBVRE ALBARET, AIRBUS FRANCE, Invité(e)

M. JEAN-LUC VIALATTE, AIRBUS FRANCE, Membre

M. JEAN-YVES TOURNERET, TOULOUSE INP, Membre

M. MAXIME LHUILLIER, CNRS AUBIERE, Membre

Remerciements

Cette thèse a été réalisée grâce au soutien d'un grand nombre de personnes. Je tiens donc à remercier tous ces collègues et amis qui m'ont soutenu pendant ces trois années.

Tout d'abord, je veux remercier mes directeurs de thèse, Jean-Yves Tournet, Denis Koumé et Adrian Basarab. Malgré le décalage entre monde industriel et académique, vous avez toujours rendu la communication facile et naturelle. J'ai apprécié nos rencontres fréquentes. Vous m'avez beaucoup appris du monde de la recherche et fourni des méthodes de travail qui me seront utiles par la suite. Vous avez toujours su vous rendre disponibles pour me venir en aide, que ce soit pour des répétitions de présentation, des cours particuliers de maths, ou pour débloquer des problèmes ensemble. Merci également de m'avoir guidé et motivé lorsque je commençais à m'égarer, sans quoi il aurait certainement fallu quelques années de plus pour finir cette thèse.

Je tiens ensuite à remercier toute mon équipe d'Airbus IVICI (Fabrice, Luc, Nico, Florent, ...) qui m'a supporté depuis quatre ans. Merci à Jean-Luc, mon mentor industriel, qui m'a accompagné lors de mon entrée dans le monde du travail, du stage à la thèse. J'ai beaucoup appris grâce à ton expérience et ta vision claire d'Airbus que tu n'as pas hésité à me partager, en particulier lors de quelques footings. Merci à François, mon mentor en vision par ordinateur. J'ai énormément appris de nos longues réflexions, pas toujours faciles à suivre, mais toujours riches en idées. Tu m'auras inculqué un peu de ton excellente appréhension des comportements physiques ("au pif") qui me servira à coup sûr dans mes prochains projets. Merci à Sylvain, l'homme aux milles astuces, spécialiste de la ouiche lorraine, collègue et bon ami (Hellfest !), grâce à qui j'ai pu monter à bord d'un avion pour suivre mes essais en vol. Cela restera une expérience inoubliable. Merci à Aldo, Maxime et Laurence qui m'ont toujours accompagné pour la préparation et mise en œuvre des essais sur avion, et avec qui nous avons passé quelques bons moments à bord de Sovam ou au dessus d'ailes d'avion. Merci à Ivan Hermanito, pour ton support moral et pour m'avoir partagé ta culture musicale. Merci à Nathalie d'avoir cru en moi et d'avoir rendu possible cette thèse, et merci à Jean-Pascal qui m'a aidé à la finir et m'a poussé à prendre plus de responsabilités.

Je souhaite également apporter ma gratitude à Benjamin Mouchet pour tout son support depuis mon arrivé à Airbus, ainsi qu'à Philippe Bras et Jean-Christophe Combier pour leur aide et expertise sur les modèles de déformation et l'étude d'incertitude. Je remercie également Maxime Lhuillier pour son aide précieuse sur la propagation d'incertitude.

Merci à tous les membres du laboratoire TéSA et tout particulièrement Corinne pour l'accueil que vous m'avez offert. Je remercie chaleureusement tous mes camarades et amis du labo qui m'ont soutenu au fil de cette thèse, Simone, Adrien, Barbara, Lorenzo, Selma, Victor, Raoul, Philippe, ... J'ai passé seulement un jour par semaine au sein du laboratoire, mais je me suis toujours senti chez moi. Ce fut un plaisir de partager des conversations autour d'un café, d'un repas, ou entre deux coups de pieds au Taekwondo.

Enfin je tiens à remercier toute ma famille pour m'avoir soutenu dans n'importe quelle épreuve. Merci à mon père (l'homme le plus classe du monde ?), qui a toujours cru en moi sans vraiment comprendre le sujet de mon travail, et qui m'a appris à relativiser. Je remercie ma mère pour m'avoir transmis sa passion des sciences qui m'a motivé dans mon parcours et mené à cette thèse. Merci à Thomas, mon poulet, quasi membre de la famille, de m'avoir aidé à décompresser hebdomadairement. Et pour finir, je souhaite remercier de tout mon cœur Laëtitia, ma moitié, pour son soutien infailible au quotidien, et sans qui je n'aurais pas pu mener cette thèse à terme.

Contents

Table des sigles et acronymes	xiii
Résumé (Français)	1
Introduction	5
1 Non Contact 3D Reconstruction	9
1.1 State of the art	10
1.2 Photogrammetry	29
1.3 Conclusion	39
2 New processing chain based on multiple view photogrammetry	41
2.1 Brief overview of the algorithmic chain	42
2.2 Use of points of interest naturally present on the wing	44
2.3 Initialization using targets	56
2.4 Optimization under constraints of <i>a priori</i> deformation limits	61
2.5 Conclusion	74
3 Uncertainty estimation for 3D-wing reconstruction	75
3.1 State of the art about uncertainty estimation	76
3.2 Uncertainty sources	82
3.3 Error propagation for 3D reconstruction	96
3.4 Results and comparison	102
3.5 Conclusion	106
4 Industrial Validation	109
4.1 Flight Tests	110

4.2	Agreement with Airbus specifications	116
4.3	Industrial perspectives	120
4.4	Conclusion	123
Conclusion		125
A Derivatives Calculation for the Constrained Bundle Adjustment		129
A.1	Constrained Bundle Adjustment - reminder	129
A.2	CBA Derivatives	130
B Gauss-Newton method		133
C Results of the Uncertainty Propagation		135
Bibliographie		149

List of Figures

1.1	Non-contact measuring methods	11
1.2	Example of industrial CT scan. (a) X25 industrial 3D X-ray inspection system from NSI [Nsi], (b) 3D scan of a scanned object.	12
1.3	Example of 3D reconstruction using: (a) - ultrasound (from Siemens Healthineers [Sie]), (b) - MRI (from Phillips [Phi]).	12
1.4	Surface reflection model (from [Mor05])	13
1.5	Illustration of shape from shading on a real face image, from [PF06].	14
1.6	Shape from textures (from [Gur+06]).	15
1.7	Example of a simple depth from focus reconstruction (from [Moe+15]): (a) - Input images with various focus, (b) - Depth map reconstruction.	16
1.8	Formation of an unsharp image illustrated from optical design (from [Bil+13]).	16
1.9	Real image experiment from [YSS10]: (a) The face model used in this experiment, (b) Example of images, (c) Initial recovered shape, (d) Final recovered shape.	17
1.10	Shadow constraints and anti-shadow constraints (from [YSS10]).	18
1.11	Shape from silhouettes method to generate 3D model data using multiple RGB cameras (from [Xia+16])	19
1.12	Illustration of the deflectometry method. (a) - Deflectometry applied to 3D reconstruction of a car surface, using robot arm (from [BW10]), (b) - BLADE wing [Bla] with deflectometry installation.	20
1.13	Example of an aircraft wing imaged using a photogrammetry system (from [Liu+12])	21
1.14	Example of pattern stripe installed for IPCT tests for an A380 in 2009. . . .	22
1.15	Structure from motion example, left: set of images, right: 3D reconstruction using the reconstruction implementation <i>Multi-View Environment</i> [FLG14]. .	23
1.16	(a) - Illustration of the structured light method (from [Zha18]), (b) - Example of 3D scanner using structured light (ATOS Compact Scan, from Gom [Gom]).	24
1.17	Example of ToF camera (from Basler) and depth image that it can capture. .	26

1.18	Illustration of the ToF method (from [Li14]): (a) - pulsed, (b) - continuous-wave.	26
1.19	Illustration of 3D reconstruction using Lidar (a), radar (b) and sonar (c) (from [Vel], [Car+14] and [Fur]).	28
1.20	Sketch of the pinhole model.	29
1.21	The different coordinate systems and mappings. From left to right: real world, camera and image coordinate systems.	30
1.22	Illustration of the camera distortions (from [Ope]).	30
1.23	Epipolar Geometry - Two cameras represented by their centers \mathbf{C}_1 and \mathbf{C}_2 observe a 3D point \mathbf{X} . The image point \mathbf{x} back-projects to a ray defined by \mathbf{C}_1 and \mathbf{X} , imaged as the epipolar line \mathbf{l}' on the second image. The image point \mathbf{x}' of \mathbf{X} has to lie on this line.	32
1.24	The four possible solutions for a calibrated reconstruction of \mathbf{P}_2 from \mathbf{E} . Between the left and right sides, one can observe the two possible translations $\pm\mathbf{u}_3$ of the camera \mathbf{B} . Between the top and bottom rows, the camera \mathbf{B} rotates of 180 degrees with respect to the baseline. Note that the only reconstructed point being in front of both cameras is displayed in (a) [HZ04]. The other solutions (b), (c) and (d) are not possible.	34
1.25	Illustration of the BA for 3 cameras observing a set of 3D points.	37
1.26	Example of sparse BA Jacobian matrix for 3 cameras and 10 points.	38
2.1	Diagram of the proposed algorithmic framework.	42
2.2	Rear camera view with some reference points zoomed.	43
2.3	Detection of points of interest for SIFT (from [Low04]). (a) - Process for calculating the DoG through the scale space, (b) - illustration of the search for a key point in the vicinity of the DoG.	45
2.4	Construction of the SIFT point descriptor (from [Low04]). In this example, the samples are grouped into an array of 2×2 orientation histograms.	46
2.5	Illustration of the corner detection in FAST (from [RD06]). The intensity of the candidate point \mathbf{p} is compared to that of the 16 pixels of the circle represented on the right.	47
2.6	BRIEF descriptor: example of a random distributions to select the pairs of points to compare (from [Cal+10]). The ends of each segment are pairs of points.	48
2.7	DAISY descriptor.	49

2.8	Example of matching error when applying SIFT. The points are represented with the scale and the orientation of their descriptor. In the cases (a) and (b), one observes errors related to the invariances of scale and rotation of the descriptor. Case (c) shows an error due to the similarity of the key points. Finally, some unjustified errors may appear, as in (d).	50
2.9	Performance comparison of the different descriptors for the matching of real images of an aircraft wing.	51
2.10	Application on an A320 wing of the matching method described in Section 2.2.2.2. (a) 14 strong matches chosen at initialization, (b) 220 matches after 3 iterations of steps iii. to v.	53
2.11	Example of stereo image rectification (from [LZ99]). (a) - Pair of initial images, (b) - Rectified images.	54
2.12	Illustration of the shearing effect of image rectification on some synthetic views of a wing. (a) - Initial image, (b) - Rectified image, (c) - rectified image with shearing reduction.	55
2.13	Example of targets commonly used in photogrammetry applications. (a) retro-reflective targets with circular and coded shapes, (b) concentric circles and cross targets, (c) 3D markers.	57
2.14	Illustration of the center eccentricity appearing when observing a circular target (from [Luh+13]).	58
2.15	Example of view on an A350 wing using a 4K camera, with concentric circular and cross targets installed.	59
2.16	Selected targets installed on an A350 wing, with red graduations stuck on the black lanes.	60
2.17	Wing shapes under maximum and minimum bending load cases from FEM simulations.	62
2.18	Static test on an A350 aircraft. In this picture, the wing bent under the forces of an Ultimate Load is overlaid with its position without forces.	63
2.19	Node illustration on the aircraft wing.	63
2.20	Example of sparse bundle adjustment Jacobian matrix for 3 cameras and 10 points. The last rows represent the two first constraints g_0 and g_4 defined in 2.4.2.	66

2.21	Bounding shapes in the (x, y) plane for the volume constraint at the beginning (a), middle (b) and end (c) of the wing. For the initial node position, displayed as a red cross, blue crosses represent all the node positions for the various load cases.	67
2.22	Evaluation of the influence of degree for the polynomial fit. The mean error (top) and standard deviation (bottom) are calculated for all the load cases at once.	67
2.23	Polynomial fitting for the bending constraints. (Top) View of the wing shapes for various Load Cases on the (y, z) plan with their fitted polynomials $z = P(y)$. The approximations by finite differences of the derivatives $\frac{\partial z^i}{\partial y}$ and $\frac{\partial^2 z^i}{\partial y^2}$ are displayed respectively in (middle) and (bottom), overlaid with the corresponding derivatives of the polynomials. Noisy estimation of the derivatives can be observed at about 10m of wing span, due to a local gap in the node sampling. .	68
2.24	Torsion along the wing span calculated using finite differences and polynomial fitting. One can observe that the calculated derivatives using finite differences and polynomial fitting do not match for this example.	69
2.25	Torsion along the wing span. The upper and lower envelopes are approximated by polynomials P and Q such that $t_{min} = P(y)$, and $t_{max} = Q(y)$. The color legend is identical to that of Fig. 2.23.	69
2.26	Relative elongation along the wing span. The upper and lower envelopes are approximated by polynomials P and Q such that $\epsilon_{min} = P(y)$, and $\epsilon_{max} = Q(y)$. The color legend is identical to that of Fig. 2.23.	69
2.27	Examples of recorded views resulting from a the test on ground with an Airbus A350-900.	71
2.28	Estimated motions (in meters) of the 4 cameras located on the aircraft windows versus time.	71
2.29	Bending results at the middle of the wing (left) and at wing tip (right). . . .	72
2.30	Comparison of the distances between the reconstructed point cloud and the theoretical model of ground shape. (a) reconstruction using only volume constraint, (b) reconstruction using both volume and bending constraints.	72
2.31	Point reconstructions in the (x, y) plane for the first and last frames. (left) without the constraint, (right) with the volume and bending constraints. Some outliers can be observed in the last ba frame.	73
2.32	Influence of the penalty parameter on the reprojection error, the constraint errors and the number of iterations required to converge.	73

3.1	Illustration of the concepts of estimation trueness, precision and uncertainty, in four different scenarios. Blue dots represent estimates of a quantity for which the true value is known and displayed as a green dot. The uncertainty decreases when precision and/or trueness increases.	76
3.2	Diagram of the uncertainty evaluation process.	79
3.3	Ishikawa diagram for listing all potential source of uncertainty.	83
3.4	Illustration of the chromatic aberration, creating a rainbow edge in high contrast areas.	86
3.5	Reconstruction framework for the uncertainty study.	89
3.6	(a) - Example of image taken from a drone for the initial 3D reconstruction of the wing. Reference markers placed around the wing are highlighted with red circles. (b) - Corresponding 3D reconstruction, where reference distances are shown with yellow lines.	93
3.7	Illustration of the method for graduation detection.	96
3.8	Examples of simulated views of quadrant markers for the estimation of 2D detection uncertainty.	98
3.9	Examples of synthetic views of the deformed wing generated with Unity. . . .	101
3.10	Result in meters for a target at wing end of the MC and PL for the uncertainty propagation with various inputs, starting with observation noise (x), plus calibration noise (x,k), and with added noise of initial reconstruction (x,k,i).	103
3.11	Result in meters of the MC for the uncertainty propagation with all considered uncertainties, including outliers. (left) - using BA, (right) - using CBA. . . .	104
3.12	Mean 3D error of the MC simulations with CBA displayed as function of the error sources of 2D detection, 3D initialization and camera calibration	105
3.13	Uncertainty results using PL for various level of camera calibration noise, at wing tip (in meters).	105
3.14	First view from camera 1 for each sequence of deformations generated with Unity.	106
3.15	Reconstruction result on sequences generated with Unity for two targets, one at the wing tip, and one at its middle.	107
4.1	Cabin installation of the cameras. (a) - Camera mounted on a fake window, (b) - Station of the flight test engineers, used to control the recordings. . . .	111

4.2	Approximate positions and orientations of the four cameras installed on the aircraft. Field of views are highlighted with colored surfaces.	111
4.3	Target installation for flight tests on the wing of an A350-1000.	112
4.4	Examples of images recorded during the first flight test.	114
4.5	Examples of blur occurring on ground displacements. (a) - Image of the wing tip during landing, (b) - same view during flight.	115
4.6	Comparison of the real and synthetic images obtained in flight and using Unity. (left) - simulated, (right) - real images.	117
4.7	Example of target views acquired during the flight.	119
C.1	BA with only observation noise at tip (a) and middle (b) of the wing, using both MC and PL (in meters).	135
C.2	BA with only observation noise and calibration noise (in meters). Since 1px (a) of calibration noise does not change the results (see Fig.C.1), 10px (b) is tested to confirm that PL works to propagate calibration uncertainty.	136
C.3	BA with observation, calibration and initial reconstruction noise, showing that the uncertainty of initial reconstruction has no impact on the result in the current application (in meters).	136
C.4	Confidence ellipses of the 3D reconstructions (in meters) for all targets of the wing displayed in (x, y) plane, with BA (a) and CBA (b).	137
C.5	Confidence ellipses of the 3D reconstructions (in meters) for all targets of the wing displayed in (x, z) plane, with BA (a) and CBA (b).	138
C.6	Results of the MC simulation propagating observation and calibration noise with outliers, using BA (a) and CBA (b) (in meters). Boundaries arising from the volume constraints may be observed in (b).	139
C.7	Confidence ellipses of a 3D point at wing tip for various levels of observation noise, obtained using PL (in meters).	139

List of Tables

2.1	Table of descriptor invariances (provided in [CLFM16])	50
3.1	Table of the main uncertainty sources	92
3.2	Comparison of the methods for uncertainty estimation.	97
3.3	Correlation matrix of the uncertainty sources for the MC simulation with CBA	104
4.1	Synthesis of system responses to Airbus requirements.	121

List of Acronyms

BA	<i>Bundle Adjustment</i>
BLADE	<i>Breakthrough Laminar Aircraft Demonstrator in Europe</i>
BRIEF	<i>Binary Robust Independent Elementary Features</i>
CBA	<i>Constrained Bundle Adjustment</i>
CT	<i>Computed Tomography</i>
DIC	<i>Digital Image Correlation</i>
DoG	<i>Difference of Gaussian</i>
DTM	<i>Digital Terrain Model</i>
FAST	<i>Features from Accelerated Segment Test</i>
FEM	<i>Finite Element Models</i>
FLANN	<i>Fast Library for Approximate Nearest Neighbors</i>
GPS	<i>Global Positioning System</i>
GUM	<i>Guide to the expression of Uncertainty in Measurement</i>
IMU	<i>Inertial Measurement Unit</i>
IPCT	<i>Image Pattern correlation Technique</i>
JPEG	<i>Joint Photographic Experts Group</i>
LIDAR	<i>Light Detection And Ranging</i>
MC	<i>Monte-Carlo</i>
MRI	<i>Magnetic Resonance Imaging</i>
ORB	<i>Oriented FAST and Rotated BRIEF</i>
PL	<i>Propagation Law</i>
SFM	<i>Structure From Motion</i>
SIFT	<i>Scale Invariant Feature Transform</i>
SLAM	<i>Simultaneous Localization And Mapping</i>
SVD	<i>Singular Value Decomposition</i>
ToF	<i>Time-of-Flight</i>

Résumé (Français)

Contexte industriel

Quels seront les moyens de transport aérien de demain ? Quelle technologie de rupture permettra de réaliser l'avion du futur ? L'industrie aérospatiale actuelle est confrontée à l'énorme défi de rendre ses véhicules plus durables, c'est-à-dire de créer des avions plus propres, plus écologiques et plus silencieux. Afin de relever ce défi, un important projet de développement d'Airbus consiste à concevoir des ailes plus intelligentes, dont les formes peuvent être optimisées pour les conditions de vol à la manière des oiseaux, ou à utiliser de nouveaux matériaux qui modifient les propriétés physiques de l'avion. Dans le cadre de la qualification et de la certification des avions, de nouveaux instruments doivent donc être proposés pour permettre ces évolutions technologiques. En particulier, de nouveaux moyens de mesure ou d'estimation des déformations des ailes doivent être proposés, permettant une meilleure compréhension des capacités des ailes et de leur comportement aérodynamique, grâce à une reconstruction 3D dynamique et dense en vol. En outre, ces recherches doivent être intégrées dans le plan de développement du centre d'essais en vol, dont les axes sont :

- la réduction du cycle de certification des avions d'essai par l'accélération du développement et de l'installation des équipements,
- la réduction de l'empreinte des instruments de mesure sur l'avion et de leurs contraintes opérationnelles,
- la réduction des coûts d'installation des instruments d'essai en vol.

Objectifs et enjeux

Dans ce contexte industriel, l'objectif de cette thèse est de développer une nouvelle méthode de mesure de déformations des ailes répondant aux spécifications du centre d'essais en vol d'Airbus et de démontrer la faisabilité d'un système industriel. Dans un premier temps, le système proposé doit être capable de mesurer la flexion (élévation de l'aile) avec une incertitude inférieure à 10cm au bout de l'aile, pour une aile d'environ 30m de long, 10m de large, et capable de se déplacer dans un volume de 10m de haut. Deuxièmement, ce système devrait pouvoir effectuer des mesures pendant toute la durée d'un vol, c'est-à-dire jusqu'à 4 heures d'enregistrement, permettant l'acquisition de phénomènes dynamiques, soit une fréquence d'acquisition de l'ordre de 1 à 30Hz. Enfin, pour être intégré dans l'environnement d'essai en vol et suivre la ligne directrice du domaine, le système doit être rapide et facile à installer tout en restant aussi peu intrusif que possible, à savoir qu'il ne doit pas perturber ni le fonctionnement de l'avion et des autres essais ni l'équipage. Parallèlement, le monde des essais en

vol présente ses propres défis. La méthode proposée doit fonctionner dans un environnement non contrôlé, avec des variations de luminosité, d'éventuelles réflexions et ombres, des vibrations et des déformations de l'ensemble de l'avion. Il est à noter que les capteurs utilisés pour acquérir les mesures ne peuvent pas être installés n'importe où, et sont contraints d'être positionnés sur les hublots de l'avion.

Résumé des chapitres

Chapitre 1

Confronté aux spécifications d'Airbus et aux défis de l'environnement de vol, le Chapitre 1 se concentre sur le choix de la technologie et des algorithmes à adopter. En s'appuyant sur la littérature et les technologies existantes du marché industriel, ce chapitre expose un état de l'art actuel dans le domaine de la reconstruction 3D sans contact. À notre connaissance, une telle vue d'ensemble n'est pas disponible dans la littérature et contribue donc au développement du domaine. En conséquence, ce chapitre argumente sur le choix d'une méthode de photogrammétrie pour le cas d'application actuel. En effet, cette méthode présente l'avantage de fournir des mesures précises conformes aux attentes d'Airbus, sur le volume complet d'une aile d'avion, de manière dense et dynamique, tout en garantissant une installation simple, rapide et non intrusive. Le principe de base de la photogrammétrie est de retrouver des coordonnées 3D à partir de leurs observations 2D, en exprimant et en résolvant les équations géométriques correspondantes aux projections des points sur une ou plusieurs images. Cette méthode est ensuite décrite plus en détail, avant d'être confrontée aux défis de l'environnement des essais en vol dans le Chapitre 2.

Chapitre 2

Dans cette deuxième partie de la thèse, un processus de reconstruction 3D est proposé à partir des images acquises par un ensemble de caméras installées sur les hublots de l'avion et sur son stabilisateur arrière. Pour estimer les coordonnées 3D des parties d'ailes, la méthode de photogrammétrie repose sur la détection et la correspondance en 2D de ces éléments sur les images. Dans ce travail, une étude des caractéristiques existantes pouvant être utilisées dans ce contexte est présentée, et une combinaison de certaines méthodes modernes est proposée pour le cas spécifique de la reconstruction d'une aile avec des éléments naturellement présents dans nos images, tel que des rivets, des inscriptions ou des bandes de joints. En outre, un aperçu de la typologie des cibles photogrammétriques est fourni afin de déterminer le meilleur équipement à utiliser en vol, afin de garantir la qualité d'estimation 3D requise dans des conditions environnementales variées. Dans un second temps, les connaissances *a priori* sur les limites mécaniques de l'aile sont exploitées pour compenser les erreurs liées aux variations environnementales, grâce à une nouvelle méthode de reconstruction 3D sous contraintes. L'approche algorithmique proposée est une amélioration de la méthode classique de photogrammétrie, introduisant les limites mécaniques de la structure comme termes de régu-

larisation dans la routine d’ajustement de faisceaux, ce qui a conduit à plusieurs publications dans des conférences [Dem+20a; Dem+20b; Dem+20c].

Chapitre 3

L’interprétation et la confiance dans une mesure ou une estimation de paramètres ne sont possibles que si une indication quantitative de cette qualité de mesure ou d’estimation est fournie. C’est pourquoi dans le Chapitre 3, la qualité de la méthode proposée, en termes d’incertitude de mesure, est évaluée selon les normes industrielles les plus pertinentes [Guma; Gumb; Gumc], et sur la base des travaux de [Eud11]. Tout d’abord, un rapide état de l’art sur l’estimation de l’incertitude est exposé pour aider à comprendre les différentes approches permettant d’évaluer la qualité d’une reconstruction 3D basée sur le traitement d’images. Dans un deuxième temps, ce chapitre fournit des lignes directrices sur la prise en compte des sources d’incertitude pour la conception d’un système de photogrammétrie. En identifiant les principales sources d’incertitude, les erreurs sont propagées pour déterminer l’incertitude de l’estimation 3D sur les estimateurs définis dans le Chapitre 2. Cette étude étend le champ de la propagation des erreurs pour les applications de traitement d’images, où la plupart des travaux se concentrent sur l’application d’un bruit gaussien au niveau de l’image, en prenant en compte les sources d’erreurs du monde réel. En outre, les différentes approches pour estimer l’incertitude sont comparées dans le cas de notre application, et leurs différents résultats ont permis de valider la réponse du système proposé au besoin d’Airbus en terme d’incertitude.

Chapitre 4

Enfin, une validation industrielle est fournie au Chapitre 4. A cet effet, un système complet de photogrammétrie a été développé pour mettre en œuvre le processus conçu dans le Chapitre 2, et pour répondre au mieux aux problèmes de sources d’incertitude du Chapitre 3. Ce système a été installé sur un Airbus A350-1000 et a permis l’acquisition des premières images expérimentales à la fin de la thèse. Par manque de temps, le traitement de ces données n’a pas pu être réalisé, mais il a néanmoins permis de tirer les premières conclusions sur la validité du système. En effet, les images et la chaîne d’acquisition en action ont été confrontées aux spécifications d’Airbus, ce qui a permis de valider le matériel et le concept d’acquisition. Entre autres perspectives, ce système sera industrialisé, contribuant ainsi aux systèmes d’essais aéronautiques.

Introduction

Industrial context

What will be tomorrow's means of air transportation? What disruptive technology will allow realizing the aircraft of the future? The current aerospace industry is confronted with the tremendous challenge of making its vehicles more sustainable, i.e., create cleaner, greener and quieter aircraft. In order to meet this challenge, one important Airbus development project is the design of smarter wings, whose shapes can be optimized for flight conditions in a bird-like manner, or the use of new materials that change the physical properties of the aircraft. In the context of aircraft qualification and certification, new instrumentation must therefore be proposed to enable these technological evolutions to take place. In particular, new means of measuring or estimating wing deformations have to be proposed, enabling deeper understanding of the wing capabilities and aerodynamic behavior, through dynamic and dense 3D-reconstruction in flight. In addition, this research should be integrated into the development plan of the flight-test center, whose axes are:

- the reduction of the certification cycle for test aircraft through faster development and installation of equipment,
- the reduction of footprint of the measuring instruments on the aircraft and their operating constraints,
- the cost reduction of installing the flight-test instrumentation.

Goals and challenges

In this industrial context, the aim of this thesis is to develop a new method for measuring wing deformations meeting the specifications of the Airbus flight test center and demonstrating the feasibility of an industrial system. First, the proposed system should be capable of measuring bending (wing elevation) with an uncertainty of less than 10cm at the wing-tip, for a wing about 30m long, 10m wide, and able to move in a volume of 10m high. Second, this system should be able to carry out measurements during the whole duration of a flight, i.e., up to 4 hours of recording, allowing the acquisition of dynamic phenomena, i.e., an acquisition frequency of the order of 1 to 30Hz. Finally, in order to be integrated into the flight test environment and follow the domain's guidelines, the system should be fast and easy to install and remain as non-intrusive as possible, i.e., it should not disrupt the operation of the aircraft and other tests or the crew. Alongside this, the world of flight testing comes with its own set of challenges. The proposed method should operate in an uncontrolled environment, with variations in luminosity, possible reflections and shadows, vibrations and deformations of the

entire aircraft. Note that the sensors used to acquire the measurements cannot be installed anywhere in the aircraft and are constrained to be positioned on the aircraft windows.

Manuscript organization and contributions

The contributions of this manuscript are the result of a three-year industrial thesis (CIFRE) in collaboration with Airbus and the laboratories T SA and IRIT in Toulouse. These contributions are related to the proposal and development of a complete in-flight aircraft wing deformation estimation system.

Chapter 1

Confronted with Airbus specifications and the challenges of the flight environment, Chapter 1 focuses on the choice of technology and algorithms to adopt. Based on literature and existing technology of the industrial market, this chapter exposes an up-to-date state of the art in the field of non contact 3D reconstruction. To the best of our knowledge, such overview is not available in the literature and therefore contributes to the development of the field. In result, this chapter argues the choice of a photogrammetry method for the current application case, with respect to the challenges and specifications. This method is then described in more details, before being confronted with the challenges of the fly-test environment in Chapter 2.

Chapter 2

In this second part of the thesis, a 3D reconstruction workflow is proposed based on images acquired by a set of cameras installed on the aircraft windows and on its rear stabilizer. To estimate the 3D coordinates of wing parts, the photogrammetry method relies on the 2D detection and matching of these elements on the images. In this work, a study of existing features that can be used in this context is presented, and a combination of some state-of-the-art methods is proposed for the specific case of wing reconstruction with features naturally present on the wing. In addition, an overview of the typology of photogrammetry targets is provided to determine the best equipment to use in flight. In a second step, the *a priori* knowledge about the mechanical limits of the wing is exploited to compensate errors related to environmental variations, through a new method of 3D reconstruction under constraints. The proposed algorithmic approach is an improvement of the classical photogrammetry method, introducing mechanical limitations of the structure as regularization terms in the bundle adjustment routine, which led to several publications in conferences [Dem+20a; Dem+20b; Dem+20c].

Chapter 3

In Chapter 3, the quality of the proposed method, in terms of its measurement uncertainty, is qualified according to the closest industrial standards [Guma; Gumb; Gumc], and based on the work of [Eud11]. First, a state of the art about the uncertainty estimation is exposed to help understanding the various approaches to assess the quality of a 3D reconstruction based on image processing. In a second step, this chapter provides guidelines on the consideration of uncertainty sources for designing a photogrammetry system. Identifying the main sources of uncertainty, the errors are propagated to determine the 3D estimation uncertainty about the estimators defined in Chapter 2. This study extends the field of error propagation for image processing application, where most works focus on the application of a Gaussian noise at the image level, by taking into account real world sources of errors. Besides, the different approaches for estimating the uncertainty are compared in the case of the Airbus application.

Chapter 4

Finally, an industrial validation is provided in Chapter 4, where the development, installation and in-flight application of the proposed system is presented and confronted with the Airbus specifications, opening the door to various perspectives. The proposed system, together with the tests performed, provided a proof of concept for the estimation of structure deformation using image processing in flight. Among other prospects, this system will be industrialized, thus contributing to aeronautics test systems.

Publications

This work led to the following conference publications:

- [Dem+20a] Q. Demoulin, F. Lefebvre-Albaret, A. Basarab, D. Kouamé, and J.-Y. Tourneret. “A New Flexible Photogrammetry Instrumentation for Estimating Wing Deformation in Airbus.” In: *Proc. Eur. Test and Telemetry Conf.* Nuremberg, Germany, 2020.
- [Dem+20b] Q. Demoulin, F. Lefebvre-Albaret, A. Basarab, D. Kouamé, and J.-Y. Tourneret. “Constrained Bundle Adjustment Applied To Wing 3D Reconstruction With Mechanical Limitations.” In: *IEEE Int. Conf. on Image Process.* Abu Dhabi, United Arab Emirates, 2020.
- [Dem+20c] Q. Demoulin, F. Lefebvre-Albaret, A. Basarab, D. Kouamé, and J.-Y. Tourneret. “Wing 3D Reconstruction by Constraining the Bundle Adjustment with Mechanical Limitations.” In: *28th Eur. Signal Process. Conf.* Amsterdam, Netherlands, 2020.

Non Contact 3D Reconstruction

Contents

1.1 State of the art	10
1.1.1 Transmissive Methods	10
1.1.2 Reflective Passive Methods	13
1.1.3 Reflective Active Methods	23
1.1.4 Conclusions on selected method	28
1.2 Photogrammetry	29
1.2.1 Camera model and calibration	29
1.2.2 Two view reconstruction	31
1.2.3 N-views and Bundle Adjustment	36
1.2.4 Model-based methods	38
1.3 Conclusion	39

Starting from the motivation of measuring or estimating wing deformation in flight described in introduction, this chapter summarizes state-of-the-art methods able to estimate such deformations. First, one could instrument the wing of interest with dedicated sensors to acquire measurements. However, placing sensors inside the wing requires difficult installation, and provides only sparse measurement points. Another solution consists in installing sensors on the wing surface, but this operation should be conducted carefully, avoiding the occurrence of disturbances regarding the aerodynamic properties of wings. For these reasons, methods based on non-contact 3D measurement could offer an interesting alternative, as discussed hereafter. Section 1.1 first presents and evaluates all potential candidates for the application of 3D reconstruction of an aircraft wing. To this aim, the properties of each method are evaluated with respect to the needs and constraints of the current application, summarized in seven key factors:

1. Volume of the scene: about $10 \times 30 \times 10$ meters.
2. Required uncertainty: less than ± 10 cm on wing elevation.
3. Measurement frequency: from 1 to 30 measurements per second.
4. Test duration: up to 4 hours.

5. Intrusivity: the system should not impact flight performances, nor disturb other installations.
6. Installation constraints: the possible positions of the sensors are limited to the windows¹. In addition, the installation should be possible in less than one day.
7. Uncontrolled environment: the system should work with uncontrolled illumination variations, potential reflections and shadows, vibrations and deformations of the full aircraft.

The conclusion on the choice of photogrammetry for the current application is drawn in Section 1.1.4, and the principle of multiple view approaches is detailed in Section 1.2.

Finally, one might have access to prior knowledge about the scene and structure, which can be used to improve the results of 3D reconstruction. This is particularly relevant in applications such as the one considered here, where the method should work in challenging conditions. Section 1.2.4 takes a closer look to the use of prior models into 3D estimation methods.

1.1 State of the art

A wide variety of methods has been proposed over the years to perform the task of 3D reconstruction without contact. These approaches are based on the sensing and processing of electromagnetic or mechanic waves reflecting from or passing through the scene to reconstruct, and can be subdivided as represented in Fig. 1.1. On the one hand, transmissive applications use the ability of certain waves to go through materials such as human tissues for X-rays. On the other hand, reflective methods rely on the reflection of waves from the object of interest. The wave source can be either naturally present in the scene, using passive methods, or transmitted by the system for active approaches. Waves mainly correspond to visible light, but some applications also take benefit from other kinds of waves such as infra red light for laser scanning or time of flight cameras, radio waves for radar reconstruction, or sound and ultrasound waves with sonar systems. The frequency of waves is already a determinant feature as it conditions the limitations of the system in terms of spatial resolution and volume of the scene. This section draws an exhaustive list of non contact reconstruction methods, describes them and evaluates their capacity to meet the requirements listed in the introduction.

1.1.1 Transmissive Methods

The first group of methods concerns the transmissive use of waves. Mainly applied in the medical field, such systems are based on the observation of waves transmitted through materials. Since the application domains of these methods have specificities not adapted to the application addressed in this work, only a brief description will be given in this manuscript. For more information, the reader is invited to read [Hai13].

¹An additional camera is available on the rear stabilizer of some aircraft.

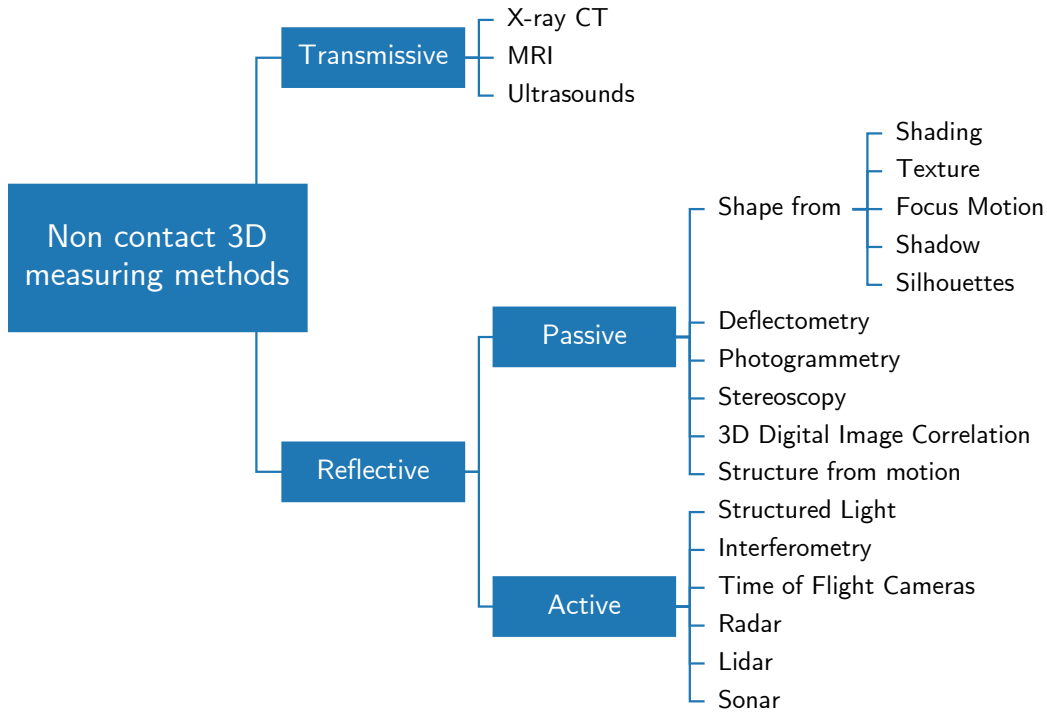


Figure 1.1: Non-contact measuring methods

The first technology developed in this domain is the X-ray scan, discovered in 1895. Such scanners are composed of an X-ray source and a detector. Objects are placed between these components to acquire images of both internal and external features by guiding X-rays through the object. The intensity of the rays received by the detector reflects the object absorption properties that vary for different materials. In 1972, a new system called computed tomography (CT) was introduced allowing us to recover cross-sectional images (or slices) of X-ray absorption. From this point, 3D reconstruction is possible from combination of multiple images from various orientations around the object, processed with a computer. This method has been extended to industrial application for metrological inspection, reverse engineering or flaw detection, as shown in Figure 1.2. In this case the object to inspect is rotated and translated between the fixed source and the detector. Current CT scanners allow reconstruction resolutions of about 500nm on small objects (usually less than 1m diameter).

Just after X-rays, ultrasound imaging was introduced resulting from the development of sonar (sound navigation and ranging) applications for the world war II. Similar to sonar using the good properties of sound propagation into water, ultrasound imaging takes benefit from the transmission properties of tissues for the ultrasound waves. Inhomogeneities in the tissues result in variations of its echogenic properties. When ultrasound pulses are sent into the tissues by a probe formed by piezoelectric elements, these echogenic variations are recorded as the pulse echoes, while the object depth is computed from the time of flight of the reflected waves. Reconstruction in three dimensions may further be computed by processing series of images taken from various spatial locations (see Fig. 1.3). The main advantages of ultrasound devices are 1) their small dimensions since one device combines both the sound



Figure 1.2: Example of industrial CT scan. (a) X25 industrial 3D X-ray inspection system from NSI [Nsi], (b) 3D scan of a scanned object.

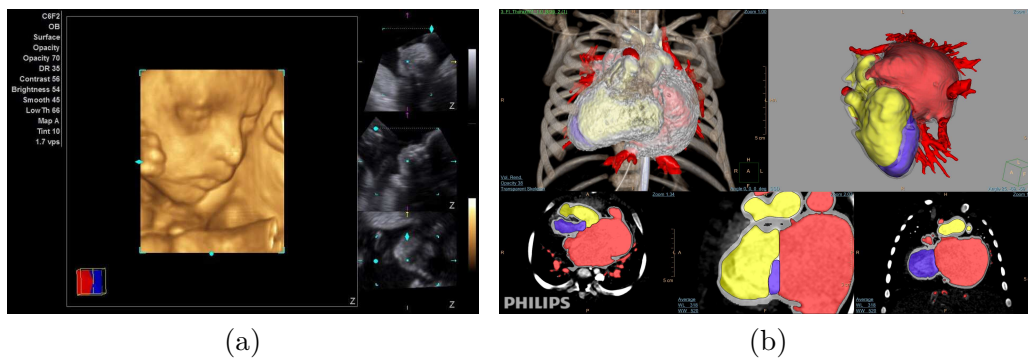


Figure 1.3: Example of 3D reconstruction using: (a) - ultrasound (from Siemens Healthineers [Sie]), (b) - MRI (from Phillips [Phi]).

emitter and the receiver in a same sensor (transducer) allowing one to transfer and receive the ultrasound waves, and 2) the fact that images can be interpreted in real time, allowing fast and agile diagnosis. However, ultrasound only works for small objects (less than $1m$), requires operator adjustment to get good contrasts, and does not work well for objects behind air because of high attenuation.

Finally, magnetic resonance imaging (MRI) was developed in the 1970s. This system exploits magnetic properties of hydrogen atoms present in the water and fat of the human body. The spin of these atoms can be oriented when the body is placed in a strong magnetic field. In the case of MRI, this field is modulated such that hydrogen atoms have different spins depending on their location. By injecting radio-frequency waves into the body, some frequencies excite the atoms depending on their type (and resonance frequency), and their level of energy is increased. When the input radio wave stops, the atoms recover their equilibrium states by releasing the stocked energy, emitting a signal that can be recorded by the MRI

antennas. The intensity of this signal depends on the type of tissues. Finally, the localization of the atoms can be computed from the observation of the atom polarization. Once again, this method is restricted to medical applications and a transfer to the case of structure 3D reconstruction during flight test is not conceivable.

1.1.2 Reflective Passive Methods

Reflective passive methods are opportunistic and use the reflections of light present in a scene to image the object to be reconstructed. An estimator of the 3D object of interest can be constructed using information conveyed by the light intensity such as textures, corners or shadows. This section explores the variety of applications encompassed by passive reflective approaches.

1.1.2.1 Light reflection on surfaces

To better understand how an image can be processed, it may be useful to understand how the light coming from an object to a camera sensor has been reflected on this object. The light emitted on a surface will be reflected differently depending mainly on the roughness of the material [Hua10; Mor05]. As illustrated in Fig. 1.4, two phenomena can occur:

- Specular reflection, in the case of homogeneous and perfectly smooth surfaces. In this case, the emitted light will be reflected symmetrically to the normal surface. When the material is rougher, the light is reflected around a specular lobe.
- Diffuse reflection in the case of rough or inhomogeneous objects. In this case, microscopic variations of the object structure reflect the light homogeneously in all direction around the normal surface.

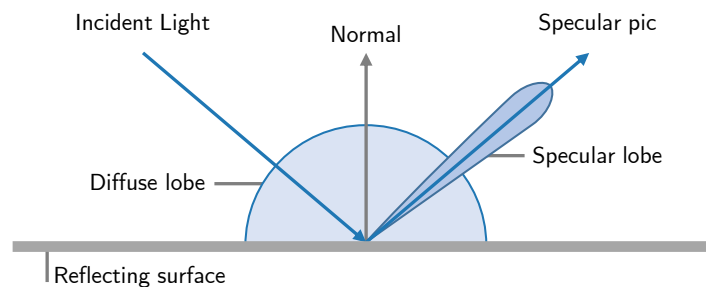


Figure 1.4: Surface reflection model (from [Mor05])

A surface reflection can be exactly predicted by electromagnetic laws if its structure is perfectly known. However, in most cases, only an approximated knowledge about these structures is available. Therefore, several models have been developed to estimate the light reflection of surfaces, depending on their properties. The simplest and most common model is the

Lambertian model, which represents the diffuse reflexions of rough or inhomogeneous surfaces. In this model, the reflected intensity I is independent of the view point, and is directly proportional to the angle of the emitted light to the surface:

$$I = I_0 k_d \cos \theta, \quad (1.1)$$

where I_0 is the emitted light intensity and k_d is the coefficient of diffuse reflexion of the material. Other models like the Nayar model [NIK91] take into account the specular lobe, the specular pic and the diffuse lobe at the same time.

In the case of Airbus aircraft, the paint used for the surfaces induces an orange peel effect, i.e., the reflexion will be diffuse and specular at the same time. On the one hand, specular reflections will arise from reflections of sun light, which could complicate the detection of features in the images. On the other hand, diffuse reflexion will degrade the precision of reflection-based methods like structured light or deflectometry.

1.1.2.2 Shape from shading

The goal of shape from shading is to recover the 3D coordinates of a scene from one single 2D image. As the reflexion of the light seen by the sensor depends on the material reflection map and its depth, shape from shading uses the knowledge of the surface reflection and the pixel intensities in the image to recover the depth of the scene. However, since the reflection properties are generally unknown, they are approximated by a Lambertian model, yielding a poor accuracy in the reconstruction [PF06; CTS95; TS94]. Moreover, this method also assumes that the light source position is known or can be recovered from the picture. Two main classes of algorithms can be distinguished to perform this task: global methods and local methods. Within global methods, shape is recovered by minimizing a cost function conveying the global smoothness and consistency of the 3D reconstruction. They are more accurate and computationally expensive than local methods, which only preserve consistency on local portions of the scene.

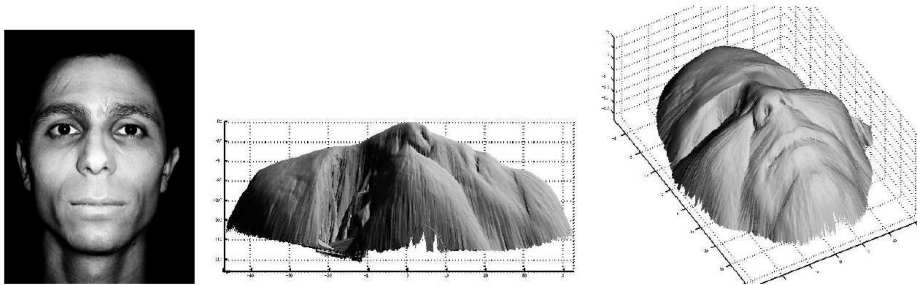


Figure 1.5: Illustration of shape from shading on a real face image, from [PF06].

Based on the statements above, shape from shading methods are not well adapted to the environment of flight tests. Specifically, such methods require a perfect knowledge of

light sources and only work with strongly diffuse surfaces, while for aircrafts an important proportion of the reflections is specular. For these reasons, these methods were not considered in this work.

1.1.2.3 Shape from texture

A texture is a surface pattern with given regularity properties. From texture distortions, one is able to distinguish broadly its shape (as illustrated in Fig. 1.6), hence motivating researchers to develop methods to recover the shape of an object from its texture. To do so, the texture elements are detected (in Fig. 1.6, the elements are points) and the shape is estimated from the distortions between them. Distortions can also be found on the element of the pattern itself if the true texture is known. Most methods are working using priors on the surface model or texture shape and distributions ([KC89; LF06]), but recent work [VZ20] seek to remove prior necessity through the use of multiple neural networks.

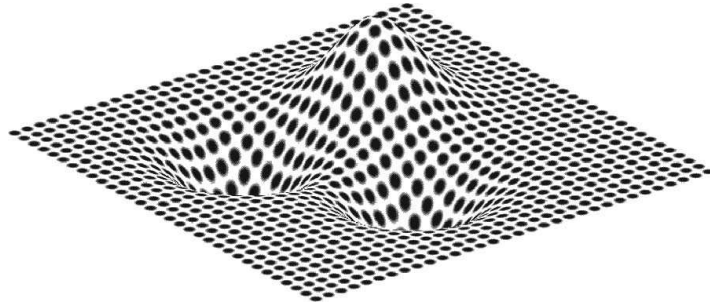


Figure 1.6: Shape from textures (from [Gur+06]).

Although these methods are definitely interesting for applications such as object perception, they are not suitable for metrological applications, as the resulting estimations of 3D shapes remain more qualitative than quantitative. Besides, in the case of our study natural textures are very sparse on the wing surface, and using additional external textures would be too complicated and onerous to comply with Airbus requirements.

1.1.2.4 Shape from focus motion

The shape from focus motion is a monocular method for depth reconstruction from sets of images. This method relies on the camera depth of field which varies in the scene by changing the distance between the camera and the object. Focus is determined by calculating pixel sharpness for each image. The spatial position of the sharpest pixels can then be measured, allowing us to reconstruct the 3D shape from the set of images (see Fig. 1.8). This method only requires one mobile camera and is not affected by occlusions. However, the process of measuring pixel sharpness relies on the high frequencies of the images, and thus requires textured scenes [Bil+13; MMI17; Mar18; Moe+15].

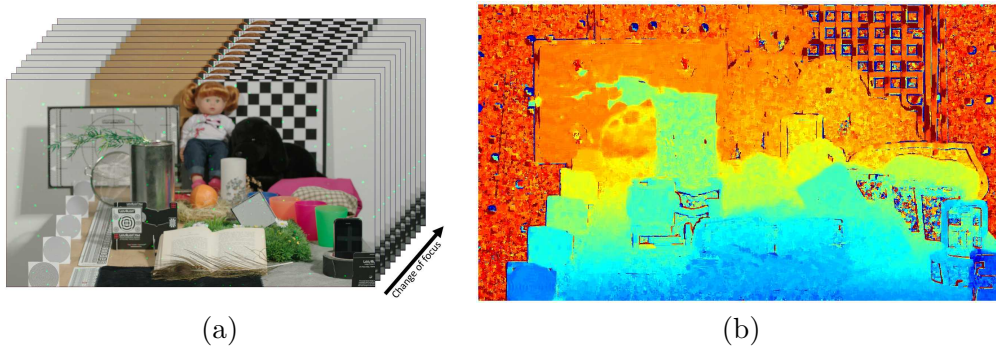


Figure 1.7: Example of a simple depth from focus reconstruction (from [Moe+15]): (a) - Input images with various focus, (b) - Depth map reconstruction.

The depth of field of a camera is the depth on the scene which appears sharp on the image. It actually represents the fact that all objects are not exactly projected on the sensor plane of the camera (see Fig. 1.7), but on another plane translated by a distance δ , thus creating a blurry point of radius r on the image. The depth of field is the depth of region in the scene for which this radius is small enough to consider the points as sharp. More details about these optical principles are given in [Bil+13]. These methods also require to be certain that blur on the image arises from the defocus at the object, i.e., no motion blur (object or camera movement during the acquisition) or Gaussian blur (atmospheric perturbations or lens errors) are tolerated. Moreover, to get high depth resolution, the depth of field for each image must be thin, which means that pictures must be taken from a close distance to the object.

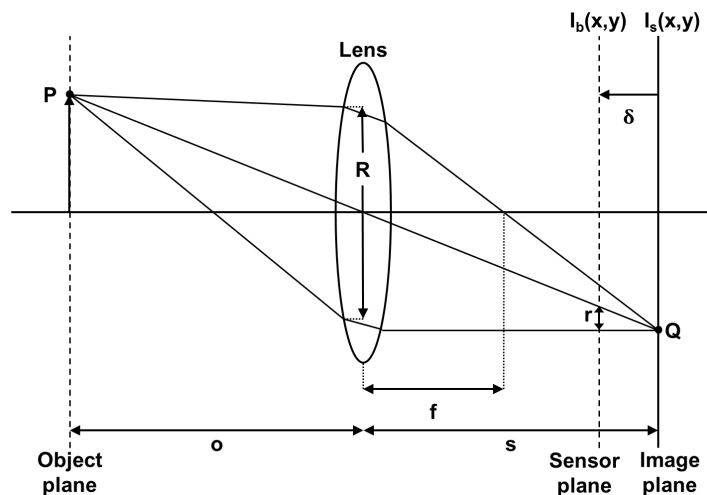


Figure 1.8: Formation of an unsharp image illustrated from optical design (from [Bil+13]).

It is also worth mentioning shape from defocus methods, for which the measure of blur amount, or blur radius is used to determine the distances in the scene. In this case, to measure

the blur, the image is considered as a sharp image convolved with a spatially variant point spread function as considered in deconvolution methods. More details about this approach are given in [TF05; FS05].

To be able to reconstruct depth on long range of a wing using this method would require taking many pictures with various focus. In addition of being too complex to operate, it would not work in our case since the scene and cameras are not static during flight tests. Moreover, this method would require the presence of texture that is lacking on the surface of the wing.

1.1.2.5 Shape from shadow

When a light source moves around a 3D object, moving shadows the 3D shape of the object to be recovered. To do so, the method requires the knowledge of the light source position [Sav+07]. In the case of unknown light source, it can be approximated, under some conditions, as circular motions of the light source. However, these methods are computationally costly. In the case of a known 3D model of the object to measure, the light source position can be deduced from simulation of shadow images on the known model [YSS10].

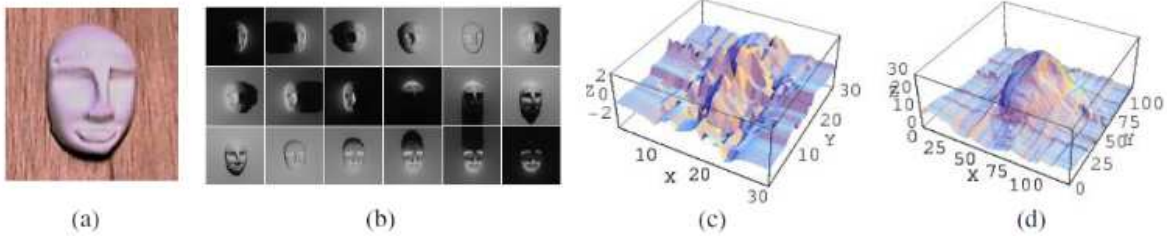


Figure 1.9: Real image experiment from [YSS10]: (a) The face model used in this experiment, (b) Example of images, (c) Initial recovered shape, (d) Final recovered shape.

Shadow graphs are used to represent shadow information in images, introduced by [YC02]. They are weighted directed graph, whose nodes are sets of points of the surface section, edges are pairs of points, and edge costs represent the relative point heights. The first graph represents shadow constraints, which states that the height $h(\mathbf{x})$ of a point \mathbf{x} in the shadow region $[\mathbf{x}_a, \mathbf{x}_c]$ delimited by two points \mathbf{x}_a and \mathbf{x}_c , is below the line passing through the points $(\mathbf{x}_a, h(\mathbf{x}_a))$ and $(\mathbf{x}_c, h(\mathbf{x}_c))$, as illustrated in Fig. 1.10. Denoting as ϕ the light source orientation, the shadow constraint can be written

$$h(\mathbf{x}) \leq h(\mathbf{x}_a) - \tan \phi(\mathbf{x}_a - \mathbf{x}), \forall \mathbf{x} \in [\mathbf{x}_c, \mathbf{x}_a], \quad (1.2)$$

where $-\tan \phi(\mathbf{x}_a - \mathbf{x})$ is the cost of the graph edges from \mathbf{x}_a to \mathbf{x} . The same type of relation holds for points without shadows, called the anti-shadow constraint, leading to another graph with cost $\tan \phi(\mathbf{x} - \mathbf{x}_l)$:

$$h(\mathbf{x}) \leq h(\mathbf{x}_l) + \tan \phi(\mathbf{x} - \mathbf{x}_l), \forall \mathbf{x} \in [\mathbf{x}_l, \mathbf{x}_e]. \quad (1.3)$$

Finally, finding the shortest paths for all the pairs of nodes allows the 3D shape of the surface to be recovered. However, this process is computationally expensive.

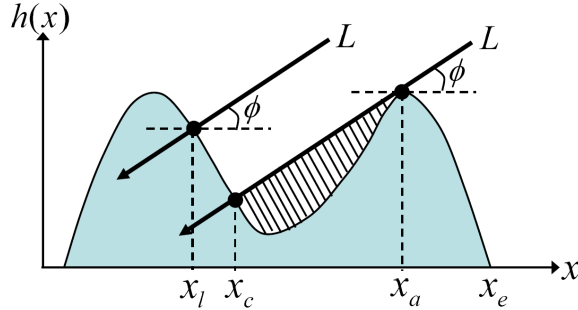


Figure 1.10: Shadow constraints and anti-shadow constraints (from [YSS10]).

Again, the method presented here depends on controlled light, which will not be available during flight, and thus was not considered hereafter.

1.1.2.6 Shape from silhouettes

Shape from silhouettes is a shape reconstruction method that reconstructs the 3D shape using the object silhouettes acquired from several surrounding cameras. This requires using multiple views of the same object without occlusions, hence the use of multiple cameras surrounding the object, with strong calibration constraints, or one camera and a moving object. Silhouettes are easily and quickly detected on images. However, the method is sensitive to noise [GM14]. These methods have potential in highly controlled environment. However in many applications where images are taken in a non-controlled environment, large errors are generated by occlusions, wrong background subtraction (due to shadows or illumination changes, similarities between object and background, etc.), noise or even calibration errors. Finally, shape from silhouettes is not applicable in our case because the test environment is not controlled, and because of the camera position constraints.

1.1.2.7 Deflectometry

Deflectometry is a method to reconstruct the shape of an object, based on the reflection of a pattern on its surface. Mathematical bases of such a reconstruction are well detailed in [KKH04]. To obtain accurate results, the reflection of a known pattern has to be recorded. The method requires also a surface with perfectly specular reflects.

Deflectometry was tested in the A340 BLADE (Breakthrough Laminar Aircraft Demonstrator in Europe) project [Bla]. The principle of this approach is to consider the reflection of a known pattern on a surface, and recover the local surface deformations from the reflected pattern deformations. To use this approach, strong assumptions on surface properties are

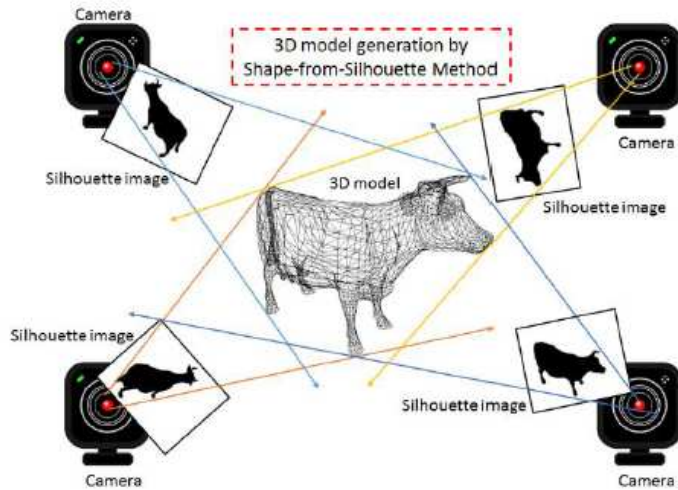


Figure 1.11: Shape from silhouettes method to generate 3D model data using multiple RGB cameras (from [Xia+16])

necessary (geometry, reflecting properties), which is only feasible within very specific applications. In the framework of the BLADE project, a pattern was painted on the wing edge, reflected on the wing, and reflections were observed by cameras installed at the wing tip (see Fig. 1.12b). To ensure good reflection of the pattern, a specific paint was used on the wing surface. Note that deflectometry requires too complex and onerous installation to fulfill the preconditions of the current application.

1.1.2.8 Photogrammetry

Photogrammetry regroups methods that estimate 3D positions and shape of objects from the measurement and interpretation of one or several 2D images. Note that projecting 3D points onto 2D images necessarily induces some information loss. The basic principle of photogrammetry is to recover this information by expressing and solving the geometric equations corresponding to the projections of points on several views (see Section 1.2). These equations include 3D point coordinates of the scene, their 2D observations on the images, but also the intrinsic (focal length, sensor size, etc.) and extrinsic parameters (orientation and position). While most of the parameters are unknown, depending on the application, some can be fixed to predefined values to simplify the problem. In particular, finding correspondences of 2D observations from one image to another is a major challenge of these methods. Specific hardwares and algorithms were developed to perform their detection and matching (more details in Sec. 2.2.2.2).

The wide range of applications covered by photogrammetry can be classified by several factors such as the number of measurement images (single-view, stereo or multiple view photogrammetry), the method of recording (plane table, digital photogrammetry, videogrammetry) or the distance between cameras and objects (satellite, close-range, etc.). This variety

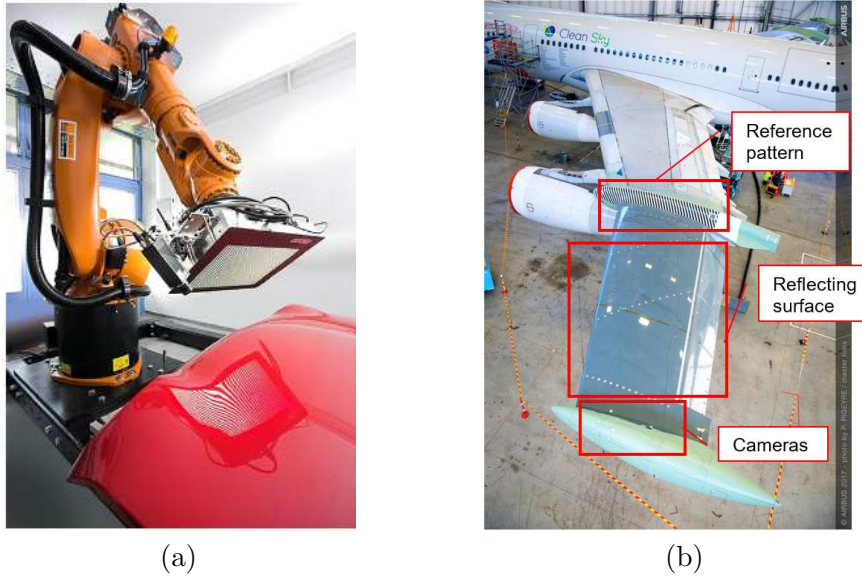


Figure 1.12: Illustration of the deflectometry method. (a) - Deflectometry applied to 3D reconstruction of a car surface, using robot arm (from [BW10]), (b) - BLADE wing [Bla] with deflectometry installation.

of approaches makes photogrammetry a flexible and scalable system that can be adapted to meet the requirements of 3D wing reconstruction. As a matter of fact, a photogrammetry system is already used by Airbus to estimate wing deformations, but does not comply with the new key factors listed in introduction. This system is based on retro-reflective targets stuck orthogonally to the wing surface, and observed by cameras installed on windows. The estimation approach is similar to the studies presented in [Bar07] and [Liu+12] (see Fig. 1.13 for illustration). To limit distortions, standard windows in front of the cameras are replaced by metrological ones. During flight, cameras are triggered synchronously with flashes, illuminating the targets to easily and accurately detect targets. Finally, the accurate position of targets and cameras is initialized through a long calibration phase, and cameras are attached such that their locations remain fixed with respect to the aircraft.

Though this system provides very satisfying results during tests, it has several drawbacks. First, the use of protuberant targets on the wing induces aerodynamic disturbances, which can alter the aerodynamic properties of the wing and reduce the flight domain of the aircraft, thus enforcing the need for dedicated flights. Secondly, to reduce the camera motions during flight, the mechanical fixations of the cameras are intrusive and not easy to install. Another drawback is the time consuming calibration step required for the system, which could be lightened. Finally, the method provides only sparse measurements associated with target locations, and the necessary time to recharge the flashes does not allow to record several images per second to be recorded. Nonetheless, many improvements of this system can be considered to meet the new requirements of this application. Note that using cameras is advantageous as this technology is already commonly used and mastered in Airbus.

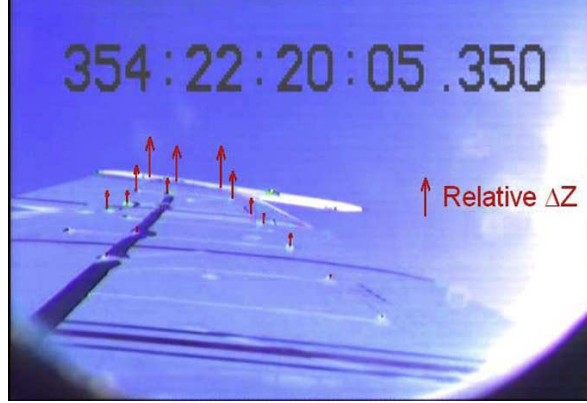


Figure 1.13: Example of an aircraft wing imaged using a photogrammetry system (from [Liu+12])

1.1.2.9 Stereo camera

Stereo camera is a type of camera inspired by human visual depth perception and is a particular application of photogrammetry using two views, where camera parameters are fixed and determined by calibration, simplifying the reconstruction problem. To ensure that camera parameters are unchanged during tests, devices integrate cameras into a rigid shell. Hence, baseline between cameras is usually small, and accuracy of the systems is better at close range. More details on a two view reconstruction method are given in Section 1.2.

In the case of this study, the stereoscopy approach using fixed cameras is not applicable because of the long distance between cameras and object to reconstruct. To adapt this method, it would be necessary to guaranty that cameras are fixed with a relative distance of about 10m, which cannot be achieved inside a flying aircraft.

1.1.2.10 3D digital image correlation

3D digital image correlation (3D DIC) is another photogrammetry approach dealing with the issue of finding correspondences between views. Using pairs of cameras, this technique combines image correlation and photogrammetry algorithms to recover the 3D shape and deformations of a surface. Given two images I and J , a $n \times m$ subset of I , centered at pixel (x, y) , is searched on J by calculating its cross correlation with all $n \times m$ subsets of J . At pixel (i, j) of J , the cross correlation can be calculated as

$$c_{i,j} = \sum_{u=-n/2}^{n/2} \sum_{v=-m/2}^{m/2} I(x+u, y+v)J(i+u, j+v). \quad (1.4)$$

Variations of this formula include normalized correlation or least-squares. Finally, correspondences are found by determining the highest values of $c_{i,j}$. To capture image correlations, the method relies on the presence of discriminative textures over the entire object. Thus, random

or pseudo-random patterns (or speckle patterns) are applied on the object of interest, allowing high definition of the 3D reconstruction. Furthermore, 3D DIC can also take into account object deformations from one image to another to adapt the shape of the search window in \mathcal{J} ([Apa+15; Hua+17]). This approach is therefore popular for the estimation of material deformations under stress, in laboratory conditions ([Yan+09; RBD17]).

3D DIC was implemented and tested for A380 and A350 aircrafts [Bod+13] under the name of IPCT (image pattern correlation technique). Stickers of random patterns were stuck on the wing surface (see Fig. 1.14), and deflections of the surface were calculated using a simplified deformation model of the wing as a function of a normal load under static conditions. Similarly to deflectometry, this method gave interesting results, but the required installations are intrusive and onerous, and hence should be avoided.



Figure 1.14: Example of pattern stripe installed for IPCT tests for an A380 in 2009.

1.1.2.11 Structure from motion

Structure from motion (SFM) uses photogrammetry on continuous series of images taken with small camera displacements between each acquisition. This is a particular case of photogrammetry (more than 3 views) in which the matching step between each image is facilitated by limited differences between consecutive images ([MMM13; SSS06; HTP10]). First, feature points of the scene are detected and matched among the set of images using adapted methods such as SIFT [Low04]. Once the points have been detected and matched between all the images, three main approaches may be used to recover the 3D structure. The first one is an incremental method. It starts with a reconstruction based on two views, and iteratively adds the new views and 3D points to the system. The first pair of images is usually defined for a pair with high feature matching rate and wide distance between cameras. Though this method may give good results, it is sensitive to initialization and may suffer from error accumulation along the iteration. An alternative approach that is less sensitive to the drift problem is the hierarchical method. In this case, the views are hierarchically ordered in a tree, and then processed from root to leaves. Finally, the third approach, referred to as global, finds all rotations between pairs of cameras and uses these rotations to solve the 3D reconstruction

problem for all views simultaneously.

In the case of wing reconstruction, SFM would require many images of the wing acquired simultaneously with close positions of the cameras, requiring a complicated installation.



Figure 1.15: Structure from motion example, left: set of images, right: 3D reconstruction using the reconstruction implementation *Multi-View Environment* [FLG14].

1.1.2.12 Conclusion

Passive reflection methods take advantage of information naturally present in a scene that is transmitted to a camera sensor using ambient light. The diversity of the methods in this category allows us to make the best use of the information contained in one or more images. In particular, these approaches are very useful in application cases where 3D reconstruction was not foreseen, and should be performed with the best accuracy with the available information. On the other hand, the 3D estimate of the interest object is often imprecise and lacks robustness, because of uncontrolled variations in ambient light or due to a lack of texture. To ensure the quality of a 3D estimation, it may be necessary to add targets to the object of interest.

1.1.3 Reflective Active Methods

As opposed to passive methods that rely on the reflections of ambient light, reflective active methods have emitters and send the waves that are reflected on the object. These waves can be used to add information to the scene and improve the passive methods seen above, or their physical properties can be directly exploited to achieve 3D reconstruction. This section describes some of these approaches and discusses their relevance for wing reconstruction.

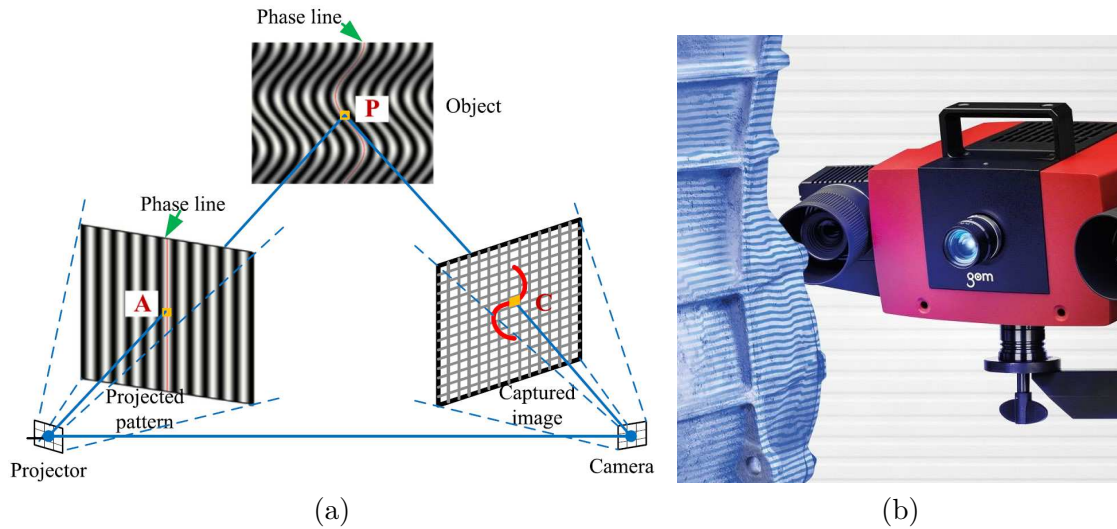


Figure 1.16: (a) - Illustration of the structured light method (from [Zha18]), (b) - Example of 3D scanner using structured light (ATOS Compact Scan, from GOM [Gom]).

1.1.3.1 Structured Light

Finding corresponding features between views is a central challenge in photogrammetry approaches, which will be one of the main subjects addressed by this manuscript. The method of structured light aims at resolving this issue by adding or replacing one of the cameras by a light projector, that projects a coded pattern on the scene of interest. The features reflected on the objects can efficiently be detected on camera images to create robust correspondences with other cameras and the projected image (see Fig. 1.16). Light source is typically visible or infrared light, and the projected patterns have various encoding appearance depending on the projector, the object and the quality of measurement. As reviewed in [Zha18] and [VD16], many encoding methods have been developed for the task. Amongst them, one can cite the use of statistically random patterns, binary coded patterns or sinusoidal phase encoding. The first one creates unique kernels of pixels that can be easily detected on images, but with a resolution limited by the size of these kernels, sensitive to noise (technology used for instance by the Microsoft Kinect, Intel RealSense or Apple Iphone X). The second one projects a sequence of black and white stripes on the object to create binary coded patterns, that are unique and discrete in one direction, and uses object features detected along the other direction. Going further, the third approach finds correspondences in both directions continuously by using sequences of structured patterns varying sinusoidally. This method allows a very good resolution of the reconstruction with very good quality. Industrial products available nowadays achieve sub-millimetric uncertainty at about one meter.

In the case of 3D wing reconstruction, the absence of information is a problem that could be mitigated by using structured light technology. However, the dimension of the aircraft implies that the light projector should be powerful enough to illuminate the wing tip such that it is clearly seen on cameras placed inside the aircraft cabin. Moreover, with tests occurring

mostly during the day, the intensity of the projected light should be brighter than the sunlight above the clouds. Such solution could be imagined using powerful lasers combined with coded apertures (see [Kaw+12]), but would reduce the resolution and quality of the reconstructions.

1.1.3.2 Interferometry

Interferometry is another method of non-contact reconstruction using active light emission. Using a beam splitter on the path of a light beam, the interferometer evaluates the interference of two reflecting wavefronts of the same beam, one reflecting on a reference surface, and the other reflecting on the inspected surface. The intensity of the resulting interference pattern conveys the information of surface height, which can therefore be recovered by analyzing all the points of the interference fringes. Interferometry allows a high quality of surface inspection, which makes it popular for fine applications such as estimation of microscopic shapes or bumps inspection in automotive industry. More details on this technology can be found in [Gro15].

At the moment, interferometry only works on small range ($< 1\text{m}$) and in a controlled environment. For instance, it is shown in [Gro15] that interferometers do not work well in the presence of vibrations. For these reasons, interferometry is not a conceivable solution to the problem of this work, and will not be further investigated.

1.1.3.3 Time-of-flight cameras

Time-of-flight (ToF) cameras are sensors that record not only light intensity, but also depth information in each image pixel (see an example in Fig. 1.17). To this aim, cameras are equipped with emitters of infrared light illuminating the scene. Reflection of the infrared waves is recorded on pixels of the sensor and processed to recover depth information. Two methods are available, using either pulsed light or continuous waves. For the first approach, the distance d to the object is determined from the delay between pulse emission and reception after reflection on the object. This delay is recorded on the pixel using two out-of-phase windows C_1 and C_2 , of size equal to the pulse duration Δt , for which the charge accumulated are Q_1 and Q_2 (as illustrated in Fig. 1.18a). The distance can be computed as

$$d = \frac{c\Delta t}{2} \frac{Q_2}{Q_1 + Q_2}, \quad (1.5)$$

where c is the speed of light. The second method uses continuous emission of light at frequency f and estimates the distance from the phase shift $\Delta\phi$ of the reflected light. In this case, light intensity is recorded on four windows with a phase shift of 90 degrees each (see Fig. 1.18b), and the distance d is expressed as

$$d = \frac{c}{4\pi f} \Delta\phi, \quad (1.6)$$

with

$$\Delta\phi = \arctan\left(\frac{Q_3 - Q_4}{Q_1 - Q_2}\right). \quad (1.7)$$

The choice between the two approaches is essentially guided by the volume of the scene. Within the first approach, the maximum distance is defined by the duration of the pulse ($d_{max} = \frac{c\Delta t}{2}$), while with continuous emission it is limited to a phase shift of 2π , and hence by the frequency of the signal ($d_{max} = \frac{c}{2f}$, which is the distance of signal aliasing). To overcome distance limitation, some cameras work with various frequencies. More details about these methods are available in [Li14; HLK13].

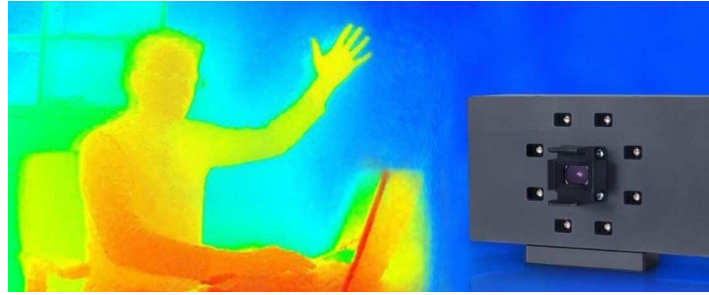


Figure 1.17: Example of ToF camera (from Basler) and depth image that it can capture.

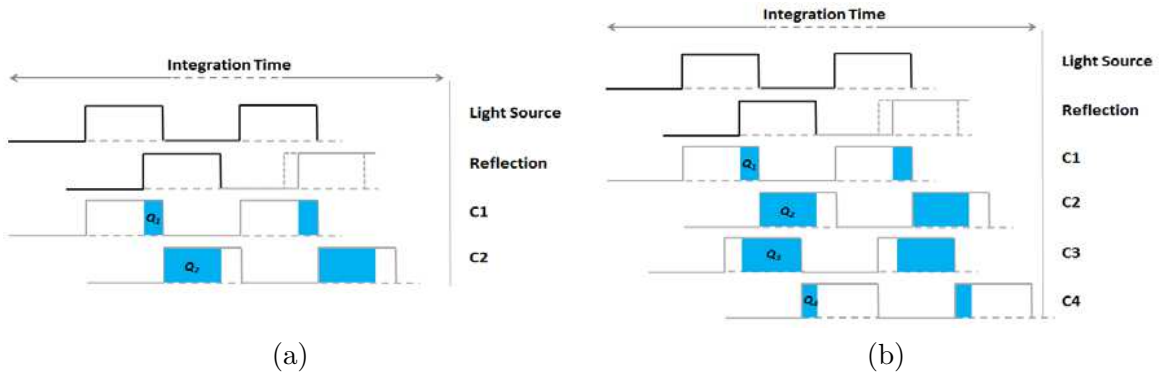


Figure 1.18: Illustration of the ToF method (from [Li14]): (a) - pulsed, (b) - continuous-wave.

ToF cameras are simple to use, cheap, fast and allow real time computation of depth maps regardless of the scene texture, making them good candidates for robotic applications such as navigation or 3D object detection. Nonetheless, they have several drawbacks. First, multiple reflections of a light beam may generate artifacts on the depth image, intense sunlight can quickly saturate pixels, mitigating their use for outside applications such as wing reconstruction in flight. These drawbacks coupled with power limitations of the light emitters, bound the volume of the reconstructed scene. Common ToF cameras have a centimeter accuracy but only up to about 10m. This is another limitation of ToF cameras preventing their use in this study.

1.1.3.4 Other time of flight methods

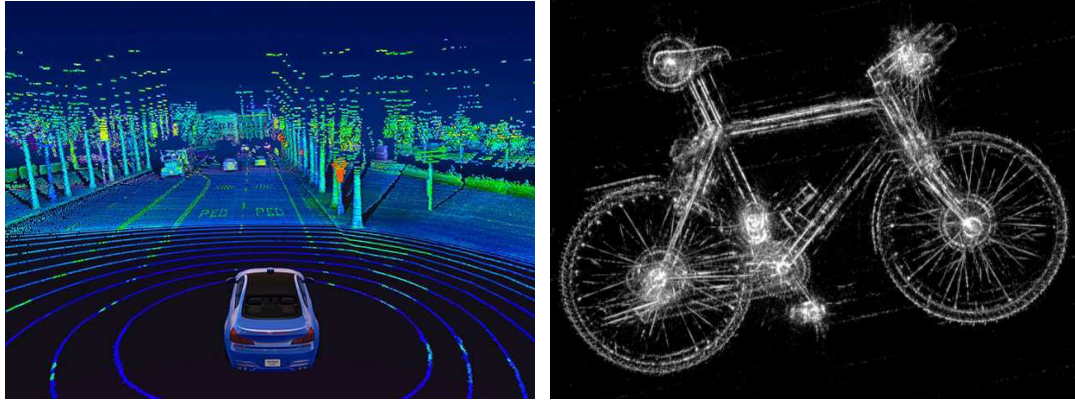
Estimating the distance from the time needed by a signal to reflect from an object is a method that can be applied using various signal types. While the camera presented above uses infrared light, sonar uses sound [Mou17], radar uses electromagnetic waves [Gei+16; Car+14], and lidar uses ultraviolet, visible or infrared light [Fil+17; Tac+19].

To be able to localize the position of the reflecting object in a scene, two approaches can be used. First, emitters can be designed to narrow the angular range of the signal. In the case of radar and sonar, this is done by using parabolic antennas to generate a narrow lobe of emission. For light waves, the use of lasers permits to create thin rays of light for an accurate positioning of the targets. Then the entire scene can be scanned using a mechanical orientation of the emitter. The time necessary to make a scene scan is a discriminative criteria to the use cases (3D laser scanners take minutes to scan a scene while embedded lidars for robotics can be used in real time, achieving only partial scene scan). The second approach is to send signals in several directions at once. In sonar and radar systems, this can be performed using beamforming with arrays of sensors, that allows us to orient angularly narrow lobes of a signal by adjusting its phase. For light, ToF cameras can be used, or similarly flash Lidar can project divergent light beam to illuminate the entire scene and acquire directly a snapshot. However, in this case, the intensity of the light is lowered and limits the depth range.

Because they use active technologies, ToF systems can be used robustly in varying environment, day and night. Moreover, waves are more or less impacted by environmental variations depending on the technology. Radar for instance can detect object through clouds, and ultrasound images are not impacted by smokes, where light would be occluded. For these reasons, ToF technologies are widely used in navigation, obstacle detection and perception applications such as autonomous car development. As a matter of fact, radar, lidar and even ultrasound imaging are combined with cameras to provide more reliable vehicles ([Ond+20]).

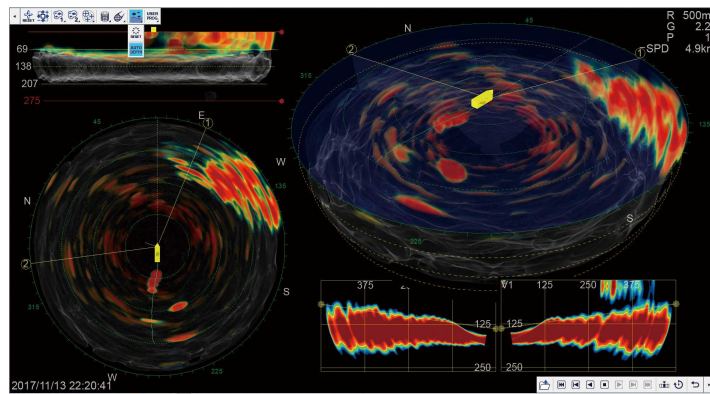
An important criterion for the application addressed in this work is the quality of 3D estimation over the volume of a wing. On this aspect, sonar is limited because of the frequency and propagation speed of the sound waves in the air (slower than in water). Common ultrasound sensors can detect objects in a range of about 10cm to 5m with an uncertainty of about 5cm, which is not enough to cover an entire wing. Regarding the radar technology, even though some recent works have proven their ability to reach high accuracy measurements ([Car+14]), embedded systems are currently not as accurate and hardly achieve centimeter uncertainty (in both sensor plane and depth). Besides, the use of radar on aircraft in flight is restricted because it can provoke perturbations of other equipments, which is not compliant with the requirements of the application. Finally, lidar scanners can guarantee very high definition and millimeter accuracy at about 40m when several minutes are available to perform the scan. In the case of our application, given the vibrations of the entire aircraft, scan should be as fast as possible. Today, faster lidar scanners used for real time applications of autonomous cars can acquire depth on sections of the scene at the frequency of about 20Hz, with a centimeter accuracy of range. The very good performance of such devices, along with their small size and ease of use (returning directly point clouds), makes them strong candi-

dates for 3D wing reconstruction. Flash lidar on the other side cannot be used on aircraft during the day as sunlight intensity would be too high with respect to the system emitted light.



(a)

(b)



(c)

Figure 1.19: Illustration of 3D reconstruction using Lidar (a), radar (b) and sonar (c) (from [Vel], [Car+14] and [Fur]).

1.1.4 Conclusions on selected method

This section presented various methods to estimate the 3D information of a scene without contact. From the existing technologies, two can fulfill the objectives of 3D wing reconstruction: photogrammetry and lidar. On the one hand, photogrammetry is a flexible solution that can be easily adapted to reach the desired accuracy by adjusting the number of cameras, the sensor sizes and the focal lengths, even with restricted camera positions. Using video cameras, the required frequency of measurements can be reached, and intrusivity can be limited by using flush stickers on the wing or natural features related to its surface. Besides, cameras are already in use on test aircraft in Airbus, and the acquisition process has been formalized during years of flight tests. Therefore, camera installation on windows is easy and the recording

tests lasting several hours is achievable without further development. On the other hand, lidar can also deliver accurate 3D reconstruction, with similar frequency, and its ability to record directly point clouds simplifies their processing. In addition, these sensors can be designed with small sizes, and simple installations at aircraft windows may be considered. The quality of measurements for both of these methods will however be degraded by the disturbances of the uncontrolled environment. In this study, we decided to focus on photogrammetry, given that cameras are already available and limit the complexity of integration onto the aircraft.

1.2 Photogrammetry

1.2.1 Camera model and calibration

Before detailing the process of reconstructing 3D objects from 2D images, it is necessary to understand the process of image acquisition. A common representation of the camera is the pinhole model, illustrated in Fig.1.20. This model considers the camera as a box with an opening hole whose diameter is almost zero. Light enters through this hole, called the projection center, to be capture on the image plane (sensor). The distance between the image plane and projection center is the focal length f . The image is then inverted, and common representations of the camera place the projection center behind the inverted image plane.

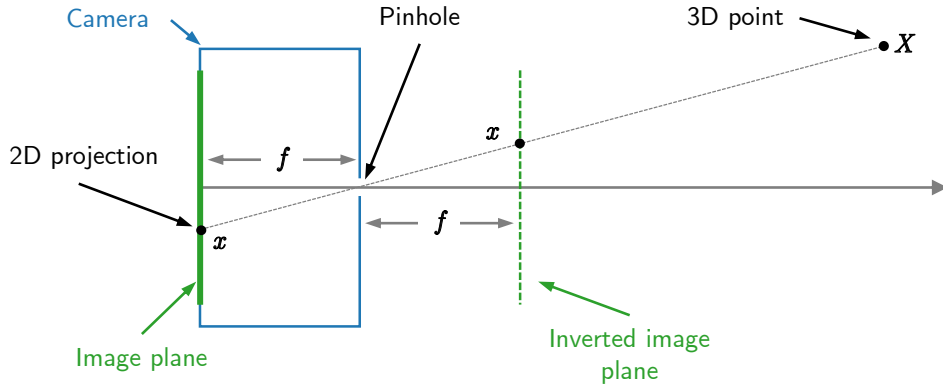


Figure 1.20: Sketch of the pinhole model.

There are three main coordinate systems to represent an object view, the real world, the camera, and the image systems (Figure 1.21). The real world 3D point \mathbf{X} is projected onto the camera system using the matrix $\mathbf{P} = [\mathbf{R}, -\mathbf{R}^T \mathbf{t}]$, composed of a 3×3 rotation matrix and a 3×1 translation matrix. The camera coordinates are then projected to the image coordinate using the matrix

$$\mathbf{K} = \begin{bmatrix} f_x & s & c_x \\ 0 & f_y & c_y \\ 0 & 0 & 1 \end{bmatrix}, \quad (1.8)$$

where f_x , f_y , c_x , c_y and s are the intrinsic camera parameters. f_x and f_y are the focal

lengths expressed in millimeters per pixel over the x and y axis of the sensor, c_x and c_y are the coordinates of the image center in pixel, and s is the skew coefficient, expressing non-orthogonality between the x and the y axis, usually neglected. The global camera equation can be written

$$\mathbf{x} = \frac{1}{c} \mathbf{K} \mathbf{l}, \quad (1.9)$$

with

$$\mathbf{l} = (a, b, c)^T = [\mathbf{R}^T, -\mathbf{R}^T \mathbf{t}] \begin{pmatrix} \mathbf{X} \\ 1 \end{pmatrix}. \quad (1.10)$$

In a two-camera system, the first camera can be set as the real world system leading to $\mathbf{P}_1 = [\mathbf{I}, \mathbf{0}]$ and $\mathbf{P}_2 = [\mathbf{R}, -\mathbf{R}^T \mathbf{t}]$. With real camera sensors this representation of the

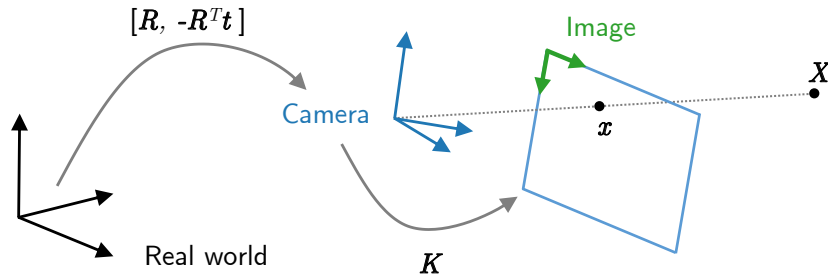


Figure 1.21: The different coordinate systems and mappings. From left to right: real world, camera and image coordinate systems.

inner parameters is inaccurate, and will deviate from the pinhole model. Indeed lenses induce image distortions, even when using high quality devices. This distortion is composed mostly by radial and tangential distortions (see Fig. 1.22), which arise from the default of the optical system (lens default and alignment imperfections for instance). Radial distortions curve straight lines, while tangential distortions influence the proportion of the image distances. Thus, the pinhole model must be adapted, as in [MN12] or [Sag+05]. A simple rule is given in [Kle14] to recover an undistorted image point $\mathbf{p}_u = (x_u, y_u)$ from a lens-distorted image point $\mathbf{p}_d = (x_d, y_d)$, as:

$$x_u = x_0 + (x_d - x_0)(1 + \kappa_1 r_d^2 + \kappa_2 r_d^4 + e_x) \quad (1.11)$$

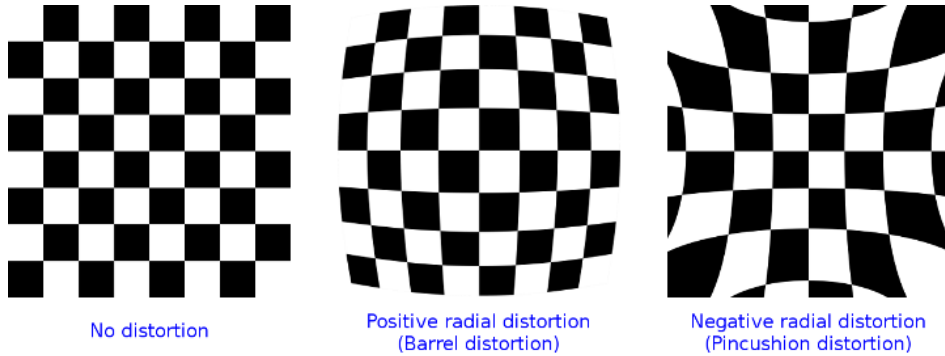


Figure 1.22: Illustration of the camera distortions (from [Ope]).

$$y_u = y_0 + (y_d - y_0)(1 + \kappa_1 r_d^2 + \kappa_2 r_d^4 + e_y), \quad (1.12)$$

where r_d is the radial distance of \mathbf{p}_d to the principal point, e_x and e_y are small negligible errors, and κ_1, κ_2 are two radial distortion coefficients. Taking only two coefficients to express the distortions already corrects more than 90% of the radial distortion ([Kle14]). More complex models taking more distortion coefficients like tangential distortions can also be used for better correction. Before a test, lens distortion should be calibrated for each camera. Once the calibration parameters are known, distortions can be corrected and the pinhole model can be used. Moreover, calibration allows all the parameters of the cameras to be recovered, such as focal length, principal point, but also extrinsic parameters of camera positions (note that if cameras are moved during the test, extrinsic parameters will change from the calibration). Calibration methods can be declined into three categories, depending on the references used:

- **Laboratory calibration:** These calibrations are performed by manufacturers, using specific instrument like goniometers, collimators or other optical alignment techniques where imaging direction or angles of light rays are measured through the lens of the camera.
- **Test field calibration:** This is the usual method for users. Using targets with known positions or geometry properties, reference objects or calibration charts [Zha00], known correlations between 3D reference and the image can be injected into the previously established distortion and pinhole model to recover the camera properties.
- **Self-calibration:** when using several views of a static object with targets or rich texture, photogrammetric process allows one recover the camera parameters without prior calibration.

1.2.2 Two view reconstruction

This subsection introduces the fundamentals of the camera model and epipolar geometry. Their understanding is necessary for the next sections. The detailed theory can be found in [HZ04].

1.2.2.1 Epipolar geometry and fundamental matrix

We consider here two cameras, with their projection centers \mathbf{C}_1 and \mathbf{C}_2 , looking at a 3D point \mathbf{X} . We call epipolar plane π a plane resulting from the three points $\mathbf{C}_1, \mathbf{C}_2$ and \mathbf{X} (see Figure 1.23). The epipolar geometry of our system is the intersection geometry of the plane π and the two image planes. The epipolar constraint states that the points $\mathbf{C}_1, \mathbf{C}_2, \mathbf{X}$, as well as the image points \mathbf{x} and \mathbf{x}' are coplanar.

Moreover, if we only know the projection \mathbf{x} of \mathbf{X} in the first image plane, the points that can project to this image point lie on a line in the 3D space. The projection \mathbf{l}' of this line in the second camera image is called epipolar line. Finally the epipol \mathbf{e} is the intersection of all

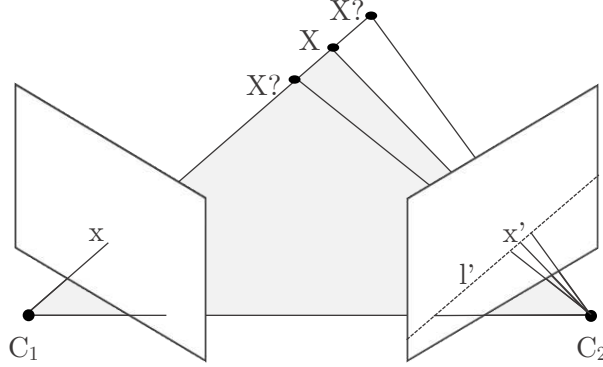


Figure 1.23: Epipolar Geometry - Two cameras represented by their centers C_1 and C_2 observe a 3D point \mathbf{X} . The image point \mathbf{x} back-projects to a ray defined by C_1 and \mathbf{X} , imaged as the epipolar line \mathbf{l}' on the second image. The image point \mathbf{x}' of \mathbf{X} has to lie on this line.

epipolar lines. It is the projection of the second camera center on the image plane. Each point \mathbf{x} in the first image is mapped to a line \mathbf{l}' in the second system. This mapping is represented by the fundamental matrix \mathbf{F} , such that

$$\mathbf{l}' = \mathbf{F}\mathbf{x}. \quad (1.13)$$

Thus, if a point \mathbf{x}' corresponds to a point \mathbf{x} in the first view, \mathbf{x}' lies on the epipolar line $\mathbf{l}' = \mathbf{F}\mathbf{x}$ yielding $0 = \mathbf{x}'^T \mathbf{l}' = \mathbf{x}'^T \mathbf{F}\mathbf{x}$. As a consequence, for any pair of corresponding points \mathbf{x}, \mathbf{x}' , the fundamental matrix satisfy an epipolar constraint

$$\mathbf{x}'^T \mathbf{F}\mathbf{x} = 0. \quad (1.14)$$

Moreover, \mathbf{l}' is passing through \mathbf{x}' and the epipole \mathbf{e}' . Thus, it can be written as $\mathbf{l}' = \mathbf{e}' \times \mathbf{x}' = [\mathbf{e}']_{\times} \mathbf{x}'$, where \times is the cross product and $[\mathbf{e}']_{\times}$ is the skew symmetric matrix

$$[\mathbf{e}']_{\times} = \begin{pmatrix} 0 & -e'_3 & e'_2 \\ e'_3 & 0 & -e'_1 \\ -e'_2 & e'_1 & 0 \end{pmatrix}. \quad (1.15)$$

Furthermore, it is shown in [HZ04] that \mathbf{x}' can be written as $\mathbf{x}' = \mathbf{H}_p \mathbf{x}$, where \mathbf{H}_p defines the transfer mapping from one image to another via any plane \mathbf{p} . Thus, we have

$$\mathbf{l}' = [\mathbf{e}']_{\times} \mathbf{H}_p \mathbf{x} = \mathbf{F}\mathbf{x}$$

and finally $\mathbf{F} = [\mathbf{e}']_{\times} \mathbf{H}_p$. Since $[\mathbf{e}']_{\times}$ is of rank 2 and \mathbf{H}_p is of rank 3, the rank of \mathbf{F} is 2. Therefore,

$$\det(\mathbf{F}) = 0, \quad (1.16)$$

where \mathbf{F} is a 3×3 matrix with 9 entries, corresponding to the camera projection unknowns (3 for \mathbf{K} , 3 for \mathbf{R} and 3 for \mathbf{t}), among which we have an arbitrary scale, reducing the number of

degrees of freedom to eight. Since each point correspondence gives an equation using (1.14), \mathbf{F} can be recovered using eight point correspondences (which leads to the 8-points algorithm) explained briefly in Section 1.2.2.4. One can finally reduce the number of matching point to 7 using the constraint (1.16).

Once the fundamental matrix has been calculated, the projection matrices can be determined, and the 3D scene can be triangulated. Since in our case we know the inner parameters of the cameras, we will rather use another form of the fundamental matrix referred to as the essential matrix, which allows us to eliminate the projection ambiguity, and only requires 5 points to be solved (leading to the 5-points algorithm).

1.2.2.2 The Essential Matrix

The essential matrix is a refinement of the fundamental matrix, which assumes that the cameras are calibrated, i.e., that the matrix \mathbf{K} is known. In this case, the normalized coordinates $\hat{\mathbf{x}}$ of the image point \mathbf{x} are used. These coordinates are given by $\hat{\mathbf{x}} = \mathbf{K}^{-1}\mathbf{x}$ and the normalized camera matrices are $\mathbf{K}^{-1}\mathbf{P} = [\mathbf{R}, \mathbf{t}]$. If we assume $\mathbf{P}_1 = [\mathbf{I}, \mathbf{0}]$ and $\mathbf{P}_2 = [\mathbf{R}, \mathbf{t}]$, the fundamental matrix of this normalized camera pair is referred to as the essential matrix $\mathbf{E} = [\mathbf{t}]_{\times}\mathbf{R}$ satisfying the following relation

$$\hat{\mathbf{x}}^T \mathbf{E} \hat{\mathbf{x}} = 0. \quad (1.17)$$

The essential matrix has only five degrees of freedom - the rotation and the translation have both three degrees of freedom, minus one for the overall scale factor. As demonstrated in [May11, p. 39], this reduction in the number of degrees of freedom results in a constraint

$$2\mathbf{E}\mathbf{E}^T\mathbf{E} - \text{tr}(\mathbf{E}\mathbf{E}^T)\mathbf{E} = 0. \quad (1.18)$$

In addition, since \mathbf{E} is a fundamental matrix, it must also verify $\det(\mathbf{E}) = 0$ as in (1.16). Thus this matrix can be recovered using only a five-points algorithm, explained briefly in Section 1.2.2.5. However, the extra constraints are non-linear, which makes the estimation of \mathbf{E} more difficult. Thus the 8-point algorithm can be preferred in some applications.

1.2.2.3 From E to camera matrices

Since $\mathbf{E} = [\mathbf{t}]_{\times}\mathbf{R}$, we can decompose the essential matrix to recover camera matrices. Using the singular value decomposition (SVD) of \mathbf{E} (i.e., $\mathbf{E} = \mathbf{U}\text{diag}(1, 1, 0)\mathbf{V}^T$) and the matrix

$$\mathbf{W} = \begin{pmatrix} 0 & -1 & 0 \\ 1 & 0 & 0 \\ 0 & 0 & 1 \end{pmatrix}, \quad (1.19)$$

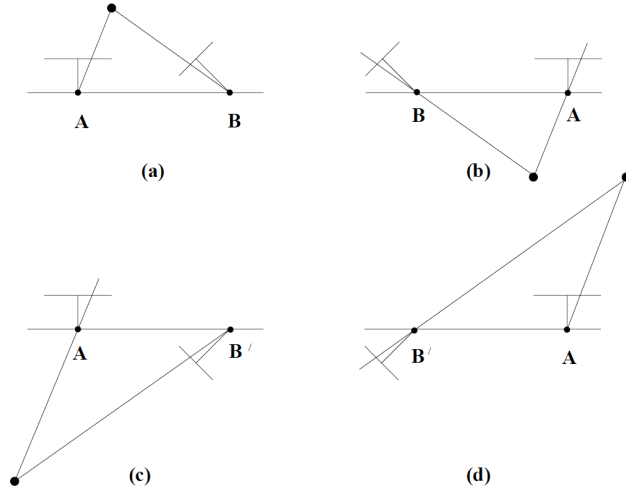


Figure 1.24: The four possible solutions for a calibrated reconstruction of P_2 from E . Between the left and right sides, one can observe the two possible translations $\pm \mathbf{u}_3$ of the camera B . Between the top and bottom rows, the camera B rotates of 180 degrees with respect to the baseline. Note that the only reconstructed point being in front of both cameras is displayed in (a) [HZ04]. The other solutions (b), (c) and (d) are not possible.

it can be shown that there are four solutions for P_2 [HZ04, p. 258]

$$P_2 \in \{UWV^T \pm \mathbf{u}_3, UW^T V^T \pm \mathbf{u}_3\}. \quad (1.20)$$

where \mathbf{u}_3 is the third column of U . Since $R \in \{UWV^T, UW^T V^T\}$, if $\det(UV) = -1$, R is not a rotation but a rotation composed with a reflexion, which is not a valid solution. Therefore, we have to select U and V such that $\det(UV) = 1$ in the SVD. The four corresponding solutions are shown in Fig. 1.24. Only one of these solutions corresponds to a 3D point cloud located in front of the two cameras. The correct solution can thus be selected by checking that the 3D points are in front of both cameras. This is usually done by checking the z coordinate of the projections $P_1 X$ and $P_2 X$, for any triangulated X .

1.2.2.4 The 8-Point Algorithm

As mentioned before, the fundamental matrix has 8 degrees of freedom, and thus can be calculated using 8 pairs of matching points from the two views. To do so, the 8-point algorithm starts with the equation

$$\mathbf{x}'^T \mathbf{F} \mathbf{x} = 0. \quad (1.21)$$

Denoting $\mathbf{x} = (u, v, 1)^T$, $\mathbf{x}' = (u', v', 1)$ and $\mathbf{F} = (f_{ij})_{1,\dots,3,j=1,\dots,3}$, the previous equation can be rewritten as

$$\begin{aligned} u'u f_{11} + u'v f_{12} + u' f_{13} + v'u f_{21} + v'v f_{22} + v' f_{23} + \\ u f_{31} + v f_{32} + f_{33} = 0, \end{aligned} \quad (1.22)$$

or

$$(u'u, u'v, u', v'u, v'v, v', u, v, 1)\mathbf{f} = 0, \quad (1.23)$$

where \mathbf{f} is the 9×1 vector with the entries of \mathbf{F} . For N point correspondences, one has

$$\begin{pmatrix} u'_1 u_1 & u'_1 v_1 & u'_1 & v'_1 u_1 & \cdots & v_1 & 1 \\ \vdots & \vdots & \vdots & \vdots & \cdots & \vdots & \vdots \\ u'_N u_N & u'_N v_N & u'_N & v'_N u_N & \cdots & v_N & 1 \end{pmatrix} \mathbf{f} = 0, \quad (1.24)$$

which can be rewritten in matrix form as

$$\mathbf{A}\mathbf{f} = 0. \quad (1.25)$$

Since the solution of this equation is not necessarily unique due to noisy point coordinates, (1.25) is usually solved using the least-square estimator. An interesting solution is to use the SVD of \mathbf{A} , i.e., $\mathbf{A} = \mathbf{U}\mathbf{D}\mathbf{V}^T$, and take the last column of \mathbf{V} as the solution vector \mathbf{f} . This solution is the singular vector corresponding to the smallest singular value of \mathbf{A} . Note that this solution minimizes $\|\mathbf{A}\mathbf{f}\|$ subject to the condition $\|\mathbf{f}\| = 1$ (where $\|\cdot\|$ denotes the Euclidean norm). An important property of the fundamental matrix is its singularity, or precisely its rank that should equal 2. To enforce this property using the calculated SVD, one can search the matrix \mathbf{F}' that minimizes the Frobenius norm $\|\mathbf{F} - \mathbf{F}'\|$ (i.e., the square root of the sum of squares of all entries) with the constraint $\det(\mathbf{F}') = 0$ [HZ04, p. 280]. For $\mathbf{F} = \mathbf{U}'\mathbf{D}'\mathbf{V}'^T$, $\mathbf{D}' = \text{diag}(a, b, c)$ with $a \geq b \geq c$, one obtains

$$\mathbf{F}' = \mathbf{U}'\text{diag}(a, b, 0)\mathbf{V}'^T. \quad (1.26)$$

Finally, a key point to ensure stable results with the 8-point algorithm is to normalize the input vectors using a transformation matrix \mathbf{T} (translation and scaling), hence improving the conditioning of the problem, and to scale back the fundamental matrix in output using the inverse transformation \mathbf{T}^{-1} .

1.2.2.5 The 5-Point Algorithm

The algorithm described in [Nis04] is designed to estimate the essential matrix using a set of 5 matching pairs of points. It can be summarized as follows.

1. Start by $\hat{\mathbf{x}}'^T \mathbf{E} \hat{\mathbf{x}} = 0$ and rewrite the problem as

$$\mathbf{Q}\mathbf{e} = 0,$$

where \mathbf{Q} is a 5×9 matrix computed as \mathbf{A} in (1.25). The null space base $(\mathbf{X}, \mathbf{Y}, \mathbf{Z}, \mathbf{W})$ of \mathbf{Q} is found using a QR-factorization (that is more efficient than the SVD for this problem). The essential matrix can then be written

$$\mathbf{E} = x\mathbf{X} + y\mathbf{Y} + z\mathbf{Z} + w\mathbf{W} \quad (1.27)$$

for some scalars x, y, z, w . Since \mathbf{E} is calculated up to a scale factor, one can choose $w = 1$.

2. A 9×20 matrix is then formed by inserting (1.27) into (1.16) and (1.18), and a Gauss-Jordan elimination is used to reduce this matrix to an upper triangle form.
3. Some suited procedures are used to extract the determinants of two 4×4 matrices, followed by a second stage of elimination. Finally, a 10-th degree univariate polynomial is obtained, whose roots provide 10 possible solutions for z .
4. The other unknowns x and y are then calculated for each real root of these 10 solutions by back-substituting them into the previous 4×4 matrices.
5. The essential matrix is then recovered from (1.27) and can be used to extract the camera matrix.

1.2.3 N-views and Bundle Adjustment

In a system with more than 2 views, where several cameras observe a set of 3D points, Bundle Adjustment (BA) is a classic method which consists in simultaneously estimating the 3D coordinates of the points and the parameters of the cameras, from the 2D observations on all the images. Let $\boldsymbol{\alpha}_j = (\mathbf{v}^j, \mathbf{t}_j)^T$ be the parameter vector of the j th camera, where \mathbf{v}^j is the 3×1 rotation vector and (\mathbf{t}_j) is the 3×1 translation vector. Given a set of M cameras and the N 3D-points \mathbf{X}^i , the algorithm seeks to minimize the distances between the projections of \mathbf{X}^i on the j th camera for $j = 1, \dots, M$, denoted as $\hat{\mathbf{x}}(\boldsymbol{\alpha}_j, \mathbf{X}^i)$, and the matching 2D points (\mathbf{x}_j^i) from camera observations:

$$\arg \min_{\boldsymbol{\alpha}_j, \mathbf{X}^i} \sum_{i,j} [\mathbf{x}_j^i - \hat{\mathbf{x}}(\boldsymbol{\alpha}_j, \mathbf{X}^i)]^2, \quad (1.28)$$

where

$$\hat{\mathbf{x}}(\boldsymbol{\alpha}_j, \mathbf{X}^i) = \frac{1}{c_j^i} \mathbf{K}_j \mathbf{l}_j^i, \quad (1.29)$$

with \mathbf{K}_j a 2×3 matrix of the intrinsic camera parameters, considered as known after system calibration, and

$$\mathbf{l}_j^i = (a_j^i, b_j^i, c_j^i)^T = [\mathbf{R}_j^T, -\mathbf{R}_j^T \mathbf{t}_j] \begin{pmatrix} \mathbf{X}^i \\ 1 \end{pmatrix}, \quad (1.30)$$

with \mathbf{R}_j the rotation matrix formed using the Euler-Rodrigues formula [GY15]

$$\mathbf{R}_j = \text{Id} + \sin \theta [\bar{\mathbf{v}}_j]_{\times} + (1 - \cos \theta) [\bar{\mathbf{v}}_j]_{\times}^2. \quad (1.31)$$

Note that \mathbf{R}_j corresponds to a rotation of angle θ_j around the axis represented by the unit vector $\bar{\mathbf{v}}_j$, such that $\mathbf{v}_j = \theta \bar{\mathbf{v}}_j$, and where $[\bar{\mathbf{v}}_j]_\times$ is the cross product matrix defines by

$$[\bar{\mathbf{v}}_j]_\times = \begin{pmatrix} 0 & -\bar{v}_{j,3} & \bar{v}_{j,2} \\ \bar{v}_{j,3} & 0 & -\bar{v}_{j,1} \\ -\bar{v}_{j,2} & \bar{v}_{j,1} & 0 \end{pmatrix}. \quad (1.32)$$

Note that one can also represent the rotations using the three Euler angles. However, the rotation vector is preferred here since it removes the ambiguity of rotation order.

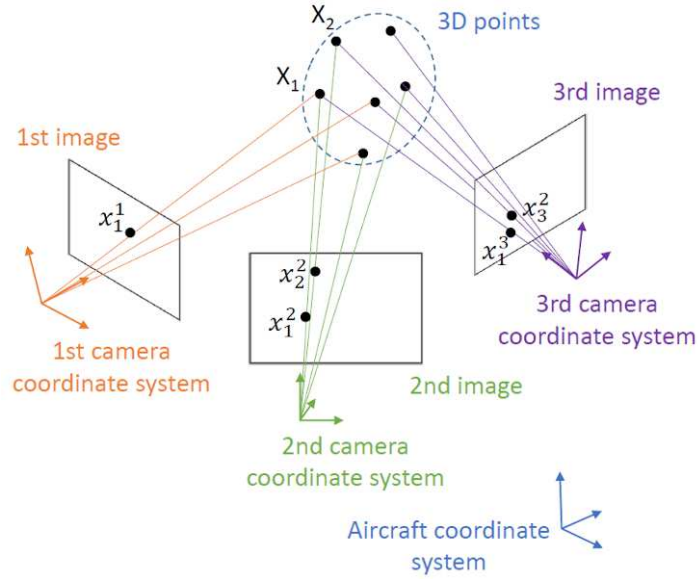


Figure 1.25: Illustration of the BA for 3 cameras observing a set of 3D points.

The 3D reconstruction problem (1.28) is non-convex and non-linear. To solve it, one can consider iterative methods such as Gauss-Newton or Levenberg Marquardt (see Appendix B or [Bri+17] [HZ04, p. 597]). These two methods use iterative steps from the initial guess to the optimum parameter using the Hessian matrix, approximated as $\mathbf{J}^T \mathbf{J}$, where \mathbf{J} is the Jacobian matrix. The Jacobian matrix in BA has the interesting characteristic of being sparse, thus significantly fastening the optimization procedure. Indeed, each projected point depends only on the corresponding 3D point and on the camera, leading to:

$$\frac{\partial(\mathbf{x}_j^p - \hat{\mathbf{x}}(\boldsymbol{\alpha}_j, \mathbf{X}^p))^2}{\partial \mathbf{X}^q} = 0, \forall p \neq q, \forall j \in \{1, \dots, M\} \quad (1.33)$$

$$\frac{\partial(\mathbf{x}_p^i - \hat{\mathbf{x}}(\boldsymbol{\alpha}_p, \mathbf{X}^i))^2}{\partial \boldsymbol{\alpha}_q} = 0, \forall p \neq q, \forall i \in \{1, \dots, N\}. \quad (1.34)$$

Furthermore, some points may not be seen by some cameras, leading to additional empty lines in the Jacobian matrix. An example of Jacobian matrix used in BA is presented in Fig. 1.26, where the only non-zero elements are displayed in white.

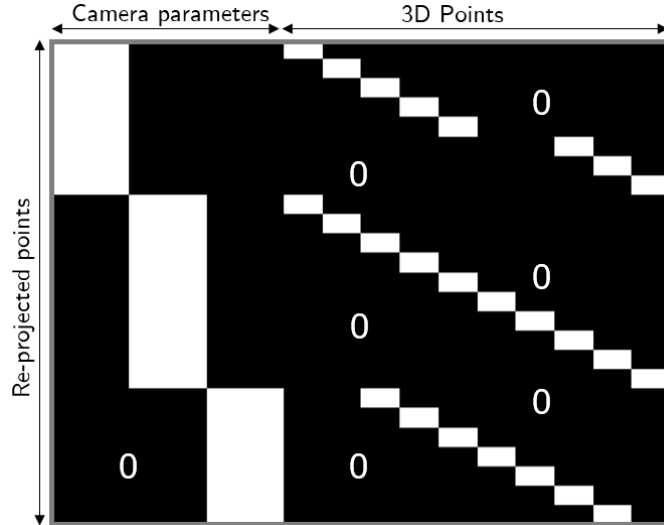


Figure 1.26: Example of sparse BA Jacobian matrix for 3 cameras and 10 points.

1.2.4 Model-based methods

BA is an iterative optimization algorithm that aims at minimizing a non convex and non-linear cost function. Therefore, one cannot guarantee its convergence to a global minimum, and the choice of the initial conditions is crucial in practical applications. Consequently, the application of photogrammetry to 3D wing reconstruction in flight is a very challenging problem. First, camera positions suffer from strong installation constraints, given that currently they can only be located on the rear vertical stabilizer of the aircraft and on the aircraft windows. With this setup, the wing end is observed under very low angles, directly impacting the accuracy of point detection in images. Besides, the distance between cameras is also restricted to guaranty covering in views of the wing, i.e., almost 15m separate for a 30m long wing. Second, highly varying environment strongly affects the observations: the whole aircraft itself is deforming and vibrating, and the 2D images are subject to luminosity changes, potential reflections and shadows. As a consequence, it will be shown in Section 2.4.5 that observation uncertainties prevent the standard BA method from obtaining accurate 3D wing reconstructions.

During the last decade, various constrained optimization methods were developed to improve the performance of the classical BA approach, taking benefit of prior knowledge about the scene or system to reconstruct. In [ZHH12; Bri+17], prior knowledge of point coplanarity between neighboring points or information about their positions constructed from a Digital Terrain Model (DTM) are introduced in BA as constraints on the unknown parameters. Similarly, information on camera positions acquired from the Global Positioning System (GPS) or Inertial Measurement Units (IMUs) is introduced in the BA as constraints for the camera parameters in [HT09; Lar+13; Lhu12]. In [Lar+12], improvements on SLAM accuracy and robustness is achieved using GPS together with DTM as priors. Finally, knowledge about 3D structure models is introduced in model-assisted BA to impose proximity between

reconstructed 3D points and a reference model [Fua99], [OJRE17].

In the case of wing deformation estimation, one cannot introduce directly prior knowledge on the wing structure model in the BA reconstruction, since the main objective is to practically evaluate this model. Instead, we propose in this work to use prior knowledge resulting from wing mechanical limits, beyond which the wing would break. This will be the topic of Section 2.4, where the BA reconstruction problem is redefined such that it efficiently constrains the 3D points to respect these mechanical limits, by introducing suitable regularization terms in the BA cost function.

1.3 Conclusion

This chapter focused on finding a suitable method to reconstruct the 3D shape of an aircraft wing in flight. To this aim, Section 1.1 covered a large variety of systems using 3D estimation without contact, and presented their pros and cons with respect to the requirements of the current application. From this evaluation, the conclusion was to employ the photogrammetry method, which fits well Airbus problematics and benefit from Airbus experience in the field of camera acquisition. Then, to be able to implement this technology on aircraft, the theory of cameras and 3D reconstruction from multiple views were reviewed in more details in Section 1.2. Finally, the reader should keep in mind that even though this study focuses on camera sensors, other alternatives such as the use of lidar should not be discarded and could be the object of further work.

New processing chain based on multiple view photogrammetry

Contents

2.1	Brief overview of the algorithmic chain	42
2.2	Use of points of interest naturally present on the wing	44
2.2.1	Detection of points of interest	44
2.2.2	Automatic and guided matching	50
2.2.3	Line detection	52
2.2.4	Limitations	55
2.3	Initialization using targets	56
2.3.1	Typology of targets used for photogrammetry	56
2.3.2	Target selection	59
2.4	Optimization under constraints of <i>a priori</i> deformation limits	61
2.4.1	Mechanical limits	61
2.4.2	Definition of mechanical constraints	62
2.4.3	Constrained bundle adjustment	65
2.4.4	Extraction of mechanical limits from the FEM	66
2.4.5	Results and discussion	70
2.5	Conclusion	74

In the previous chapter, a state of the art of non-contact 3D reconstruction methods highlighted the photogrammetry method as a good solution for estimating wing deformation in flight. This approach is hence detailed in Section 1.2 and its implantation on an aircraft application is detailed in this chapter. The method is globally presented in Section 2.1 and aims at finding the 3D coordinates of points observed using several 2D views, as well as the position of the cameras observing these points. These estimates are obtained using an optimization process presented in Section 1.2.3, which requires a set of observations from several views.

While classical methods of detection and point matching can be easily applied in standard cases such as architectural 3D reconstruction [SSS07; THP09], the generation of observations in the case of an aircraft wing becomes a critical point for the success of the approach.

Thus, the problem of generating observations from features naturally present on the wing is considered in Section 2.2. Finally, when possible, and in order to guarantee the precision and robustness of the system with respect to environmental variations, photogrammetric targets can be used, which is the object of Section 2.3.

Finally, in order to compensate the loss of precision from the system geometry defaults, we take advantage of *a priori* knowledge of the mechanical limits of the wing to define a new 3D reconstruction method under constraints, detailed in Section 2.4.

2.1 Brief overview of the algorithmic chain

The objective of the proposed processing chain is to give as output the coordinates of points of the wing surface in the aircraft coordinate system. Keeping in mind the challenges presented introduction of this manuscript, the framework of the proposed algorithm is displayed in Fig.2.1 and summarized as follows:

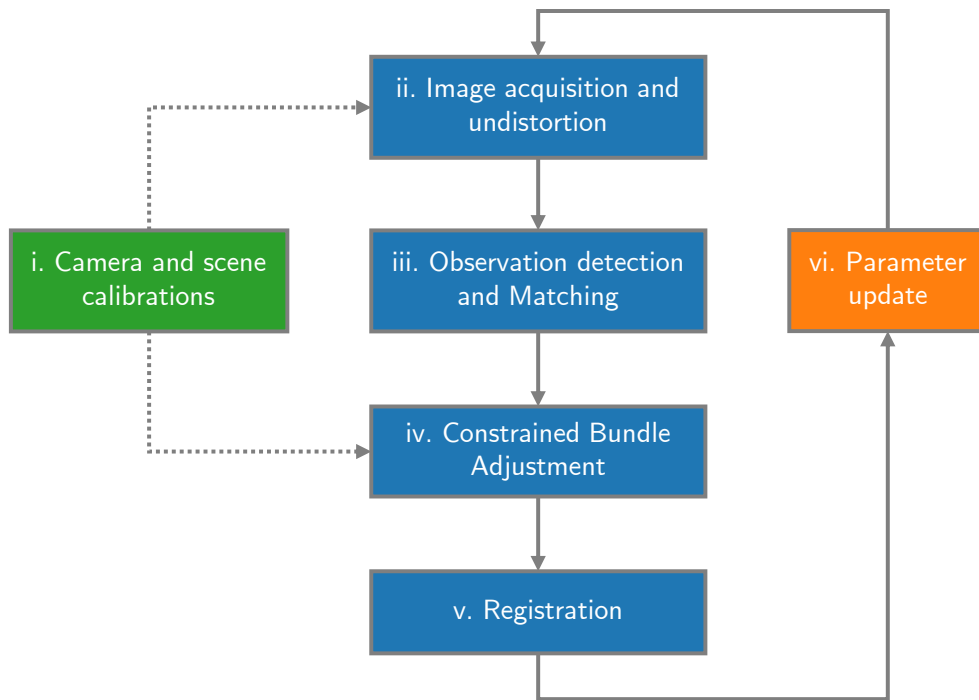


Figure 2.1: Diagram of the proposed algorithmic framework.

- i. **Camera and scene calibration:** This step is performed using pictures of a chessboard from different angles and distances, and using the OpenCV calibration functions [5], which estimates the intrinsic parameters of the cameras and distortion coefficients. The scene is then calibrated to initialize the positions of the 3D points and cameras. This is conveniently performed using pictures from a drone and the photogrammetry software

Metashape [6]. Note that a drone can take pictures of a wing from a wide range of angles in less than 30 minutes.

- ii. **Image acquisition and undistortion:** For each new image acquisition, we use the OpenCV undistortion function with the distortion parameters estimated in Step (i).
- iii. **Observation detection:** The proposed algorithm offers different ways to detect the 2D observations of the 3D points. First, one can use the natural features present on the wing surface (corners, joints, writing, etc.), using the methods presented in Section 2.2. Another solution, when possible, is to use markers stuck on the wing surface. Markers allow an easy, robust and accurate localization of the observations, as described in Section 2.3.
- iv. **Constrained Bundle Adjustment:** The initialization from step (i) and the set of 2D observations from step (iii) are used as input to the constrained bundle adjustment detailed in Section 2.4.3. The algorithm outputs the optimum 3D points \mathbf{X}_i and the camera matrices \mathbf{P}^j in the coordinate system of the cameras.
- v. **Registration:** The registration phase is performed using the rear camera. This camera can observe reference points close to the aircraft fuselage (see Fig. 2.2), for which the displacement in the aircraft coordinate system are negligible. By detecting these points on the rear view image, one can recover the transfer matrix from the rear camera to the aircraft coordinate system. Since the rear camera is also part of bundle adjustment in Step (iv), one also knows the transfer matrix from this camera to the global camera coordinate system. Finally these matrices are combined to transfer the 3D points and cameras to the aircraft coordinate system.
- vi. **Parameter update:** The initial parameters are updated, taking the output of Step (v) as new initial positions of the algorithm.

Step (i) is performed before flight and steps (ii) to (v) are repeated for each new camera acquisition.

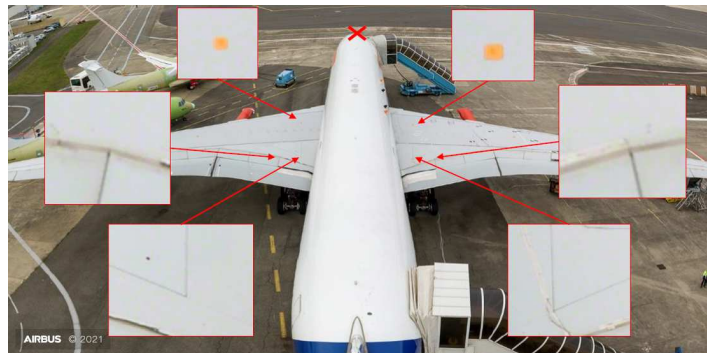


Figure 2.2: Rear camera view with some reference points zoomed.

2.2 Use of points of interest naturally present on the wing

To reconstruct the 3D shape of a structure, the bundle adjustment algorithm presented in Section 1.2.3 requires an observation set. These observations are the projections on the cameras of the 3D points to be reconstructed. The first challenge of the method studied to reconstruct an aircraft's wing is therefore to generate point observations. Given the need to reduce the intrusiveness of the flight measurement system, a first idea is to exploit points of interest naturally present on the wing. To this aim, these points must be detected, described and matched with their projections on other views. This chapter details the standard methods that are available for detection and matching, as well as the process proposed in this study.

2.2.1 Detection of points of interest

Points of interest (or keys points) are salient points which can be recognized from one image to another by analyzing the specific properties of their vicinity. These points can be contours of the image or corners, for which the intensity gradients are locally high, or textured zones, rich in information.

The initial step to find corresponding points between several images is first of all to detect the points of interest present in each image. This detection is carried out by searching for spatial information of high-frequency. For this, we can cite many methods such as the contour detectors of Canny [Can86] or Sobel, the contour and corner detectors of Harris [HS88], Shi-Tomasi [ST94], and many others [Low04; TLF10; Rub+11; HTG06].

Once the points of interest have been detected, it is necessary to assign them a signature which will allow their identification, and then to find their correspondences between images. A major issue in the description of key points is to be able to recognize them on images with various properties, such as orientations, changes of scale, points of view or brightness. Many descriptors have been developed such as SIFT [Low04], ORB [Rub+11], SURF [HTG06], DAISY [TLF10], BRIEF [Cal+10], BRISK [LCS11], or AKAZE [PA13] distinct with respect to their properties of invariance [CLFM16], and their complexities of application. In the system proposed here, it was chosen to study the methods based on the descriptors SIFT, ORB and DAISY for their complementary properties of invariance, and they are therefore presented in the paragraphs 2.2.1.1 to 2.2.1.3.

2.2.1.1 SIFT

Probably the most famous method for detecting and describing points of interest, SIFT (Scale Invariant Feature Transform) offers a fast detector and an invariant descriptor in all domains. As described in [Low04], this method begins by detecting the key points through a scale space defined for an initial image $I(x, y)$ and a scale factor σ by

$$L(x, y, \sigma) = G(x, y, \sigma) * I(x, y) \quad (2.1)$$

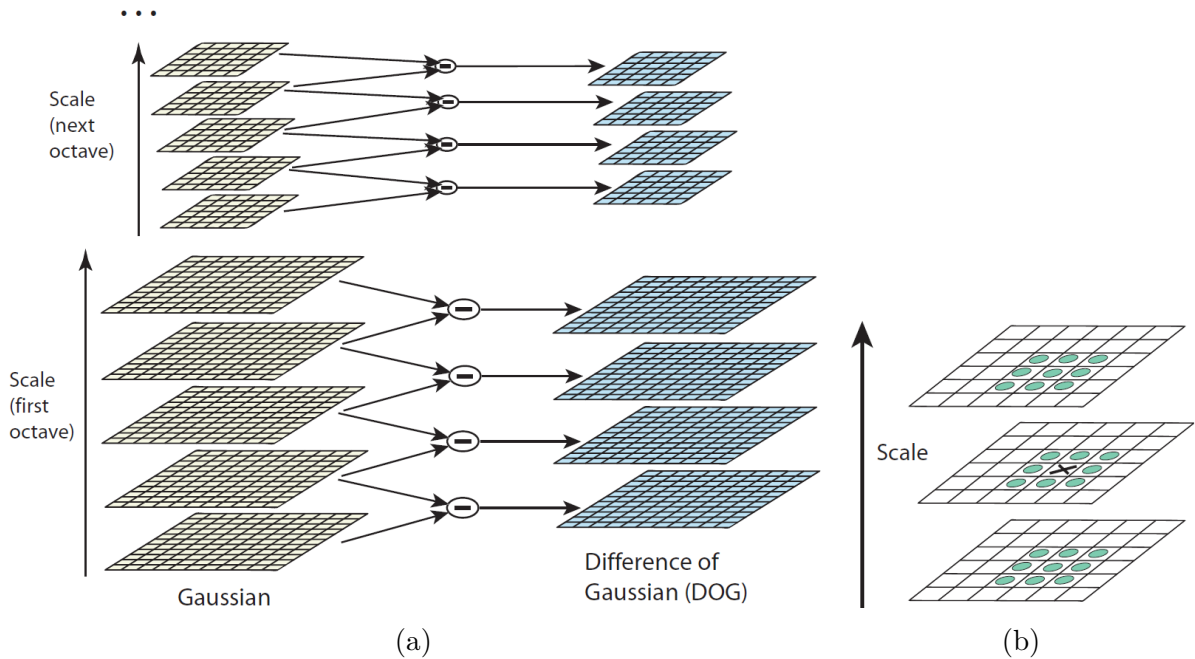


Figure 2.3: Detection of points of interest for SIFT (from [Low04]). (a) - Process for calculating the DoG through the scale space, (b) - illustration of the search for a key point in the vicinity of the DoG.

with G a Gaussian filter of standard deviation σ , and $*$ the 2D convolution operator. To detect the stable points of interest of this scale space, the Difference of Gaussian method (DoG) is used, which calculates the difference between two near scale spaces, separated by a factor k :

$$D(x, y, \sigma) = L(x, y, k * \sigma) - L(x, y, \sigma). \quad (2.2)$$

The DoG method is summarized in Fig. 2.3a. The key points will then be the points whose values of DoG are strictly the minimum or maximum in their neighborhood, the neighborhood being defined by the set of connected points on the scale space of the point of interest, and all the connected points neighboring scale spaces (see Fig. 2.3b). The choice of this approach is justified by the efficiency of the DoG calculation and also by the stability of the points it allows to detect.

Once a key point has been detected, its precise position is obtained by means of an approximation of the Taylor series of the function D in its neighborhood. During this step, a thresholding is performed on the value of the DoG at this point, which makes it possible to eliminate the key points with too low contrast. A thresholding is also carried out regarding the ratio of the eigenvalues from the Hessian matrix calculated around the point, in order to reject the key points detected on lines. Indeed, this ratio of eigenvalues represents the curvature of the function D (phenomenon initially exploited to detect the Harris corners [HS88]). The third step of the method consists in assigning an orientation to the points of interest to guarantee the invariance in rotation. For this, the amplitude $m(x, y, \hat{\sigma})$ and the orientation

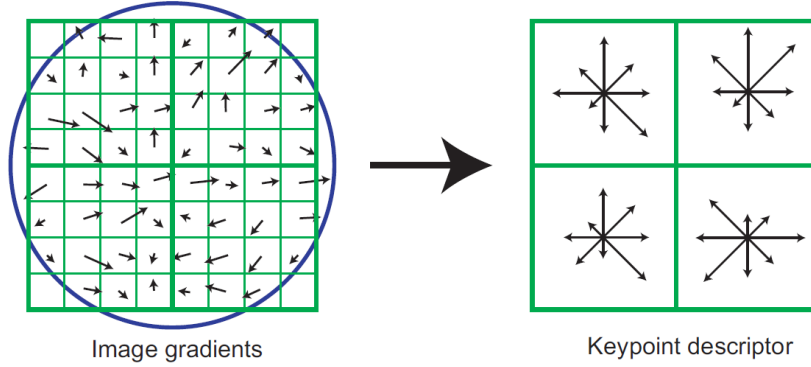


Figure 2.4: Construction of the SIFT point descriptor (from [Low04]). In this example, the samples are grouped into an array of 2×2 orientation histograms.

$\theta(x, y, \hat{\sigma})$ of the gradients are calculated locally around the point at its scale $\hat{\sigma}$:

$$m(x, y, \hat{\sigma}) = \sqrt{(L(x+1, y, \hat{\sigma}) - L(x-1, y, \hat{\sigma}))^2 + (L(x, y+1, \hat{\sigma}) - L(x, y-1, \hat{\sigma}))^2} \quad (2.3)$$

$$\theta(x, y, \hat{\sigma}) = \arctan \left[\frac{L(x, y+1, \hat{\sigma}) - L(x, y-1, \hat{\sigma})}{L(x+1, y, \hat{\sigma}) - L(x-1, y, \hat{\sigma})} \right]. \quad (2.4)$$

The values $m(x, y, \hat{\sigma})$ and $\theta(x, y, \hat{\sigma})$ are then collected to form an orientation histogram over 36 intervals, covering 360 degrees. The values of $m(x, y, \hat{\sigma})$ are weighted by a circular Gaussian window whose standard deviation is fixed at $1.5\hat{\sigma}$. The main peak of this histogram represents the dominant direction of the gradient, which is then assigned to the key point. If several peaks are obtained, several key points with different orientations are retained.

The point of interest is now defined by its position, scale, and orientation. The final step in SIFT is to describe this point. This operation is illustrated in Fig. 2.4. The amplitudes and orientations of the gradient in the vicinity of the point are sampled and weighted by a circular Gaussian window (shown in blue). These samples are then accumulated to form a table of orientation histograms. A rotation of angle equal to the orientation of the key point is then applied to the coordinates and orientations of the gradients to guarantee the invariance in rotation. The vector of descriptors is finally obtained by concatenating the values of the obtained histograms. [Low04] shows that the best results are reached by forming an array of 4×4 histograms of 8 orientation intervals, which gives a descriptor of dimension 128. Finally, the descriptor is normalized to remove the effect of affine variations in illumination. Concerning non-linear variations, since they generate significant changes in the amplitude of the gradients, the latter are clipped, which makes it possible to attenuate their importance, and to promote the orientation information of the descriptor.

2.2.1.2 ORB

The ORB (Oriented FAST and Rotated BRIEF) method is a good alternative to SIFT, whose results and complexity are comparable, and which has the major advantage of being free to

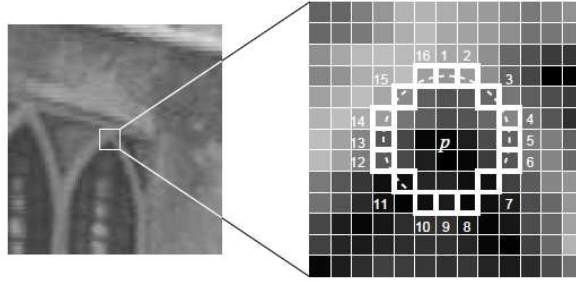


Figure 2.5: Illustration of the corner detection in FAST (from [RD06]). The intensity of the candidate point p is compared to that of the 16 pixels of the circle represented on the right.

use. ORB mainly uses a fusion of the methods of FAST [RD06] and BRIEF [Cal+10], with some modifications. In order to understand how it works, these underlying methods are briefly explained here.

FAST (Features from Accelerated Segment Test) is a point of interest detector designed for real-time applications, which has less complexity than most of its counterparts. To define if a point p is a key point, FAST compares its intensity I_p to that of the 16 pixels of the circle C of which it is the center, and of radius 3 pixels (see Fig. 2.5). For a chosen threshold t , this point is then retained if:

- it exists a set of n connected points whose intensities are greater than $I_p + t$,
- it exists a set of n connected points whose intensities are less than $I_p - t$.

In [RD06], n is equal to 12. In order to reject more quickly the points that do not validate one of these two conditions, a first test is performed on pixels 1, 5, 9 and 13 of the 16 points of C . Furthermore, a Machine Learning based approach is employed to better select the parameters and locations of tested pixels, by training the detector on a set of images from the same test domain. Finally, when several neighboring pixels are detected, a last step called "Non-Max Suppression" is applied. A score function V is calculated for each key point by summing the absolute difference between its intensity and those of the 16 pixels of C . If several neighboring points are detected, only the one with the highest value of V will be retained.

BRIEF (Binary Robust Independent Elementary Features) can be used to describe the detected points. The primary objective of this method is to reduce the memory consumption to be applicable in embedded systems. For this, BRIEF takes a smoothed region of the image around the key point, and selects a set $n_d(x, y)$ of point pairs. The point intensities of these pairs is compared and the result of the comparison is coded as 1 if the first intensity is greater, or 0 otherwise. The point descriptor is directly created using this binary series of comparisons, and can therefore be easily compared using the Hamming distance. Regarding the choice of $n_d(x, y)$, [Cal+10] shows that a random distribution is the most suitable (see Fig. 2.6). The dimension of the descriptor is 128, 256 or 512, which translates directly into bits because the descriptor is binary (unlike SIFT).

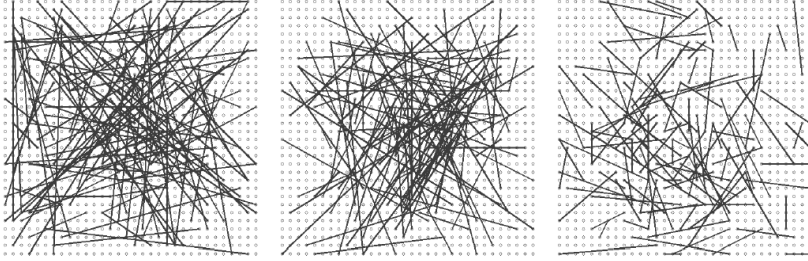


Figure 2.6: BRIEF descriptor: example of a random distributions to select the pairs of points to compare (from [Cal+10]). The ends of each segment are pairs of points.

After introducing FAST and BRIEF, the ORB method can be detailed. First of all, ORB uses FAST to detect the points of interest present in the image. However, to obtain scale invariance, the algorithm also uses an image pyramid (similar to the scale space of SIFT). The points are then evaluated using the Harris measure [HS88] to keep only the N best points. After that, the centroids of the points are estimated (see (2.7)), and the direction between each point and its centroid is calculated, then assigned as the orientation of the key point. Then comes the description phase of the key points. For this, ORB uses BRIEF. However, to guarantee the rotation invariance, a rotation corresponding to the orientation of each interest point is applied to the set $n_d(x, y)$ of point pairs to be compared. Finally, in order to ensure the discriminatory nature of the descriptors, a greedy algorithm is applied to all of the possible binary tests, to select the one that offers the greatest variance.

2.2.1.3 DAISY

DAISY is a key point descriptor designed mainly for dense application cases, offering a lower complexity and memory requirement than SIFT. This method also reduces the rate of matching error compared to SIFT. For this purpose, DAISY uses gradient histograms like SIFT, but the region of descriptor calculation is a set of overlapping circles, centered on the point of interest (see Fig. 2.7). The radius of these circles increases with the distance to the key point, and the variance of the Gaussian filter smoothing the region of the circle is proportional to the radius. For each circle, an orientation histogram is calculated and normalized. The descriptor vector is finally formed by concatenating the histograms.

2.2.1.4 Combination of descriptors

By applying to aircraft wings the conventional methods detailed in the preceding paragraphs, numerous errors occur. Indeed, a wing is a structure that has very little texture, and whose key points are similar, and can easily be confused. This can be seen in Fig. 2.10 which shows a case of a pair of images from two cameras placed on the aircraft windows, a few meters away. Fig. 2.8 shows points of interest mapping errors using the SIFT detector and descriptor, and the pairing functions of FLANN (Fast Library for Approximate Nearest Neighbors) [ML09]. One may notice that a lot of bad matches are linked to the similarity of the key points and to

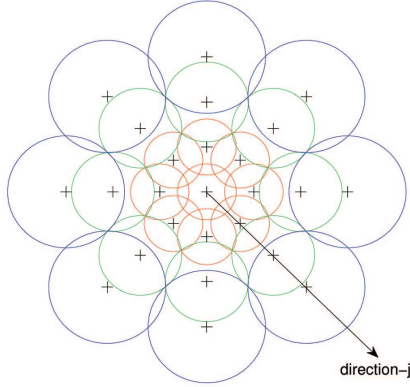


Figure 2.7: DAISY descriptor.

the invariances of the descriptors. [CLFM16] offers a detailed comparison of these descriptor invariances (see Table 2.1). Knowing that in the case of an aircraft wing, the camera shots are close, we can assume that the points of interest will have the same scale and the same orientation. However, using a descriptor with restricted invariances like DAISY does not necessarily give better results.

In view of the complementary properties of the diverse methods, a combination of descriptors from SIFT, DAISY and ORB is also proposed. The descriptor thus generated is the concatenation of descriptor vectors resulting from the three methods (for ORB, the descriptor is first converted from binary to floating numbers). Points are detected with ORB, and paired with FLANN functions. This combination of descriptor will improve the matching results.

To compare the performance of the descriptors, a study is proposed on the pairing of two real images of wing in flight. This study focuses on three criteria, the mapping error, the rate of outlier points, and the method complexity. Having no ground truth to evaluate the mapping error, the epipolar constraint (presented in Section 1.2.2) is used to define an error metric, by checking the validity level of the epipolar constraint. In other words, for a set of point pairs $(\mathbf{x}_i, \mathbf{x}'_i)_{i=1, \dots, N}$, where N is the number of correspondences, the fundamental matrix F of the system is calculated (see method in Section 1.2.2), and the error of epipolar constraint for each pair of points is defined as:

$$e_i = \mathbf{x}_i \mathbf{F} \mathbf{x}'_i. \quad (2.5)$$

The total epipolar error is calculated as the sum of the errors e_i . Concerning the rate of outliers, these are defined as points whose error e_i is greater than a fixed threshold (the choice of the threshold can be made by hand as long as the number of matches is low). Finally, the complexities are compared on the same machine by measuring the time required for each method to reach the same number of matches. The results of these evaluations are presented in Fig. 2.9. One can see that the SIFT method provides the worst results in this experimentation. This is in part due to its invariance properties seen earlier, which create a higher number of incorrect matches (outliers) and thus increase the total error. Fig. 2.9 shows that the combination of descriptors provides the best results, having less outliers, a

Table 2.1: Table of descriptor invariances (provided in [CLFM16])

	Scale	Rotation	Viewpoint	Lightness
SIFT	x	x	x	x
DAISY			x	x
BRIEF				x
ORB		x		x

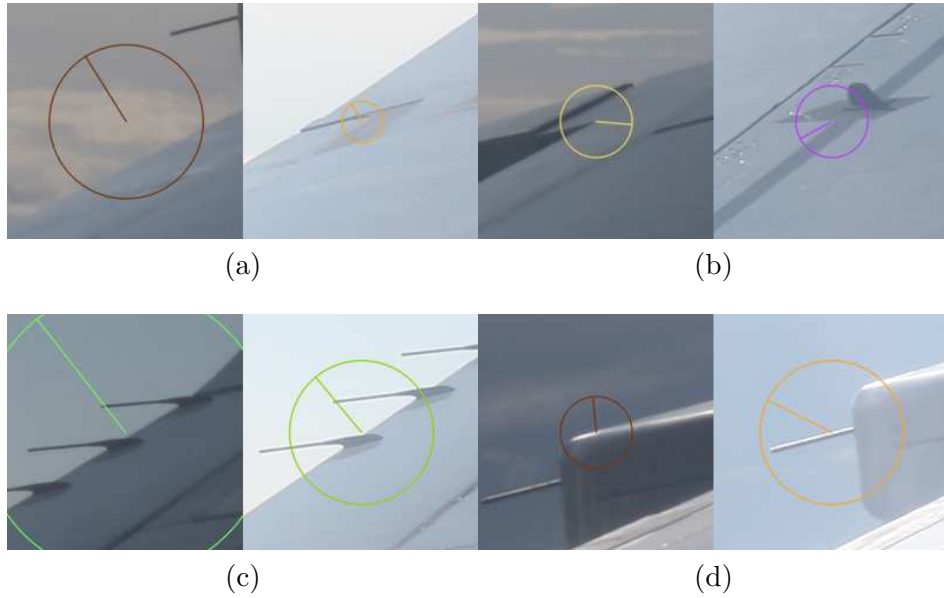


Figure 2.8: Example of matching error when applying SIFT. The points are represented with the scale and the orientation of their descriptor. In the cases (a) and (b), one observes errors related to the invariances of scale and rotation of the descriptor. Case (c) shows an error due to the similarity of the key points. Finally, some unjustified errors may appear, as in (d).

lower error, and a faster combination of descriptors, thanks to more discriminant descriptors, which yields to less ambiguous matchings, as expected from the study of descriptor invariances from [CLFM16], listed in Table 2.1.

2.2.2 Automatic and guided matching

The last step to generate point correspondences is the matching. This phase is achieved by comparing the descriptors of the detected points in each image, and by matching those having similar properties. In this study, the algorithm used is the approximate nearest neighbor from the FLANN library [ML09], introduced in a guided matching scheme presented hereafter.

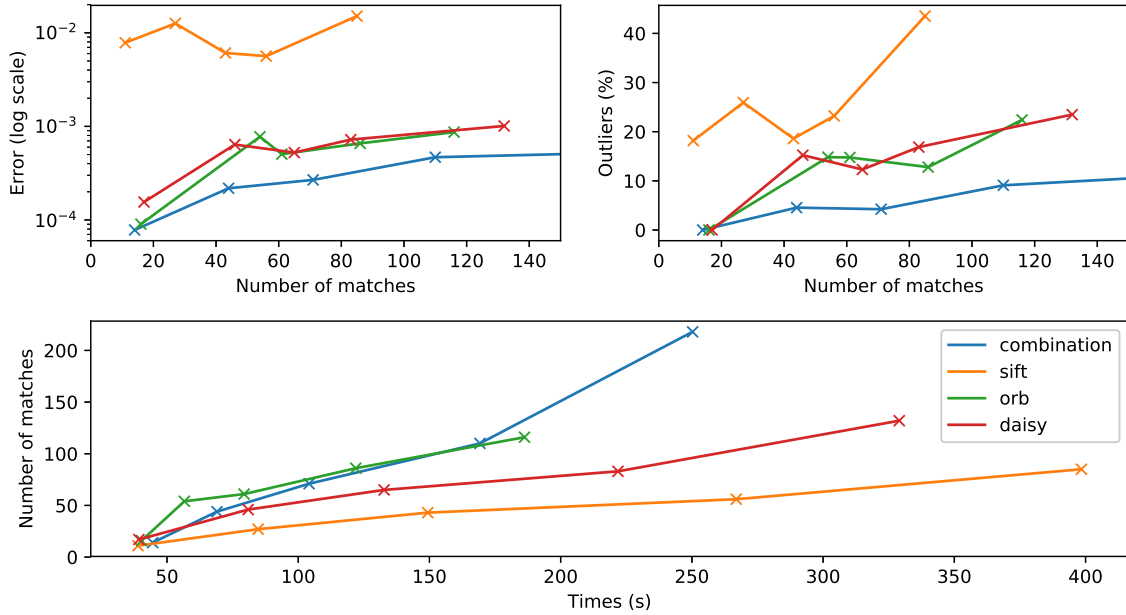


Figure 2.9: Performance comparison of the different descriptors for the matching of real images of an aircraft wing.

2.2.2.1 Feature matching

When key points are detected and described in pairs of images, corresponding features can be obtained by comparing the descriptors. To this aim, distances between descriptor vectors are computed using the Euclidean norm (ℓ_2) in the case of SIFT and DAISY descriptors, and Hamming norm for ORB binary descriptors. Then, several algorithms can be applied to find the closest matches. First, a simple linear search can be computed, comparing each query point to all possible features of the other images. While simple to implement, this approach will quickly become computationally expensive with high number of points to compare. A common alternative to fasten the comparison is to begin by sorting point descriptors using binary (k-d) trees, and then search the correspondence of a query point on the constructed tree.

In this study, comparisons have been made for hundreds of point descriptors, with the combination of SIFT, DAISY and ORB descriptors. A weighted combination of these descriptors was also tested, but is not detailed in this work as the best results were found without weights. To this end, and to speed up the processing, FLANN [ML09] has been employed. This library offers a collection of algorithms optimized for fast nearest neighbor search in high dimension spaces, and selects automatically the most suited method and optimum parameters to work on the input dataset.

2.2.2.2 Guided matching

As seen previously, the mapping of points for an aircraft wing is not trivial, mainly because of the similarity of the key points and their lack of information (texture). This problem also exists in other applications such as the reconstruction of buildings with very repetitive geometric structures. So our algorithm borrows from the literature [HZ04, algo. 11.4] [SSN15] guided mapping methods which rely on the geometry of the system to improve the pairings. The method can be described into five steps:

- i. **Detection and description of the key points:** This step is achieved using the ORB point detector, and the combination of the descriptors of SIFT, ORB and DAISY, as described in Section 2.2.1.4.
- ii. **Strong feature matching:** A first phase of pairing is realized by using FLANN. During this step, a high threshold t_{init} is applied on the distance between descriptors to keep only the matches with high score, which results in pairs of points with the most discriminating signatures.
- iii. **Automatic calibration of the cameras:** Using the methods presented in Section 1.2.2, the fundamental matrix \mathbf{F} (or essential matrix when the intrinsic parameters are known) of the system is estimated using the set of strong matches. The RANSAC method used for this estimation allows at the same time outliers to be rejected.
- iv. **Optimization:** It is then possible to refine the estimate of \mathbf{F} by minimizing the epipolar error (2.5) using an iterative optimization process, such as Gauss-Newton or Levenberg-Marquardt.
- v. **Guided matching:** this method takes a point \mathbf{x} to match from a first image and calculates its epipolar line $\mathbf{l} = \mathbf{F}\mathbf{x}$ in the second image (see paragraph 1.2.2 and Fig. 1.23). A first selection of point candidates for matching is then performed, keeping only the points whose distance to \mathbf{l} is less than a threshold d ("Grid based Search" method of [SSN15]). The descriptors of the retained key points are then evaluated to find the best match with FLANN. This time, the chosen threshold t is smaller than t_{init} .

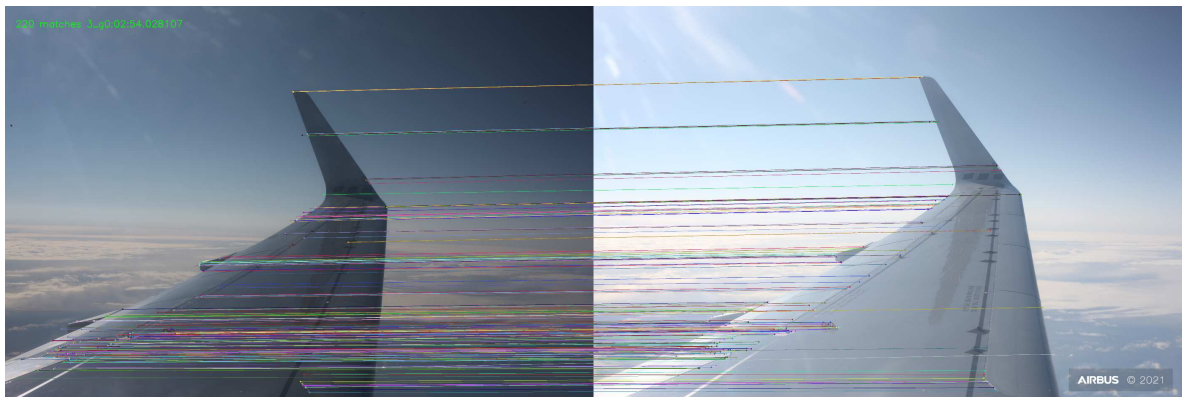
The steps (iii.) to (v.) can be repeated by decreasing iteratively d and t , until a sufficient or stable number of matches is reached. An example of result obtained with this algorithm on an aircraft wing is shown in Fig. 2.10.

2.2.3 Line detection

Starting from the observation that black lanes are present on the majority of aircraft wings (see Fig. 2.10), this paragraph goes deeper in the exploitation of information naturally present on the images, by proposing a procedure to detect and match these lanes. They are particularly interesting since they are present over the entire span of the wing, and correspond to the front and rear spars, which carry the main information of the bending and torsion of the wing.



(a)



(b)

Figure 2.10: Application on an A320 wing of the matching method described in Section 2.2.2.2. (a) 14 strong matches chosen at initialization, (b) 220 matches after 3 iterations of steps iii. to v.

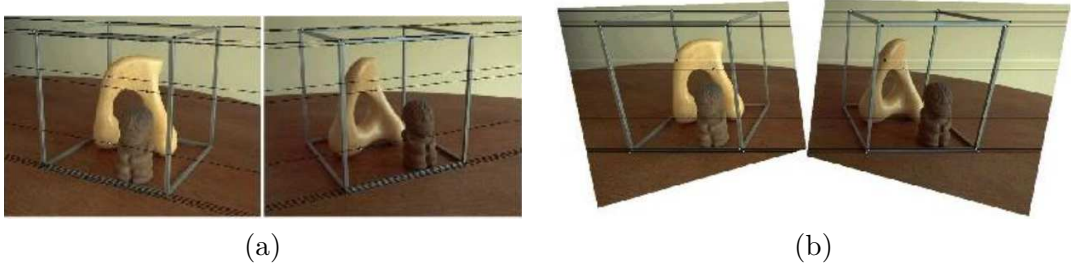


Figure 2.11: Example of stereo image rectification (from [LZ99]). (a) - Pair of initial images, (b) - Rectified images.

To detect these lanes in each image, an approach based on the gradient intensity is proposed. By using the gradient, the method overcomes the problems of variation in the appearance of the lanes as the brightness changes. Indeed, the reflections generated by the material of these lanes are mainly specular, and will therefore be seen as being more or less dark than their vicinity depending on the orientation of the sun. An initial detection of the lines can be realized using Canny or Sobel filters, or by an initial manual selection. Subsequently, this detection is refined using line location methods at the sub-pixel level. More details on this line detection is given in Section 3.2.3.3.

The proposed algorithm is thus able to detect the lanes of the wing. However, the points thus detected are very similar, which raises the question of finding the correspondences between images. This problem is solved by rectifying the image pairs. The goal of image rectification is to find the projection transformations \mathbf{H} and \mathbf{H}' of an image pair that will project the epipole at a point at infinity, generally defined as $\mathbf{i} = [1, 0, 0]^T$ (in uniform coordinates). This operation makes the epipolar lines parallel to the x axis of the images, i.e., all the corresponding points from one image to the other are aligned horizontally, and therefore simpler to compare and associate. The rectification phenomenon is illustrated in Fig. 2.11. To compute the correction, the method of [Har99] is used. From a set of N initial or target matches $(\mathbf{x}_i, \mathbf{x}'_i)_{i=1, \dots, N}$, and the fundamental matrix \mathbf{F} of the image pair, the algorithm is defined in three steps:

1. \mathbf{F} is used to calculate the epipolar lines \mathbf{l} and \mathbf{l}' of the images,
2. a first projective transformation \mathbf{H}' is selected that projects \mathbf{l}' at infinity point \mathbf{i} ,
3. the second projection transformation \mathbf{H} is obtained by minimizing

$$\mathbf{H} = \arg \min_M \sum_i \|M\mathbf{x}_i - \mathbf{H}'\mathbf{x}'_i\|^2. \quad (2.6)$$

Then, using the method of [LZ99], a shear transformation is calculated and applied after the rectification. This transformation makes it possible to reduce the shear distortions introduced by \mathbf{H} and \mathbf{H}' , while trying to preserve the orthogonality and the aspect ratio of the axes of the image (see example on Fig.2.12).

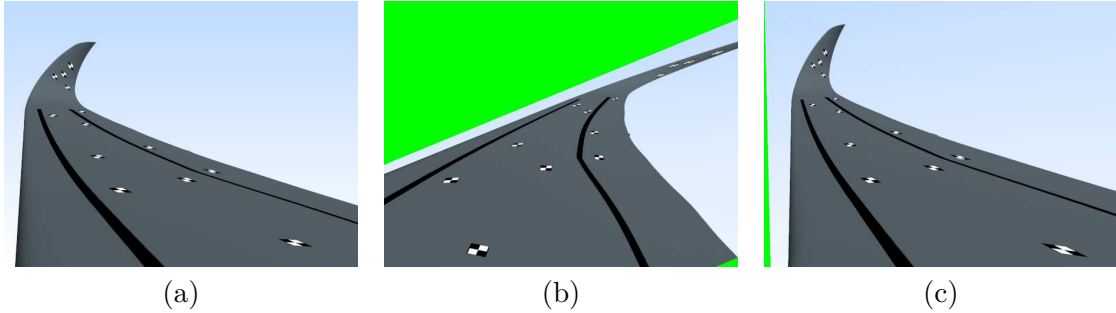


Figure 2.12: Illustration of the shearing effect of image rectification on some synthetic views of a wing. (a) - Initial image, (b) - Rectified image, (c) - rectified image with shearing reduction.

Once the lanes have been detected and the images have been rectified, since the corresponding points are now aligned horizontally, pairings can be obtained by scanning each line of the images. In addition, one can think of also using the wing edges. However, the latter are actually bent and the stops thus observed by the different cameras do not coincide. This is why the presented method focuses on the detection of the black lanes at the top of the wing, visible similarly by all the cameras.

2.2.4 Limitations

The main objective of the system presented here is to estimate wing deformation for the aircraft certifications. Therefore, great care should be given to the reliability, accuracy and robustness of the 3D shape estimations. While using natural features allows us to obtain estimations without any disturbance, and offers a system that is simple to install, it comes with great limitations. First of all, key-point detection lacks in robustness because wing appearance changes with luminosity variations, i.e., a point could be observed at an instant and not at another. Moreover, points of interest are detected only on parts of the wing where rich information is available (texture or corners), which is limited since wings have almost no texture on their upper surface, and not accurate since corners are not exactly seen similarly from one view to the other.

Concerning lane detection, inaccuracy of reconstruction is introduced by errors of matching. Indeed while the detection on the x axis (horizontal) of the image benefits from an accurate algorithm of sub-pixel detectors, the coordinates on the y axis (vertical) rely on a correct rectification of the images, yielding associations of points with slightly erroneous y coordinates. The rectification itself relying on a correct first set of matching key points (also affected by errors) will not be perfect. Besides, for a good rectification on views of the entire wing span, points of interest should be spread evenly over the wing surface, which cannot be ensured where no texture is present. As a consequence, errors in y coordinates matching are observed on the lanes of the wing middle, of about 10 pixels in the worst case. Finally, the identification of points on the lanes is another issue. With the approach of detecting points for each line of the image, one cannot guarantee that the detected points will remain

the same from one instant to the other. This will then induce difficulties to estimate wing deformations between consecutive frames, and will become a problem for the application of some mechanical limits introduced in Section 2.4 (that will be applied to points identified before flight). Nonetheless, this approach could deliver an order of deformation magnitude in case no additional installation permitted on the wing.

2.3 Initialization using targets

As explained in the previous sections, the detection of natural features of the wing can be an interesting solution to gather point matches all along the wing to recover its 3D shape, while remaining totally contact-less. However, their use comes with great limitations of accuracy and robustness, which could be lightened by installing targets on the wing. Preventing the introduction of aerodynamic disturbances, it is indeed possible to stuck markers on the surface of a test aircraft. This section presents a range of existing targets employed in photogrammetry applications, exploring the pros and cons of each one, and finally justify the retained solution.

2.3.1 Typology of targets used for photogrammetry

In photogrammetry and many other image-processing applications, targets are used to mark elements of the scene, allowing them to be easily located and identified. They are especially useful when no other strong features are present on the scene (e.g., wing surfaces). Thanks to their specific shapes and marks, their detection is accurate and robust. Using an appropriate algorithm, one can locate them with sub-pixel accuracy. To answer the needs of diverse applications, targets have been designed with various geometries and materials, resulting in different properties, as illustrated in Fig. 2.13. Regarding the geometric properties, we provide below a list of the most common target shapes:

- i **Circular targets:** They are the most commonly used targets for industrial applications, thanks to their small size and invariance in rotation and scale. To be correctly detected once projected onto a camera sensor, their diameter must be at least 5px [Luh+13]. Targets are detected using for instance pixel intensity threshold or the generalized Hough Transform for circle detection. Then, denoting $(\mathbf{x}_i)_{i=1,\dots,n}$ the n points lying inside the circle, one of the method to locate the center of the target with sub-pixel accuracy consists in calculating its centroid:

$$\mathbf{c} = \frac{1}{n} \sum_1^n \mathbf{x}_i. \quad (2.7)$$

An alternative is to detect the contours of the image ellipse with sup-pixel accuracy in order to refine the detected center [ARK01]. Now the main drawback of this circular shape is that once it is observed with a sensor non parallel to the target, it is projected as an ellipse onto the image plane, for which the center is not exactly the circle center. This

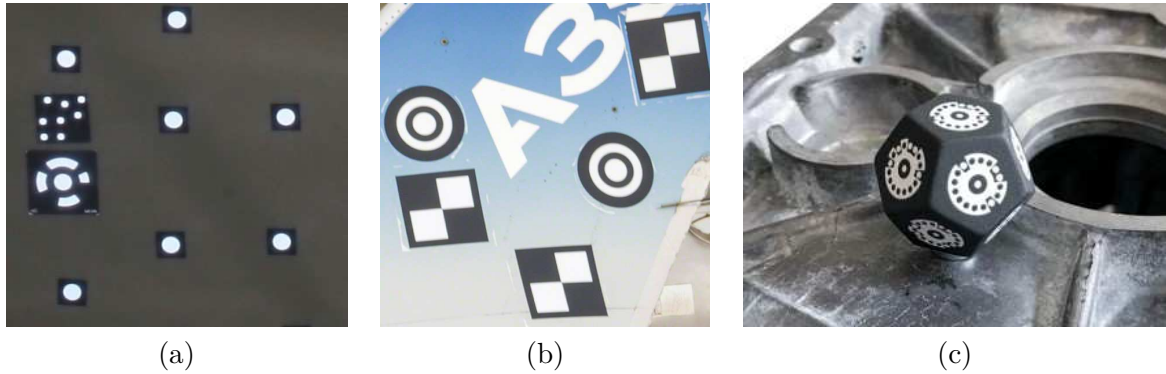


Figure 2.13: Example of targets commonly used in photogrammetry applications. (a) retro-reflective targets with circular and coded shapes, (b) concentric circles and cross targets, (c) 3D markers.

phenomenon is illustrated in Fig. 2.14. To reduce the eccentricity error, it is recommended to stay as parallel as possible to the target plane, and to use small targets (diameter between 5 and 10 pixel on the image projection), so that the eccentricity error is negligible.

- ii **Concentric circles:** To solve the problem of center eccentricity from the circular targets, target formed by concentric circles were proposed [He+12]. The idea is that from the eccentricity error of the different circles, it is possible to recover the position of the real center. Concentric circles can also be used to improve the robustness of the detection against motion blur or occlusions [Cal+16].
- iii **Cross targets:** Another commonly used shape of target is the cross targets. Here the targets can be easily detected using a template matching approach, and a sub-pixel refinement is possible by first detecting the lines and then calculating their intersection. These targets do not suffer from the eccentricity problem as the center is detected directly from the line intersection.
- iv **Coded targets:** In applications where target identification is mandatory, coded targets are used, as they directly carry their signature. These targets will usually be composed of pattern like code bars or shape codes, plus a circular target, allowing precise localization. A direct drawback of these targets is the bigger size due to the quantity of information carried.
- v **3D targets:** while 2D targets cannot (or badly) be seen from too large viewing angles, 3D targets have the advantage of being visible consistently from much larger viewing angles, making them particularly suited for multiple-view applications with distant point of views, or for tracking moving objects (e.g., motion capture for cinema or video games). These markers can be spherical, detected using similar approach than for circular targets, or some polyhedron with 2D targets printed on the facets. These targets must be attached to the marked 3D points, and their protuberant aspect can be a flaw in embedded applications.

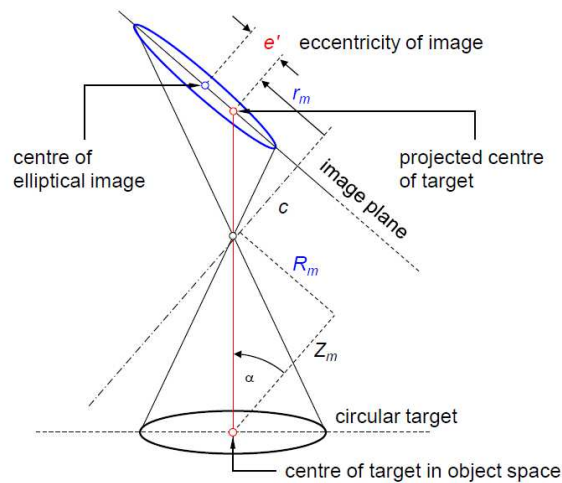


Figure 2.14: Illustration of the center eccentricity appearing when observing a circular target (from [Luh+13]).

Regarding the physical properties of the targets, the first thing to ensure is that they are visible. Indeed, detecting targets may become an issue in environment with uncontrolled light, inducing a low contrast of the targets on the image. On this matter, several material or devices are used to ensure good visibility. The first one, and most popular, is the retro-reflective material, usually employed with circular targets but also available for all other shapes. These targets reflect the light almost entirely back to its original source. Hence, the light source should be placed as close as possible to the camera optical centre (using annular light for instance). In such configuration, the target contrast with respect to the background increases and makes the detection straightforward. Nonetheless, the intensity of the light reflection from retro-reflective targets is the best when the source is in front of the targets, and decreases quickly when the angle between the target normal and the light axis increases. Basically, retro-reflective targets with circular shapes are visible at ± 45 degrees around the target normal. Moreover, it is worth mentioning that some targets are designed to reflect only infra-red light to ensure correct detection in bright scenes. To go further, when no light source is available to illuminate the targets, the light source can be directly embedded into the targets (using LEDs for instance). Self-luminous or active targets offer a good contrast when their luminosity is higher than the background light, but require a power supply and a bigger shape factor due to their instrumentation. Finally, when the light source cannot be controlled, special mate printing can be applied on the targets to prevent reflections and ensure a good contrast on the image. Such targets will require more processing to be detected as the background of the scene will still be visible, and the accuracy of the detection will depend more on the contrast and the camera resolution and sensitivity.

The second physical property to consider will be the fixation. On this point, the main ways to install targets is to use stickers, magnets, or to directly print or engrave them in the scene. The selected fixation solution will impact the intrusiveness and ease of installation, as well as the manufacturing cost and the ability to sustain environmental conditions (temperature, vibrations, or others like air flow in this study).



Figure 2.15: Example of view on an A350 wing using a 4K camera, with concentric circular and cross targets installed.

2.3.2 Target selection

In the case of this study, the numerous constraints of installation, non intrusiveness and camera positions have guided the target selection. First of all, the photogrammetry system should be as less intrusive as possible and prevent any disturbance of the aircraft aerodynamic, otherwise, flight tests would be erroneous. For this reason, markers should be flat and flush with the surface of the wing. If their thickness is small enough, the impact on the wing aerodynamic is negligible.

The second aspect to consider is the resistance to flight conditions, such as temperature shifts, air flow, pressure and humidity. Hence, the choice was made to use a sticker paper able to withstand flight conditions, that also provide an easy installation on the wing.

Then, to ensure correct detection on all images, targets should appear almost similar on each view. Yet, camera positions are distant from each others, especially for the rear camera with respect to the others, which induces rotation and scale variations of the observations. A similar aspect of the targets could be obtained by employing 3D markers, but it is prohibited by the aerodynamic constraints mentioned before, hence the necessity to use 2D targets.

Besides, circular targets could be installed to benefit from their rotation and scale invariances. However, since our cameras are mainly installed at the windows of the aircraft, the obvious drawback of using flat markers on the wing surface is that they will be observed with grazing angles of view, i.e., the angles between the camera axes and the target normal are high (about 80 degrees at the end of the wing), introducing eccentricity errors that are non negligible. Moreover, concentric circles were presented in the previous section, that could be used to compensate this error. Nevertheless, a correct detection of the circles would necessitate bigger targets that would be complicated to install, or higher camera resolutions. In Fig. 2.15, the projection size of circular targets at the end the wing on a 4K camera does not allow a correct detection, while the radius of the circles is 60cm. For all these reasons, printed stickers of 2D cross markers were selected for the wing reconstruction system. Even if they have a greater dependency on the rotation angle, they offer almost similar aspects on



Figure 2.16: Selected targets installed on an A350 wing, with red graduations stuck on the black lanes.

images. Indeed, cross targets have an invariance in rotation of right angles, which coincides roughly with the rotation between cameras at windows and rear of the aircraft. Furthermore, using cross targets, we can ensure a good visibility and similar projection sizes of the cross lines, by adjusting the length of the target according to its position on the wing.

Another problem that will be encountered in flight is the variation of the light source due to the motion of the sun with respect to the aircraft, which will generate variations of the scene illumination, and potential presence of reflections and shadows on the wing. To control the luminosity of the light, one might consider using retro-reflective targets. These targets were used in previous Airbus method for estimating the shape of 3D wings. Markers were illuminated by flashes installed close to the cameras, resulting in images where only the targets were visible. In this way, target detection was straight-forward, even if it required good synchronization between flashes and cameras, source of errors during some tests. Another requirement for the markers to reflect the light to the cameras was that they were placed orthogonally to the wing surface, which disturbed the aerodynamic of the wing, and hence limited the flight domain of the aircraft.

Light source might also be controlled with self-luminous markers, but it would require for the lights to be brighter than the background luminosity, that is already high in flight, and thus not feasible on a wing. Moreover, it would need a power supply which is not compliant with the non intrusiveness constraint. Here the retained solution is to use mate printing of the cross targets to ensure a good visibility in all possible luminosity, and prevent sun reflections that would saturate the camera sensor. These targets are less accurate but more robust to luminosity variations.

One could also think about using coded targets, that would make the identification easier while providing sub-pixel detection. Nonetheless, as the camera and wing motions are limited in flight, the targets will always appear at almost the same positions in flight. Thus their identification is already easy, and coded markers are not required. Besides, they would necessitate to be bigger for a correct identification, which should be avoided. Finally here we use 2D targets of crosses printed on stickers using a mate ink, which are detected using template matching algorithm plus a sub-pixel cross detection refinement. In addition, graduations were

stuck on the black lanes of the wing for better line matching between views, as displayed in Fig. 2.16.

2.4 Optimization under constraints of *a priori* deformation limits

Although challenging because of the specific flight test environment, wing deformation estimation can rely on a range of prior information. On the image processing side, views in flight are always the same, facilitating the detection and tracking of points of interest. The latter is also facilitated by the presence of two black lines along the wing span, that can be exploited as exposed in Section 2.2.3, or using graduations allowing one to define a set of nodes to track. Wing mechanical properties enable the use of even richer prior information, since wings are build on theoretical models using Finite Element Models (FEM), defined in Section 2.4.1. In addition to geometry scales, predicted wing deformations are thus available for any flight configuration. However, these predictions cannot be used in the particular application addressed herein. More precisely, theoretical deformation models cannot be used to robustify 3D wing reconstructions, because these reconstructions are supposed to validate (or not) these models. Instead, this work aims at exploiting the mechanical limits derived from the FEM. Specifically, limit conditions corresponding to situations where the structure materials would break are considered. We assume that these extreme cases, corresponding to the wing shattering, will not occur during tests. This work defines maximum and minimum deformations as constraints in the BA algorithm defined in Section 1.2.3.

2.4.1 Mechanical limits

An aircraft is always submitted to mechanical forces called loads, in flight as well as on ground. These loads can be static forces caused by gravity, dynamic forces from the aircraft motion (lift, drag and traction) or cyclical forces produced by repeated pressurizations and depressurizations, or temperature variations [ME17]. At the molecular structure level, loads are called stresses, that generate deformations of the structure (bending, torsion, shear, traction or compression). To withstand stress through the entire aircraft life cycle, its structure should be designed so that deformations remain always reversible, i.e., deformations are only elastic and not plastic. This is ensured by testing the structure on two types of load cases, fatigue and static cases.

The fatigue case corresponds to testing the deformation response of the structure to realistic cycles of flight (take off, flights in various conditions, and landing). These tests are necessary as it is known that structure tolerance to stress decreases gradually with the number of cycles. To certify an aircraft, there should be no damage of the structure after two aircraft life cycles. Static cases on the other side are tests to validate the structure stability for maximum loads that an aircraft can encounter in its life, including maximum cabin pressure and mechanical loads. By applying **limit loads**, that only occurs once in an aircraft life, structure should

not break. Breakage could only occur when exceptional loads are applied, called **ultimate loads**, for which the rate of occurrence is almost 0. In facts, ultimate loads correspond to 1.5 times the limit loads in the case of Airbus aircraft. To evaluate static cases, simulations are conducted with theoretical calculation using the FEM, and further tests are performed on real aircraft parts to validate simulations (illustrated in Fig. 2.18).

Finally, thanks to the FEM models, we have access to the 3D shapes of the wing under limit and ultimate loads. Assuming that the wing will not break during tests, this means that knowledge of its deformation limits can be exploited to improve the 3D reconstruction from the BA (1.28). To this aim, several relevant limit loads were selected to estimate the mechanical limits of an A350 wing. Fig. 2.17 displays the shapes of the wing for some limit loads.

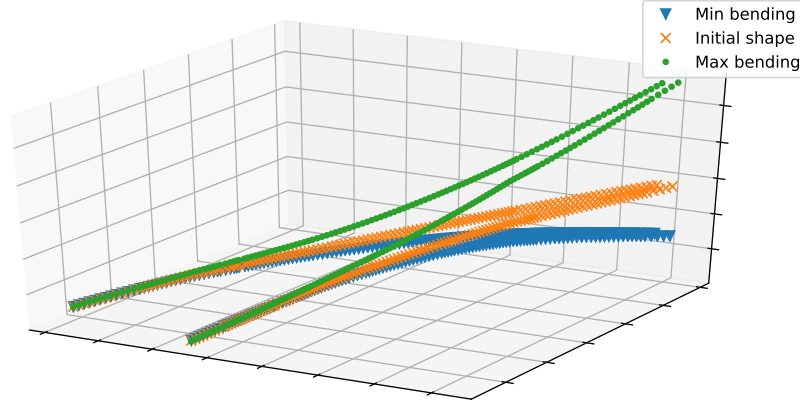


Figure 2.17: Wing shapes under maximum and minimum bending load cases from FEM simulations.

2.4.2 Definition of mechanical constraints

Thanks to the knowledge of mechanical limits of the wing, various mechanical constraints can be defined. Consider N 3D-points used for wing reconstruction denoted as \mathbf{X}^i for $i = 1, \dots, N$, and denote as $\mathbf{X}^i = (x^i, y^i, z^i)$ the i th deformation point, using axes as shown in Fig. 2.19. This work proposes to use the following set of limits

- i. Volume limits: each point has a specific maximum volume (sphere, ellipsoid, or some volume defined according to the FEM data).
- ii. Bending limits: $\forall i, \exists (b_{\min}^i, b_{\max}^i)$, such that the bending $\frac{\partial^2 z^i}{\partial y^2}$ ranges in $[b_{\min}^i, b_{\max}^i]$.
- iii. Torsion limits: $\forall i, \exists (t_{\min}^i, t_{\max}^i)$, such that the torsion $\frac{\partial^2 z^i}{\partial x \partial y}$ ranges in $[t_{\min}^i, t_{\max}^i]$.

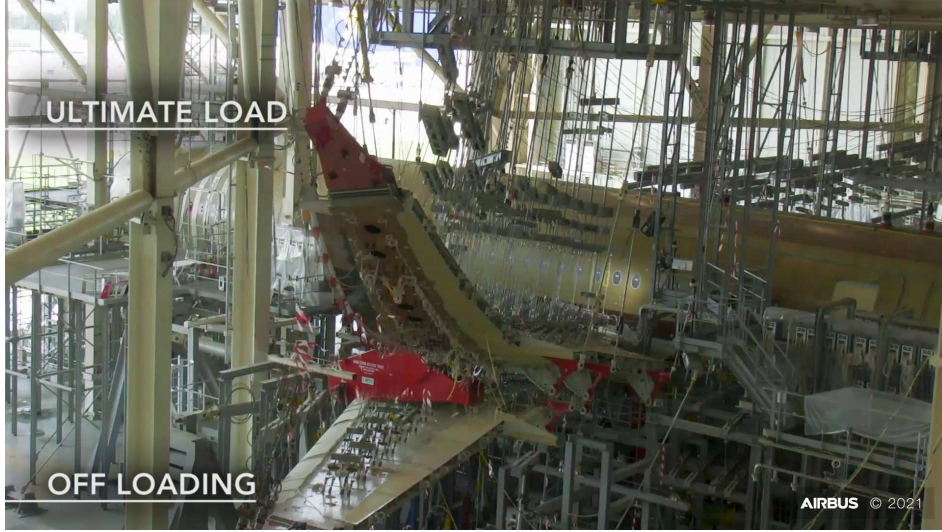


Figure 2.18: Static test on an A350 aircraft. In this picture, the wing bent under the forces of an Ultimate Load is overlaid with its position without forces.

iv. Relative elongation limits: $\forall i, \exists (\epsilon_{min}^i, \epsilon_{max}^i)$, such that

$$\epsilon_{min}^i < \frac{d(\mathbf{X}^i, \mathbf{X}^{i-1}) - d_0(\mathbf{X}^i, \mathbf{X}^{i-1})}{d_0(\mathbf{X}^i, \mathbf{X}^{i-1})} < \epsilon_{max}^i \quad (2.8)$$

where $d(\mathbf{X}^i, \mathbf{X}^{i-1})$ is the Euclidean distance between points \mathbf{X}^i and \mathbf{X}^{i-1} in the (x, y) plane, and $d_0(\mathbf{X}^i, \mathbf{X}^{i-1})$ is the initial distance before deformation.

To integrate these limits in the wing reconstruction process, we assume that the limits are locally valid, which allows their definition using finite differences on a set of nodes in the (x, y) plane. Considering the node \mathbf{X}^i and its neighborhood $(\mathbf{X}^{i-2}, \dots, \mathbf{X}^{i+2}, \mathbf{X}'^{i-2}, \dots, \mathbf{X}'^{i+2})$, detected on the wing lines as illustrated in Fig. 2.19 (\mathbf{X}^i and \mathbf{X}'^i are on the same i th wing section (i.e., along the same coordinate y axis), one can define a set of C constraints $(g_k)_{k=0, \dots, C}$.

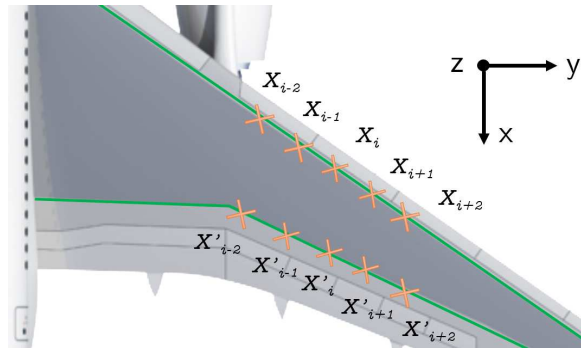


Figure 2.19: Node illustration on the aircraft wing.

- i. Volume constraint is expressed as 3D points having a limited displacements in the (x, y) plane, bounded by boxes defined by their center (r_x^i, r_y^i) width r_w^i and height r_h^i , leading to:

$$\begin{aligned} g_0(\boldsymbol{\alpha}_r, \mathbf{X}^i) &= (r_x^i - x^i) < 0, & g_1(\boldsymbol{\alpha}_r, \mathbf{X}^i) &= (x^i - r_x^i - r_w^i) < 0, \\ g_2(\boldsymbol{\alpha}_r, \mathbf{X}^i) &= (r_y^i - y^i) < 0, & g_3(\boldsymbol{\alpha}_r, \mathbf{X}^i) &= (y^i - r_y^i - r_h^i) < 0. \end{aligned} \quad (2.9)$$

- ii. Bending constraints: $\forall i, \exists (b_{\min}, b_{\max})$, such that

$$g_4(\mathbf{X}^i) = \frac{z_{i+1} - 2z_i + z_{i-1}}{(y_{i+1} - y_i)^2} - b_{\max}^i < 0, \quad (2.10)$$

$$g_5(\mathbf{X}^i) = b_{\min}^i - \frac{z_{i+1} - 2z_i + z_{i-1}}{(y_{i+1} - y_i)^2} < 0. \quad (2.11)$$

- iii. Torsion constraints: a first approach for the torsion calculation is to use finite differences. However, due to sampling irregularities, this calculation introduces too much noise (see details in Section 2.4.4). Another approach is thus considered. Assuming that on each facet of 4 points $(\mathbf{X}_i, \mathbf{X}_{i+1}, \mathbf{X}'_i, \mathbf{X}'_{i+1})$, a polynomial can be estimated as:

$$z = a_i + b_i x + c_i y + d_i xy \quad (2.12)$$

where (a_i, b_i, c_i, d_i) are the polynomial coefficients, the following system of equations can be obtained:

$$\mathbf{M}_i \mathbf{A}_i = \mathbf{Z}_i \quad (2.13)$$

with

$$\mathbf{M}_i = \begin{pmatrix} 1 & x_i & y_i & x_i y_i \\ 1 & x_{i+1} & y_{i+1} & x_{i+1} y_{i+1} \\ 1 & x'_i & y'_i & x'_i y'_i \\ 1 & x'_{i+1} & y'_{i+1} & x'_{i+1} y'_{i+1} \end{pmatrix}, \mathbf{A}_i = \begin{pmatrix} a_i \\ b_i \\ c_i \\ d_i \end{pmatrix}, \text{ and } \mathbf{Z}_i = \begin{pmatrix} z_i \\ z_{i+1} \\ z'_i \\ z'_{i+1} \end{pmatrix}. \quad (2.14)$$

With this formulation, the polynomial coefficients can be calculated as

$$\mathbf{A}_i = \mathbf{M}_i^{-1} \mathbf{Z}_i \quad (2.15)$$

where $\mathbf{M}_i^{-1} = (\mathbf{C}_i^1, \mathbf{C}_i^2, \mathbf{C}_i^3, \mathbf{C}_i^4)^T$ is the inverse matrix of \mathbf{M}_i . Therefore, the torsion on a facet is calculated directly as

$$\frac{\partial^2 z_i}{\partial x \partial y} = d_i = \mathbf{C}_i^4 \mathbf{Z}_i. \quad (2.16)$$

Finally, the torsion constraints can be expressed as: $\forall i, \exists (t_{\min}^i, t_{\max}^i)$ such that

$$g_6(\mathbf{X}^i) = d_i - t_{\max}^i < 0, \quad g_7(\mathbf{X}^i) = t_{\min}^i - d_i < 0. \quad (2.17)$$

Note that another possible approach would be to calculate d_i by solving directly the linear system, using classical methods such as the LU decomposition. However, the inversion of \mathbf{M}_i is preferred because it is as fast as using an LU decomposition for \mathbf{M}_i of size 4×4 .

Moreover, since the point coordinates in the (x, y) plane are supposed to remain close to their initial position, the matrix \mathbf{M}_i can be calculated only once at initialization, and then conveniently used to calculate the torsion for every frame.

iv. Relative elongation constraint: $\forall i, \exists (\epsilon_{\min}^i, \epsilon_{\max}^i)$, such that

$$g_8(\mathbf{X}^i) = \frac{d(\mathbf{X}^i, \mathbf{X}^{i-1}) - d_0(\mathbf{X}^i, \mathbf{X}^{i-1})}{d_0(\mathbf{X}^i, \mathbf{X}^{i-1})} - \epsilon_{\max}^i < 0, \quad (2.18)$$

$$g_9(\mathbf{X}^i) = \epsilon_{\min}^i - \frac{d(\mathbf{X}^i, \mathbf{X}^{i-1}) - d_0(\mathbf{X}^i, \mathbf{X}^{i-1})}{d_0(\mathbf{X}^i, \mathbf{X}^{i-1})} < 0. \quad (2.19)$$

One could consider that some of these constraints are redundant and hence that some of them are not necessary. However, they are in fact complementary. For instance, volume constraints apply to individual points while elongation constraints are associated with pairs of points, and bending constraints are defined for triplets of points. In addition, it is worth noting that the use of inequations creates bounds on the 3D points but do not enforce them to follow any deformation model.

2.4.3 Constrained bundle adjustment

This section explains how to introduce the previously defined constraints in BA. In this work, because of camera motions during the flight, 3D coordinates of the points and cameras are estimated in a moving coordinate system, while the considered constraints are considered in the aircraft coordinate system. Therefore, an additional registration phase is required to transfer the points in the aircraft coordinate system. To perform this operation, the aircraft reference points are detected from the rear camera image, further used to estimate the transfer matrix \mathbf{P} from the aircraft coordinate system to the camera system. Using the estimated parameters $\boldsymbol{\alpha}_r$ from the same camera, the points $\tilde{\mathbf{X}}^i$ are then registered as:

$$\tilde{\mathbf{X}}^i = \mathbf{P} \left[\mathbf{R}_r^T, -\mathbf{R}_r^T \mathbf{t}_r \right] \mathbf{X}^i, \quad (2.20)$$

where \mathbf{R}_r and \mathbf{t}_r are the parameters of the r th camera, as defined in Section 1.2.3.

After the registration phase, the constraints introduced in Section 2.4.2 are expressed as regularization terms to penalize the objective function (1.28) [CZ13, p. 564], defining the new regularized optimization problem (called CBA hereafter):

$$\arg \min_{\boldsymbol{\alpha}_j, \mathbf{X}^i} \sum_{i,j} [\mathbf{x}_j^i - \hat{\mathbf{x}}(\boldsymbol{\alpha}_j, \mathbf{X}^i)]^2 + \sum_k \mu_k \left\{ \sum_i [g_k^+(\boldsymbol{\alpha}_r, \tilde{\mathbf{X}}^i)]^2 \right\}, \quad (2.21)$$

where μ_k are positive hyperparameters and $g_k^+(\boldsymbol{\alpha}_r, \tilde{\mathbf{X}}^i) = \max(0, g_k(\boldsymbol{\alpha}_r, \tilde{\mathbf{X}}^i))$, with g_k the k th constraint.

With this formulation, μ_k equals zero when the corresponding constraint is respected, and therefore this penalty does not impact the results. As explained previously, the optimization

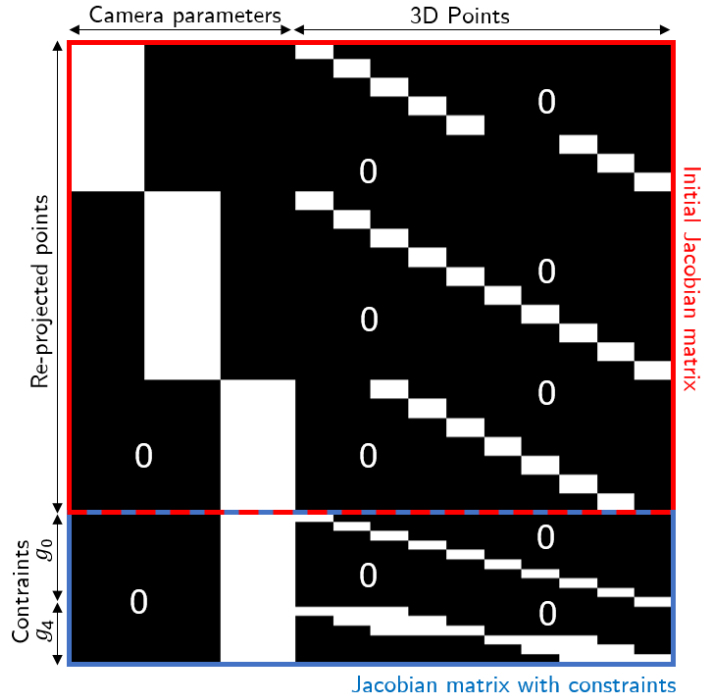


Figure 2.20: Example of sparse bundle adjustment Jacobian matrix for 3 cameras and 10 points. The last rows represent the two first constraints g_0 and g_4 defined in 2.4.2.

method used by BA is based on the Jacobian matrix, which requires the objective function to be differentiable. To enforce differentiability of (2.21), we use the *Courant-Beltrami* penalty function [CZ13, p. 566], with a quadratic term on g_k^+ , which also smooths this function. Finally, since the constraints are applied to specific point neighborhoods, and depend only on the rear camera parameters, the sparsity of the Jacobian matrix is preserved, as shown by the example in Fig. 2.20, considering the derivative of each element of the projection error and constraints with respect to all camera and point parameters. Similarly to the classical BA problem, the sparsity of the Jacobian matrix significantly reduces the computational cost of the optimization algorithm. To further improve the computational cost of the optimization, this work proposes to use an analytical form of the Jacobian matrix (see Appendix A for details), instead of the usual estimation approach using finite differences.

2.4.4 Extraction of mechanical limits from the FEM

In the previous section, CBA was introduced to take advantage of the prior knowledge about the aircraft mechanical limits to improve the 3D reconstruction of wings. These limits were defined in Section 2.4.2 and this section will now expose how to extract them from the FEM. Shapes of the wing were simulated under a set of ultimate loads, defined by experts to be representative of the most substantial wing deformations. The set of ultimate loads include maximum bending with aircraft fuselage bent in various ways, minimum bending and ground shape. Maximum pressurization loads were also included to evaluate window motions where

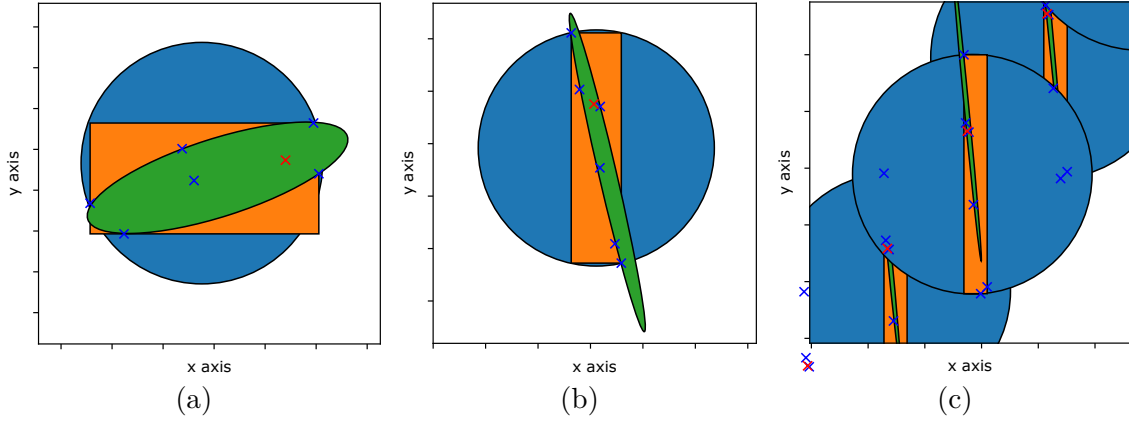


Figure 2.21: Bounding shapes in the (x, y) plane for the volume constraint at the beginning (a), middle (b) and end (c) of the wing. For the initial node position, displayed as a red cross, blue crosses represent all the node positions for the various load cases.

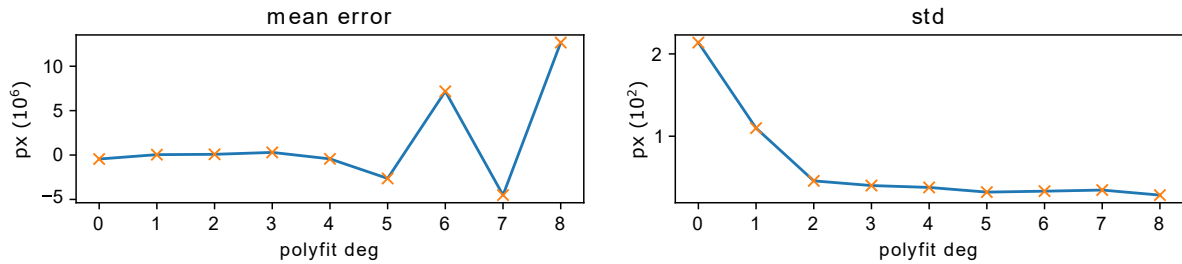


Figure 2.22: Evaluation of the influence of degree for the polynomial fit. The mean error (top) and standard deviation (bottom) are calculated for all the load cases at once.

cameras are fixed.

Volume constraints: for the volume constraints, limit displacements of the wing nodes in the (x, y) plane were extracted and bounded. Circular, rectangular and elliptical bounding shapes were tested, as displayed in Fig. 2.21. Circular shapes allow a very simple implementation but are not very accurate at the wing end, where displacements along the y axis are about ten times higher than those along the x axis. On the other side, bounding ellipses are more complex to implement and may generate errors. Therefore, we selected bounding boxes, that have low complexity of implementation while closely fitting the displacement limits. During experimentation, dimensions and positions of the bounding boxes can be interpolated at specific point coordinates in the (x, y) plane. Note that the displacement limits could also be evaluated in 3D to obtain a narrower volume limit. However, this study focuses more on the practical implementation foreseen for real time applications.

Bending constraint: To calculate the derivatives $\frac{\partial^2 z^i}{\partial y^2}$, a polynomial fitting was first performed on each FEM shape, such that $z = P(y)$, with P a polynomial of degree 5. With this representation, the bending derivatives are easily calculated as new polynomials, and the

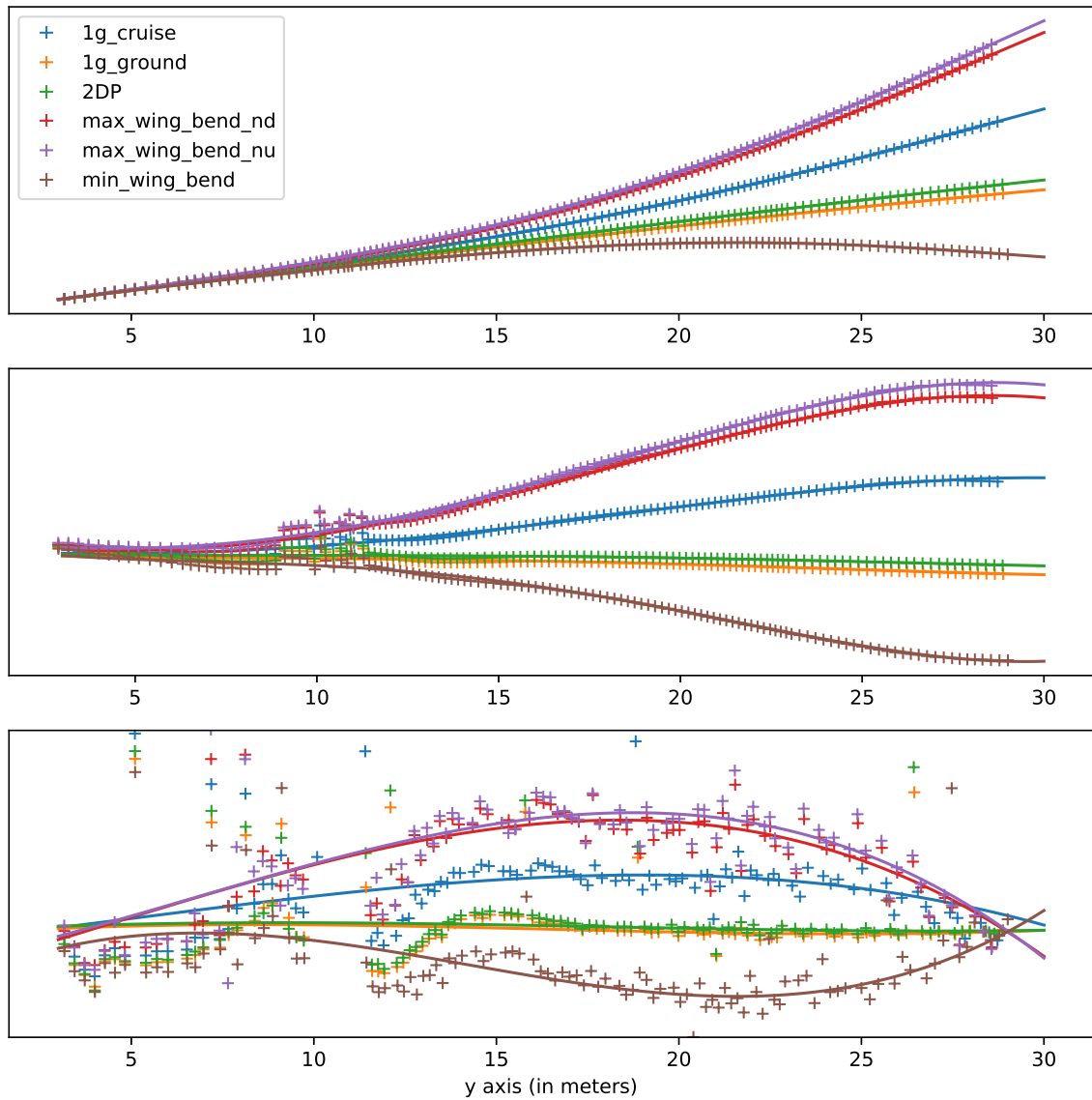


Figure 2.23: Polynomial fitting for the bending constraints. (Top) View of the wing shapes for various Load Cases on the (y, z) plan with their fitted polynomials $z = P(y)$. The approximations by finite differences of the derivatives $\frac{\partial z^i}{\partial y}$ and $\frac{\partial^2 z^i}{\partial y^2}$ are displayed respectively in (middle) and (bottom), overlaid with the corresponding derivatives of the polynomials. Noisy estimation of the derivatives can be observed at about 10m of wing span, due to a local gap in the node sampling.

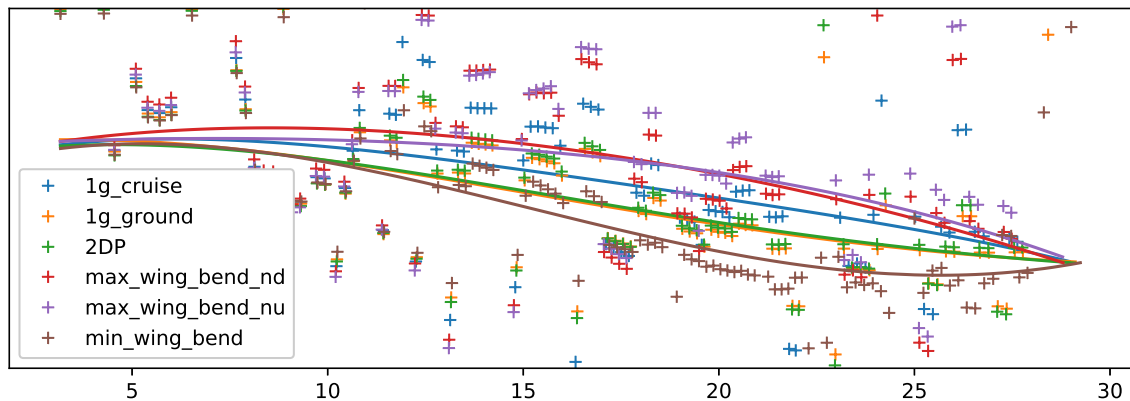


Figure 2.24: Torsion along the wing span calculated using finite differences and polynomial fitting. One can observe that the calculated derivatives using finite differences and polynomial fitting do not match for this example.

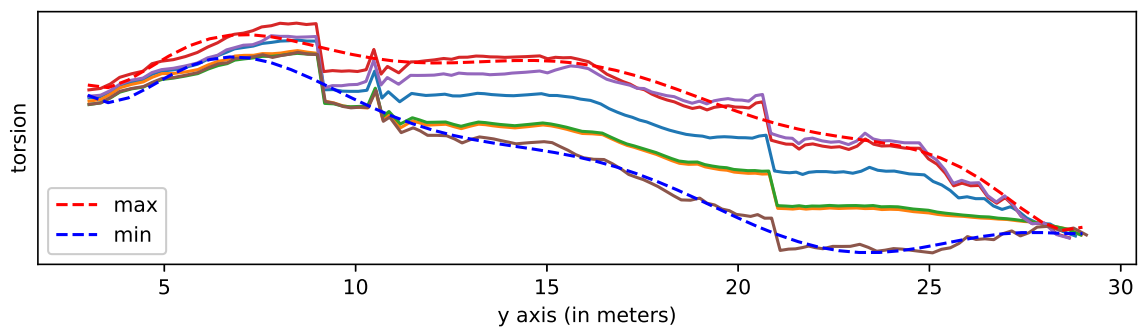


Figure 2.25: Torsion along the wing span. The upper and lower envelopes are approximated by polynomials P and Q such that $t_{min} = P(y)$, and $t_{max} = Q(y)$. The color legend is identical to that of Fig. 2.23.

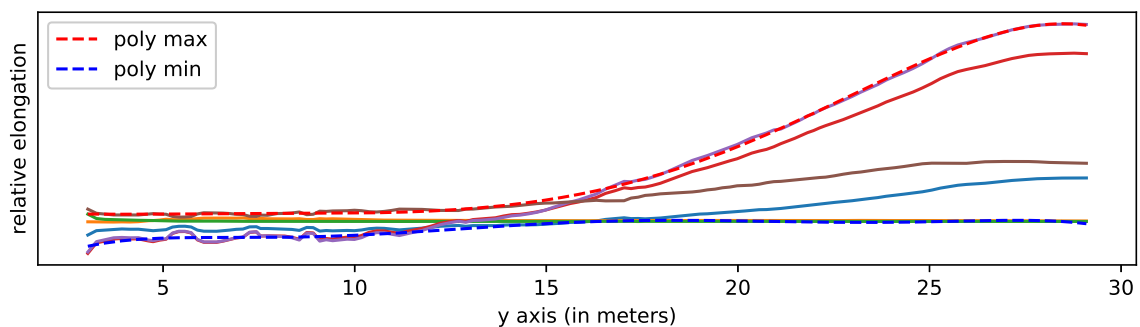


Figure 2.26: Relative elongation along the wing span. The upper and lower envelopes are approximated by polynomials P and Q such that $\epsilon_{min} = P(y)$, and $\epsilon_{max} = Q(y)$. The color legend is identical to that of Fig. 2.23.

envelope of bending can be extracted using two polynomials corresponding to the upper and lower limits (displayed in Fig. 2.23). The best degree for the polynomial was determined by calculating the global error and standard deviations of the fits for all load cases, as displayed in Fig. 2.22, which shows calculation errors occurring for too high degrees. Fig. 2.23 also demonstrates that the polynomial derivatives correctly match the estimations from finite differences, expressed in (2.10). Finally, the use of polynomials has a practical advantage during tests, where limits can be easily calculated from the y coordinate of the estimated 3D point.

Torsion constraint: following the approach proposed for the bending limitations, the torsion $\frac{\partial^2 z^i}{\partial x \partial y}$ was first calculated by fitting a polynomial Q such that $z = Q(x, y)$. However, due to sampling irregularities, resulting curves do not match the calculation from finite differences, as illustrated in Fig. 2.24. Since the same errors could appear during real tests where graduations are not placed perfectly, the approach of calculating torsion for each facet was selected. Using the formulation defined in (2.16), the torsion is calculated for each facet and for each load case, and the minimum and maximum envelopes are approximated as polynomials to be easily implemented during the tests (see Fig. 2.25).

Relative elongation constraint: Here the relative elongation defined in (2.8) was calculated between nodes of each load case, and the envelope of maximum and minimum relative elongation was approximated by two polynomials (see Fig. 2.26).

2.4.5 Results and discussion

Real data from a ground test was acquired on an Airbus A350-900 to evaluate the proposed method. To reproduce an installation similar to the one foreseen during flights, cross targets were installed on the wing surface to improve the accuracy of point detection in the images. Four 4K cameras were installed on the aircraft windows. The rear camera was simulated by a drone placed on the vertical stabilizer. Examples of images acquired by these cameras are displayed in Fig. 2.27. To clearly identify the points on which deformation constraints are applied, graduations were stuck on the two black lines every 30 cm, which will define the nodes of the proposed wing reconstruction.

After installation, a drone was used along with the software Agisoft Metashape [Met] to perform a scan of the wing and initialize the camera and point positions. Finally, wing vibration was generated by manually shaking the wing tip of about 5 cm (the vertical motion amplitude was estimated using a scale board). As expected, the detection of graduations observed with low angles was less accurate compared to large angles (see wing tips in cameras 1 and 3 in Fig. 2.27). In addition, graduation detection was not possible in some images because of reflections on the wing (see camera 3 in Fig. 2.27).

The proposed constrained algorithm (CBA) was implemented in Python and compared to the classical unconstrained BA algorithm. The constrained optimization was performed using the least-squares “trust region reflective” method implemented in the Scipy library [Va20], benefiting from its capability to take as input a function to construct the Jacobian matrix



(a) Camera 1

(b) Camera 3

Figure 2.27: Examples of recorded views resulting from a the test on ground with an Airbus A350-900.

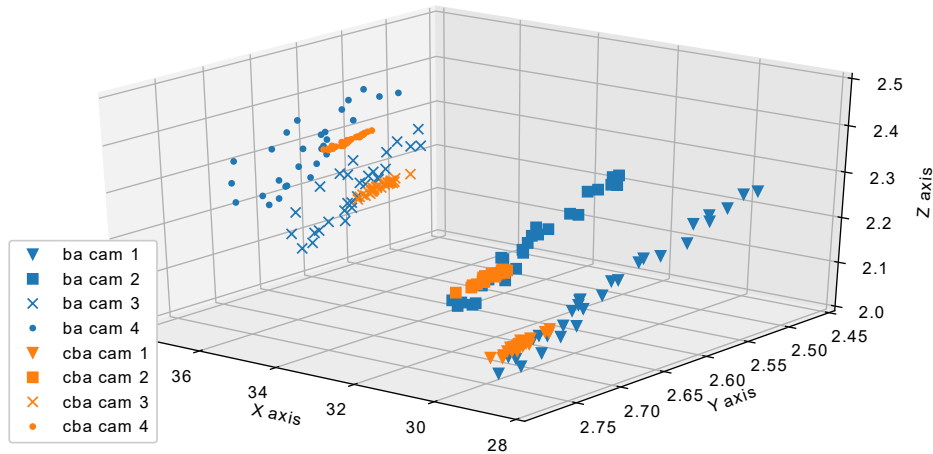


Figure 2.28: Estimated motions (in meters) of the 4 cameras located on the aircraft windows versus time.

for each step of the optimization, as opposed to estimating it, which would also calculate elements that are known to be zeros. All the mechanical limits were estimated from the FEM data as presented in Section 2.4.4. Point and camera positions were extracted from a representative video of the moving wing, by running 30 frames using our algorithm. For comparison, we used unconstrained BA, and BA with combinations of all defined constrains, of volume, bending, torsion, and elongation. A first observation was that using combination of constrains without the volume constrain yields important errors due to scale loss. Thus at least the volume constraint should be used. Fig. 2.28 shows that the camera estimation precision is enhanced using the CBA algorithm, as cameras were supposed to have negligible motions during the ground test. In particular, it can be observed that camera motions using CBA are reduced compared to BA.

Furthermore, Fig. 2.29 shows that using constrains also significantly improves the estimation results, resulting into an amplitude of 5cm at wing tip and of less than 1cm in the

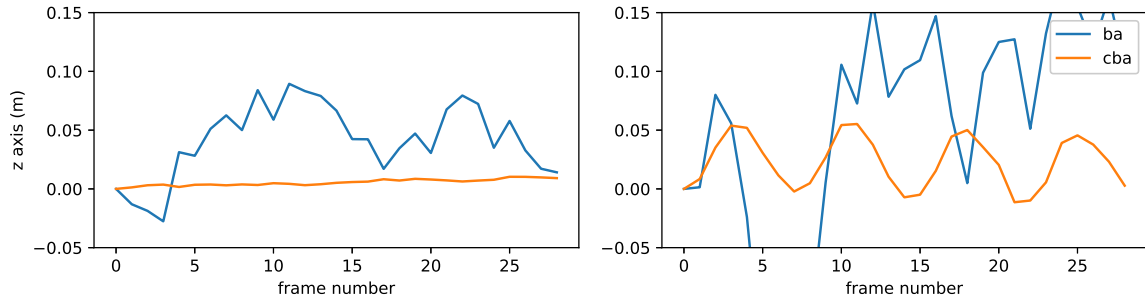


Figure 2.29: Bending results at the middle of the wing (left) and at wing tip (right).

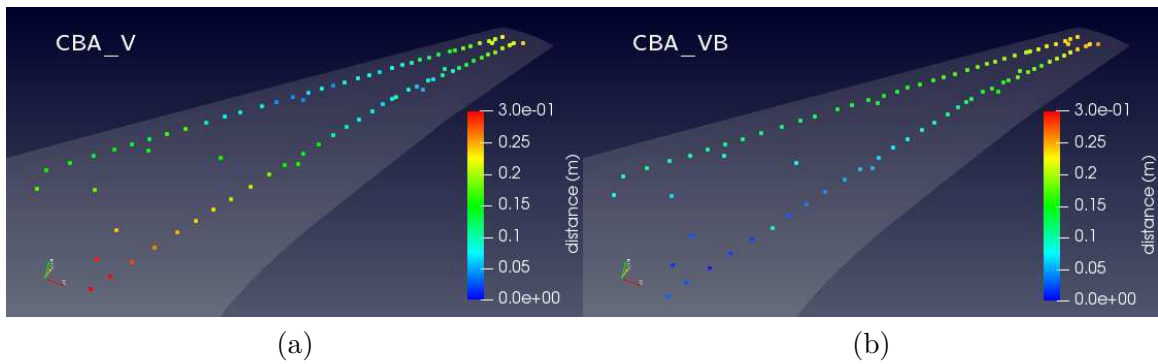


Figure 2.30: Comparison of the distances between the reconstructed point cloud and the theoretical model of ground shape. (a) reconstruction using only volume constraint, (b) reconstruction using both volume and bending constraints.

middle of the wing, which is consistent with our measurements using the scale board. Besides, the distance between the wing reconstruction and the theoretical ground shape (computed using Cloud Compare [Clo]) displayed in Fig. 2.30 shows that the distance at the wing start is reduced using volume and bending constraints "CBA_VB" (of more than 0.2m compared to using only volume constraint "CBA_V"). As a consequence, the combination of local volume and bending constraints improves the global estimation, as points at the wing start should be closer to the model, where it is more rigid, than at the end. Note that the FEM is only a model, which is not supposed to perfectly fit the data. Thus, a deviation from this model is possible. Finally, estimation results versus time, illustrated in Fig. 2.31, suggest that the volume constraint is correctly respected and improves point position tracking, all points remaining close to their initial location in the (x, y) plan. As soon as volume and bending constraints are applied, the use of additional constraints only slightly improve the results of the estimated 3D points. Thus one cannot tell how it improves the reconstruction on this set of data where no ground trough is available. Regarding the hyperparameters used for the penalization, we considered equal values of the parameters $(\mu_j)_{j=0,\dots,6}$ mainly by simplicity. Then the value of each parameter was selected by evaluating its impact on the reprojection error $\sum_{i,j} [\mathbf{x}_j^i - \hat{\mathbf{x}}(\boldsymbol{\alpha}_j, \mathbf{X}^i)]^2$, the constraint error $\sum_i [g_k^+(\boldsymbol{\alpha}_r, \tilde{\mathbf{X}}^i)]^2$ and the

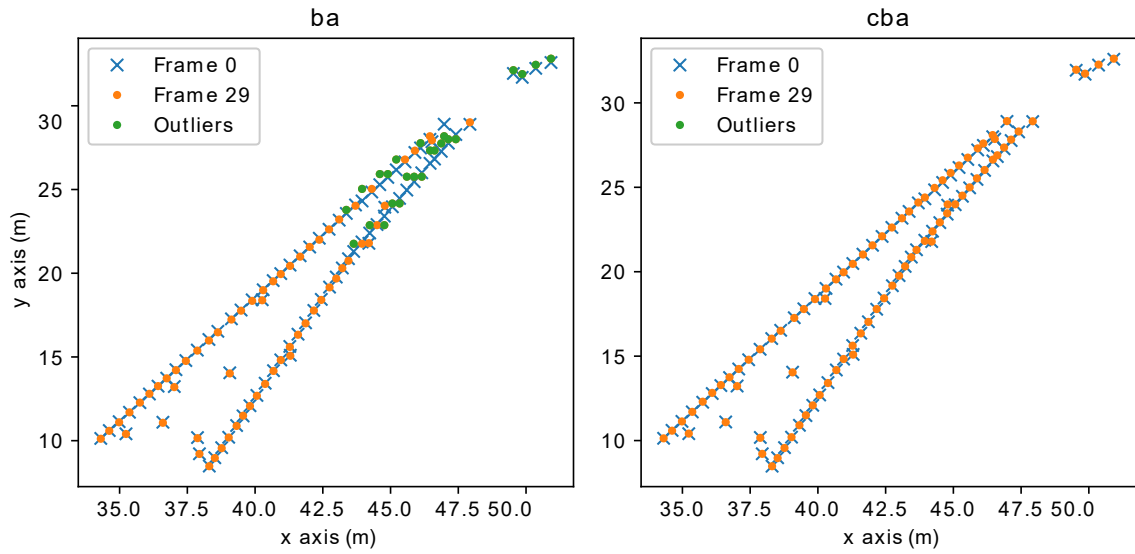


Figure 2.31: Point reconstructions in the (x, y) plane for the first and last frames. (left) without the constraint, (right) with the volume and bending constraints. Some outliers can be observed in the last ba frame.

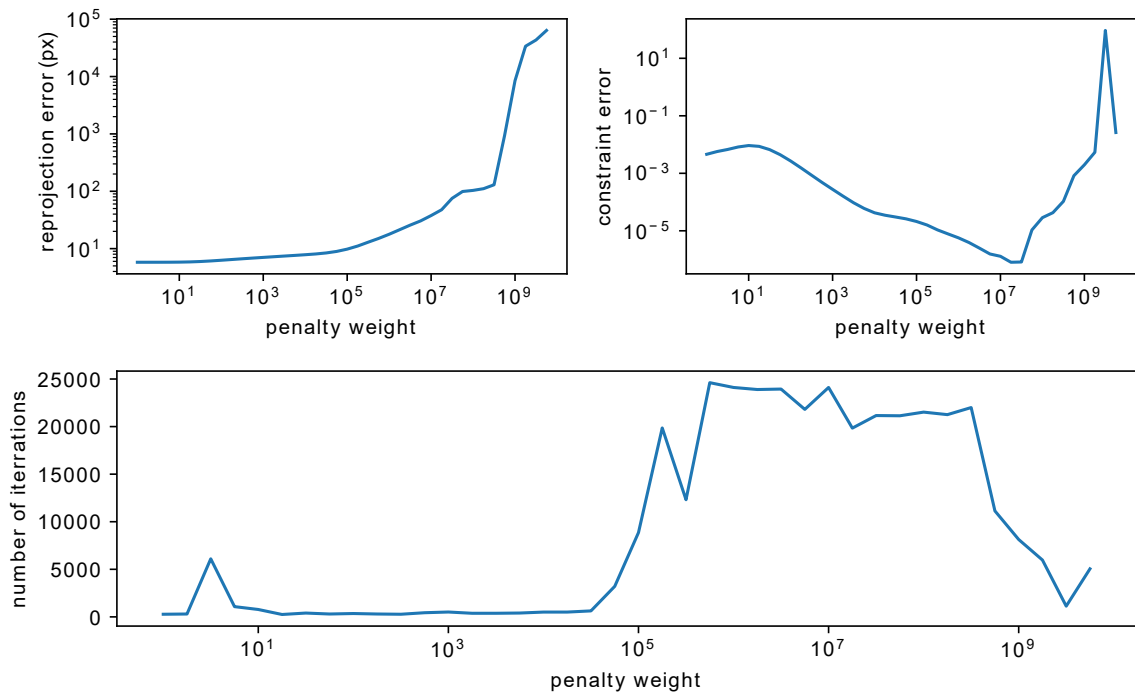


Figure 2.32: Influence of the penalty parameter on the reprojection error, the constraint errors and the number of iterations required to converge.

number of iterations required for the CBA optimization to converge. The result of this test is shown in Fig. 2.32, where one can see that increasing the value of the penalty parameter lowers the constraint errors, but increases the reprojection error and the convergence time. Moreover, when the value of the hyperparameter reaches about 10^7 , results become aberrant with large errors, which can probably be imputed to the routine used for optimization. Finally, the penalty parameter was set to 10^4 in all our experiments. This value makes a compromise between the different errors depicted in Fig. 2.32. Further studies could concentrate on finding automatically the optimum individual hyperparameters associated with the different constraints.

2.5 Conclusion

This chapter proposed a new approach for estimating wing deformations in flight using a photogrammetry approach, using natural features of the wing or markers. The proposed method introduced mechanical limits of an aircraft wing deformation into a bundle adjustment algorithm for 3D estimation using multi-view photogrammetry. For this purpose, regularization terms were considered into the classical bundle adjustment method. The potential of the proposed method was demonstrated through realistic experiments conducted on images acquired on an aircraft located on the ground. The application of all the proposed constraints in flight is clearly an interesting prospect. Another area of improvement is to use weighted bundle adjustment to reduce the influence of wrong observations on the reconstruction. Finally, it would be interesting to study the hybridization of the proposed method with data from other sensors such as inertial units.

Uncertainty estimation for 3D-wing reconstruction

Contents

3.1	State of the art about uncertainty estimation	76
3.1.1	Uncertainty estimation	77
3.1.2	Propagation using a mathematical model	79
3.1.3	Experimental validation	81
3.2	Uncertainty sources	82
3.2.1	Inventory of the sources	83
3.2.2	Summary of the system chain	88
3.2.3	Quantification of the main error sources	92
3.3	Error propagation for 3D reconstruction	96
3.3.1	Uncertainty estimation by the Monte Carlo method	97
3.3.2	Uncertainty from the propagation law	98
3.3.3	Simulation scenario using synthetic images	101
3.4	Results and comparison	102
3.5	Conclusion	106

In the previous chapter, a new flexible method for 3D reconstruction of a wing in flight was presented based on multiple view videogrammetry. In particular, considering mechanical limitations to improve the estimation of wing deformations provided encouraging results in the perspective of the targeted application. Yet, to this point, one cannot guaranty that the estimated 3D deformations are compliant with Airbus requirements in terms of precision. Consequently, the goal of this chapter is to lift the veil on the reconstruction uncertainty of the proposed method.

Since the notion of measurement precision may be confusing, Section 3.1 defines the basics of uncertainty estimation, with focus on the different terms and methodologies. Then, Section 3.2 focuses on the consideration and the evaluation of uncertainty sources, and the effect of varying parameters such as light that may impact the reconstruction results. In Section 3.3, various methods for propagating the uncertainty of the main sources are presented. Simulation results are exposed and compared in Section 3.3. Finally, conclusions and perspectives on this assessment of 3D-reconstruction quality are drawn in Section 3.5.

3.1 State of the art about uncertainty estimation

Interpretation and ability to rely on data measurement or parameter estimates is only possible if a quantitative indication of that measurement or estimation quality is provided. For instance, measuring a distance using a laser or a ruler can deliver two different quantities, and test results cannot be compared without the knowledge of their qualities. This indication is brought by the evaluation of uncertainty about the parameter estimates. To introduce these concepts, it is necessary to first present the basics.

A physical quantity has always a true value, which is most of the time unknown. If one seeks to measure or to estimate this quantity, the result will have an error, representing the difference between the measurement and the true value. The first component of this error is a systematic error, that can be corrected when the ground truth is known (during the calibration for instance). The second component is random, arising from varying parameters that influence the estimation. In the case of wing reconstruction, a systematic error could be induced by the distortion of camera optics, while luminosity variations would introduce random errors in the 3D estimation. The smaller the error, the more accurate the estimation.

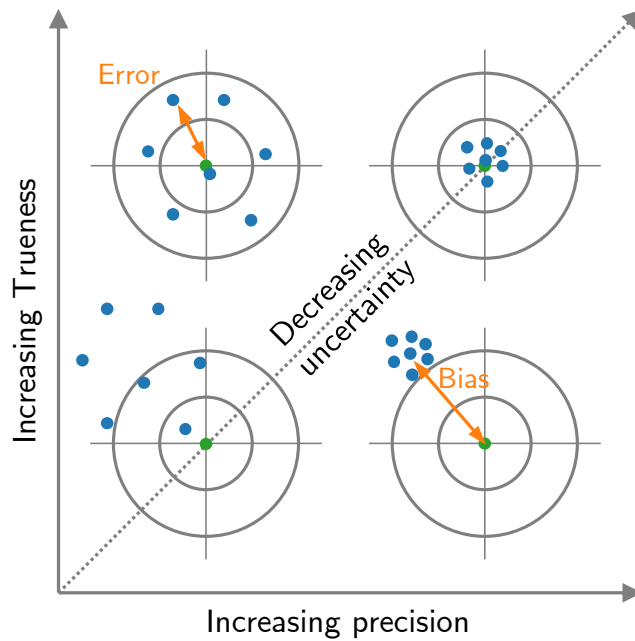


Figure 3.1: Illustration of the concepts of estimation trueness, precision and uncertainty, in four different scenarios. Blue dots represent estimates of a quantity for which the true value is known and displayed as a green dot. The uncertainty decreases when precision and/or trueness increases.

In the case of multiple estimates of the same quantity, the difference between the average value of these estimates and the true value is called the bias, corresponding to the systematic

error. The trueness of the measurement increases when the bias decreases. Furthermore, the random errors induce a dispersion of the results, called the precision. Finally, the uncertainty of an estimate represents the doubt on the result. More precisely, it gives a range around the estimate within which the true value is known to lie. These concepts are illustrated in Fig. 3.1.

To evaluate and express the error and uncertainty so that it is globally understood and accepted, procedures have been proposed in the principle standard GUM (Guide to the expression of Uncertainty in Measurement), its supplements [Guma; Gumb; Gumc], and in the ISO 5725 [Iso]. While these norms do not directly apply to image processing applications, they give guidelines that will be followed in this chapter. To our knowledge, the standard VDI/VDE 2634 on optical 3-D measuring systems [Vdi] is the only standard that addresses the subject of 3D estimation using photogrammetry, where it is recommended that uncertainty evaluation is performed by reconstructing the geometry of a known cuboid mock-up with spherical targets.

3.1.1 Uncertainty estimation

In general, the uncertainty of an estimation is used to give an appreciation of the confidence interval of the estimated parameter. For a parameter x , the confidence interval is an interval $[d_1, d_2]$ such that the probability

$$P[d_1 < x < d_2] = \alpha, \quad (3.1)$$

where α is the confidence parameter, usually equal to 0.95 or 0.99. To determine this interval, from a observation set (x_1, x_2, \dots, x_n) of $X_i \sim \mathcal{N}(x, \sigma^2)$, one seeks to express these estimators as a statistics $T(x_1, \dots, x_n)$ whose law is known and depends on x , and for which one can calculate (3.1). In the Gaussian context, one can proceed as follows: the estimators \bar{x} and $\bar{\sigma}$ of the parameters are first calculated using

$$\bar{x} = \frac{1}{n} \sum_{i=1}^n x_i, \quad \text{and} \quad \bar{\sigma}^2 = \frac{1}{n-1} \sum_{i=1}^n (x_i - \bar{x})^2. \quad (3.2)$$

Then, using the following notations

$$U = \frac{\bar{x} - x}{\sigma/\sqrt{n}} \sim \mathcal{N}(0, 1), \quad \text{and} \quad V = \frac{1}{\sigma^2} \sum_{i=1}^n (x_i - \bar{x})^2 \sim \chi_{n-1}^2, \quad (3.3)$$

one has

$$T(x_1, \dots, x_n) = \frac{U}{\sqrt{\frac{V}{n-1}}} = \frac{\sqrt{n(n-1)}(\bar{x} - x)}{\sqrt{\sum_{i=1}^n (x_i - \bar{x})^2}} \sim t_{n-1}, \quad (3.4)$$

where t_{n-1} used for the Student distribution with $n - 1$ degrees of freedom. Using the cumulative distribution function of a Student distribution t_n , one can determine a scalar t_α

such that the following inequality is satisfied with probability α :

$$-t_\alpha < T(x_1, \dots, x_n) < t_\alpha, \quad (3.5)$$

yielding

$$\bar{x} - t_\alpha \bar{u} < x < \bar{x} + t_\alpha \bar{u}. \quad (3.6)$$

Finally, the standard uncertainty for the estimated parameter \bar{x} is denoted

$$\bar{u} = \frac{\bar{\sigma}}{\sqrt{n}}. \quad (3.7)$$

In metrology standards, this uncertainty estimated from a statistical approach is referred to as *type A* uncertainty. Note that when the number of observations n tends towards infinity, the Student distribution can be approximated by a standard normal distribution $\mathcal{N}(0, 1)$.

In the case where the estimate of a quantity x is given by a unique observation x_i , the uncertainty is evaluated from all available information of x variability, such as past test measurements, engineer judgment based on knowledge of the system, or specifications from the manufacturer and reference data from handbooks. This uncertainty is referred to as *type B* uncertainty. For instance, for a numerical plot x_i of some quantity with a resolution r , the true value is known to be in the interval $[x_i - r/2, x_i + r/2]$ and to follow a uniform distribution. In this case, the uncertainty of the estimation is given by the standard deviation of the uniform distribution, yielding $\bar{u} = \frac{r}{2\sqrt{3}}$.

In our case, the question is how to evaluate the estimation uncertainty in a complex framework such as the one presented in Chapter 2. Several approaches are proposed in this chapter, based on the available knowledge of the system. Fig. 3.2 summarizes this process of uncertainty evaluation. Once the main step of the estimation system have been analyzed, the first indicator to orient the method choice is the availability of a mathematical model. If available, standard uncertainties of all parameters influencing the measurement result should be determined. An efficient way to list all potential sources of uncertainty is to follow the Ishikawa diagram [Lil16] (also called cause-and-effect diagram), that suggests to look at the system under five main aspects: process, equipment, operator, environment and the quantity intended to be measured (called measurand or parameter). Fig. 3.3 presents the application of this approach to list the uncertainty sources in the photogrammetry system of this study. Then, the global uncertainty can be evaluated using either the propagation law or using distribution propagation, both described in Sec. 3.1.2. On the other side, in the case no mathematical model is available, one will have to analyze the variations of the estimates in a controlled experimentation, as developed in Sec. 3.1.3. Note that it is also possible to mix the various methods.

As depicted in the diagram in Fig. 3.2, once the uncertainty has been estimated, a phase of validation and update is required. Indeed, the GUM points out that the provided guide "*cannot substitute for critical thinking, intellectual honesty and professional skill*" [Guma]. Therefore, it is the engineer's work to check for results consistency and integrity with respect to its knowledge and comprehension of the system and measurand, and further update the test

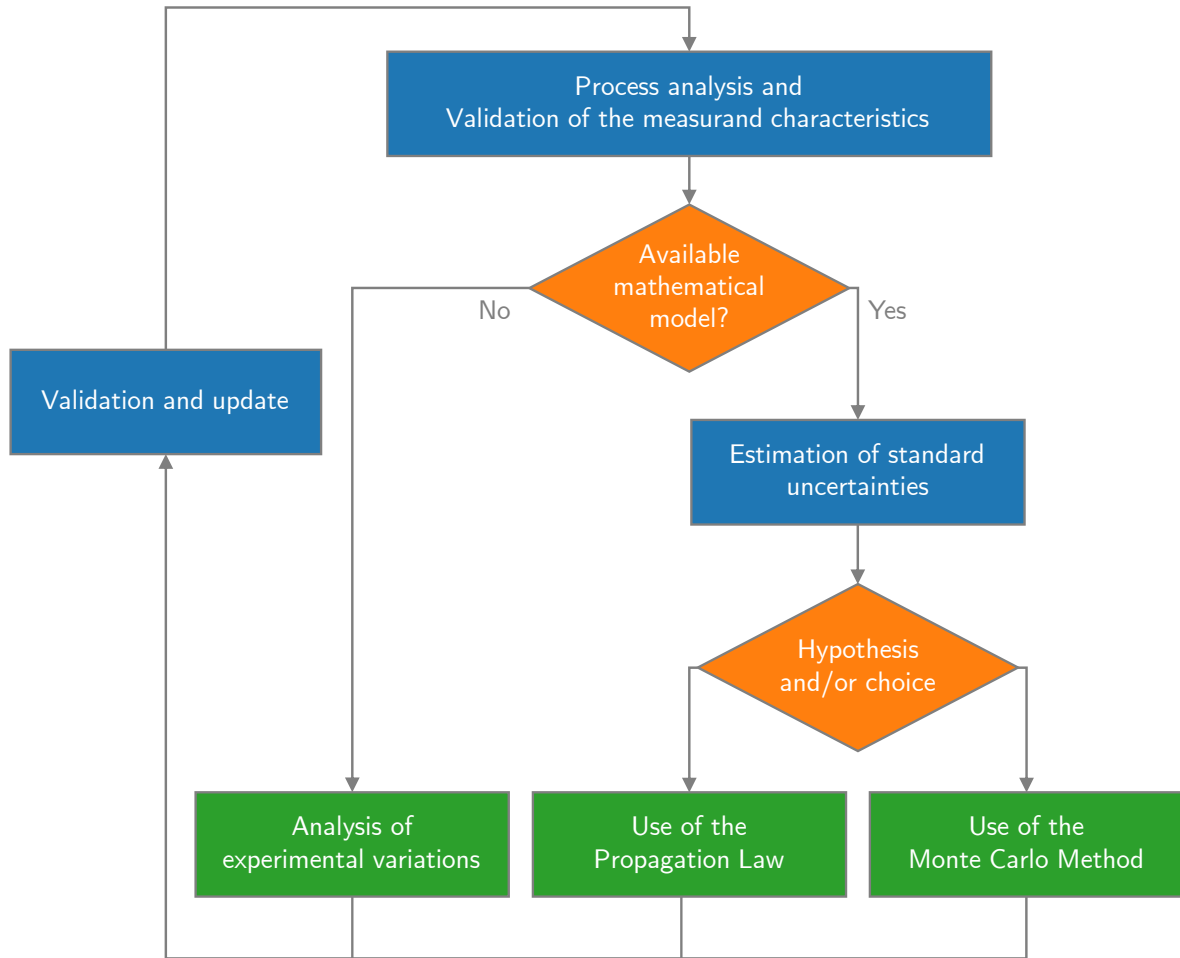


Figure 3.2: Diagram of the uncertainty evaluation process.

accordingly. Besides, in practical applications, it is often too long and tedious to consider all possible sources of uncertainties, and therefore a broad to fine approach is recommended. In this manner, broad uncertainties of the principal sources are first evaluated and propagated, to bring out the main error sources. Then a finer evaluation of these contributors is performed.

3.1.2 Propagation using a mathematical model

In this context, a mathematical model for a quantity y means that its measurement is known to be related to an identified set of N random variables $(X_i)_{i=1,\dots,N}$, such that

$$y = f(x_1, x_2, \dots, x_N), \quad (3.8)$$

where the function f is not always exactly known. As mentioned previously, it is possible to make a broad evaluation using an approximate model before refining the real model. Identifying $(x_i)_{i=1,\dots,N}$ involves that their probability distributions are known, and that their standard deviations can be estimated. In practice, it is common to use rectangular, triangular

or Gaussian distribution functions.

3.1.2.1 Uncertainty propagation law

Calculating uncertainties by the means of standard deviations allows considering all parameters similarly and using known properties of probability, such as the variance additivity in the case of independent random variables. Thus, if $u(x_i)$ denotes the uncertainty of x_i , the combined uncertainty $u_c(y)$ of the output y in (3.8) can be calculated using the propagation law (PL)

$$u_c^2(y) = \sum_{i=1}^N \left[\frac{\partial f}{\partial x_i} \right]^2 u^2(x_i) + 2 \sum_{i=1}^{N-1} \sum_{j=i+1}^N \frac{\partial f}{\partial x_i} \frac{\partial f}{\partial x_j} u(x_i, x_j), \quad (3.9)$$

where

$$u(x_i)^2 = E \left[(x_i - E[x_i])^2 \right] \quad (3.10)$$

is the variance of x_i , and

$$u(x_i, x_j) = E \left[(x_i - E[x_i]) (x_j - E[x_j]) \right] \quad (3.11)$$

is the covariance of x_i and x_j , with E the mean. In practice, we estimated these scalars by

$$\bar{u}(x_i)^2 = \frac{1}{n-1} \sum_{k=1}^n (x_i^k - \bar{x})^2, \quad (3.12)$$

$$\bar{u}(x_i, x_j) = \frac{1}{n-1} \sum_{k=1}^n (x_i^k - \bar{x}_i) (x_j^k - \bar{x}_j), \quad (3.13)$$

where $(x_i^k, x_j^k)_{k=1, \dots, n}$ are n realizations of the random variable pair (x_i, x_j) . Note that the covariance equals zero when parameters are uncorrelated. Expression (3.9) comes from the first non zero terms of a Taylor series expansion applied to the mathematical model in (3.8) (see proof in [Guma, p. 55]). Using the central limit theorem, the distribution of y can be considered as a Gaussian distribution, as it results from a combination of multiple and different distributions. According to (3.9), to use the propagation law and evaluate $u_c^2(y)$, f and its derivatives have to be known.

Going further, the GUM supplement 2 [Gumc] generalizes the PL to any number of input and output quantities. Denoting by $\mathbf{y} = (y_1, \dots, y_m)^T$ the random variable of the m measured quantities and $\mathbf{x} = (x_1, \dots, x_n)^T$ the vector of the n random variables in input, such that $\mathbf{y} = f(\mathbf{x})$, the generalized uncertainty PL states that the covariance matrix \mathbf{U}_y of the output variable \mathbf{y} is linked to the input covariance matrix \mathbf{U}_x as follows

$$\mathbf{U}_y = \mathbf{J}_x^f \mathbf{U}_x \mathbf{J}_x^{fT}, \quad (3.14)$$

where \mathbf{J}_x^f is the Jacobian matrix of f with respect to \mathbf{x} . Once again, this expression results from the computation of the covariance matrix of \mathbf{y} using a Taylor series expansion. Finally, the problem of uncertainty propagating reduces to the problem of calculating the Jacobian

matrix of the transformation f .

3.1.2.2 Application to Least Square Optimization

In the specific case of a least square optimization, used in the CBA approach described in Sec. 2.4.3, the mathematical model between the realizations \mathbf{y} and \mathbf{x} of the random input and output variables \mathbf{X} and \mathbf{Y} , can be expressed as

$$\mathbf{y} = f(\mathbf{x}) = \arg \min_{\mathbf{z}} e(\mathbf{z}, \mathbf{x}), \quad (3.15)$$

where $e : \mathbb{R}^m \times \mathbb{R}^n \rightarrow \mathbb{R}$, and \mathbf{z} is the vector of m parameters to optimize. To apply the propagation law (3.14), the Jacobian matrix of the implicit function f must be calculated with respect to \mathbf{x} . As described in [Eud11, p. 26] [Fau93, p. 155], this can be achieved by using the implicit function theorem, stating that if the Hessian of e is invertible at a local minimum, then around this point, the derivative of f may be expressed as

$$\mathbf{J}_x^f = \frac{\partial f}{\partial \mathbf{x}} = -\mathbf{H}^{-1} \frac{\partial \Phi}{\partial \mathbf{x}} \quad (3.16)$$

where $\mathbf{H} = \frac{\partial^2 \Phi}{\partial \mathbf{z}^2}$ is the Hessian matrix and $\Phi = \frac{\partial e}{\partial \mathbf{z}}^T$.

3.1.2.3 Monte-Carlo Method

When the application of the propagation law cannot be done, an alternative is required. A solution suggested in GUM supplement 1 [Gumb], is to use simulations following the Monte-Carlo method (MC), that allows one to calculate approximative numerical value of the measurement uncertainty using Monte Carlo simulations. The number of trials N to perform depends on the shape of the probability density function in output, and on the desired confidence. However, it is commonly admitted that $N > 10^6$ ensures a close approximation of the 95% coverage interval [Gumb]. This approach is convenient and easy-to-implement to propagate uncertainties through algorithmic frameworks, as the detailed mathematical model is not required. The main drawback remains the computational cost of simulating high numbers of trials.

3.1.3 Experimental validation

In the case where no mathematical model is provided and uncertainty sources cannot be identified, the last option is to evaluate the estimation uncertainty through experimental validations. Experimentations should be conducted on realistic scenarios representative of the application setup, with real environmental disturbances. The best solution to ensure this is to evaluate the system directly on the real use case. To be able to obtain errors and standard deviations of parameter estimates, a countermeasure is needed, and the uncertainty

estimation will be limited by the countermeasure uncertainty. For the application of wing 3D estimation, the experimental validation consists in acquiring real images in flight and comparing the result of the proposed system with other measurement systems based on other sensors. This approach is detailed in Chap. 4.

Besides, it can be difficult or even impossible to obtain countermeasures in real applications. A first alternative would be then to make use of mock-ups, with similar properties than the actual system, up to a scale factor, in a fully controlled environment. In the case of 3D estimation for aircraft structures, it involves recreating smaller parts of the aircraft, with similar materials, painting, deformation properties, but also recreating the flight environment and mimicking the behavior of the structure during the flight. A final and more accessible option is to use simulations. In the case of image processing applications, this consists in creating synthetic images of the system simulating its realistic behavior. To this aim, game engines can be used to render 3D views of the scene of interest in varying environment. In this study, the game engine Unity [Uni] is used to perform this task. Created in 2005 for the development of video games, this platform now allows creating 2D and 3D applications, as well as augmented and virtual reality, and even simulations. It offers realistic rendering of illuminations with high dynamic range (HDR), which makes it popular for instance in architecture or automobile industries. Unity is a good option for the specific case of flight tests, where illumination variations are a main concern.

The main challenge when using mock-ups and simulations is making the measurand and measurement system as realistic as possible. If some influencing parameters are not considered in the tests, the estimated uncertainty can be questioned. For example in Sec. 2.4.5, tests were performed on a real aircraft on ground, which can be considered as a mock-up of the real measurand. However, while this test provides information on the uncertainty for 3D reconstruction of a still wing under varying illumination, it cannot fully represent the real scenario where the wing is moving in flight.

3.2 Uncertainty sources

The uncertainty principles being exposed in the previous sections, we can now focus on their application to the wing deformation addressed in this work. When using a mathematical model or experimental validation to estimate the uncertainty of 3D reconstruction, the first step is to determine all the sources that can impact the estimates. On the one hand, when using the mathematical model, standard deviation or probability distributions of these sources will have to be evaluated before propagation. On the other hand, for the definition of experimentations, this inventory is also required to ensure that the evaluation is performed on realistic use cases.

3.2.1 Inventory of the sources

To consider all potential sources of uncertainty in this study, the Ishikawa method declined in the guide [Exe] is used, considering the error sources in the photogrammetric reconstruction over five main aspects: process, equipment, operator, environment and measurand (illustrated in Fig. 3.3). The goal of this section is to provide the most exhaustive list as possible of uncertainty sources that should be taken into account when designing a photogrammetry system and evaluate the quality of its 3D reconstruction.

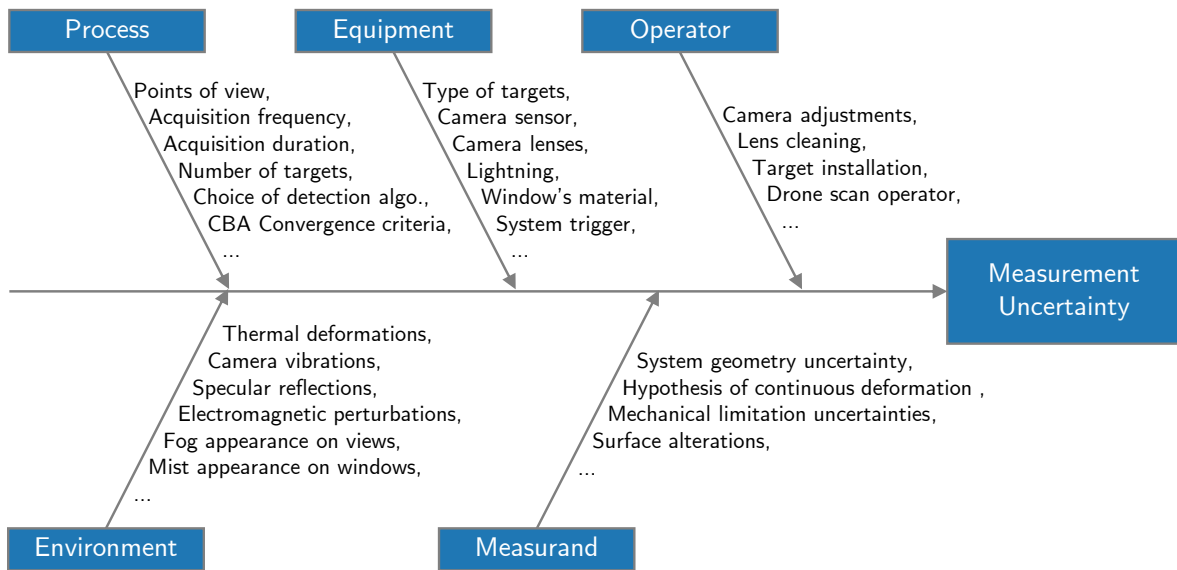


Figure 3.3: Ishikawa diagram for listing all potential source of uncertainty.

Process: This aspect focuses on the used framework and designed system. Here the sources of interest are:

- **Number of measurements.** The number of view points can influence the final 3D estimation, given that a point is more likely to be well reconstructed when seen by a high number of views from various positions. This also brings out the next influencing factor, which is the type of views, i.e., the orientations and positions of the cameras with respect to the object of interest. It is obvious that a camera with grazing view of the wing will be less accurate than a camera with an orthogonal view. Furthermore, the number of measurements also depends on the frequency of acquisition, or more specifically on the number of frames per second. Frequency will impact the size of the window for filtering the estimation results over time. Finally, the number of tracked points on the wing and their distribution can also influence the results.
- **Measurement duration.** For the 3D reconstruction of a wing during flight tests, shapes are estimated at stationary points of the flight, meaning that flight conditions are constant during the time of camera acquisition, and the wing is quasi static. The duration of this stationary phase is another uncertainty source.

- **Choice of the method.** The proposed framework is constructed from algorithmic bricks presented in Section 2.1. The selection of a specific algorithm is an additional factor that influences the estimation result. In particular, here, the choice of using CBA instead of BA will change the uncertainty, but also the choice of mechanical limitations. Besides, the selected hyperparameters for the algorithm are further influencing factors. For instance, the choice of stopping conditions for the CBA optimization should be considered.
- **Choice of reference.** Using the camera coordinate system, linked to the wing, or the aircraft coordinate system, is an important source of uncertainty, as the registration phase to go from one to the other is also introducing errors.
- **Calibrations.** Camera inner parameters, as well as distortions and geometric aberrations of the system (camera, lens, filter and window) can be estimated by a calibration phase. The estimation accuracy will depend on the model and method used (described in Section 1.2.1), the selected reference target, and how well the calibration is performed. For instance, if pictures of the reference targets are not taken homogeneously over the entire image space, the residual errors of the calibration will be greater in image regions that were less covered.

Equipment. Each device of the designed system can influence the global uncertainty based on its own error, its resolution, calibration uncertainty, but also the corrections applied to mitigate the error. In the proposed system, the aspects to consider include the choice of equipment and how they are calibrated:

- **Targets.** The various types of markers that could be used in this application were introduced in Section 2.3. The choice of shapes, dimensions, material and color can be a source of uncertainty as it influences the accuracy of detection in the images, and induces different behaviors with respect to illumination variations.
- **Cameras.** Many uncertainty sources result from the choice of camera sensor. The dimension and resolution of the sensor, coupled with the number of scene views to reconstruct will influence the number of pixels available to detect interest or marker points. Moreover, the dynamic range, sensitivity, signal-to-noise ratio or even linearity of the sensor will influence how well the details of the scene are acquired with respect to various illumination intensities. Besides, the choice of wavelength range for the sensor is to be considered as well. For instance, a camera with a wavelength range in both the visible and near infrared ranges will have a better sensitivity, allowing us to see clearer in darker scenes. The choice of whether using black and white or color sensors, and in the second case, the choice of the Bayer filter will also impact the sensitivity and the resolution of the sensor. Furthermore, uncertainty on the residual distortions of geometry can occur at the sensor level, such as the skew parameters or the pixel size. Last but not least, camera shutters can be global or rolling. In the first case, all pixels of the sensor are captured at the same time, while they are acquired line by line for the rolling shutter, which engenders deformations on the image of moving object or camera.

- **Optics.** The first source of uncertainty concerning the optics is the focal length. This parameter will change the number of pixels per meter for the scene, by playing on the viewing angle of the camera, but also the distortions of the images. A fisheye lens, with a short focal length, introduces stronger distortions than lenses with longer focal lengths. The choice of optics also impacts the sharpness of the image, and high resolution sensors require high resolution lenses. Sharpness can also vary with the type of diaphragm, which impacts the depth of field of the camera by controlling its aperture. In addition, optical aberrations due to light scattering inside the lens, called lens flare, can be the source of contrast decrease in the images. The choice of optics further impacts the light transmission rate, and vignetting occurs when an optic is too small for a sensor. Finally, this choice will influence the importance of chromatic aberrations, i.e., the variation of focus plan of the lens with respect to wavelengths, illustrated in Fig. 3.4.
- **Additional filters.** They can be installed at the end of optics to block some wavelength or light reflections on surfaces using a polarizer. Their use will influence the quantity of light transmitted to the sensor and may produce additional geometric or chromatic aberrations.
- **Lights.** The proposed system does not have light complementing natural illumination. However a future version of the system might include light, allowing one to reconstruct the wing during the night. Anyway, when using lights, the influence factors to examine are the directivity or shape of the light lobes, its wavelength, intensity, homogeneity (for instance dirt on the light source can create local variations of intensity), and the temporal profile (that can be a flash, a constant source or a fluctuating profile).
- **Windows.** To view the wing from the cabin of the aircraft, cameras have to look through windows, that are strong sources of uncertainties. Indeed, just as lenses, windows convey geometric deformations, chromatic aberrations, and local blur can occur when they are not cleaned. On top of that, the material used can impact the light transmission to the camera with respect to the wavelength, and even impact the light reflection from inside the cabin. Moreover, the geometry of the window can create distortions, but also doubling of the light passing through the windows due to its thickness and the angle between the camera and its surface.
- **Trigger.** Trigger is the device that initializes the acquisition of all cameras synchronously. In a 3D reconstruction system based on multiple cameras, the trigger can be the source of acquisition lag between cameras. If the object of interest moves in between the acquisition of the different cameras, the corresponding observations of a point in images will be not exactly related to the same 3D point. Moreover, the absolute time precision of the acquisitions is a source of uncertainty when reconstruction data are to be evaluated against time, or when comparing to counter-measurements. The delay between the time stamp of the acquisition and reference time is a source of uncertainty.
- **Acquisition device.** While image acquisition can be performed directly using the cameras, some applications such as the one addressed here use specific computers with

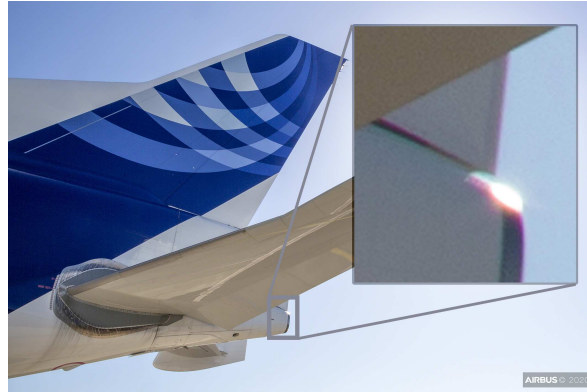


Figure 3.4: Illustration of the chromatic aberration, creating a rainbow edge in high contrast areas.

suited grabbers to perform the image acquisition and storage. A first concern about this device is its reliability, i.e., the probability to loose frames or even to stop recording during tests. A second aspect is the data compression. It can be used to reduce the data size when storing a large amount of images, for instance when recording hours of flight. Using image compression allows us to reduce the redundancy of information with or without loss of information. Moreover, for lossy compression, the level of compression will greatly influence the precision of details in the image. To further reduce the data size, the video compression can be used to reduce the redundancy over time in quasi-static scenes. However, this compression has the disadvantage of reducing or removing the details of displacements over time.

Operator: The largest source of uncertainty is often related to how the system is operated for the measurement. In the current application, it means how the operators have been trained for:

- **Camera set-up.** Preparing the camera for a flight first involves correctly framing the scene to observe, tighten the fixations of the cameras, and setting the lenses by adjusting and securing the focus and the diaphragm. A badly tuned optic can induce blur in the scene, and this can variate during the test if optics are not well secured. A second phase is to properly clean the camera sensors, the optics and the aircraft windows, to ensure that no dust, junks or fingerprints are left, that would produce local blur or occlusions in the images. In particular, cleaning camera sensors is a meticulous task that should be made in laboratory using dry air and specific swabs. Sensors can be quickly polluted if the operator is not careful during the installation of the optic. Finally, when installing the cameras, an anti-reflection hood could be installed around the camera to ensure that the acquired images are not capturing reflections of the aircraft cabin on the windows. If the operator leaves a gap between the window and the hood, this will alter the images and hence influence the uncertainty.
- **Target installation.** Attention should be taken by the operator to correctly stick the targets on the wing at appropriated positions, with suitable orientations such that they

can be seen by all the cameras with similar aspects. For instance, targets stuck on dirty surfaces can unstuck during the flight, causing the permanent loss of a measurement point.

- **Drone scan.** As mentioned in Section 2.1, the initial scene reconstruction is obtained by reconstructing the wing 3D shape from a set of images taken by a drone from various points of view. Here the sources of uncertainty from the operator taking pictures are similar to the uncertainties obtained using the operator setting up the cameras inside the aircraft, to the extent that operators should also know how to pilot the drone, and where to position the device to obtain correct pictures.

Environment. Although it can be controlled in laboratory, the environment in field application such as flight tests is varying regardless of our will. These variations can nonetheless be anticipated, and convey uncertainties sources around the following parameters:

- **Temperature.** Temperature fluctuations can be source of variations in the intrinsic parameters of the cameras by dilating the optics. It can also engender deformations of the camera fixations, or create shifts of the air refraction indexes, as is the case for a wing during flight.
- **Hygrometry.** The first problem that can be encountered in a humid environment is the formation of mist at the surfaces of lenses and windows, generating blur and a decrease of the light transmittance to the sensor. In some other conditions, fog may also form and reduce the intensity of light in the scene. Finally, water droplets could appear on the windows, for example when flying through a cloud, producing local occlusions and distortions in images.
- **Pressure.** Similarly to temperature, pressure variations may generate variations of the air refraction index. Furthermore, in the case of flight test, these fluctuations coupled with the pressurization of the cabin are responsible for some of the aircraft deformations, and more precisely of the windows, changing their properties of geometric deformations through the flight duration.
- **Luminosity.** All the variations of light color, intensity and orientation are major sources of uncertainties in the current application. During a long flight, one can record a full day of sunlight variations, with additional rotations due to the aircraft rotation with respect to the light orientation. All the resulting reflections (from outside or inside the cabin), the shadows and intensity changes are sources of local and global contrast variations, and make difficult the task of setting the lens aperture and acquisition exposure time. Reflections often produce overexposure on the images while shadows notably reduce the contrast. Hence luminosity variations influence the aspect of all or parts of the images, yielding uncertainties in the 2D detection of target points.
- **Electromagnetic perturbations.** Noise may be added to the images while signal transmission from the sensor to the acquisition device because of electromagnetic perturbations. This is more likely to appear when working with other devices emitting high electromagnetic radiations and when using long cables that are poorly isolated.

- **Vibrations.** When exposed to vibrations for a long time, as during flights, camera lenses may move slightly, resulting in random variations of the intrinsic parameters, and prematurely degrading the optics. Besides, the camera support may deform after suffering from repeated vibrations.

Measurand. For the last component of the Ishikawa method, uncertainties sources are considered as derived from the uncertainty of the measurand itself. Indeed, the latter can sometimes behave or differ from expectations. Here, the two main error sources are:

- **The measurand knowledge.** First, when making assumptions on the measurand properties, all of them should be verified and could be sources of uncertainty. A known system geometry raises questions of how accurately it is known, and hence with what uncertainty. Likewise, uncertainty needs to be considered on expectation of component rigidity, kinematic, elastic behavior, deformation continuity, dynamic or mechanical limitations. Furthermore, approximations on the knowledge of surface material can induce errors on the presumed reflection model. This will particularly impact the uncertainty evaluation when generating synthetic images that require to set the reflection properties of the surfaces.
- **The measurand state.** In the case where natural features of the measurand are used as key points to detect (see Section 2.2), a source of uncertainty is the saliency. The aspect of the object surface can vary over time, and so goes the ability to discriminate points of interest. Besides, dirt can accumulate on the object through tests, which can alter the quality of features or targets to detect. In particular, alterations of the surface between the reference and the actual tests can also induce errors. Finally, the object shape may vary between the moment of reference reconstruction and the actual test. For example, the wing shape on ground varies as a function of the temperature and quantity of fuel loaded.

3.2.2 Summary of the system chain

The previous section highlighted a large number of uncertainty sources. The strategy adopted in this work consists in sorting these sources to bring out those that have the major impact, and quantify broadly the uncertainty of these sources to further refine them after validation (see Fig. 3.2). As a matter of fact, many uncertainty sources are negligible for a given problem thanks to a fine choice of equipment or specific test conditions. To perform this sorting for the application of wing reconstruction, the system framework is decomposed in blocks, as shown in Fig. 3.5.

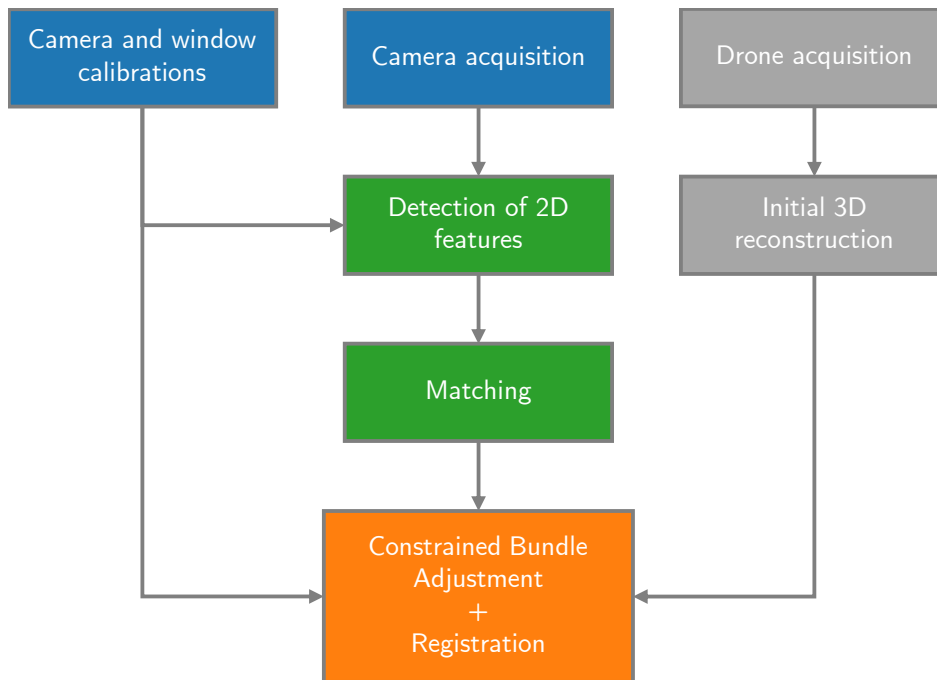


Figure 3.5: Reconstruction framework for the uncertainty study.

3.2.2.1 Constrained bundle adjustment

Starting from the bottom of the diagram in Fig. 3.5, CBA returns 3D estimations from 2D observations of the cameras. For this step, the minimization of (2.21) shows that the estimation result will be influenced by the uncertainty of the camera calibration, as it defines the intrinsic parameters of the cameras (and windows) in the matrices $(\mathbf{K}_i)_{i=1,\dots,N}$ used for the projection of the estimated 3D points. Moreover, the quality of this operation will depend on the quality of the 2D detection, but also on the matching errors. The number of views along with their positions and orientations with respect to the wing is another influencing parameter of CBA. In the current application, the number of views and positions is limited, but it could be interesting to study its influence. Concerning the selected algorithms, the choice of CBA or BA, and as well as the mechanical limits to use has an influence on the results. Moreover, the optimization method and its stopping criteria may also be a source of variation in the estimates. Finally, Eq. (2.21) also shows that the optimization initialization can also affect the estimation. Uncertainty about the initial reconstruction using drone picture should thus be propagated.

3.2.2.2 Drone scan

Regarding the drone scan, the accuracy of the initial reconstruction can be provided by the reconstructing software Metashape [Met] depending on the quality of the images taken by the drone. This operation is performed on ground, at selected hours with correct illumination,

and plenty of views taken from all possible angles, with professional photographers and pilots aware of how to correctly operate the drone. Hence the impact of image quality from drone will be ignored for this study. The uncertainty of 3D point initial positions is therefore studied from the reconstruction result of real applications on an A350 aircraft, with raw pictures of 20Mpx resolution coded on 10bits. The second source of uncertainty related to this step is due to the deformations of the scene between test, drone scan, but also ground shape model.

3.2.2.3 Matching

Before feeding the camera observations to the CBA, a matching phase is required to determine the correspondence between points seen from the various cameras, and also reference points that were scanned by the drone. The quality of the 2D detection, the discriminative power of the feature descriptors, and also the positions of the points in images, will influence the matching quality, leading to some wrong correspondences, or rejected observations. For those points, a great uncertainty with respect to the detection precision should be added to their coordinates before propagation through the CBA.

3.2.2.4 Detection of 2D features

The 2D detection is a major step of the process, and is subject to many uncertainty sources. First of all, several approaches were suggested to perform this task, and the choice of a method will strongly impact the results. The use of targets increases the robustness of the method, while natural features reduce the system complexity but decrease the stability. As a matter of fact, features may variate with respect to environment change, particularly illumination variations, but also from alteration of the surfaces. This means that from one instant to another during tests, the quality of detection and description may completely differ, and the number of observations can fluctuate. The choice of detectors and descriptors, as exposed in Section 2.2.1.4, influences the results. In practice, for industrial applications where uncertainty is a concern, natural features are too random to be used, hence addition of markers on the test structure. Here cross targets are chosen as justified in Section 2.3. According to this choice, several uncertainty sources arise. First, the dimensions and orientation of the targets may influence the detection, and those variations should be evaluated. Curvature or material could also impact the results. Here assumptions are made that the targets are locally planes, and that the material is fixed (stickers with mate ink printing preventing reflections). On the other hand, one cannot set the material of the wing panels and black lanes, and the assumption on reflectance properties may be a source of uncertainty. In addition, the method used to detect markers, graduation and lines with sub-pixel precision is a source of uncertainty too. The last source impacting the detection accuracy is the image quality.

3.2.2.5 Camera acquisition

On the side of camera acquisition, the selected equipment (described in Chapter 4) allows one to considerably reduce the impact of potential uncertainty sources. First, some parameters are fixed, since the cameras have high resolution sensors of 31Mpx, taking black and white images in the visible spectrum, with a global shutter, an acquisition frequency of 25.1 images per second max, pixels coded over 8 bits, and a dynamic range of 71dB. High quality optics are selected to work with these cameras, ensuring no blur due to resolution flaws and chromatic aberrations, or vignetting due to lack of light transmissivity. These optics have fixed focal lengths, which reduces the possibility of unwanted variations during flights. In continuation of the optical path, specific windows were designed for flight, aiming at reducing all distortions. These windows introduce image duplication though, and will be qualified in the calibration phase. Concerning lightning, it was chosen not to use light since it would require to surpass the sunlight intensity, and would imply other installation difficulties. Beside, the selected triggering device allows one to synchronize camera acquisitions at the order of nanoseconds, and the time stamp of the cameras is synchronized with the aircraft time reference using Precision Time Protocol. Thus these sources of uncertainty can be neglected with respect to the wing dynamic. Electromagnetic perturbations are also neglected due to the use of shielded cables inside the aircraft cabin, where equipment emissivity is controlled. For the settings, diaphragms and focuses of the lenses are arranged so that all the targets lie in the camera depth-of-field, reducing focus blur. On the acquisition device, the exposition time is fixed to prevent motion blur, while the impact of image compression and gain noise should be evaluated. Furthermore, referring to environmental variations, the image quality may be impacted by all fluctuations of light, temperature, hygrometry and pressure, as discussed in the previous section. This work however will focus on the influence study of light variations, introducing contrast changes, non uniform intensity, shadows and reflections.

3.2.2.6 Camera and window calibrations

To correct the distortions produced by the combinations of cameras, lenses, and windows, a calibration phase is performed. As described in Section 1.2.1, several models can be used to express image distortions. The model choice can influence the final uncertainty. Moreover, the calibration phase is basically a bundle adjustment algorithm with fixed object coordinates and free intrinsic and distortion parameters. Regarding the CBA of the current system, the main impacting variables are related to the optimization method and the hyperparameters. This time though, the object scene can be defined by the user, and the target choice is another uncertainty source for the calibration. Regarding image acquisition, it is considered that since this step is not urgent, it can be performed at any time with ideal environmental conditions and will not suffer from uncertainty sources such as illumination changes or vibrations. Finally, an uncertainty should be added and quantified to represent lens dilatation relative to temperature variations or deformations of windows during the flight. Variations of intrinsic parameters due to vibrations in flight on the other side are supposed negligible since the lens focus and diaphragm rings are secured with screws and tape before flight.

3.2.2.7 Summary of the error sources

To summarize, after iterating through the 3D-reconstruction pipeline, many influencing parameters may be discarded thanks to an adapted equipment, or because of their negligible influence with respect to the current system. Remaining uncertainty sources to be evaluated are:

- the number of views,
- the use of constraints in the BA,
- the dimensions and orientations of the targets and graduations,
- the detection method for lines and markers,
- the blur, noise, contrast, and non homogeneous intensity of the images,
- the camera calibration,
- the accuracy of initial reconstruction from the drone scan.

To analyze if some sources have real impact or not on the final 3D estimation, their uncertainties will first be broadly evaluated, and further refined if needed.

3.2.3 Quantification of the main error sources

The aim of this section is to quantify the uncertainty of all the sources that were retained after the analysis presented in the previous subsection. Herein, we evaluate each relevant part of the reconstruction framework depicted in Fig. 3.5, and the resulting uncertainties are summarized in Table 3.1.

Table 3.1: Table of the main uncertainty sources

Source	Distribution	Source	Distribution
Initial 3D scan with drone (mm)	$\sigma_{\bar{x}} \sim \mathcal{U}(0, 3.1)$	Target rotations (deg)	$\sigma_{rx} \sim \mathcal{U}(0, 80)$
	$\sigma_{\bar{y}} \sim \mathcal{U}(0, 3.1)$		$\sigma_{ry} \sim \mathcal{U}(0, 80)$
	$\sigma_{\bar{z}} \sim \mathcal{U}(0, 25.9)$		$\sigma_{rz} \sim \mathcal{U}(0, 180)$
Image duplication (px)	$\sigma_d \sim \mathcal{U}(0, 10)$	Image blur (px)	$\sigma_b \sim \mathcal{U}(0, 1)$
Image noise	$\sigma_n \sim \mathcal{U}(0, 1)$	Image compression (%)	$\sigma_{jpg} \sim \mathcal{U}(75, 101)$
Target contrast	$\sigma_c \sim \mathcal{U}(0.1, 1)$	Light dissimilarity	$\sigma_i \sim \mathcal{U}(0, 1)$
Target translations (px)	$\sigma_{tx} \sim \mathcal{U}(0, 1)$	Camera and window calibration (px)	$\sigma_k \sim \mathcal{N}(0, 1)$
	$\sigma_{ty} \sim \mathcal{U}(0, 1)$		

3.2.3.1 Initial 3D reconstruction

The initial 3D reconstruction is performed using the software Metashape [Met] and a set of images taken with a drone from various view points. To evaluate the accuracy of the 3D positions, real images were taken on the A350-1000 aircraft selected to validate the proposed framework in flight (see Chapter 4), with targets already stuck onto the wing. Six reference markers were placed on ground, such that at least two of them were visible on every image, and the distances between each pair were measured using a laser range-finder. Note that distance between the targets of the wing were not measured as it would require more difficult operations. In the software, distance measurements were given as input to set the 3D-reconstruction scale. An example of 2D image, along with the estimated reconstruction are shown in Fig. 3.6. To estimate the reconstruction uncertainty on the ground plane, one reference distance was removed from the reconstruction, and its estimation from the software was recorded. Repeating this operation for every distance, one is able to estimate the standard deviation of the estimation with respect to the true measurement. Besides, since the targets are all placed on the same ground plane, the previous approach cannot be applied to evaluate the uncertainty on the third axis. Instead, we proposed to evaluate the distance of the estimated points to the fitting plane obtain by linear regression on all the reference points. With these methods, standard deviations equal to 3.1mm and 25.9mm were obtained for the ground plane (x,y) and the elevation axis (z). The uncertainty along the x , y and z axes are respectively denoted by $\sigma_{\hat{x}}$, $\sigma_{\hat{y}}$ and $\sigma_{\hat{z}}$. These results show a higher precision in the (x,y) plane, which is coherent with the fact that images are taken from above the wing, and often parallel to the ground plane.

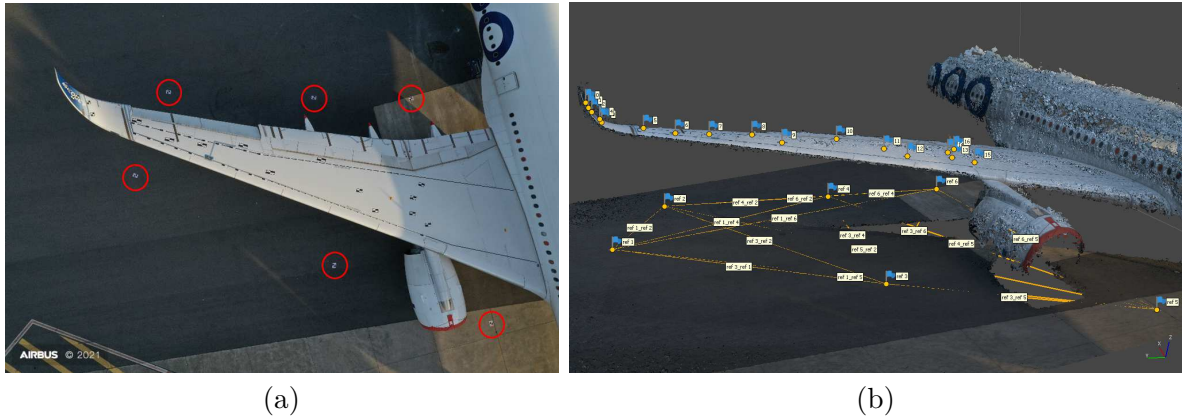


Figure 3.6: (a) - Example of image taken from a drone for the initial 3D reconstruction of the wing. Reference markers placed around the wing are highlighted with red circles. (b) - Corresponding 3D reconstruction, where reference distances are shown with yellow lines.

3.2.3.2 Camera acquisition

Most of the influencing parameters for camera acquisition were first estimated roughly from experience of past tests and from engineer judgment, and some others being evaluated with basic laboratory tests. Before giving the estimation of these parameters, the impact they have on the images should be detailed.

First, the image duplication induced by the angle between the cameras and the thick windows is accounted for by creating a new image \mathbf{I}_d that is the superposition of two translated and weighted versions of the initial image \mathbf{I} , such that the intensity of pixel (u, v) can be expressed as

$$\mathbf{I}_d(u, v) = \mathbf{I}(u, v) \left(0.9 + \frac{\sigma_d}{100}\right) + \mathbf{I}(u + \sigma_d, v) \left(0.1 - \frac{\sigma_d}{100}\right), \quad (3.17)$$

with the uncertainty parameter σ_d corresponding to the translation applied to each pixel. For the application on the aircraft, the cameras are rotated slightly towards the rear of the aircraft, which creates a duplication along the x axis of the image. Note that using this formulation, the intensity of the translated image will be higher for larger translations, which simply models the real behavior of image duplication observed through prior tests.

Then, the received image \mathbf{I}_d is blurred because of factors mentioned above, such as vibration or dirt on the optical path, resulting in a image \mathbf{I}_b . Here, this blur is defined as a 2D Gaussian filter, defined as G convolved with the image, defined as

$$G(x, y) = \frac{1}{2\pi\sigma_b^2} \exp\left(-\frac{x^2+y^2}{2\sigma_b^2}\right), \quad (3.18)$$

where σ_b is the uncertainty parameter to evaluate, characterizing the sharpness of the image. Finally, a white noise \mathbf{n} is added to the received image \mathbf{I}_b (duplicated and blurred) during the acquisition process, such that the recorded image is

$$\mathbf{I}_n = G * \mathbf{I}_d + \mathbf{n}, \quad (3.19)$$

with $*$ the convolution operator and \mathbf{n} distributed according to a Gaussian distribution $\mathcal{N}(0, \sigma_n^2)$, where the standard deviation σ_n is the uncertainty source.

The impact of the uncertainty sources being defined, their estimations can be provided. Existing tests demonstrated that since the light intensity above the clouds is high, clear images can be recorded with low exposure time, low gain and a small aperture size. This means that the blur caused either by depth-of-field limitations or motion blur is very limited. Therefore, the standard deviation of the blur, σ_b , was chosen to follow a uniform law $\mathcal{U}(0, 1)$ in pixel. In addition, using a low gain coupled with high quality sensors, the noise level in images remains very low. Thus it was decided that the noise parameter σ_n should also follow a uniform law $\mathcal{U}(0, 1)$, such that the signal-to-noise ratio of the image remains higher than 15dB. For the duplication coefficient, preliminary tests in lab with the actual cameras and windows showed that the translation σ_d never exceeds 10px. A uniform law $\mathcal{U}(0, 10)$ in pixel was thus selected

to model this uncertainty source. Finally, even though one may prefer recording raw images to ensure no loss of information, image compression is considered as it may significantly extend the recording duration (roughly from half duration of a flight to several full flights). Therefore, images are compressed and decompressed using JPEG [Hud+17] with a compression factor $\sigma_{jpg} \sim \mathcal{U}(75, 101)$, where the value 101 corresponds to absence of compression. Furthermore, regarding the quality of the image acquisition for targets installed on the wing, it was shown in past tests that the marker contrast σ_c (ratio between black and white colors) is always high in flight thanks to the design of the targets. However in this study, we assumed $\sigma_c \sim \mathcal{U}(0.1, 1)$ to account for tests at twilight. Finally, illumination inhomogeneities at the target level are considered by multiplying the marker image by a gradient matrix whose values goes from $\sigma_i \sim \mathcal{U}(0, 1)$ to 1 along the x axis.

3.2.3.3 Detection of 2D features and matching

Within the proposed framework, the first processing step after image acquisition is the detection of 2D observations of the scene (the wing) to be reconstructed in 3D. In this step, the first influencing parameters are the type of markers and the detection algorithm. As described in Section 2.3, the selected markers are mainly quadrant targets, along with graduation placed on the black lanes of the wing. Using OpenCV functions [Ope], markers are first detected using template matching, and localization is further refined using sub-pixel corner detection. Regarding the graduations, a similar step of template matching is used to find the initial position of the markers between frames. Then, a refined detection is performed following the next steps:

- i. the local gradient of the image is calculated along the normal of the segment formed by two graduations,
- ii. the borders of the black lanes are detected as peaks of the gradient,
- iii. the center of the lane is detected with sub-pixel accuracy by averaging the coordinates of its borders,
- iv. a polynomial fit is performed on the detected lane to remove outliers,
- v. graduations are detected as gradient peaks along the polynomial curves.

An example of graduation detection following this method is shown in Fig. 3.7. Note that other algorithms of line detection could be investigated, such as LSD (Line Segment Detector) or Canny/Devernay [Gio+12; GR17].

Given this detection method, the remaining influencing parameters are the dimensions and orientations of the targets and the graduations. For the dimension, it is expected that all targets are seen with a width of at least 20px, by design of the markers and camera views. For the orientations, since targets can be installed on the wing plane and the wing tip, with angles of about 70 and 10 degrees between the surface normal and the optical axis of the

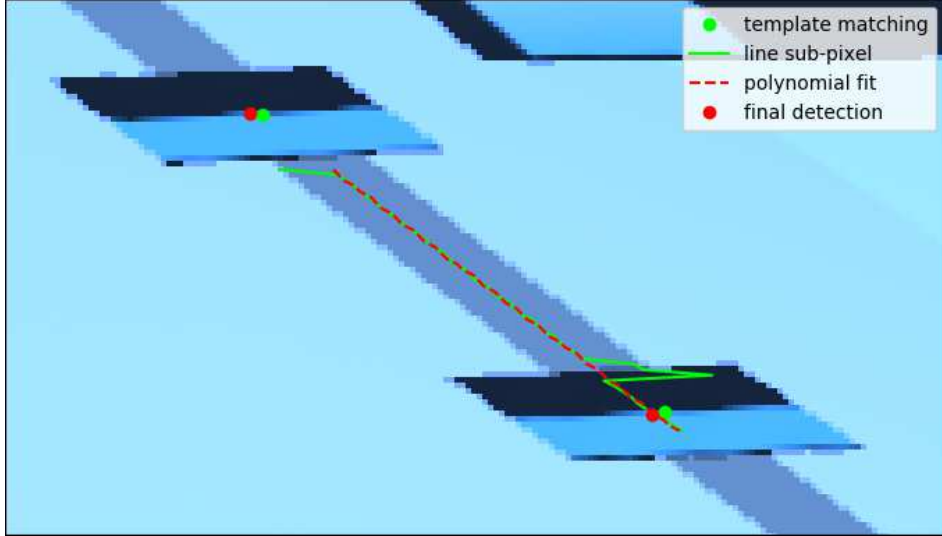


Figure 3.7: Illustration of the method for graduation detection.

camera, it was set that the rotation uncertainties (σ_{rx} , σ_{ry}) for the x and y axes follow a uniform law $\mathcal{U}(0, 80)$. To consider all possible orientations of the targets around the z axis, we assumed that the corresponding uncertainty is $\sigma_{rz} \sim \mathcal{U}(0, 180)$. Finally, to evaluate the target detection with sub-pixel accuracy, a translation of a tenth of pixels is introduced with uniform laws on image axes, $\sigma_{tx} \sim \mathcal{U}(0.0, 1.0)$ and $\sigma_{ty} \sim \mathcal{U}(0.0, 1.0)$. To further determine the uncertainty of target 2D detection, a Monte-Carlo approach is proposed and developed in Section 3.3.1.1.

3.2.3.4 Camera and window calibration

The calibration step returns the intrinsic parameters of the cameras, i.e., the focal length in pixel size, the optical center, and the distortion parameters (see Section 1.2.1). The combination of all these uncertainties can be expressed as an uncertainty on the parameters of the projection matrix \mathbf{K} . It has been demonstrated in the literature that calibration can be achieved with a sub-pixel uncertainty [Wan+05] [Bu+21]. In this work, this will be obtained by calibrating the cameras with a 3D reference structure with circular targets. However, based on the experience of previous tests in Airbus, an error $\sigma_k \sim \mathcal{N}(0, 1)$ in pixel is introduced to take into account the potential shifts during test due to vibrations of the optics with respect to the sensor, or because of temperature related dilatation.

3.3 Error propagation for 3D reconstruction

Several methods were introduced in Section 3.1 to estimate the uncertainty of an estimation. Each approach has advantages and drawbacks which make them more or less suitable for real life applications. The main criteria for comparison are the complexity of implementation, the

time (or computational) complexity, the availability of ground truth, and the data fidelity. For the various methods applied in this study, Table 3.2 briefly exposes the different performances with respect to these criteria. In this section, three approaches are evaluated, using Monte-Carlo, propagation law, and synthetic images. An additional confrontation with real data is covered in Chapter 4 for the industrial validation.

Table 3.2: Comparison of the methods for uncertainty estimation.

Method	Implementation complexity	Time complexity	Ground truth	Data fidelity
Monte-Carlo	+	+++	+++	++
Propagation Law	+	+	++	+
Simulations	++	++	+++	+++
Real tests	+++	++	+	+++

3.3.1 Uncertainty estimation by the Monte Carlo method

Once the uncertainty sources have been determined, the Monte-Carlo (MC) approach is straightforward. It simply generates random trials of the input variables using their distribution laws, and inputs them to the system framework. The MC method usually takes the current algorithm as a black box and its implementation does not require complex developments. Moreover, as long as uncertainty sources have been correctly identified, MC results are realistic because they are based on the actual algorithm. In this section, MC simulations are conducted for 2D detection and BA with or without constraints.

3.3.1.1 2D detection

To estimate the uncertainty of marker detection on 2D images, an MC approach is applied along with a simulation algorithm for generating images of the targets. The OpenGL library was used to create views of the targets for all the uncertainty sources related to camera acquisition and target positioning (that were listed in the previous section). Fig. 3.8 displays examples of such simulated images. These target views are then used as input of the marker detection algorithm, and the result was compared to the ground-truth coordinate of the simulated center.

MC was performed for quadrant marker detection with a set of $N = 10^6$ trials. The Gaussian distributions for the x and y coordinates in pixels were estimated as

$$x \sim \mathcal{N}(-0.15, 0.76),$$

$$y \sim \mathcal{N}(0.02, 0.69),$$

calculated with the standard sample mean and variance estimators. This uncertainty is slightly higher than the state of the art, which is not surprising under these unfavorable

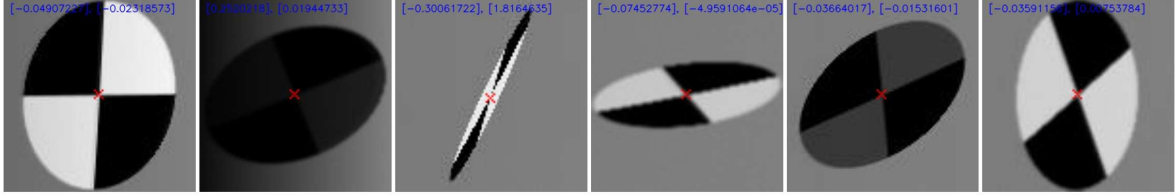


Figure 3.8: Examples of simulated views of quadrant markers for the estimation of 2D detection uncertainty.

conditions. These results can be better appreciated once the error propagation has been completed. An interesting result here is that the compression level of the JPEG encoder does not influence the uncertainty of the detection as long as it is higher than 75%. Regarding the graduation detection, the uncertainty was set to 1px in both x and y axis to save up development and calculation time. In fact, this value is quite large when working with sub-pixel methods of line detection. Nonetheless, this estimation should be confirmed in future work.

3.3.1.2 Constrained Bundle Adjustment

The uncertainty of 3D reconstruction can be estimated using MC simulations at the CBA stage with the uncertainty of calibration, 2D detection and initial reconstruction as inputs. For this step, the test configuration on an A350-900 aircraft, presented in Section 2.4.5, was used to initialize the cameras, the 3D points and the constraints. Exact observations of the point cloud were simulated for all views using the camera parameters. Then, following the distributions summarized in Table 3.1, noise was added to the 2D observations, the inner parameters of the cameras, and the initial 3D reconstitution for each trial of MC, and injected into the CBA. To ensure that the final results are compared in the same reference system, with the same scale, at least seven parameters should be fixed during the optimization process. To do so, here the registration phase was included into the CBA by fixing the coordinates of reference points.

For the CBA step, several runs of the MC method were performed with different combinations of influencing parameters to evaluate their impact on the final reconstruction. Although this MC implementation does not require complex developments, the computational complexity of CBA is high due to the optimization routines employed. Therefore, sets of only $N = 10^4$ trials were simulated, that already took about a day each to return results (on an Intel i9-9980HK CPU). To fully comply with the standard, one million trials should be performed.

3.3.2 Uncertainty from the propagation law

The uncertainty estimation of the CBA reconstruction is studied in this section using analytical calculations. The proposed approach is inspired by the work of [Eud11], and is based on the covariance matrix of the reconstruction in (3.14) with the Jacobian of the implicit func-

tion defined in (3.16). The sources of uncertainty considered for the propagation are those for 2D detection and calibration of the cameras and windows. Since the calculation is performed around the CBA solution, the uncertainty of the initial reconstruction is not propagated. We might consider two subsections devoted to the unconstrained and constrained cases (1.28). In this case, the function to minimize is

$$e(\mathbf{x}, z, \mathbf{K}) = \frac{1}{2} \|\mathbf{x} - \hat{\mathbf{x}}(z, \mathbf{K})\|^2 \quad (3.20)$$

with \mathbf{x} the vector of all 2D observations, $\hat{\mathbf{x}}(z, \mathbf{K})$ the vector of all reprojected points, and $z = (\boldsymbol{\alpha}, \mathbf{X})$ for notation simplification. This function can be rewritten as

$$e(\mathbf{x}, z, \mathbf{K}) = \frac{1}{2} [\mathbf{x} - \hat{\mathbf{x}}(z, \mathbf{K})]^T [\mathbf{x} - \hat{\mathbf{x}}(z, \mathbf{K})], \quad (3.21)$$

leading to

$$\begin{aligned} \boldsymbol{\Phi} &= \frac{\partial e(\mathbf{x}, z, \mathbf{K})^T}{\partial z}, \\ &= \frac{\partial}{\partial z} \left(\frac{1}{2} [\mathbf{x} - \hat{\mathbf{x}}(z, \mathbf{K})] [\mathbf{x} - \hat{\mathbf{x}}(z, \mathbf{K})]^T \right), \\ &= -\frac{\partial \hat{\mathbf{x}}(z)^T}{\partial z} [\mathbf{x} - \hat{\mathbf{x}}(z, \mathbf{K})], \end{aligned} \quad (3.22)$$

where the derivative of the reprojected points with respect to camera and 3D-point parameters actually corresponds to the Jacobian $\mathbf{J}_z^{\hat{\mathbf{x}}}$ calculated for the BA (see Appendix A). Then, the Gauss-Newton approximation is used to obtain the Hessian matrix \mathbf{H} without calculating the second derivatives (see Appendix B), allowing the computational complexity to be reduced, which gives

$$\begin{aligned} \mathbf{H} &= \frac{\partial \boldsymbol{\Phi}}{\partial z}, \\ &\approx \mathbf{J}_z^{\hat{\mathbf{x}}} \mathbf{J}_z^{\hat{\mathbf{x}}}. \end{aligned} \quad (3.23)$$

Finally, the derivatives with respect to the uncertainty parameters are

$$\begin{aligned} \frac{\partial \boldsymbol{\Phi}}{\partial \mathbf{x}} &= \frac{\partial}{\partial \mathbf{x}} \left(-\frac{\partial \hat{\mathbf{x}}(z, \mathbf{K})^T}{\partial z} [\mathbf{x} - \hat{\mathbf{x}}(z)] \right), \\ &= -\frac{\partial \hat{\mathbf{x}}(z, \mathbf{K})^T}{\partial z}, \end{aligned} \quad (3.24)$$

and

$$\begin{aligned} \frac{\partial \boldsymbol{\Phi}}{\partial \mathbf{K}} &= \frac{\partial}{\partial \mathbf{K}} \left(-\frac{\partial \hat{\mathbf{x}}(z, \mathbf{K})^T}{\partial z} [\mathbf{x} - \hat{\mathbf{x}}(z, \mathbf{K})] \right), \\ &= -\frac{\partial^2 \hat{\mathbf{x}}(z, \mathbf{K})^T}{\partial \mathbf{K} \partial z} [\mathbf{x} - \hat{\mathbf{x}}(z, \mathbf{K})] + \frac{\partial \hat{\mathbf{x}}(z, \mathbf{K})^T}{\partial z} \frac{\partial \hat{\mathbf{x}}(z, \mathbf{K})}{\partial \mathbf{K}}, \\ &\approx \frac{\partial \hat{\mathbf{x}}(z, \mathbf{K})^T}{\partial z} \frac{\partial \hat{\mathbf{x}}(z, \mathbf{K})}{\partial \mathbf{K}}. \end{aligned} \quad (3.25)$$

More details about the determination of $\mathbf{J}_{\mathbf{K}}^{\hat{\mathbf{x}}} = \frac{\partial \hat{\mathbf{x}}(z, \mathbf{K})}{\partial \mathbf{K}}$ are given in Appendix A. Finally, using the theorem of implicit function (3.16) and Jacobian notations, the matrices of derivatives of the CBA with respect to \mathbf{x} and \mathbf{K} can be expressed as

$$\mathbf{J}_{\mathbf{x}}^f = (\mathbf{J}_z^{\hat{\mathbf{x}T}} \mathbf{J}_z^{\hat{\mathbf{x}}})^{-1} \mathbf{J}_z^{\hat{\mathbf{x}T}} \quad (3.26)$$

$$\mathbf{J}_{\mathbf{K}}^f = -(\mathbf{J}_z^{\hat{\mathbf{x}T}} \mathbf{J}_z^{\hat{\mathbf{x}}})^{-1} \mathbf{J}_z^{\hat{\mathbf{x}T}} \mathbf{J}_{\mathbf{K}}^{\hat{\mathbf{x}}}. \quad (3.27)$$

Note that $\mathbf{J}_{\mathbf{x}}^f$ is actually the pseudo-inverse of $\mathbf{J}_z^{\hat{\mathbf{x}}}$, which simplifies even more the implementation. Once these derivatives have been calculated, the covariance matrix $\mathbf{C}_{\mathbf{x}, \mathbf{K}}$, whose diagonal terms are the variances (σ_x^2, σ_y^2) and σ_k^2 , is propagated to estimate the covariance $\mathbf{C}_{\mathbf{X}}$ of the reconstructed 3D-points, yielding

$$\mathbf{C}_{\mathbf{X}} = [\mathbf{J}_{\mathbf{x}}^f, \mathbf{J}_{\mathbf{K}}^f] \mathbf{C}_{\mathbf{x}, \mathbf{K}} [\mathbf{J}_{\mathbf{x}}^f, \mathbf{J}_{\mathbf{K}}^f]^T. \quad (3.28)$$

Furthermore, in a same manner as for MC, it is important to set the coordinate system and the scale of the BA. Otherwise, BA has an infinite number of solutions, and the propagation cannot be calculated. To enforce the unicity of the solution, constraints on the system should be applied (commonly called gauge constraints). While for MC this is done by removing at least seven parameters, in the case of the propagation law this is fulfilled by removing the columns of the Jacobian matrix for the corresponding parameters. Since these columns correspond to the derivatives of f with respect to the reference points, deleting them is equivalent to fixing the reference points in the error propagation. This step is primordial for the propagation success and to be able to compare the results.

Concerning the case of mechanical constraints (2.21), one may observe that near the solution of the CBA, constraints are not activated, and are thus not taken into account when applying the theorem of implicit functions. To tackle this issue and ensure that constraints are included in the propagation, one may rewrite the problem using a Lagrangian (non-constrained) formulation

$$\arg \min_{\alpha_j, \mathbf{X}^i} \sum_{i,j} [\mathbf{x}_j^i - \hat{\mathbf{x}}(\alpha_j, \mathbf{X}^i, \mathbf{K}_j)]^2 + \sum_k \sum_i \mu_{k,i} [g_k(\alpha_r, \tilde{\mathbf{X}}^i)]^2. \quad (3.29)$$

The optimization problem 3.29 requires to adjust the hyperparameters $\mu_{k,i}$ in order to obtain solutions in agreement with CBA. We argue that this could be achieved by adjusting the weight iteratively so that the resulting reconstruction and uncertainty remains within the mechanical limitations. So far this has not been demonstrated in this work but it would make an interesting prolongation of the study.

Overall, the propagation law is easy to implement and has the great advantage of returning results instantaneously. Even though it does not take into account all uncertainty sources, it gives a good understanding of the system limitations and can be used to rapidly answer application requests in industrial environment.

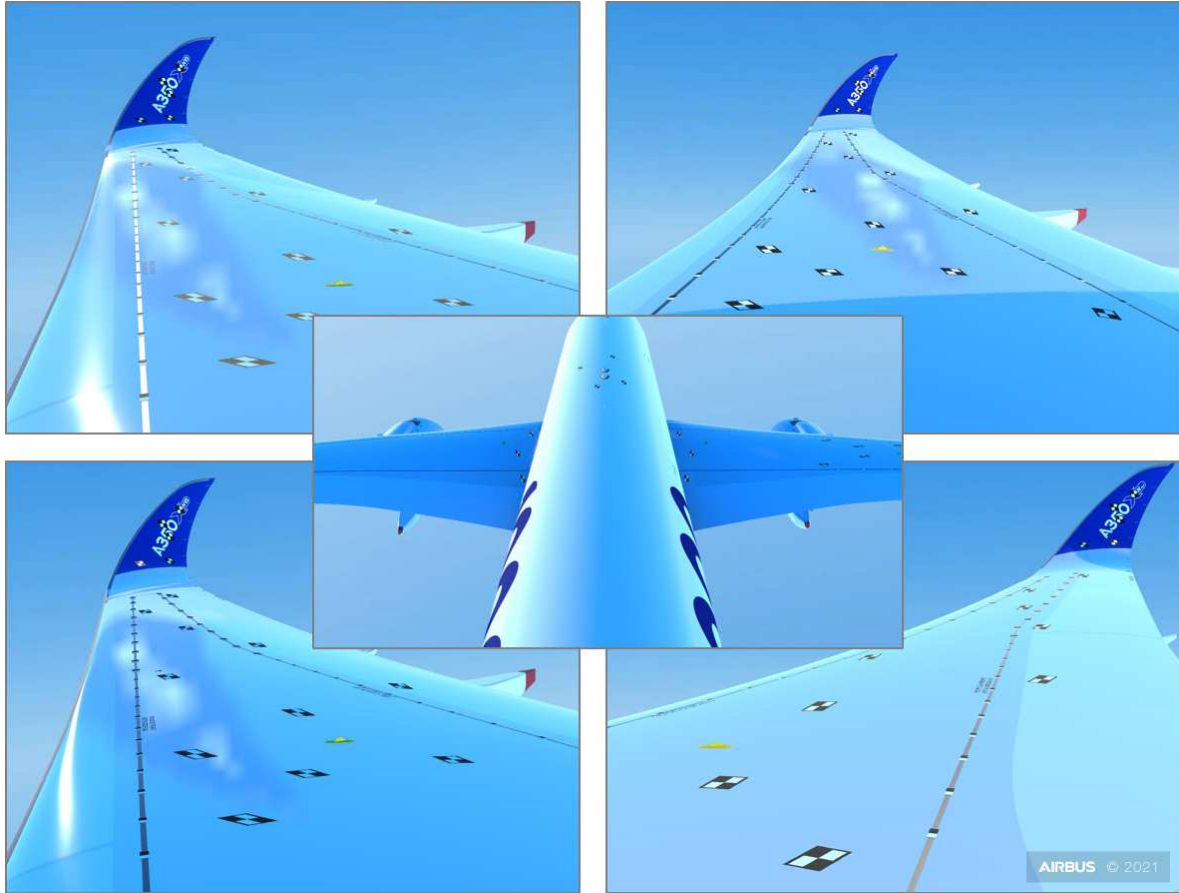


Figure 3.9: Examples of synthetic views of the deformed wing generated with Unity.

3.3.3 Simulation scenario using synthetic images

The third method to evaluate the measurement uncertainty is the experimental validation. At first glance, it may appear to be the easiest approach, by directly applying the system in actual conditions. However, in this work it is the most complex method, and will be the object of Chapter 4. A more accessible alternative is to create synthetic images of the wing in flight. To do so, a numerical 3D mock-up of the A350-1000 on ground (from Airbus) was rendered with the game engine Unity [Uni]. Targets with similar dimension than the ones designed for real tests were then added to the 3D mock-up. Using the information of FEM deformations (see Section. 2.4.4), the point 3D coordinates of the aircraft model were transformed to match the cruise shape of the wing. In addition, several coefficients of wing deformation were applied to the transformation, generating close variations of the wing shape around its flight form, that were further used to recreate motion animations. The materials of 3D parts were set to faithfully represent the colors and reflection properties of the wing, and cameras were simulated on windows and on the rear stabilizer of the aircraft. Thanks to Unity's functionalities, the orientation of light source was animated to recreate illumination variations. Finally, image sequences were recorded for different wing deformations and changing light orientations. Due to limitations of recording resolution using Unity, the camera resolutions

were down-scaled to 3840×2160 for the rear view and 5760×4320 for the others. Thus, to enable the comparison of the results to those of the other approaches, the focal lengths of each camera were changed to match the millimeter per pixel resolution of objects in the real test. Note that the implementation is time consuming but the result is very realistic, as can be seen in Fig. 3.9 or on the videos available at [Dem21b]. This implementation allows one to apply the algorithm exactly as it would be in real test.

To make images even more realistic, a degradation phase was added in the algorithm. First, more or less blur was introduced depending on the wing region relative to the focus position, i.e., the top or bottom half of the image. More $\sigma_b = 0.5px$ on focused area and $\sigma_b = 1.5px$ elsewhere (using notations from Section 3.2.3.2). Second, image duplication was computed with σ_d equal 0 to 4 px depending on the inclination of the camera with respect to the window in the real application. Third, white noise was added with $\sigma_n = 1$. With these final images, the proposed framework was ran and the 3D reconstruction can be compared with the ground truth calculated while deforming the wing.

3.4 Results and comparison

This chapter presented several ways of evaluating the uncertainty of an estimator, and how it applies to the case of 3D wing reconstruction. This section evaluates the quality of the proposed method using the three methods previously introduced for uncertainty estimation. In this section, the system configuration is similar to the one used during the real test, with quadrant targets and graduations stuck on the wing, four cameras installed on windows and one rear view. In the first experiments, the MC approach was applied with various uncertainty sources, starting with Gaussian observation noises $x \sim \mathcal{N}(-0.15, 0.76)$, $y \sim \mathcal{N}(0.02, 0.69)$ for the cross targets, and $\mathcal{N}(0, 1)$ noises for both x and y coordinates of the graduations. To limit the number of tests, this work evaluates the BA and CBA algorithms with volume constraint only. Examples of MC results are displayed in Fig. 3.10 for a target placed at the wing end. Only 10% of the MC outputs are shown in the graphics to simplify the reading. Covariance matrices of the 3D points are represented as confidence ellipses in the three projection planes, allowing one to appreciate how coordinates are correlated. In this case, the estimated points have a probability of 95% to fall inside the drawn ellipses. Furthermore, the uncertainty of camera calibration was also included, with $\sigma_k \sim \mathcal{N}(0, 1)$. Our experiments showed that for such quality of camera calibration, the output uncertainty is not influenced by σ_k . Similarly, the MC approach showed that estimating the initial shape of the wing, with drone picture and Methashape software, does not generate additional error on the final reconstruction (see Fig. 3.10). These results are particularly interesting for Airbus as they confirm that for the proposed system, drone scans can replace the long and costly laser scans that were required in past methods.

Finally, the influence of matching errors was investigated by adding a noise $\sigma_o \sim \mathcal{N}(0, 200)$ on some 2D observations considered as outliers, randomly chosen with an occurrence probability in the observations arbitrarily fixed to 1/8. Such noise showed a strong impact on

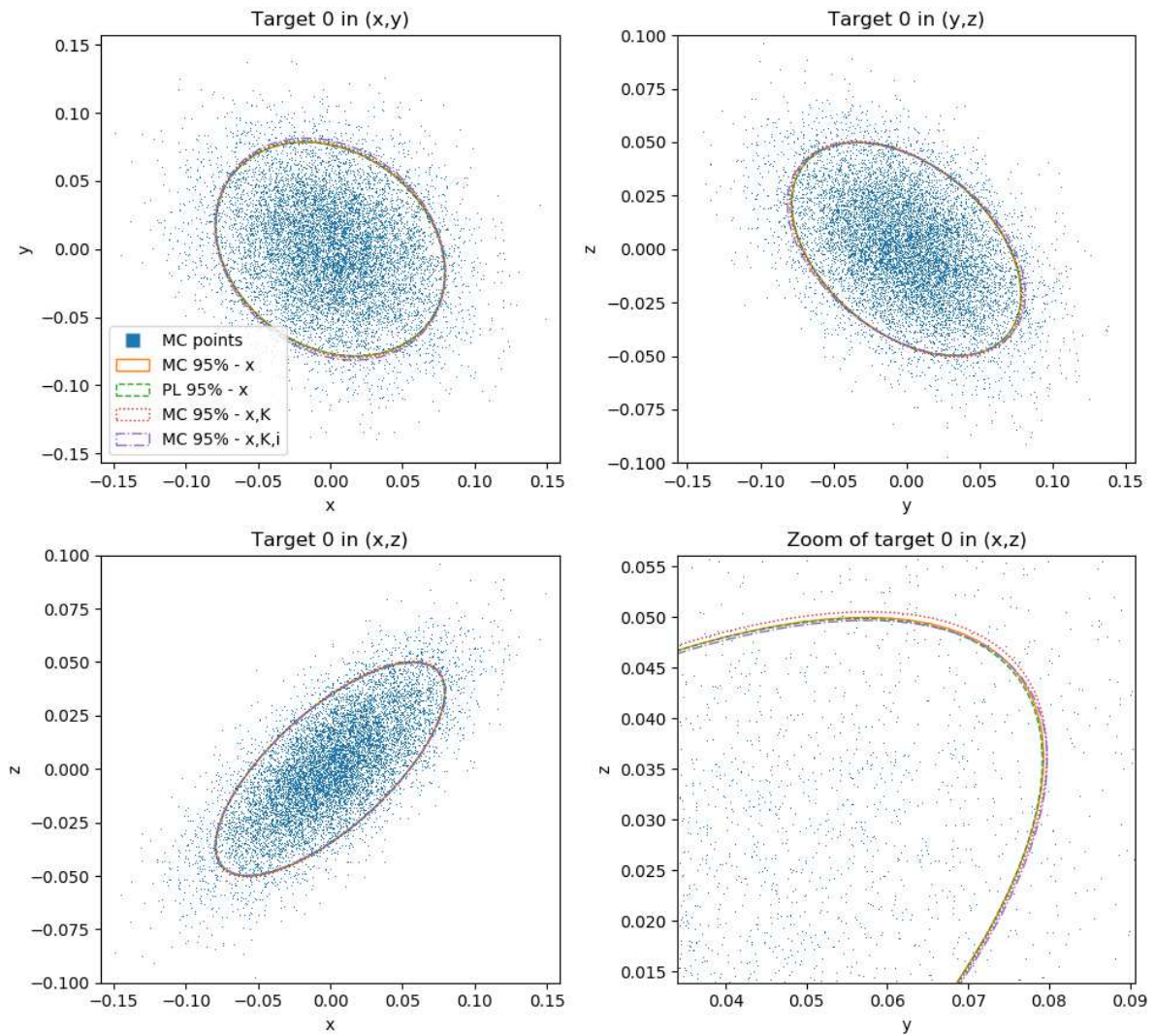


Figure 3.10: Result in meters for a target at wing end of the MC and PL for the uncertainty propagation with various inputs, starting with observation noise (x), plus calibration noise (x,k), and with added noise of initial reconstruction (x,k,i).

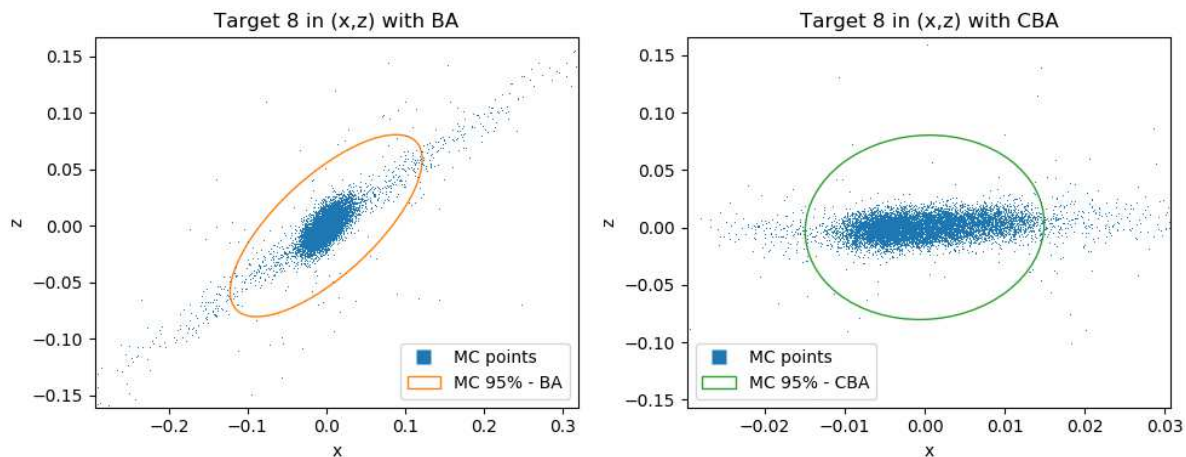


Figure 3.11: Result in meters of the MC for the uncertainty propagation with all considered uncertainties, including outliers. (left) - using BA, (right) - using CBA.

the output reconstruction, as highlighted in Fig. 3.11, which comforts the choice of using targets that considerably reduces the matching errors (in comparison with natural features that may be confused). Besides, this result raises questions on the relevance of using a Gaussian distribution to represent the 3D-point cloud. Further work may focus on finding a more suitable distribution to analyze reconstruction results. Globally, if outliers are avoided, the MC method allows us to guaranty that the reconstruction is compliant with the requirement of an uncertainty (3σ) being less than 10cm.

Based on the MC results, a first study on the influence of the uncertainty sources was conducted, aiming at identifying an axis of improvement. For this purpose, the mean error of the 3D reconstruction was compared with the mean input errors of 2D detection, 3D initialization and camera calibration. Mean errors were calculated using the standard sample mean. In Fig. 3.12, the results of the MC trials are plotted with respect to the three uncertainty sources separately. From these results, it is not possible to identify one source that has a greater impact than the others on the final results. The correlation matrix of the three sources of uncertainty was also calculated to see if the combination of two errors could be connected to the output error. However, the results presented in Table 3.3 show that these three sources are not correlated pairwise. Note that the results are presented for CBA, but similar behavior was observed with BA. In conclusion, no major contributor to the reconstruction error emerges from this brief study, and an in-depth analysis could be the subject of future work.

Table 3.3: Correlation matrix of the uncertainty sources for the MC simulation with CBA

	2D detection noise	3D Initialization noise	Calibration noise
2D detection noise	1	0.041	-0.012
3D Initialization noise	0.041	1	0.014
Calibration noise	-0.012	0.014	1

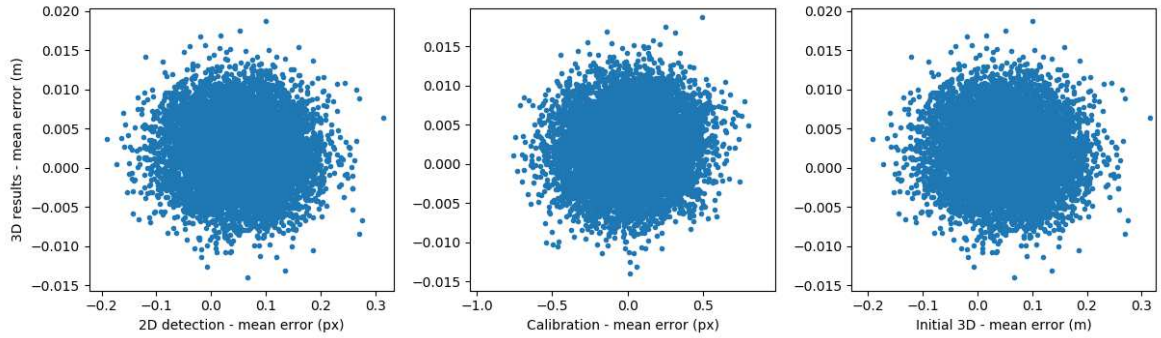


Figure 3.12: Mean 3D error of the MC simulations with CBA displayed as function of the error sources of 2D detection, 3D initialization and camera calibration

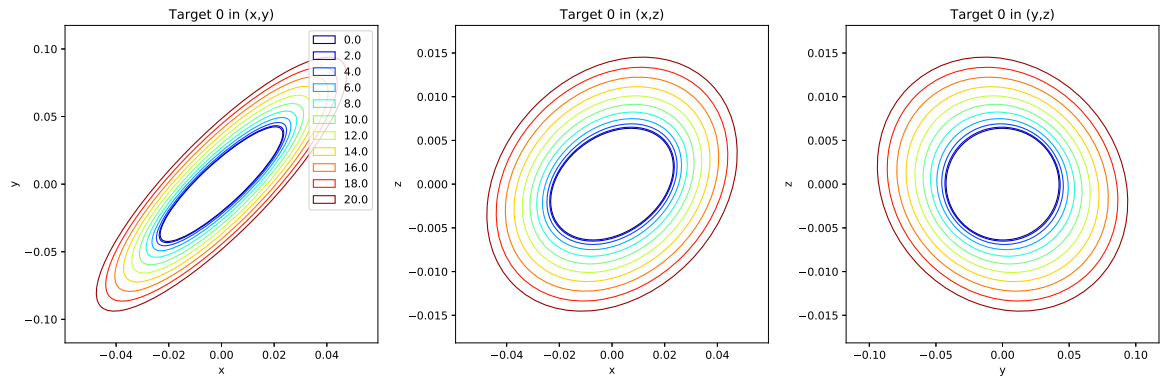


Figure 3.13: Uncertainty results using PL for various level of camera calibration noise, at wing tip (in meters).

In a second set of experiments, the calculation of uncertainty using the propagation law (PL) was evaluated and compared with the MC results without constraints. As displayed in Fig. 3.10 with the overlapping confidence ellipses, covariances obtained using the analytical calculation described in 3.3.2 match those obtained using the MC approach. Since the uncertainty of camera calibration has no impact on the result for $\sigma_k \sim \mathcal{N}(0, 1)$, the correspondence between the results of the two methods was also confirmed for $\sigma_k \sim \mathcal{N}(0, 10)$. While the MC method can take days to calculate the uncertainty for a fixed set of input parameters, PL instantly returns results and allows for a quick interpretation of the impact of the different sources. For instance, the reconstruction quality can be evaluated very fast for several values of calibration uncertainties, as shown in Fig. 3.13. PL is therefore an interesting approach for fast decision making. Subsequently, an in-depth study of the CBA would also enable quick conclusions to be drawn on the impact of the constraints in different application cases. More results on both MC and PL are available in Appendix C.

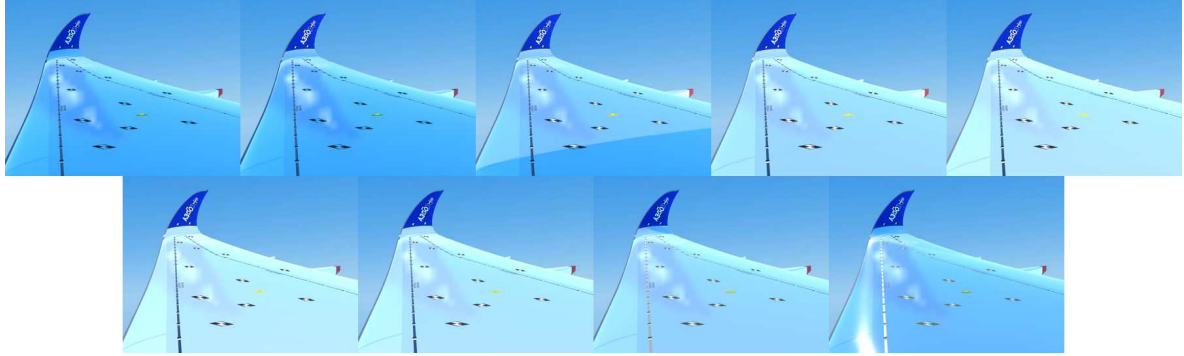


Figure 3.14: First view from camera 1 for each sequence of deformations generated with Unity.

Finally, the uncertainty was evaluated on the synthetic images obtained with Unity. Eight sequences were generated with varying luminosity (see Fig. 3.14). Each sequence is composed of 39 images recording the wing motions with the tip going down 20cm, then up 40cm and finally down 20cm back to its original position. These sequences were passed through the designed framework using BA and CBA. Fig. 3.15 shows the reconstruction results of the proposed method for the eight sequences, with reset of all parameters at the beginning of each sequence. As foreseen from the results of Chapter 2, the 3D estimation is improved using the constrained approach. Particularly, one can observe that the volume constraint on the x coordinate plays a major role on the results, where bounds are frequently reached. Over the entire sequence, the standard deviation of the coordinates along z axis is 3cm in the worst case at the wing tip. These results are also compliant with Airbus requirements. However, the uncertainties are higher than those estimated with the MC and PL approaches. This may arise from the fact that there are still errors due to strong reflections on images of the two last sequences. Besides, here displacements are recorded with a very low acquisition frame rate, which makes the target tracking more difficult, and convergence of the CBA may fail when the step between initial and new shapes from one frame to another is large. In real applications with video acquisition, it would be interesting to add time filtering and tracking methods such as those based on the Kalman filter.

3.5 Conclusion

This chapter evaluated the quality of 3D estimation resulting from the system proposed in Chapter 2 for 3D wing reconstruction. Several methods for estimating the uncertainty of an estimator were introduced and applied to the case of wing reconstruction. A detailed analysis was provided explaining how to define the many uncertainty sources that result from the challenging environment of flight tests, and how to narrow the search by broadly evaluating the impact of the major factors. Uncertainties about these key factors were then propagated using Monte-Carlo simulations, analytical calculation using the propagation law, and realistic images synthesized with a game engine Unity.

The comparison of uncertainty propagation using these various methods demonstrated

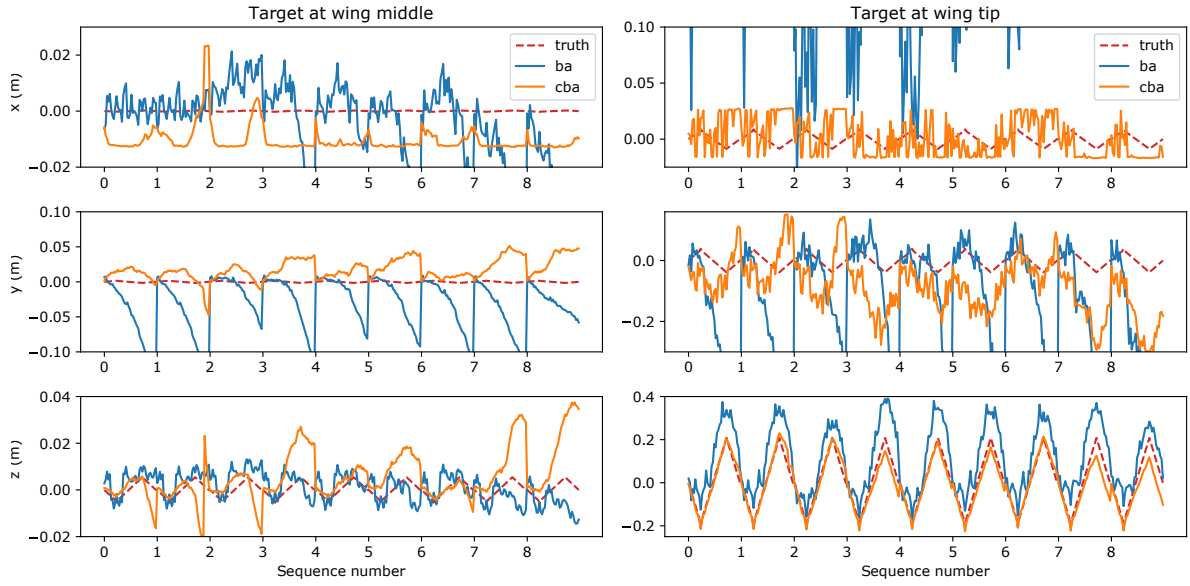


Figure 3.15: Reconstruction result on sequences generated with Unity for two targets, one at the wing tip, and one at its middle.

their potential and limitations with respect to data fidelity, time complexity, implementation cost and availability of ground truth. Moreover, the concordance between the various results validated the implementations, but also the compliance of the proposed system with Airbus requirements. Some very interesting conclusions can be drawn from these experimentations on the influence of some uncertainty sources. For instance, our results demonstrated that some uncertainty sources could be neglected due to their reduced impact on wing reconstruction. It is the case for JPEG compression and drone scans whose impact on the final uncertainty can be neglected.

In addition to the concepts and results, this chapter also introduced several perspectives. First, it was shown in Chapter 2 that 2D observations could be detected using natural features and black lanes located on the wing. It would be interesting to quantify the uncertainty that these observations would propagate. Furthermore, the propagation law was successfully applied to the case of bundle adjustment without constraint. Further work could focus on extending this uncertainty propagation law to the constrained case, and check the consistency with real tests in flight. Finally, now that the various uncertainties of the system have been evaluated, one could take them into account to improve 3D reconstruction using a weighted bundle adjustment.

Industrial Validation

Contents

4.1 Flight Tests	110
4.1.1 Test preparation	110
4.1.2 Aircraft installation	110
4.1.3 Data acquisition	112
4.1.4 Remarks and observations	113
4.2 Agreement with Airbus specifications	116
4.2.1 Installation	116
4.2.2 Measurand	118
4.2.3 Uncontrolled environment	119
4.2.4 Final uncertainty	120
4.3 Industrial perspectives	120
4.3.1 Extension to other applications	120
4.3.2 Requirement refinement	122
4.3.3 Hybridization	122
4.4 Conclusion	123

This PhD thesis was driven by an important problem for Airbus related to the analysis of wing deformations. The proposed study was led by keeping in mind that the method should work on an aircraft in flight, with strong environmental and installation constraints. In Chapter 2, a new framework was introduced to ensure robust 3D reconstruction in such environment, using multiple cameras, targets and mechanical limitations. Furthermore, the accuracy of the proposed approach was evaluated based on assumptions on the real system behavior in Chapter 3. It is now time to see the system in action in real flight conditions. Unfortunately, installation of the system on aircraft was delayed because of lack of priority during the pandemic, and real tests only took place lately in February 2021. Therefore, the reader should be advised that this chapter will only focus on a qualitative evaluation of the flight data, and that the quantitative processing of these data will be performed after the manuscript submission.

First, the experimentation course, in terms of installation, flight and acquired data, is presented in Section 4.1, along with a qualitative study of the recorded images. Second, Section 4.2 discusses how this tested system answers to the industrial requirements. Looking

towards future works, Section 4.3 then introduces perspectives related to the proposed system, and conclusions are reported in Section 4.4.

4.1 Flight Tests

To validate the system developed during this thesis, a specific installation was designed and validated through Airbus strict procedures. After months of preparation, the final system was installed on an aircraft, and the first images were recorded in February 2021. In this section, the proposed equipment architecture together with the details of the first test are described, and comments are formulated on the resulting data.

4.1.1 Test preparation

The world of flight testing is a hostile environment where the probability is high that an unforeseen error will occur between laboratory development, installation, and actual testing. Therefore, it can be expected that everything will not work out as planned from the very first attempt. However, one hour of flight test is expensive, and the aircraft schedules are busy, so it is absolutely crucial to minimize the risk of a test failure. A long preparation phase is therefore necessary on the ground before flying. Part of the work for this industrial thesis was therefore to develop a complete measurement chain, adapted to the proposed algorithms, meeting Airbus specifications, while being able to be integrated into the complex and regulated system of the test aircraft. All the equipment presented in this manuscript has therefore been carefully selected in order to best address the various challenges, from the choice of optics to the camera recording software. All the different parts were configured, tested and qualified in the laboratory before being installed on the aircraft. In addition, compromises had to be made to meet Airbus criteria for robustness, safety and specifications.

4.1.2 Aircraft installation

The proposed installation has been designed to meet Airbus requirements in terms of accuracy, frequency and recording duration in a highly variable environment, while ensuring that this installation is as simple and as less intrusive as possible. Four industrial cameras of 6464×4860 pixel resolution were installed at window positions, as depicted in Figure 4.2. These cameras were selected for their very good size factor with respect to their high image quality, making them suitable candidates for metrological applications while ensuring a simple installation. Moreover, these cameras are ruggedized and can sustain the vibrations and temperature shifts during flights. Their positions and orientations were optimized using the simulated views (as presented in Section 3.3.3), i.e., cameras were placed as far as possible from each others to get the best depth estimation, while ensuring that the wing targets remain visible during the flight for all views. Cameras were installed directly on windows using 3D printed fixations to facilitate the installation, and specific windows were placed instead of classical ones to reduce

their impact on the image distortions. Fig. 4.1 displays the installation inside the aircraft cabin.



Figure 4.1: Cabin installation of the cameras. (a) - Camera mounted on a fake window, (b) - Station of the flight test engineers, used to control the recordings.

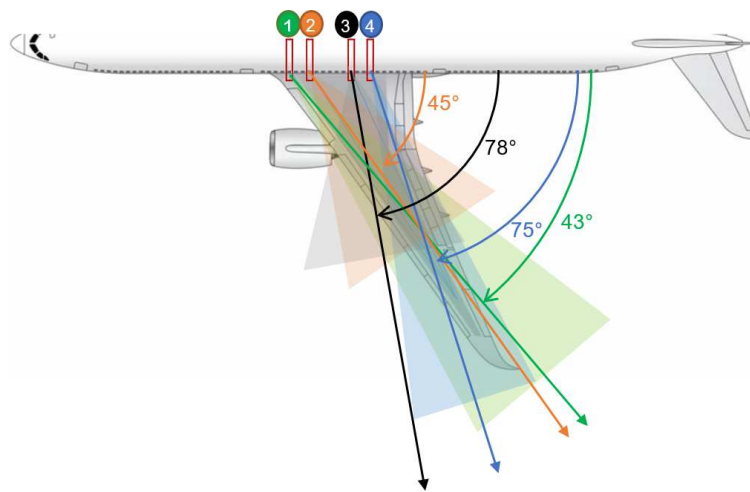


Figure 4.2: Approximate positions and orientations of the four cameras installed on the aircraft. Field of views are highlighted with colored surfaces.

As described in Section 2.3, quadrant targets printed with mat ink were used for robust detection with respect to varying illuminations and view angles. Similar stickers were used as graduations placed along the black lanes of the wing. Markers were stuck on the wing and secured using specific varnish on the borders, so that they do not unstuck during flight. Figure 4.3 illustrates the installation of the targets on the aircraft wing. Due to the presence of other test equipment on the wing, the graduations could not be installed exactly on the

black lines of the wing as planned. However, the graduations will still be found in the images by adjusting the detection algorithm. This is not the case for the black line at leading edge, which will be almost impossible to detect in this configuration. Since this system is intended to be operated in a test environment, this kind of situation is likely to occur frequently, which supports the choice of using targets.

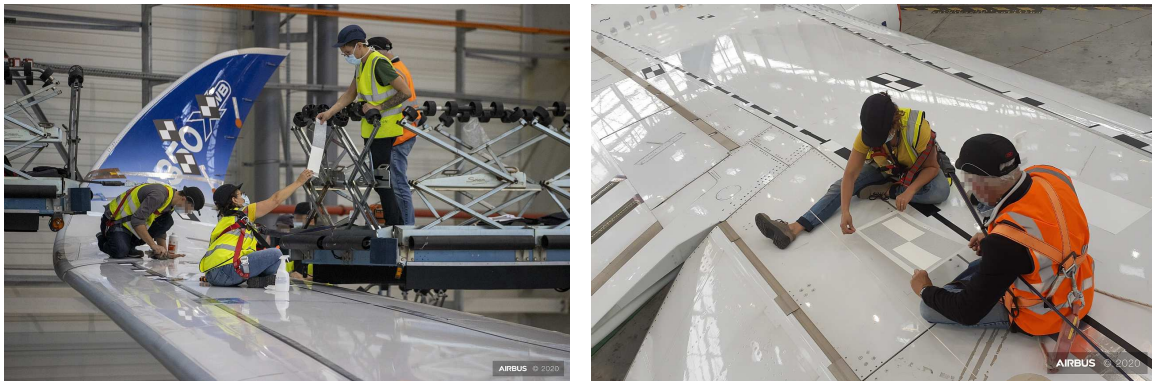


Figure 4.3: Target installation for flight tests on the wing of an A350-1000.

To evaluate the quality of the 3D reconstruction provided by the proposed framework, a countermeasure is required during the experimental validation. To estimate wing twist and bending, recent aircraft used in Airbus flight tests consider inertial motion units (IMU) installed inside the wing. These systems can deliver real time and accurate measurements of the wing bending and twist with respect to a reference inertial unit at the center of the aircraft. As a matter of fact, six of such IMUs were installed inside the wing of the specific aircraft selected for testing our method. IMU measurements are certified by Airbus and will allow the proposed system to be validated. Moreover, in the current configuration of the test aircraft, the rear view, considered in the previous chapters for registration of the reconstruction with respect to the aircraft coordinate system, cannot be recorded. Hence, registration should be performed using the data acquired with one IMU.

Finally, a drone scan was performed before flight as detailed in Section 3.2.3.1, to estimate the initial 3D state of the wing points and cameras on ground. In future work, a fine calibration of the cameras and windows will be performed to determine the intrinsic parameters of the device. For this purpose, a calibrated 3D structure, equipped with circular targets, will be moved in the fields of view of the cameras during a recording. In parallel, a laboratory calibration will be carried out to precisely qualify the cameras and their optics.

4.1.3 Data acquisition

Images of the wing were acquired during a real flight test in February 2021 using the proposed system. Because of hardware issues, one of the cameras did not record during this flight, but

will be operational during the next tests. Before flight, a short record was acquired on ground to get a reference shape of the wing, which may vary due to the quantity of loaded fuel or temperature. Then, videos were recorded for approximately four hours of flight, during which the crew performed several tests, such as turns, roll, touch and go, or ups and downs, resulting in a wide variety of aircraft configuration and environmental conditions, but also recordings under strong vibrations that may impact the quality of the images. Besides, the aircraft changed its course several times during the flight, yielding various orientations with respect to the sun. Furthermore, some of the tests were performed inside the clouds, producing a complete occultation of the wing.

For the camera acquisition, a trade-off between frequency and data storage was made to allow the computers to store the data of several consecutive flights. Indeed, due to the very high resolution of the cameras, if no compression was performed, only about half an hour would have been acquired in the current setup. Using image compression, the computing resources becomes the limiting factor. Hence, it was chosen to record data with a frequency of 4 images per second. Note that this does not exclude the possibility to record at higher frequencies. Besides, even though it was proven that a JPEG compression with 75% quality factor does not alter the final 3D estimation, here it was set to 100% to secure a correct acquisition with respect to the lack of previous tests. Some examples of images acquired during this flight are displayed in Fig. 4.4, or on videos available at [Dem21a], demonstrating the variety of views. Concerning the exposure time, this parameter was changed during flight to evaluate how it influences the chance of over or under exposition of the sensor.

4.1.4 Remarks and observations

The images presented in Fig. 4.4 seem to show a large proportion of unfavorable cases for the method proposed here, where strong illuminations completely hide the targets. However, a large majority of the acquired data (at least 80% at first glance) has a remarkable quality and may be processed. Although the processing of this data is not possible at the moment due to a lack of time, a first qualitative study of the images is possible and already allows several conclusions to be drawn.

First, tests show that ambient light can change more quickly than expected when the aircraft is performing maneuvers. Indeed, recordings have shown that due to the rapid rotations of the test aircraft, the scene brightness can change completely in less than one minute. Therefore, further developments should be conducted to make the template matching algorithm more robust to ensure correct target detection from one image to another. Even more strikingly, the images have shown that the sun can appear directly in the field of view of the cameras during maneuvers, inducing partial or even total overexposure of all the images. In such cases, information on the target position is lost, and the 3D reconstruction cannot be performed.

Now regarding the taxiing phase before and after flight, but also during take off and landing, the test showed much stronger vibrations than in flight conditions, creating more



Figure 4.4: Examples of images recorded during the first flight test.



Figure 4.5: Examples of blur occurring on ground displacements. (a) - Image of the wing tip during landing, (b) - same view during flight.

blur on the images due to both cameras and wings vibrating, which can make the targets tracking from reference to flight shape more difficult. Such blurry image is displayed in Fig. 4.5 and would be enhanced with additional post processing of deblurring. In addition, the wing shape on ground makes targets at its end barely visible. Hence, it would be very useful to have a rear camera that records and that is oriented such that it can see the entire wing, or to enhance the images with additional post processing of deblurring.

Besides these specific cases, in nominal conditions, strong reflections of the sun may appear on the wing. However, recordings show that these reflections are not visible on all the images at the same time. Thus, the 3D estimation for these data may be less accurate, but remains possible. In addition, during this test, the lens hoods were not yet installed, letting reflections from the inside of the plane appear on the windows. Sometimes, it is even possible to see the sun from behind the camera, passing through the cabin to reflect on the glass in front of the camera. This phenomenon is particularly visible in the last image of Fig. 4.4, where one may see the window reflection of sunlight on the top left of the image, and even the reflection of a serial number from inside the cabin on the top right of the image. It supports the idea that hoods should be installed between the optics and the windows for the next tests. In addition, in order to reduce the impact of significant variations in ambient luminosity induced by changes in the orientation of the aircraft with respect to the sun, or by flying above or below the clouds, such as during takeoff, an automatic adjustment of the exposure time should definitely be considered.

One can also observe that camera 3 captures mostly the sky. In fact, the orientation of the camera was limited for this installation because the optics were very close to the windows. For future tests, an adjustment of this camera support should be considered.

Furthermore, one may observe that the images simulated in Section 3.3.3 using Unity are fairly realistic, as displayed in Fig. 4.6. Nonetheless, some improvements could be made based

on the test observations. For example, targets during flight can turn almost overexposed when the sun is grazing, even with a matte printing. Similarly, the occultation of certain targets, as well as the projection of shadows due to the opening of the speed brakes on the wing during flight had not been anticipated. Consequently, these behaviors had not been taken into account for the image synthesis with Unity in Section 3.3.3 and should be added.

Finally, the presence of other means of testing on the wing does not have only disadvantages. Indeed, if one recalls the use of interest points presented in Section 2.2, these installations can be seen as additional information that could be exploited to provide more measurement points.

4.2 Agreement with Airbus specifications

Looking back at Airbus requirements summarized in the introduction of Chapter 1, the first flight test presented here provides an opportunity to validate the proposed system against most of the criteria. This section therefore discusses this validation by distinguishing the main categories of factors, namely installation, measurand, uncontrolled environment, and measurement uncertainty. A synthesis of these main specifications and proposed solutions is given in Table 4.1.

4.2.1 Installation

In terms of installation, several major criteria were raised by Airbus. First of all, the proposed system must be able to be installed in a constrained environment, with limited sensor positions. Since the cameras are installed on the windows of the aircraft, this criterion is validated. In addition, the proposed system is flexible and can therefore be adapted to other installation constraints. Note that one of the cameras had to be moved by one window during the installation because the chosen position was no longer available, which does not prevent the system from working.

The second constraint to respect in terms of installation is to guarantee the non-intrusiveness of the system with respect to flight performance or other tests performed in parallel. This point is satisfied thanks to the use of flush targets on the wing, which do not introduce aerodynamic disturbances and therefore do not limit the flight domain. In addition, the compact size of the acquisition devices installed in the cabin allows them to be installed without disturbing the systems in place. Finally, all the equipment is certified so as not to disturb the various systems on board the aircraft from an electromagnetic point of view.

The third crucial criterion for the system to be effectively installed in an aircraft is the speed of installation. While previous systems used in Airbus may require a week to be installed, the new system presented in this work can be installed in one day. Indeed, the fact that the camera positions are recalculated during the bundle adjustment allows the system to operate even if the cameras move slightly during the flight. It is then possible, as realized

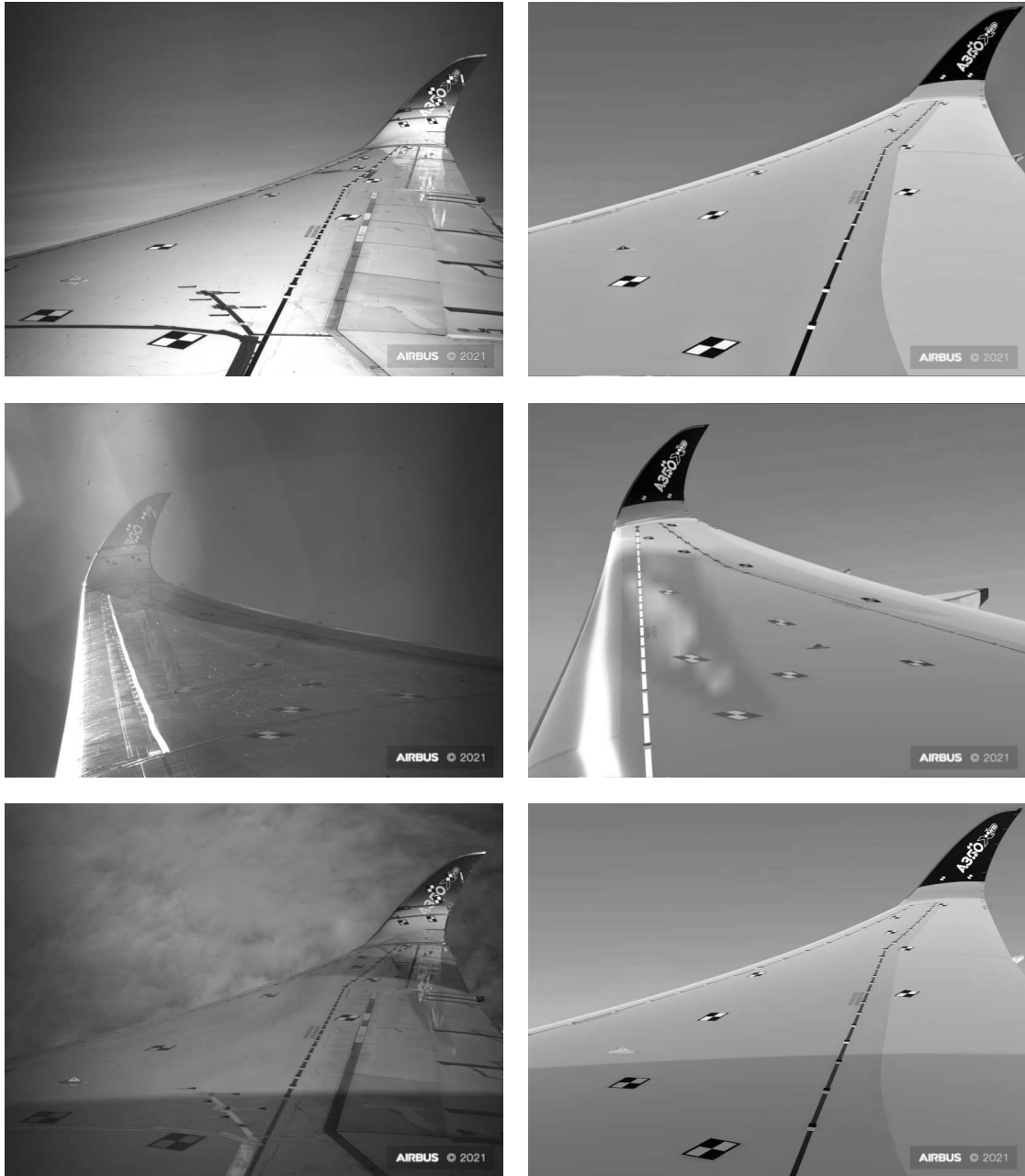


Figure 4.6: Comparison of the real and synthetic images obtained in flight and using Unity. (left) - simulated, (right) - real images.

here, to fix the cameras directly on the false windows, which can be done in less than an hour. Furthermore, since the targets do not need to be positioned at very precise points on the wing, and since they are installed using stickers and varnish, this installation can be achieved in less than half a day. In addition, once the installation is complete, the calibration of the cameras and windows, as well as the wing scan by drone, can be performed without impacting the aircraft schedule. Even though these operations would be counted in the installation time, calibration is a matter of about an hour, while the drone scan takes only thirty minutes.

Last but not least, this first test demonstrated that the system works in flight, i.e., that the targets did not stall during takeoff, that the camera supports, cameras and acquisition PCs did not suffer from vibrations or variations in temperature and humidity.

4.2.2 Measurand

In this study, the measurand is the wing deformation between its resting and flying positions. Thus, the first requirement is to realize measurements on a volume of approximately $10 \times 30 \times 10$ meters with an important sampling. In particular, the need is to be able to estimate the deformations of the wing between its engine and its tip. Through the tested installation, it has been demonstrated that the use of cameras allows a very flexible response to this need. An adaptation of the system to visualize different volumes is easily possible. Depending on the expected accuracy, it is possible to simply change the focal length so as to modify the viewing angle. Another solution would be to add more points of view, which can be considered thanks to the simplicity of installation. Furthermore, following the constant evolution of video sensors, it is also feasible to use higher resolution cameras to cover larger areas of the wing without modifying the accuracy of 3D reconstruction.

Another important criterion was related to the temporal dimension. Wing deformations should be recorded at a frame-rate between 1 and 30 images per second, for a test duration of about 4 hours, with limited capacity of storage in the aircraft. Here, the proposed system enables the acquisition frequency and the compression rate of the images to be adjusted according to the need, which is thus satisfied. In addition, within the proposed framework, it was chosen to prepare the acquisition to record several flights on the same storage disks, and thus simplify the procedure of data transfer. Yet the simple fact of changing disks for each flight would make it possible to increase the acquisition frequency. Another limiting factor concerning the frame-rate is the JPEG compression. Within the current setup, this compression is performed on CPU, which limits the writing frequency for high-resolution images. One way of improvement would be to use the graphics processor unit to perform this task. Finally, the recording is currently launched before the flight and stopped after the aircraft returns to its parking area. An automatic triggering of the recordings based on the flight configuration is currently under development for this system and would allow reducing the recording time to the relevant phases of the flight.

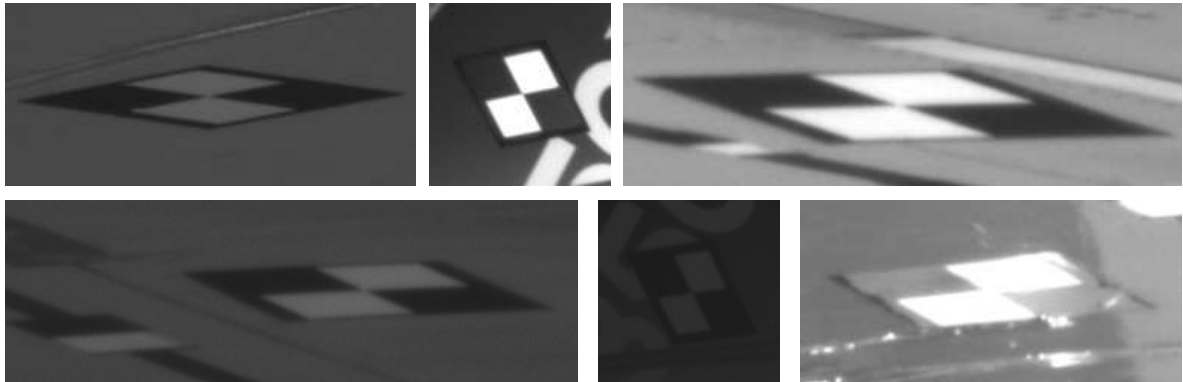


Figure 4.7: Example of target views acquired during the flight.

4.2.3 Uncontrolled environment

A major criterion of the aircraft application is that the system should be able to operate in an uncontrolled environment, with significant luminosity variations, potential shadows and reflections, but also vibrations and deformations of the entire aircraft. First of all, regarding illumination variations, the simulations presented in Section 3.3.1.1 have shown that detection could be performed even at very low contrast between the white and black parts of the target. The use of a matte ink to print the targets therefore allowed, as expected, to provide sufficient contrast for detection over a majority of the flight test, as illustrated in Fig. 4.7. It would be interesting to subsequently quantify the level of contrast during the flight and compare this information to the uncertainty of the final reconstruction. Finally, the acquired images show that the contrast between the black lines and the surrounding metal plates may become very reduced in some configurations. In these cases, the line contours disappear completely and detection is impossible, which further supports the choice to use targets.

During the flight, shadows of the fuselage or the rear stabilizer can be projected on the wing according to the orientation of the plane compared to the sun. Concerning this challenge, this first experiment showed that the impact of the shadows on the contrast of the targets was minimal during the flight. As mentioned previously, the detection of the targets can be done at low contrast. Therefore, the presence of shadows will have no impact on the proposed system.

Concerning the presence of reflection, we can distinguish two types of reflections. First, there are the wingtip reflections on the wing surface. In some images, one can recognize the specular property of the wing at the sight of the "A350 XWB" logo reflecting clearly on the wing surface. In this case, there is no concern for the proposed system because targets on their side do not reflect these inscriptions. However, the second type of reflections, of the sun, is more important and may impact the 3D estimation in cases where complete regions of the wing are overexposed.

Finally, the last challenging criterion for 3D reconstruction in flight is the fact that the entire aircraft can deform and vibrate in flight. On this point, the proposed system has been designed to operate in an onboard environment, which was demonstrated during the test, and is therefore not disturbed by these elements. In addition, the positions and orientations of the cameras are validated by the fact that the targets remain well within their field of view throughout the test, despite all deformations. Moreover, due to the low exposure times selected, the vibrations of the cameras or the wing do not add considerable blur to the in-flight images, which validates well the predictions made on the image blur in simulation (see Section 3.2.3.2).

4.2.4 Final uncertainty

The need for deformation measurement expressed by Airbus results in a request for 3D measurement of the wing points with an uncertainty of less than 10cm in elevation. As the data has not yet been processed, it is not possible to state that this criterion is satisfied by the proposed system. However, the images acquired during the flight are very promising and allow one hoping to reach the required accuracy without too much doubt. Moreover, these images have made it possible to validate to a large extent the sources of uncertainty to which the approach will be exposed. This validation justifies the error propagation studied in Section 4, which allows one to affirm system success in terms of measurement uncertainty.

In addition, the evaluation of the reconstruction uncertainty is performed using the results of different reconstruction methods. In this case, this countermeasure is provided by six IMUs present in the wing. In view of the difference in density of spatial sampling, it will be necessary to make assumptions about the deformation of the wing between these measurement points, which may not be accurate. An alternative would be to use the former photogrammetry system developed by Airbus as a countermeasure, although complex, which would allow one to have a sampling as dense as the proposed method. However, this method also relies on approximations of the deformation model of the wing. Finally, the question can be asked about which method, between simulation or experimental validation, is the most reliable.

4.3 Industrial perspectives

The potential of the proposed method has been demonstrated through the course of this manuscript. From an industrial point of view, this approach paves the way to some perspectives described in this section.

4.3.1 Extension to other applications

This work focused on the application case of 3D reconstruction of an airplane wing. However, the proposed system can be extended to other fields of application. Indeed, the key points

Table 4.1: Synthesis of system responses to Airbus requirements.

Installation

Specification	Solution	Validation
Limited sensor positions	- Flexible installation at windows	OK
Non-intrusiveness	- Flush markers - Compact devices - Limited electromagnetic emissions	OK
Fast installation	- Simple device installation - Camera motions allowed - Sticker targets - Fast calibration and drone scan	1 day

Measurand

Specification	Solution	Validation
Scene volume of $10 \times 30 \times 10\text{m}$	- 4 Cameras looking focusing on different parts of the wing	OK
Frequency between 1 and 30 Hz	- Adjustable frame-rate set to 4Hz	OK
4 hours duration, limited disk capacity	- Adjustable frame-rate, compression set for about 10h of recording	OK

Uncontrolled environment

Specification	Solution	Validation
Illumination variations and potential shadows	- Algorithm detection 2D targets 2D on low contrast - Target printed with matte ink	OK
Work with reflections	- Multiple views enabling redundancy and limitation of target loss - No solution yet when the sun is in the camera field of views	Partial

Final uncertainty

Specification	Solution	Validation
Bending uncertainty lesser than 10cm	- Constrained Bundle Adjustment - Countermeasure from IMUs - Validation of errors propagated in Chapter 3	Partial

of this system is to operate without contact, in a non-intrusive way, and in an embedded environment not very favorable to 3D measurements, thanks to the use of mechanical limit constraints. One may think about applications in similar environment that may be found for instance in the space, military, or robotics fields.

In the case of aeronautics, the proposed 3D reconstruction method is interesting to estimate deformations of areas that are difficult to instrument or areas that should not be polluted by the installation of additional equipment. For example, the proposed system can be used to estimate engine deformations, allowing a better understanding of engine performance. In addition, as for the wing, the use of mechanical limits would be adapted to improve the estimation without introducing a deformation model.

4.3.2 Requirement refinement

Other perspectives can be brought with respect to the need expressed by Airbus in terms of measurement uncertainty. Indeed, the request for an estimate with an uncertainty of less than 10cm has been established from the measurement results provided by the former photogrammetry system. The proposed method having more degrees of freedom, and offering a more dynamic and dense measurement, one could imagine refining the need, or even refining the metric used. Specifically, if the measurement is used to recover the forces applied to the wing, one can imagine directly providing the bending as a derivative of the elevation as a function of the wingspan. In the past, this was not possible because of the non-deformability approximations of the wing part. Subsequently, it would be interesting to present the capabilities of this new approach to experts to discuss how their needs can be better met and how the system can be improved in this way.

4.3.3 Hybridization

A final area of investigation could be to combine the developed system with other technologies used by Airbus or under development. One can think here specifically to the IMUs present in the wing, but also to other systems that are currently being tested by Airbus, such as the LIDAR, which was presented in the state of the art, or a new technology for measuring deformation by optical fiber. The latter, based on the principle of "Optical Frequency Domain Reflectometry", makes it possible to find the deformation of the wing according to the strain applied to an optical fiber installed on the leading edge of the wing. More details on this subject can be found in [Ric+12].

Such hybridization would combine the advantages of the different technologies, and thus make the deformation measurement more robust to environmental variations. For example, the fiber and IMUs can deliver measurements even when the wing is no longer visible on the images, such as when passing through clouds or when the sun blinds the cameras. On the other hand, the proposed method based on target detection easily provides measurement points at any location on the wing, whereas the installation of other sensors is more limited,

such as on the flaps for instance.

In addition, a hybrid approach would benefit from the uncertainty study proposed in Chapter 3. The knowledge of the uncertainty of 3D reconstruction would allow one to weight the information provided in the combined estimate.

4.4 Conclusion

The objective of this chapter was to validate as many characteristics of the proposed system as possible for flight tests, with the limited data available and in a limited time. To do this, the first flight test was exposed, and the system was confronted with the initial needs of Airbus with regard to the acquired images. It was thus possible to validate a majority of the acquisition device in terms of its functioning and behavior in an embedded environment with significant environmental variations. This proof of concept paves the way for the industrialization of the acquisition system.

Regarding the perspectives, future work will obviously have to focus on the validation of the 3D reconstruction algorithms proposed in Chapter 3. In addition, this industrial validation provides interesting leads for expanding the application field, improving the system by hybridization, but also refining the measurand specifications. The work in previous chapters show very interesting prospects, that were refined thanks to the first tests. Yet, we can expect to see new interesting phenomena occurring during the next flights.

Conclusion and perspectives

The work presented in this manuscript is mainly related to the development of a new method for estimating the deformation of wings in flight, in accordance with specifications established with Airbus experts, adapted to the constraints of flight tests and to the challenges of a variable environment in flight.

The proposed method is primarily the result of an in-depth study of the state of the art in the field of non-contact 3D estimation, presented in Chapter 1. The wide variety of available methods was confronted with the challenges of the application defined by Airbus, which allowed to establish the interest of an approach of multi-view photogrammetry for the 3D reconstruction of aircraft wings. Indeed, this method has the valuable attributes of delivering precise measurements according to Airbus expectations, on the complete volume of an aircraft wing, in a dense and dynamic way, while ensuring a simple, fast and non-intrusive installation. In addition, Airbus expertise in the field of embedded video acquisition is another key factor that supported this choice. This method has therefore been the subject of a more detailed study in order to allow its implementation on aircraft.

In Chapter 2, a complete framework for estimating deformations of the wing in flight has been proposed, based on 2D detection of natural features of the wing or the use of targets. This photogrammetry method uses cameras installed at locations constrained by the application that are not necessarily optimal for 3D reconstruction, i.e., on the windows and the rear stabilizer of the aircraft. In addition, the images are acquired in an uncontrolled environment, with brightness variations, reflections and shadows, but also vibrations and deformations of the aircraft. In order to improve the 3D wing estimation, we have proposed a new reconstruction method exploiting constraints of the mechanical limits of the wing as regularization terms in the classical bundle adjustment. Finally, the potential of this method has been demonstrated through realistic experiments conducted on an A350 on ground. In conclusion, it is clear that the use of key points that are naturally present on the wing is interesting in cases where the processed videos have not been intended for this purpose. On the other hand, to ensure the quality of 3D estimation in an industrial context, this approach should not be considered, and the use of specific targets should be favored. In the case of aircraft wings, the use of quadrant targets is therefore relevant. However, we could have gone even further by placing circular targets on the wingtip to improve accuracy. In addition, the proposed method based on mechanical constraints responds well to the Airbus problem as it provides a good 3D reconstruction, while ensuring that the deformation models are not directly used. In fact, the addition of mechanical limitations may be considered as equivalent to adding a supplementary top view of the wing, providing a more favorable case for standard photogrammetry.

The proposed method is suited to the flight test environment, but cannot be used by Airbus design office without a complete analysis of its uncertainty. This was therefore the subject of Chapter 3, which first introduced the standards and methodologies for estimating

measurement uncertainty. Next, this part focused on an in-depth analysis of how to define the various sources of error occurring in an embedded system for processing flight images. The propagation of the errors considered in the current application was then conducted using the different methods presented, i.e., using Monte Carlo simulation, analytical computation via the propagation law, and experimentation on realistic computer-generated images. This work allowed us to compare the three approaches in the present application and to demonstrate the strengths and weaknesses of the three approaches with respect to data fidelity, temporal complexity, implementation and ground-truth availability. Finally, conclusions were drawn on the influence of some error sources on the final 3D reconstruction.

Finally, a proof of concept showed the validity of the proposed process with respect to the industrial expectations, which is the subject of Chapter 4. For this purpose, a complete photogrammetry system was developed to operate the framework designed in Chapter 2, and to answer as well as possible to the problems of sources of uncertainty of Chapter 3. This system was installed on an Airbus A350-1000 and enabled the acquisition of the first experimental images at the end of the thesis. Due to lack of time, the processing of these data could not be achieved, but it nevertheless permitted to draw the first conclusions on the validity of the system. Indeed, the images and the acquisition chain in action were confronted to Airbus specifications, leading to the validation of the equipment and the acquisition concept.

Perspectives

Regarding the perspectives of this thesis, several axes are considered, both from an academic and an industrial point of view. First, since the proposed system has been installed on an aircraft, a natural perspective is to test the proposed algorithms on the real data. This would allow one to clearly demonstrate the advantages of a reconstruction method under mechanical constraints in the real environment, but also to evaluate which type of constraint is the most interesting in order to reduce the algorithmic complexity. Moreover, the processing of these experimental data would allow us to compare the uncertainty of the real system to that estimated in Chapter 3 using simulations and analytical computations. One should however remain vigilant on the fact that the countermeasure data are sparse or introduce approximations about the wing deformations.

A second area of investigation is to improve the proposed algorithm by considering a weighted bundle adjustment approach in addition to the constraints. Indeed, in this study the 2D observations used as the input of the bundle adjustment may be erroneous and lead to a local minimum of the reprojection error, thus corrupting the 3D estimation. Given the uncertainty study provided in Chapter 3, it would be possible to weight these 2D observations in the cost function according to their detection uncertainty and their position on the wing. In addition, tracking algorithms could be implemented in order to improve the detection on successive images.

Another future work could be devoted to deepening the study of system uncertainty. On the one hand, the uncertainty estimation of the detection of natural features of the wing would

enable us to predict the performance of the algorithm in the case where no target could be installed. On the other hand, the analytical propagation method presented in Section 3.3.2 allows one to quickly estimate the reconstruction uncertainty according to the application case, and thus to shorten the time of decision making in an industrial context. It would therefore be relevant to study the application of the propagation law to the bundle adjustment under constraints. In addition, it would be appropriate to evaluate the 3D-reconstruction uncertainty as a function of the flight parameters to predict the ideal situation, the average situation, but also the situations to be avoided. One can thus think of imposing a heading to the aircraft for ensuring optimal 3D-estimates.

Finally, several industrial prospects have emerged from this work and the tests presented in Chapter 4. Indeed, the proposed system is particularly well suited to constrained installations requiring limited intrusiveness, making it a good candidate for other applications such as the deformation measurement of aircraft nacelles. In addition, a fine-tuning of the measurement needs could be studied on the Airbus side thanks to the extended capabilities of the new method compared to the previous ones. Finally, a hybridization of the developed method of photogrammetry with the various methods currently studied at Airbus, such as lidar and optical fibers, could be investigated in order to guarantee redundancy and improve the final estimation. This combination of measurement means will most certainly be the key to the development of Airbus future generation of wings.

Derivatives Calculation for the Constrained Bundle Adjustment

A.1 Constrained Bundle Adjustment - reminder

In this section, we shortly remind the constrained bundle adjustment formulation with a first constraint function g_0 . We have a set of M camera and N points. Observation on camera j of the point i is noted \mathbf{x}_j^i and camera parameters are represented as vectors $\boldsymbol{\alpha}_j = (\mathbf{v}_j, \mathbf{t}_j)^T$. \mathbf{v}_j and \mathbf{t}_j are respectively the rotation and translation vectors of the camera j . $\hat{\mathbf{x}}(\boldsymbol{\alpha}_j, \mathbf{X}^i)$ is the projection of the estimated point \mathbf{X}^i on camera j with estimated parameters $\boldsymbol{\alpha}_j$. The optimization function in our model is written:

$$\arg \min_{\boldsymbol{\alpha}_j, \mathbf{X}^i} \sum_{i,j} \left[\mathbf{x}_j^i - \hat{\mathbf{x}}(\boldsymbol{\alpha}_j, \mathbf{X}^i) \right]^2 + \mu_0 \sum_i \left[g_0^+(\boldsymbol{\alpha}_r, \mathbf{X}^i) \right]^2, \quad (\text{A.1})$$

where μ_0 is the first penalty parameter,

$$\hat{\mathbf{x}}(\boldsymbol{\alpha}_j, \mathbf{X}^i) = \frac{1}{c_j^i} \mathbf{K}_j \mathbf{l}_j^i, \quad (\text{A.2})$$

where \mathbf{K}_j is the 2×3 matrix of the intrinsic camera parameters, considered as known after system calibration, and

$$\mathbf{l}_j^i = (a_j^i, b_j^i, c_j^i)^T = \left[\mathbf{R}_j^T, -\mathbf{R}_j^T \mathbf{t}_j \right] \begin{pmatrix} \mathbf{X}^i \\ 1 \end{pmatrix} \quad (\text{A.3})$$

with \mathbf{R}_j the rotation matrix formed using Euler-Rodrigues formula [GY15]

$$\mathbf{R}_j = \text{Id} + \sin \theta [\bar{\mathbf{v}}_j]_{\times} + (1 - \cos \theta) [\bar{\mathbf{v}}_j]_{\times}^2,$$

where θ is the rotation angle around the unit vector $\bar{\mathbf{v}}_j = (\bar{v}_{j,1}, \bar{v}_{j,2}, \bar{v}_{j,3})$, such that $\mathbf{v}_j = \theta \bar{\mathbf{v}}_j$, and $[\bar{\mathbf{v}}_j]_{\times}$ is the cross product matrix defined as

$$[\bar{\mathbf{v}}_j]_{\times} = \begin{pmatrix} 0 & -\bar{v}_{j,3} & \bar{v}_{j,2} \\ \bar{v}_{j,3} & 0 & -\bar{v}_{j,1} \\ -\bar{v}_{j,2} & \bar{v}_{j,1} & 0 \end{pmatrix} \quad (\text{A.4})$$

And $g_0^+(\boldsymbol{\alpha}_r, \mathbf{X}^i) = \max(0, g_0(\boldsymbol{\alpha}_r, \mathbf{X}^i))$, with in the simple example

$$g_0(\boldsymbol{\alpha}_r, \mathbf{X}^i) = (r_x^i - \tilde{x}^i), \quad (\text{A.5})$$

Registration:

$$\tilde{\mathbf{X}}^i = P \begin{bmatrix} \mathbf{R}_r^T & -\mathbf{R}_r^T \mathbf{t}_r \\ 0 & 1 \end{bmatrix} \begin{pmatrix} \mathbf{X}^i \\ 1 \end{pmatrix}. \quad (\text{A.6})$$

A.2 CBA Derivatives

Now we will calculate the non-zero elements of the Jacobian:

$$\frac{\partial (\mathbf{x}_j^i - \hat{\mathbf{x}}(\boldsymbol{\alpha}_j, \mathbf{X}^i))^2}{\partial (\boldsymbol{\alpha}_j, \mathbf{X}^i)} = -2 \text{diag}(\mathbf{x}_j^i - \hat{\mathbf{x}}(\boldsymbol{\alpha}_j, \mathbf{X}^i)) \frac{\partial \hat{\mathbf{x}}(\boldsymbol{\alpha}_j, \mathbf{X}^i)}{\partial (\boldsymbol{\alpha}_j, \mathbf{X}^i)}, \quad (\text{A.7})$$

where

$$\frac{\partial \hat{\mathbf{x}}(\boldsymbol{\alpha}_j, \mathbf{X}^i)}{\partial (\boldsymbol{\alpha}_j, \mathbf{X}^i)} = \mathbf{K}_j \left(\frac{1}{c_j^i} \frac{\partial \mathbf{l}_j^i}{\partial (\boldsymbol{\alpha}_j, \mathbf{X}^i)} - \frac{1}{(c_j^i)^2} \mathbf{l}_j^i \frac{\partial c_j^i}{\partial (\boldsymbol{\alpha}_j, \mathbf{X}^i)} \right), \quad (\text{A.8})$$

where

$$\frac{\partial \mathbf{l}_j^i}{\partial (\boldsymbol{\alpha}_j, \mathbf{X}^i)} = \left(\frac{\partial a_j^i}{\partial (\boldsymbol{\alpha}_j, \mathbf{X}^i)}, \frac{\partial b_j^i}{\partial (\boldsymbol{\alpha}_j, \mathbf{X}^i)}, \frac{\partial c_j^i}{\partial (\boldsymbol{\alpha}_j, \mathbf{X}^i)} \right)^T = \frac{\partial \mathbf{T}_j}{\partial (\boldsymbol{\alpha}_j, \mathbf{X}^i)} \begin{pmatrix} \mathbf{X}^i \\ 1 \end{pmatrix} + \mathbf{T}_j \frac{\partial (\mathbf{X}^i, 1)^T}{\partial (\boldsymbol{\alpha}_j, \mathbf{X}^i)} \quad (\text{A.9})$$

where $\mathbf{T}_j = [\mathbf{R}_j^T, -\mathbf{R}_j^T \mathbf{t}_j]$.

First regarding the points parameters, we have $\frac{\partial \mathbf{T}_j}{\partial \mathbf{X}^i} = 0$, thus

$$\frac{\partial \mathbf{l}_j^i}{\partial \mathbf{X}^i} = \mathbf{R}_j^T \quad (\text{A.10})$$

Now, regarding the camera parameters, since \mathbf{X}^i does not depend on the camera parameters, $\frac{\partial (\mathbf{X}^i, 1)^T}{\partial \boldsymbol{\alpha}_j} = 0$, and

$$\frac{\partial \mathbf{l}_j^i}{\partial \boldsymbol{\alpha}_j} = \frac{\partial \mathbf{T}_j}{\partial \boldsymbol{\alpha}_j} \begin{pmatrix} \mathbf{X}^i \\ 1 \end{pmatrix}, \quad (\text{A.11})$$

where

$$\frac{\partial \mathbf{T}_j}{\partial \boldsymbol{\alpha}_j} = \begin{bmatrix} \frac{\partial \mathbf{R}_j^T}{\partial \boldsymbol{\alpha}_j} & -\frac{\partial \mathbf{R}_j^T}{\partial \boldsymbol{\alpha}_j} \mathbf{t}_j - \mathbf{R}_j^T \frac{\partial \mathbf{t}_j}{\partial \boldsymbol{\alpha}_j} \end{bmatrix} \quad (\text{A.12})$$

with

$$\frac{\partial \mathbf{t}_j}{\partial \boldsymbol{\alpha}_j} = [0_3, I_3], \quad \frac{\partial \mathbf{R}_j^T}{\partial \boldsymbol{\alpha}_j} = \begin{bmatrix} \frac{\partial \mathbf{R}_j^T}{\partial v_{j,1}} & \frac{\partial \mathbf{R}_j^T}{\partial v_{j,2}} & \frac{\partial \mathbf{R}_j^T}{\partial v_{j,3}} & 0_3 \end{bmatrix}, \quad (\text{A.13})$$

and $\forall p \in (1, 2, 3)$

$$\frac{\partial \mathbf{R}_j}{\partial v_{j,p}} = \cos \theta \bar{v}_{j,p} [\bar{\mathbf{v}}_j]_{\times} + \sin \theta \bar{v}_{j,p} [\bar{\mathbf{v}}_j]_{\times}^2 + \frac{\sin \theta}{\theta} [\mathbf{e}_p - \bar{v}_{j,p} \bar{\mathbf{v}}_j]_{\times} + \frac{1 - \cos \theta}{\theta} (\mathbf{e}_p \bar{\mathbf{v}}_j^T + \bar{\mathbf{v}}_j \mathbf{e}_p^T - 2 \bar{v}_{j,p} \bar{\mathbf{v}}_j \bar{\mathbf{v}}_j^T) \quad (\text{A.14})$$

as demonstrated in [GY15], with (e1, e2, e3) the standard basis in \mathbb{R}^3 . Then, for the constraint formulation in (2.21)

$$\frac{\partial (g_0^+(\boldsymbol{\alpha}_r, \mathbf{X}^i))^2}{\partial (\boldsymbol{\alpha}_r, \mathbf{X}^i)} = 2g_0^+(\boldsymbol{\alpha}_r, \mathbf{X}^i) \frac{\partial g_0^+(\boldsymbol{\alpha}_r, \mathbf{X}^i)}{\partial (\boldsymbol{\alpha}_r, \mathbf{X}^i)}, \quad (\text{A.15})$$

with

$$\frac{\partial g_0^+(\boldsymbol{\alpha}_r, \mathbf{X}^i)}{\partial (\boldsymbol{\alpha}_r, \mathbf{X}^i)} = \begin{cases} 0 & \text{if } g_0(\boldsymbol{\alpha}_r, \mathbf{X}^i) \leq 0 \\ \frac{\partial g_0(\boldsymbol{\alpha}_r, \mathbf{X}^i)}{\partial (\boldsymbol{\alpha}_r, \mathbf{X}^i)} & \text{otherwise} \end{cases} \quad (\text{A.16})$$

In the particular case of (A.5),

$$\frac{\partial g_0(\boldsymbol{\alpha}_r, \mathbf{X}^i)}{\partial (\boldsymbol{\alpha}_r, \mathbf{X}^i)} = -\frac{\partial \tilde{\mathbf{x}}^i}{\partial (\boldsymbol{\alpha}_r, \mathbf{X}^i)}, \quad (\text{A.17})$$

with $\tilde{\mathbf{X}}^i = (\tilde{x}^i, \tilde{y}^i, \tilde{z}^i)$ defined in (A.6), and

$$\frac{\partial \tilde{\mathbf{X}}^i}{\partial (\boldsymbol{\alpha}_r, \mathbf{X}^i)} = \mathbf{P} \left[\frac{\partial \tilde{\mathbf{T}}^k}{\partial (\boldsymbol{\alpha}_r, \mathbf{X}^i)} \begin{pmatrix} \mathbf{X}^i \\ 1 \end{pmatrix} + \tilde{\mathbf{T}}^k \frac{\partial (\mathbf{X}^i, 1)^T}{\partial (\boldsymbol{\alpha}_r, \mathbf{X}^i)} \right]. \quad (\text{A.18})$$

where $\tilde{\mathbf{T}}_j = \begin{bmatrix} \mathbf{R}_r^T & -\mathbf{R}_r^T \mathbf{t}_r \\ 0 & 1 \end{bmatrix}$.

Finally,

$$\frac{\partial \tilde{\mathbf{X}}^i}{\partial \mathbf{X}^i} = \mathbf{P} \begin{bmatrix} \mathbf{R}_r^T \\ 0 \end{bmatrix}, \quad (\text{A.19})$$

and

$$\begin{cases} \frac{\partial \tilde{\mathbf{X}}^i}{\partial \boldsymbol{\alpha}_j} = 0 & \text{if } j \neq k \\ \frac{\partial \tilde{\mathbf{X}}^i}{\partial \boldsymbol{\alpha}_r} = \mathbf{P} \begin{bmatrix} \partial \mathbf{T}^k \\ 0 \end{bmatrix} \begin{pmatrix} \mathbf{X}^i \\ 1 \end{pmatrix} \end{cases}, \quad (\text{A.20})$$

where $\frac{\partial \mathbf{T}^k}{\partial \boldsymbol{\alpha}_r}$ is calculated in (A.12) to (A.14).

Gauss-Newton method

The Gauss-Newton method is an iterative algorithm for solving the least-squares of a non linear function, and is described in this appendix.

We note $e : \mathbb{R}^n \rightarrow \mathbb{R}$ the cost function to minimize over all values of a n parameter vector \mathbf{p} , and \mathbf{p}_0 an initial guess close to a well-defined minimum value of e . Using the Taylor series expansion of e at \mathbf{p}_0 , one can write

$$e(\mathbf{p}_0 + \boldsymbol{\delta}) = e(\mathbf{p}_0) + \frac{\partial e}{\partial \mathbf{p}}(\mathbf{p}_0)\boldsymbol{\delta} + \frac{1}{2}\boldsymbol{\delta}^T \frac{\partial^2 e}{\partial \mathbf{p}^2}(\mathbf{p}_0)\boldsymbol{\delta} + \dots, \quad (\text{B.1})$$

where derivatives of higher order than two are neglected. To minimize e with respect to $\boldsymbol{\delta}$, one differentiates Eq. (B.1) with respect to $\boldsymbol{\delta}$ and seeks where it equals zero, leading to

$$\frac{\partial e}{\partial \mathbf{p}}(\mathbf{p}_0) + \frac{\partial^2 e}{\partial \mathbf{p}^2}(\mathbf{p}_0)\boldsymbol{\delta} = 0 \quad (\text{B.2})$$

or

$$\frac{\partial^2 e}{\partial \mathbf{p}^2}(\mathbf{p}_0)\boldsymbol{\delta} = -\frac{\partial e}{\partial \mathbf{p}}(\mathbf{p}_0). \quad (\text{B.3})$$

Starting from \mathbf{p}_0 , the Newton method computes the parameter increment $\boldsymbol{\delta}$ using Eq. (B.3) until convergence of the cost function e is reached.

For the specific case of least-squares minimization, we note $e = \frac{1}{2}\mathbf{g}(\mathbf{p})^T \mathbf{g}(\mathbf{p})$, with $\mathbf{g} : \mathbb{R}^n \rightarrow \mathbb{R}^m$, and $\mathbf{g}(\mathbf{p}) = \mathbf{x} - \hat{\mathbf{x}}(\mathbf{p})$ for the reprojection error presented in Section 3.3.2. Calculating the derivatives of e gives

$$\frac{\partial e}{\partial \mathbf{p}} = \frac{\partial \mathbf{g}^T}{\partial \mathbf{p}} \mathbf{g} = -\mathbf{J}_{\hat{\mathbf{x}}}^T \mathbf{g}, \quad (\text{B.4})$$

and

$$\frac{\partial^2 e}{\partial \mathbf{p}^2} = \frac{\partial \mathbf{g}^T}{\partial \mathbf{p}} \frac{\partial \mathbf{g}}{\partial \mathbf{p}} + \frac{\partial^2 \mathbf{g}}{\partial \mathbf{p}^2} \mathbf{g} \quad (\text{B.5})$$

with $\mathbf{J}_{\hat{\mathbf{x}}}$ the Jacobian matrix of $\hat{\mathbf{x}}$ with respect to \mathbf{p} . Now making the assumption that the function $\hat{\mathbf{x}}$ is linear around the solution (called the Gauss-Newton approximation), the second order derivative of \mathbf{g} equals zero, resulting in

$$\frac{\partial^2 e}{\partial \mathbf{p}^2} \approx \frac{\partial \mathbf{g}^T}{\partial \mathbf{p}} \frac{\partial \mathbf{g}}{\partial \mathbf{p}} = \mathbf{J}_{\hat{\mathbf{x}}}^T \mathbf{J}_{\hat{\mathbf{x}}}. \quad (\text{B.6})$$

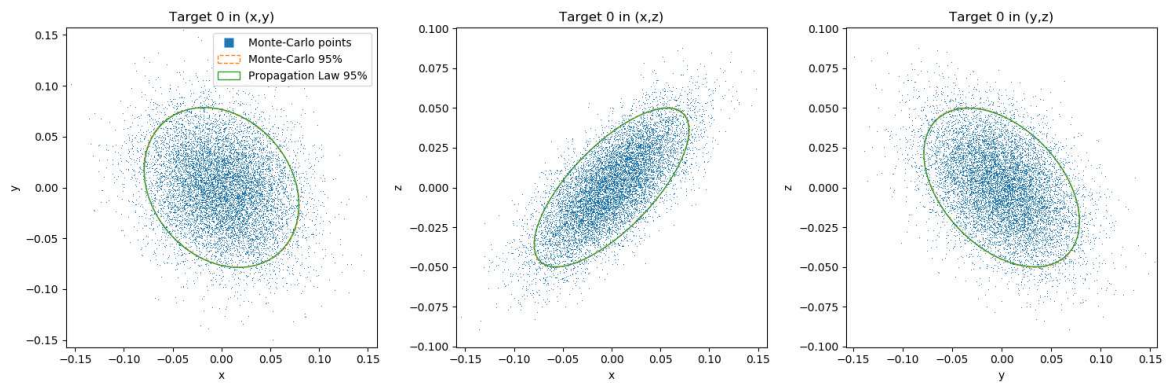
Finally, one may iteratively compute the increment $\boldsymbol{\delta}$ of the least-squares problem using

$$\mathbf{J}_{\mathbf{p}}^{\hat{\mathbf{x}}^T} \mathbf{J}_{\mathbf{p}}^{\hat{\mathbf{x}}} \boldsymbol{\delta} = \mathbf{J}_{\mathbf{p}}^{\hat{\mathbf{x}}^T} \mathbf{g}. \quad (\text{B.7})$$

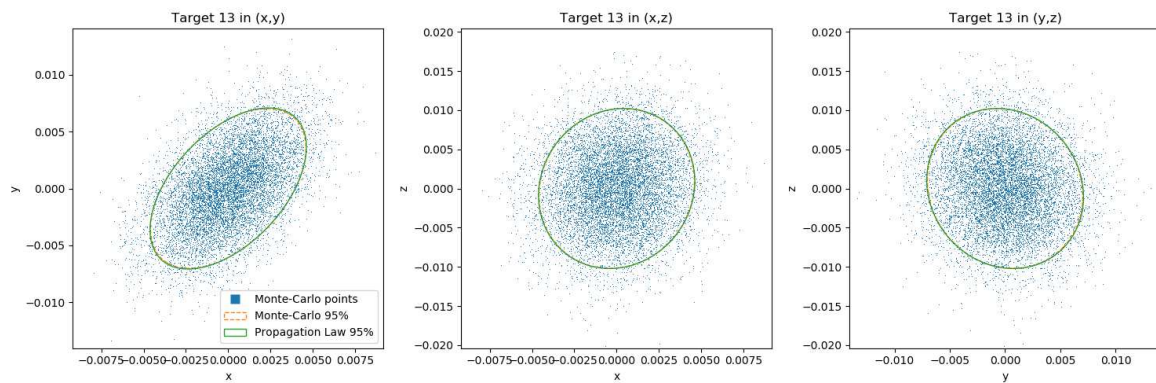
Interested reader may refer to [HZ04, p. 597] for more information on iterative estimation methods.

Results of the Uncertainty Propagation

This appendix displays some additional results of the uncertainty study presented in Section 3.4, obtained from Monte-Carlo (MC) simulations and computation using the propagation law (PL).

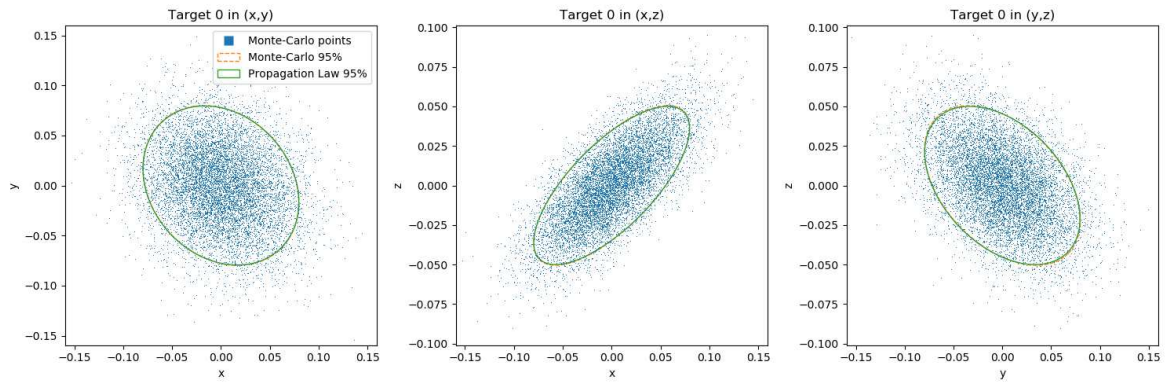


(a)

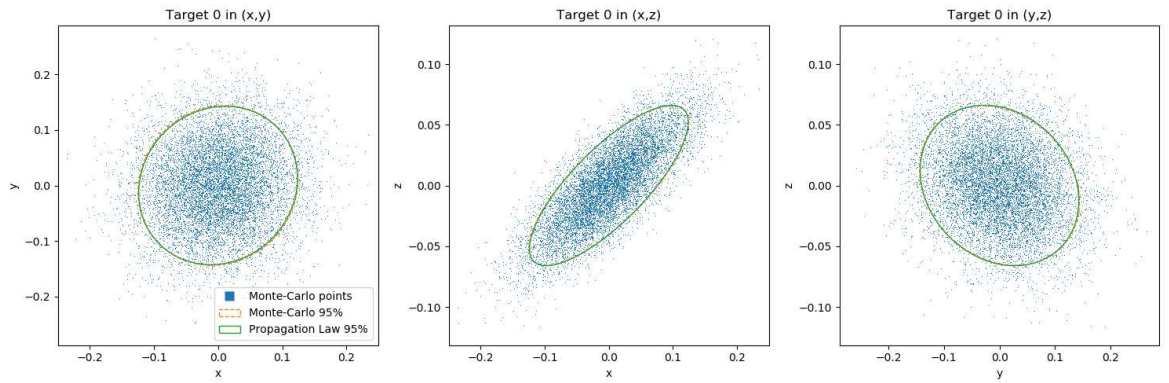


(b)

Figure C.1: BA with only observation noise at tip (a) and middle (b) of the wing, using both MC and PL (in meters).



(a)



(b)

Figure C.2: BA with only observation noise and calibration noise (in meters). Since 1px (a) of calibration noise does not change the results (see Fig.C.1), 10px (b) is tested to confirm that PL works to propagate calibration uncertainty.

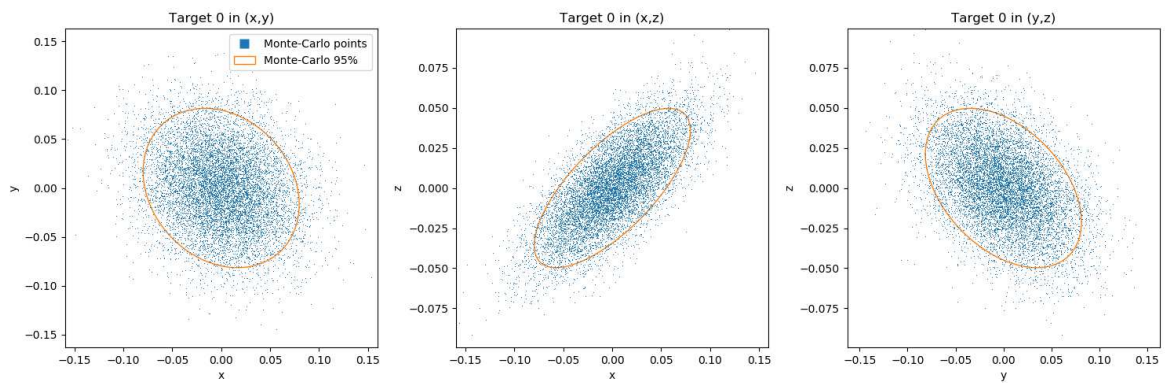


Figure C.3: BA with observation, calibration and initial reconstruction noise, showing that the uncertainty of initial reconstruction has no impact on the result in the current application (in meters).

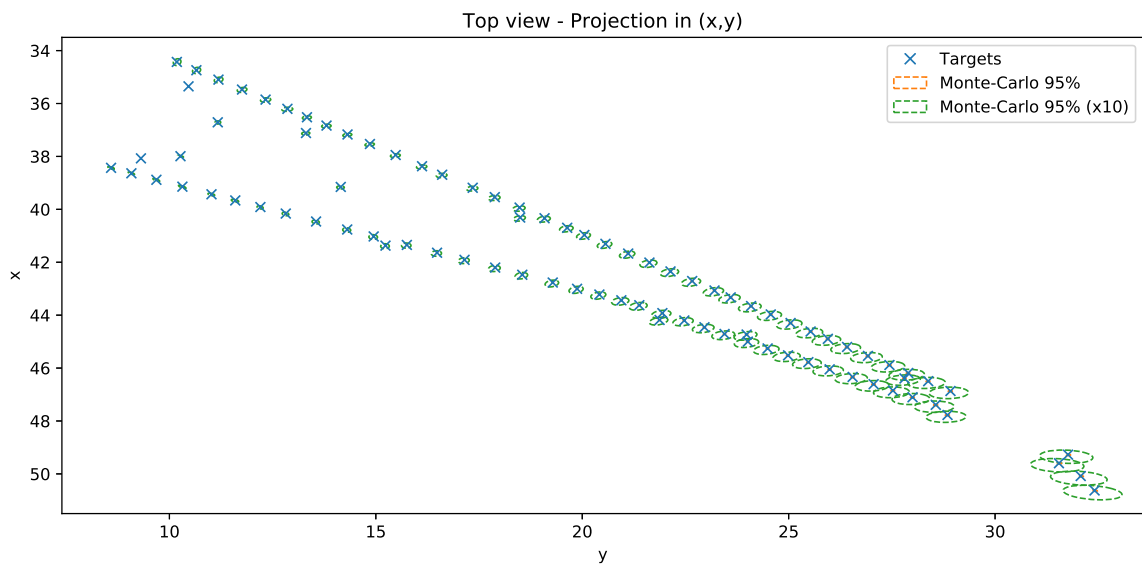
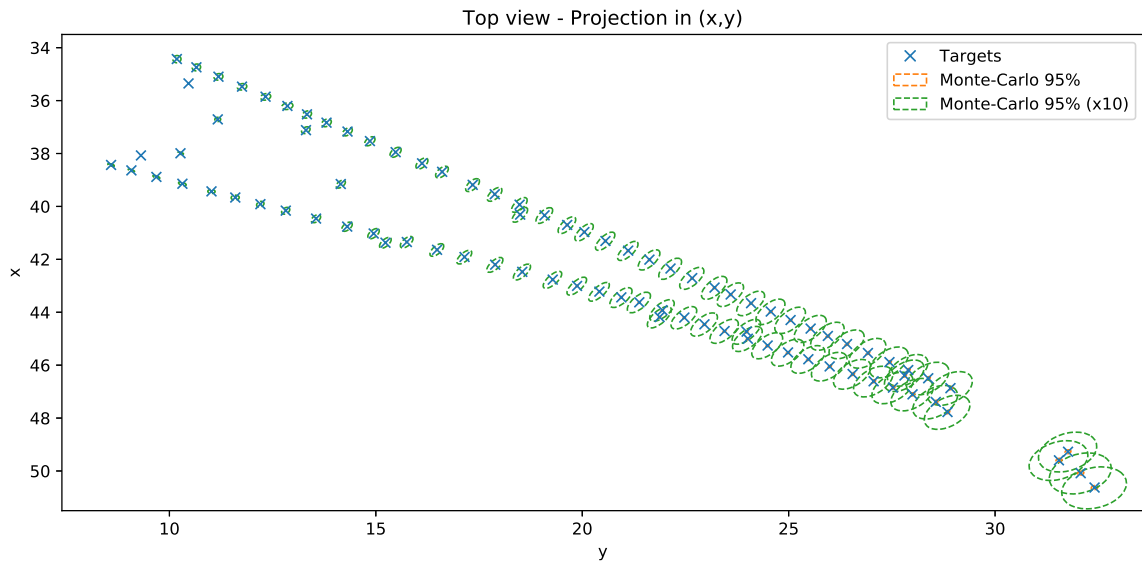
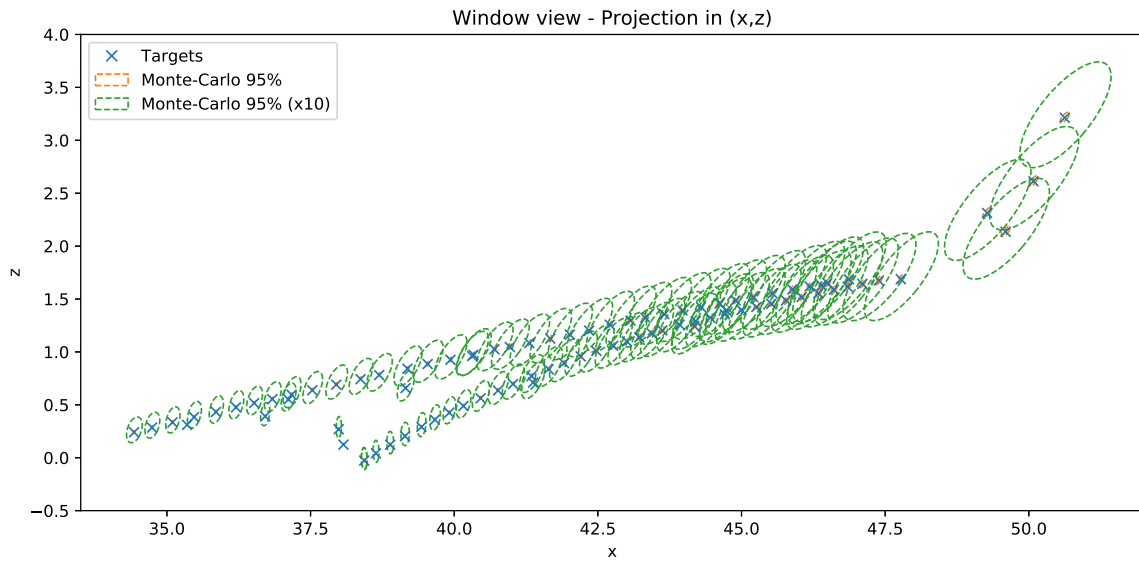
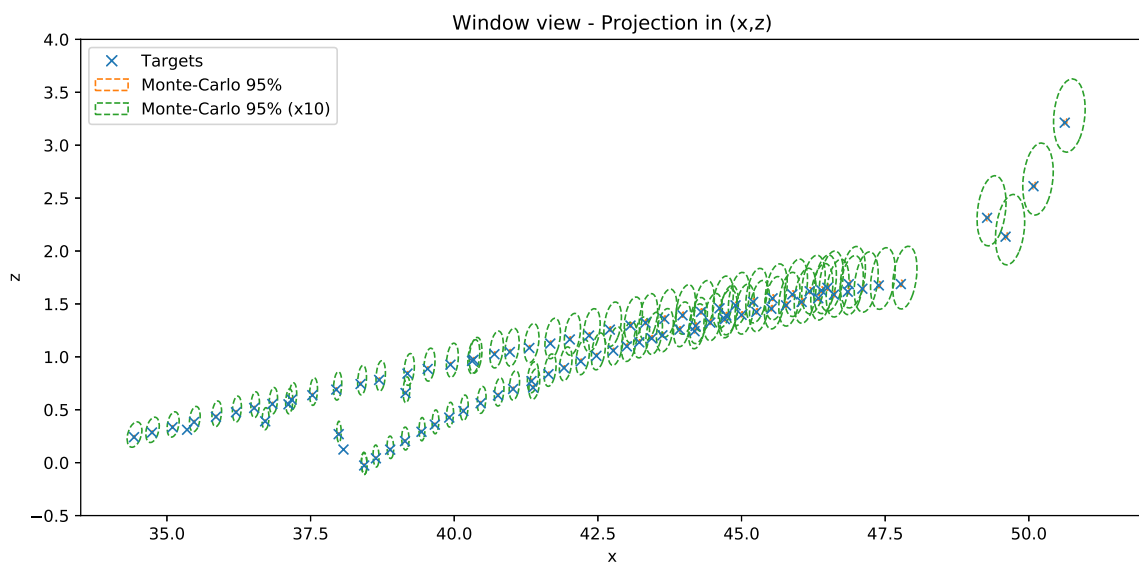


Figure C.4: Confidence ellipses of the 3D reconstructions (in meters) for all targets of the wing displayed in (x, y) plane, with BA (a) and CBA (b).



(a) BA



(b) CBA

Figure C.5: Confidence ellipses of the 3D reconstructions (in meters) for all targets of the wing displayed in (x, z) plane, with BA (a) and CBA (b).

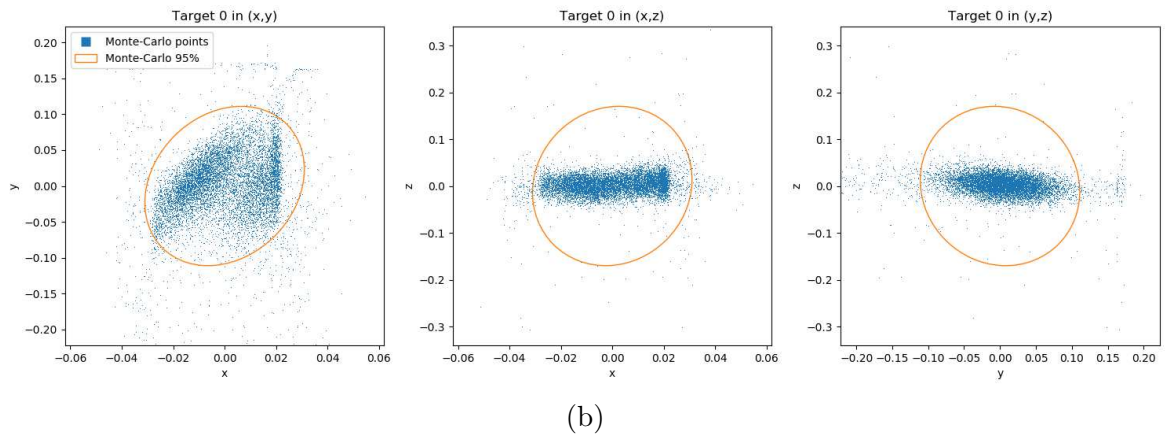
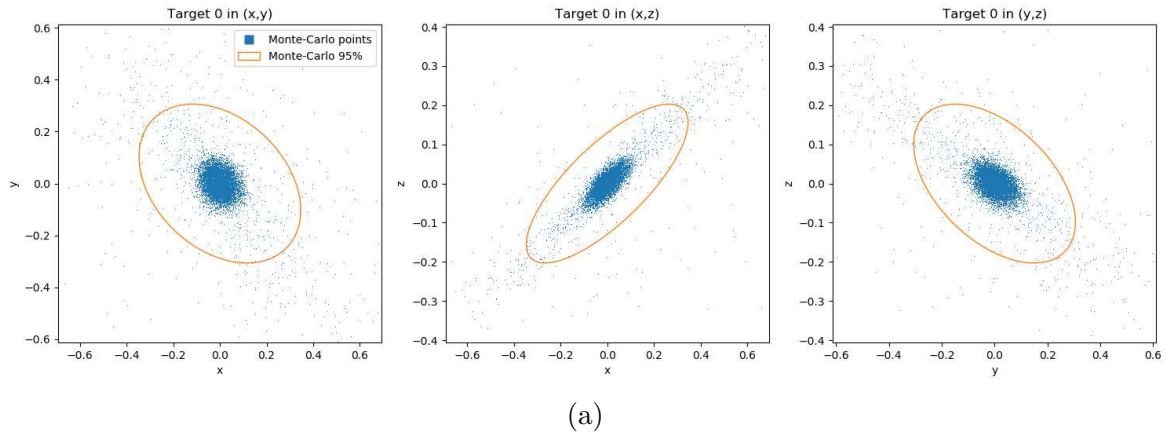


Figure C.6: Results of the MC simulation propagating observation and calibration noise with outliers, using BA (a) and CBA (b) (in meters). Boundaries arising from the volume constraints may be observed in (b).

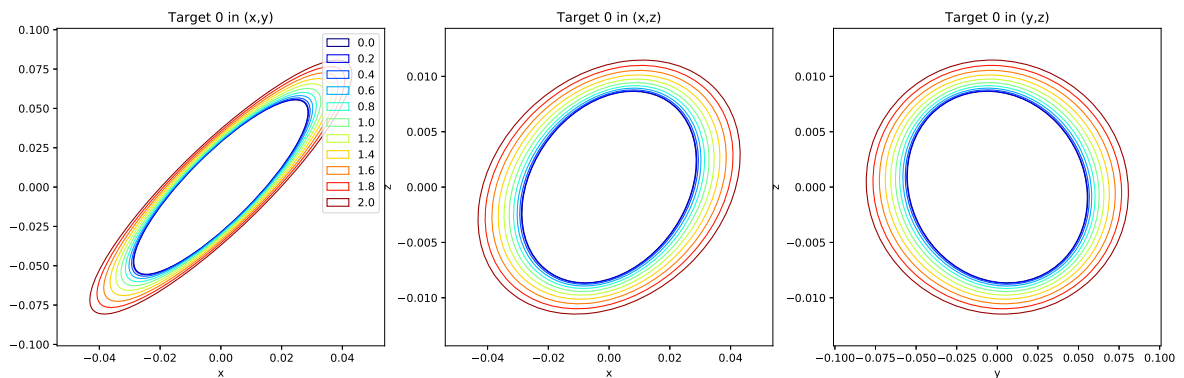


Figure C.7: Confidence ellipses of a 3D point at wing tip for various levels of observation noise, obtained using PL (in meters).

Bibliography

- [Apa+15] M. L. Aparna, G. Chaitanya, K. Srinivas, and J. A. Rao. “Fatigue Testing of Continuous GFRP Composites Using Digital Image Correlation (DIC) Technique a Review.” In: *Int. Conf. on Materials Process. and Characterization*. Hyderabad, India, 2015.
- [ARK01] S. J. Ahn, W. Rauh, and S. I. Kim. “Circular Coded Target for Automation of Optical 3D-Measurement and Camera Calibration.” In: *Int. J. of Pattern Recogn. and Artificial Intell.* 15.6 (2001), pp. 905–919.
- [Bar07] D. Barrows. “Videogrammetric Model Deformation Measurement Technique for Wind Tunnel Applications.” In: *45th AIAA Aerospace Sciences Meeting and Exhibit*. Reno, Nev., USA, 2007.
- [Bil+13] B. Billiot, F. Cointault, L. Journaux, J.-C. Simon, and P. Gouton. “3D image acquisition system based on shape from focus technique.” In: *Sensors* 13.4 (2013), pp. 5040–5053.
- [Bla] “Airbus BLADE” laminar flow wing demonstrator makes first flight (Press release). Tech. rep. Available at: https://www.airbus.com/news-room/press-releases/en/2017/09/airbus_-_blade_-_laminar_flow_wing_demonstrator_makes_first_flight.html. Airbus, 2017.
- [Bod+13] F. Boden, N. Lawson, H. W. Jentink, and J. Kompenhans. *Advanced In-Flight Measurement Techniques*. Springer Berlin Heidelberg, 2013.
- [Bri+17] G. Briskin, A. Geva, E. Rivlin, and H. Rotstein. “Estimating Pose and Motion Using Bundle Adjustment and Digital Elevation Model Constraints.” In: *IEEE Trans. Aerosp. Electron. Syst.* 53.4 (2017), pp. 1614–1624.
- [Bu+21] L. Bu, H. Huo, X. Liu, and F. Bu. “Concentric circle grids for camera calibration with considering lens distortion.” In: *Optics and Lasers in Engineering* 140 (2021), p. 106527.
- [BW10] J. Balzer and S. Werling. “Principles of Shape from Specular Reflection.” In: *Measurement* 43.10 (2010), pp. 1305–1317.
- [Cal+10] M. Calonder, V. Lepetit, C. Strecha, and P. Fua. “BRIEF: Binary Robust Independent Elementary Features.” In: *Eur. Conf. Comput. Vis.* Heraklion, Greece, 2010.
- [Cal+16] L. Calvet, P. Gurdjos, C. Griwodz, and S. Gasparini. “Detection and Accurate Localization of Circular Fiducials under Highly Challenging Conditions.” In: *IEEE Conf. Comput. Vis. and Pattern Recogn.* Las Vegas, NV, USA, 2016.
- [Can86] J. Canny. “A Computational Approach to Edge Detection.” In: *IEEE Trans. Pattern Anal. Mach. Intell.* PAMI-8.6 (1986), pp. 679–698.

- [Car+14] M. Caris, S. Stanko, A. Wahlen, R. Sommer, J. Wilcke, N. Pohl, A. Leuther, and A. Tessmann. “Very high resolution radar at 300 GHz.” In: *44th Eur. Microwave Conf.* Rome, Italy, 2014.
- [CLFM16] H. Chatoux, F. Lecellier, and C. Fernandez-Maloigne. “Comparative study of descriptors with dense key points.” In: *23rd Int. Conf. on Pattern Recognition.* Cancun, Mexico, 2016.
- [Clo] *CloudCompare Version 2.6.1 – user manual.* GPL software available at: <http://www.cloudcompare.org/>. 2015.
- [CTS95] J. E. Cryer, P.-S. Tsai, and M. Shah. “Integration of shape from shading and stereo.” In: *Pattern Recognition* 28.7 (1995), pp. 1033–1043.
- [CZ13] E. K. P. Chong and S. H. Zak. *An Introduction to Optimization.* Wiley, 2013.
- [Dem+20a] Q. Demoulin, F. Lefebvre-Albaret, A. Basarab, D. Kouamé, and J.-Y. Tourneret. “A New Flexible Photogrammetry Instrumentation for Estimating Wing Deformation in Airbus.” In: *Proc. Eur. Test and Telemetry Conf.* Nuremberg, Germany, 2020.
- [Dem+20b] Q. Demoulin, F. Lefebvre-Albaret, A. Basarab, D. Kouamé, and J.-Y. Tourneret. “Constrained Bundle Adjustment Applied To Wing 3D Reconstruction With Mechanical Limitations.” In: *IEEE Int. Conf. on Image Process.* Abu Dhabi, United Arab Emirates, 2020.
- [Dem+20c] Q. Demoulin, F. Lefebvre-Albaret, A. Basarab, D. Kouamé, and J.-Y. Tourneret. “Wing 3D Reconstruction by Constraining the Bundle Adjustment with Mechanical Limitations.” In: *28th Eur. Signal Process. Conf.* Amsterdam, Netherlands, 2020.
- [Dem21a] Q. Demoulin. *Flight-test videos.* Available at:
<https://vimeo.com/514347016>
<https://vimeo.com/514347056>
<https://vimeo.com/514347092>
<https://vimeo.com/514347134>
<https://vimeo.com/514347172>
 with the password "PhD_2021!Demoulin". 2021.
- [Dem21b] Q. Demoulin. *Simulation videos.* Available at:
<https://vimeo.com/514372904>
<https://vimeo.com/514361081>
<https://vimeo.com/514365935>
 with the password "PhD_2021!Demoulin". 2021.
- [Eud11] A. Eudes. “Localisation et cartographie simultanées par ajustement de faisceaux local : propagation d’erreurs et réduction de la dérive à l’aide d’un odomètre.” PhD thesis. Université Blaise Pascal - Clermont-Ferrand II, 2011.
- [Exe] *Guide d’analyse des besoins S 3762 X 01, Mesures sur site et qualité : aide pratique.* Tech. rep. EXERA, Association des exploitans d’équipements de mesure, de régulation et d’automatisme, Commission technique qualité de la mesure, 2001.

- [Fau93] O. Faugeras. *Three-dimensional computer vision : a geometric viewpoint*. the MIT Press, 1993.
- [Fil+17] A. Filgueira, H. Gonzalez-Jorge, S. Lagueta, L. Dia-Vilarino, and P. Arias. “Quantifying the influence of rain in LiDAR performance.” In: *Measurement* 95 (2017), pp. 143–148.
- [FLG14] S. Fuhrmann, F. Langguth, and M. Goesele. “MVE - A Multi-View Reconstruction Environment.” In: *Eurographics Workshop on Graphics and Cultural Heritage*. Darmstadt, Germany, 2014.
- [FS05] P. Favaro and S. Soatto. “A geometric approach to shape from defocus.” In: *IEEE Trans. Pattern Anal. Mach. Intell.* 27.3 (2005), pp. 406–417.
- [Fua99] P. Fua. “Using model-driven bundle-adjustment to model heads from raw video sequences.” In: *Proc. Int. Conf. Comput. Vis.* Kerkyra, Greece, 1999.
- [Fur] *Operator’s Manual, 3D Sonar Visualizer, model F3D-S*. Tech. rep. available at: <https://www.furuno.com>. Furuno Electric, 2019.
- [Gei+16] T. Geibig, A. Shoykhetbrod, A. Hommes, R. Herschel, and N. Pohl. “Compact 3D imaging radar based on FMCW driven frequency-scanning antennas.” In: *IEEE Radar Conf.* Philadelphia, PA, USA, 2016.
- [Gio+12] R. G. Gioi, J. Jakubowicz, J. M. Morel, and G. Randall. “LSD: a Line Segment Detector.” In: *Image Process. On Line* 2 (2012), pp. 35–55.
- [GM14] R. Gouiaa and J. Meunier. “3D Reconstruction by Fusioning Shadow and Silhouette Information.” In: *Canadian Conf. on Comput. and Robot Vis.* Montreal, QC, Canada, 2014.
- [Gom] *ATOS Compact Scan*. Tech. rep. available at: <https://www.gom.com>. GOM, ZEISS Group, 2017.
- [GR17] R. G. Gioi and G. Randall. “A Sub-Pixel Edge Detector: an Implementation of the Canny/Devernavy Algorithm.” In: *Image Process. On Line* 7 (2017), pp. 347–372.
- [Gro15] P. de Groot. “Principles of interference microscopy for the measurement of surface topography.” In: *Adv. Opt. Photon.* 7 (2015), pp. 1–65.
- [Guma] *JCGM 100:2008. Evaluation of measurement data - Guide to the expression of uncertainty in measurement*. Tech. rep. available at: https://www.bipm.org/utils/common/documents/jcgm/JCGM_100_2008_E.pdf. Joint Committee for Guides in Metrology, 2008.
- [Gumb] *JCGM 101:2011. Evaluation of measurement data - Supplement 1*. Tech. rep. available at: https://www.bipm.org/utils/common/documents/jcgm/JCGM_101_2008_E.pdf. Joint Committee for Guides in Metrology, 2008.
- [Gumc] *JCGM 102:2011. Evaluation of measurement data - Supplement 2*. Tech. rep. available at: https://www.bipm.org/utils/common/documents/jcgm/JCGM_102_2011_E.pdf. Joint Committee for Guides in Metrology, 2011.

- [Gur+06] R. Gurnsey, F. J. A. M. Poirier, P. Bluett, and L. Leibov. “Identification of 3D shape from texture and motion across the visual field.” In: *J. of Vis.* 6 (2006), pp. 543–553.
- [GY15] G. Gallego and A. Yezzi. “A Compact Formula for the Derivative of a 3-D Rotation in Exponential Coordinates.” In: *J. of Mathematical Imaging and Vis.* 51 (2015), pp. 378–384.
- [Hai13] M. A. Haidekker. *Medical Imaging Technology*. Springer-Verlag New York, 2013.
- [Har99] R. Hartley. “Theory and Practice of Projective Rectification.” In: *International J. of Comput. Vis.* 35.2 (1999), pp. 115–127.
- [He+12] D. He, X. Liu, Y. Yin, A. Li, and X. Peng. “Correction of Circular Center Deviation in Perspective Projection.” In: *Applications of Digital Image Process. XXXV*. San Diego, CA, USA, 2012.
- [HLK13] T. Hoegg, D. Lefloch, and A. Kolb. “Time-of-Flight camera based 3D point cloud reconstruction of a car.” In: *Computers in Industry* 64.9 (2013), pp. 1099–1114.
- [HS88] C. G. Harris and M. Stephens. “A Combined Corner and Edge Detector.” In: *Proc. Alvey Vis. Conf.* Manchester, UK, 1988.
- [HT09] B. Heiner and C. N. Taylor. “Creation of geo-referenced mosaics from MAV video and telemetry using constrained optimization bundle adjustment.” In: *Proc. Int. Conf. on Intelligent Robots and Systems*. St Louis, St Louis, USA, 2009.
- [HTG06] B. Herbert, T. Tuytelaars, and L. Van Gool. “SURF: Speeded Up Robust Features.” In: *Eur. Conf. on Comput. Vis.* Graz, Austria, 2006.
- [HTP10] M. Havlena, A. Torii, and T. Pajdla. “Efficient Structure from Motion by Graph Optimization.” In: *Eur. Conf. on Comput. Vis.* Heraklion, Crete, Greece, 2010.
- [Hua+17] A. Huang, Y. Wang, X. Dan, Y. Hu, and S. Bao. “Digital image correlation using ring template for 3D reconstruction.” In: *Int. Conf. on Imaging Systems and Techniques*. Beijing, China, 2017.
- [Hua10] X. Huang. “Extraction de Relief de Surface Texturée Rugueuse à Comportement Photométrique Hétérogène.” PhD thesis. Université de Poitiers, 2010.
- [Hud+17] G. Hudson, A. Léger, B. Niss, and I. Sebestyén. “JPEG at 25: Still Going Strong.” In: *IEEE MultiMedia* 24.2 (2017), pp. 96–103.
- [HZ04] R. Hartley and A. Zisserman. *Multiple View Geometry in Computer Vision*. Cambridge University Press, 2004.
- [Iso] *NF ISO 5725-1, Accuracy (trueness and precision) of measurement methods and results - Part 1: General principles*. Tech. rep. ISO, 1994.
- [Kaw+12] H. Kawasaki, Y. Horita, H. Morinaga, Y. Matugano, S. Ono, M. Kimura, and Y. Takane. “Structured light with coded aperture for wide range 3D measurement.” In: *IEEE Int. Conf. on Image Process.* Orlando, FL, USA, 2012.
- [KC89] K. Kanatani and T.-C. Chou. “Shape from texture: General principle.” In: *Artificial Intelligence* 38.1 (1989), pp. 1–48.

- [KKH04] M. C. Knauer, J. Kaminski, and G. Hausler. “Phase measuring deflectometry: a new approach to measure specular free-form surfaces.” In: *Optical Metrology in Production Engineering*. Ed. by Wolfgang Osten and Mitsuo Takeda. Vol. 5457. International Society for Optics and Photonics. SPIE, 2004, pp. 366–376.
- [Kle14] R. Klette. *Concise Computer Vision - An Introduction into Theory and Algorithms*. Springer-Verlag London, 2014.
- [Lar+12] D. Larnaout, S. Bourgeois, V. Gay-Bellile, and M. Dhome. “Towards Bundle Adjustment with GIS Constraints for Online Geo-Localization of a Vehicle in Urban Center.” In: *Proc. Int. Conf. on 3D Imaging, Modeling, Process., Visualization & Transmission*. Zurich, Switzerland, 2012.
- [Lar+13] D. Larnaout, V. Gay-Bellile, S. Bourgeois, and M. Dhome. “Vehicle 6-DoF localization based on SLAM constrained by GPS and digital elevation model information.” In: *Proc. Int. Conf Image Process*. Melbourne, Australia, 2013.
- [LCS11] S. Leutenegger, M. Chli, and R. Siegwart. “BRISK: Binary Robust invariant scalable keypoints.” In: *Proc. Int. Conf. on Comput. Vis.* Barcelona, Spain, 2011.
- [LF06] A. Lobay and D.A. Forsyth. “Shape from Texture without Boundaries.” In: *Int. J. of Comput. Vis.* 67 (2006), pp. 71–91.
- [Lhu12] M. Lhuillier. “Incremental Fusion of Structure-from-Motion and GPS Using Constrained Bundle Adjustments.” In: *IEEE Trans. Pattern Anal. Mach. Intell.* 34.12 (2012), pp. 2489–2495.
- [Li14] L. Li. *Time-of-Flight Camera – An Introduction*. Tech. rep. Texas Instrument, 2014.
- [Lil16] L. Liliana. “A new model of Ishikawa diagram for quality assessment.” In: *IOP Conf. Series: Materials Science and Engineering* 161.1 (2016), pp. 012–099.
- [Liu+12] T. Liu, A. W. Burner, T. W. Jones, and D. A. Barrows. “Photogrammetric techniques for aerospace applications.” In: *Progress in Aerospace Sciences* 54 (2012), pp. 1–58.
- [Low04] D. G. Lowe. “Distinctive Image Features from Scale-Invariant Keypoints.” In: *International J. of Comput. Vis.* 60 (2004), pp. 91–110.
- [Luh+13] T. Luhmann, S. Robson, S. Kyle, and J. Boehm. *Close Range Photogrammetry and 3D Imaging*. De Gruyter, 2013.
- [LZ99] C. Loop and Z. Zhang. “Computing rectifying homographies for stereo vision.” In: *Proc. Comput. Society Conf. on Comput. Vis. and Pattern Recognition*. Fort Collins, Colo., USA, 1999.
- [Mar18] D. Martišek. “Fast Shape-From-Focus method for 3D object reconstruction.” In: *Optik* 169 (2018), pp. 16–26.
- [May11] S. Maybank. *Theory of Reconstruction from Image Motion*. Springer-Verlag Berlin Heidelberg, 2011.

- [ME17] Institut Mermoz and in cooperation with AIRBUS ENAC. *General knowledge of aircraft : 021. Volume 1, Airframe and systems*. Institut Mermoz and ENAC, 2017.
- [Met] *Agisoft Metashape User Manual: Professional Edition, Version 1.6*. available at: <https://www.agisoft.com/downloads/user-manuals/>. Agisoft LLC. St. Petersburg, Russia, 2020.
- [ML09] M. Muja and D. G. Lowe. "Fast Approximate Nearest Neighbors with Automatic Algorithm Configuration." In: *Int. Conf. on Comput. Vis. Theory and Appl.* Lisboa, Portugal, 2009.
- [MMI17] F. Mahmood, M. T. Mahmood, and J. Iqbal. "3-D shape recovery from image focus using no-reference sharpness metric based on inherent sharpness." In: *17th Int. Conf. on Control, Automation and Systems*. Jeju, South Korea, 2017.
- [MMM13] P. Moulon, P. Monasse, and R. Marlet. "Global Fusion of Relative Motions for Robust, Accurate and Scalable Structure from Motion." In: *IEEE Int. Conf. on Comput. Vis.* Sydney, NSW, Australia, 2013.
- [MN12] A. Miks and J. Novak. "Dependence of camera lens induced radial distortion and circle of confusion on object position." In: *Optics & Laser Technology* 44.4 (2012), pp. 1043–1049.
- [Moe+15] M. Moeller, M. Benning, C. Schönlieb, and D. Cremers. "Variational Depth From Focus Reconstruction." In: *IEEE Trans. on Image Process.* 24.12 (2015), pp. 5369–5378.
- [Mor05] O. Morel. "Environnement Actif pour la Reconstruction Tridimensionnelle de Surfaces Métalliques Spéculaires par Imagerie Polarimétrique." PhD thesis. Université de Bourgogne, 2005.
- [Mou17] A. Mours. "Localisation de cible en sonar actif." PhD thesis. Université Grenoble Alpes, 2017.
- [NIK91] S.K. Nayar, K. Ikeuchi, and T. Kanade. "Surface reflection: physical and geometrical perspectives." In: *IEEE Trans. Pattern Anal. Mach. Intell.* 13 (1991), pp. 611–634.
- [Nis04] D. Nister. "An efficient solution to the five-point relative pose problem." In: *IEEE Trans. Pattern Anal. Mach. Intell.* 26.6 (2004), pp. 756–770.
- [Nsi] *NSI Systems and Services Overview Brochure*. Tech. rep. available at: <https://4nsi.com>. North Star Imaging (NSI), 2020.
- [OJRE17] P. Ozog, M. Johnson-Roberson, and R. M. Eustice. "Mapping underwater ship hulls using a model-assisted bundle adjustment framework." In: *Robotics and Autonomous Systems* 87 (2017), pp. 329–347.
- [Ond+20] J. Ondruš, E. Kolla, P. Vertal, and Z. Saric. "How Do Autonomous Cars Work?" In: *Transportation Research Procedia* 44 (2020), pp. 226–233.
- [Ope] *The OpenCV Reference Manual*. 2.4.13.7. Intel. 2019.

- [PA13] A. Bartoli P. Alcantarilla J. Nuevo. “Fast Explicit Diffusion for Accelerated Features in Nonlinear Scale Spaces.” In: *British Machine Vis. Conf.* Bristol, UK, 2013.
- [PF06] E. Prados and O. Faugeras. “Shape From Shading.” In: *Handbook of Mathematical Models in Comput. Vis.* (2006), pp. 375–388.
- [Phi] *IntelliSpace Portal 10 Brochure*. Tech. rep. available at: <https://www.philips.fr/healthcare>. Philips, 2017.
- [RBD17] K. Rankin, M. Browne, and A. Dickinson. “Chapter 5 - Digital Image Correlation for Strain Analysis of Whole Bones and Implants.” In: *Experimental Methods in Orthopaedic Biomechanics*. Ed. by Radovan Zdero. Academic Press, 2017, pp. 65–83.
- [RD06] E. Rosten and T. Drummond. “Machine Learning for High-Speed Corner Detection.” In: *Eur. Conf. on Comput. Vis.* Graz, Austria, 2006.
- [Ric+12] W. L. Richards, A. R. Parker, A. Piazza W. L. Ko, and P. Chan. *Application of Fiber Optic Instrumentation*. Tech. rep. available at: <https://www.sto.nato.int/>. Research and technology organisation, and North atlantic treaty organisation, 2012.
- [Rub+11] E. Rublee, V. Rabaud, K. Konolige, and G. Bradski. “ORB: An efficient alternative to SIFT or SURF.” In: *Int. Conf. on Comput. Vis.* Barcelona, Spain, 2011.
- [Sag+05] R. Sagawa, M. Takatsuji, T. Echigo, and Y. Yagi. “Calibration of lens distortion by structured-light scanning.” In: *Int. Conf. on Intell. Robots and Systems*. Edmonton, Alta., Canada, 2005.
- [Sav+07] S. Savarese, M. Andreetto, H. Rushmeier, F. Bernardini, and P. Perona. “3D Reconstruction by Shadow Carving: Theory and Practical Evaluation.” In: *Int. J. of Comput. Vis.* 71.3 (2007), pp. 305–336.
- [Sie] *ACUSON X600 Ultrasound Brochure*. Tech. rep. available at: <https://www.siemens-healthineers.com>. Siemens, 2015.
- [SSN15] R. Shah, V. Srivastava, and P.J. Narayanan. “Geometry-Aware Feature Matching for Structure from Motion Applications.” In: *Winter Conf. on Applications of Comput. Vis.* Waikoloa, HI, USA, 2015.
- [SSS06] N. Snavely, S. M. Seitz, and R. Szeliski. “Photo Tourism: Exploring Photo Collections in 3D.” In: *ACM Trans. Graph.* 25.3 (2006), pp. 835–846.
- [SSS07] N. Snavely, S. M. Seitz, and R. Szeliski. “Modeling the World from Internet Photo Collections.” In: *International J. of Comput. Vis.* 80.2 (2007), pp. 189–210.
- [ST94] J. Shi and C. Tomasi. “Good features to track.” In: *IEEE Conf. Comput. Vis. and Pattern Recognit.* Seattle, WA, USA, 1994.

- [Tac+19] J. Tachella, Y. Altmann, N. Mellado, A. McCarthy, R. Tobin, G. Buller, J.-Y. Tourneret, and S. McLaughlin. “Real-time 3D reconstruction from single-photon lidar data using plug-and-play point cloud denoisers.” In: *Nature Communications* 10 (2019), pp. 4984.
- [TF05] J. R. A. Torreao and J. L. Fernandes. “Single-Image Shape from Defocus.” In: *XVIII Brazilian Symposium on Comput. Graphics and Image Process.* Natal, Rio Grande do Norte, Brazil, 2005.
- [THP09] A. Torii, M. Havlena, and T. Pajdla. “From Google Street View to 3D city models.” In: *Proc. Int. Conf. Comput. Vis. Workshops.* Kyoto, Japan, 2009.
- [TLF10] E. Tola, V. Lepetit, and P. Fua. “DAISY: An Efficient Dense Descriptor Applied to Wide-Baseline Stereo.” In: *Trans. Pattern Anal. Mach. Intell.* 32 (2010), pp. 815–830.
- [TS94] P.-S. Tsai and M. Shah. “Shape from shading using linear approximation.” In: *Image and Vis. Computing* 12.8 (1994), pp. 487–498.
- [Uni] *Unity User Manual 2020.2.* Tech. rep. available at: <https://docs.unity3d.com/>. Unity, 2020.
- [Va20] P. Virtanen and al. “SciPy 1.0: Fundamental Algorithms for Scientific Computing in Python.” In: *Nature Methods* (2020).
- [VD16] S. Van der Jeught and J. J.J. Dirckx. “Real-time structured light profilometry: a review.” In: *Optics and Lasers in Engineering* 87 (2016), pp. 18–31.
- [Vdi] *VDI/VDE 2634 Part 3. Optical 3D-measuring systems, Multiple view systems based on area scanning.* Tech. rep. VDI-RICHTLINIEN, 2008.
- [Vel] *A Guide to Lidar Wavelengths (Blog release).* Tech. rep. available at: <https://velodynelidar.com/>. Velodyne Lidar, 2018.
- [VZ20] D. Verbin and T. Zickler. “Toward a Universal Model for Shape from Texture.” In: *IEEE Conf. Comput. Vis. and Pattern Recognit.* Seattle, WA, USA, 2020.
- [Wan+05] G. Wang, H.-T. Tsui, Z. Hu, and F. Wu. “Camera calibration and 3D reconstruction from a single view based on scene constraints.” In: *Image and Vis. Computing* 23.3 (2005), pp. 311–323.
- [Xia+16] Y. Xiang, S. Nakamura, H. Tamari, S. Takano, and Y. Okada. “3D Model Generation of Cattle by Shape-from-Silhouette Method for ICT Agriculture.” In: *10th Int. Conf. on Complex, Intell., and Softw. Intensive Syst.* Fukuoka, Japan, 2016.
- [Yan+09] J.-H. Yan, M. A. Sutton, X. Deng, Z. Wei, and P. Zavattieri. “Mixed-mode crack growth in ductile thin-sheet materials under combined in-plane and out-of-plane loading.” In: *Int. J. of Fracture* 160 (2009), pp. 169–188.
- [YC02] Y. Yu and J. Chang. “Shadow Graphs and Surface Reconstruction.” In: *Eur. Conf. on Comput. Vis. (ECCV).* Copenhagen, Denmark, 2002.
- [YSS10] Y. Yamashita, F. Sakaue, and J. Sato. “Recovering 3D Shape and Light Source Positions from Non-planar Shadows.” In: *20th Int. Conf. on Pattern Recogn.* Istanbul, Turkey, 2010.

- [Zha00] Z. Zhang. “A flexible new technique for camera calibration.” In: *IEEE Trans. Pattern Anal. Mach. Intell.* 22.11 (2000), pp. 1330–1334.
- [Zha18] S. Zhang. “High-speed 3D shape measurement with structured light methods: A review.” In: *Optics and Lasers in Engineering* 106 (2018), pp. 119–131.
- [ZHH12] Y. Zhang, K. Hu, and R. Huang. “Bundle adjustment with additional constraints applied to imagery of the Dunhuang wall paintings.” In: *J. of Photogrammetry and Remote Sensing* 72 (2012), pp. 113–120.

Résumé — Si vous avez déjà été à bord d'un avion et que vous avez regardé par le hublot, vous avez sans doute remarqué les déformations impressionnantes de ses ailes. Ces observations sont en fait très instructives sur les efforts aérodynamiques qui sont appliqués à l'avion. Bien avant le premier vol d'un avion, les constructeurs sont en mesure de prédire son comportement mécanique dans divers scénarii en fonction par exemple du poids de l'avion, de sa vitesse ou de son angle d'attaque, sur la base de modèles théoriques précis. Dans le cadre de la procédure de certification des avions, ces modèles doivent être validés et affinés par l'estimation en vol des déformations des ailes. Cependant, à mesure que la qualité et la précision des modèles d'ailes augmentent, les méthodes utilisées pour obtenir les mesures réelles devraient également évoluer.

Dans le cadre de ce travail, un nouveau système est développé et évalué pour estimer la forme 3D d'une aile en vol. Pour répondre aux nouveaux besoins de cartographie dense, de précision ou de fréquence, sans pour autant introduire de perturbation sur le comportement aérodynamique de l'aile, cette étude se concentre sur les méthodes de reconstruction 3D sans contact. Après avoir réalisé une analyse détaillée de l'état de l'art dans ce domaine, une approche photogrammétrique utilisant plusieurs caméras installées aux fenêtres de l'avion a été retenue, et un système algorithmique et matériel complet a été développé.

Comme la plupart des méthodes de photogrammétrie standard, l'approche proposée est basée sur l'ajustement des faisceaux (ou en anglais Bundle Adjustment, BA), une méthode classique qui estime simultanément les positions des caméras et la scène 3D environnante. Le BA est un algorithme d'optimisation itératif qui vise à minimiser une fonction de coût non convexe et non linéaire. On ne peut donc pas garantir sa convergence à un minimum global, et le choix des conditions initiales est crucial dans les applications pratiques. Par conséquent, l'application de la photogrammétrie à la reconstruction 3D des ailes en vol est un véritable défi, en raison de fortes contraintes d'installation et d'un environnement très variable avec des vibrations, des changements de luminosité, des réflexions potentielles et des ombres. Pour faire face à ces défis, ce travail présente un nouveau BA contraint, qui utilise les connaissances préalables résultant des limites mécaniques de l'aile au-delà desquelles la voilure se briserait, et améliore les résultats de la reconstruction comme démontré par des tests réalistes.

Dans un deuxième temps, une étude approfondie des sources d'erreur et de l'incertitude de la reconstruction est fournie afin de garantir la qualité de l'estimation 3D, ainsi que la possibilité d'avoir une meilleure interprétation des erreurs de reconstruction. Pour ce faire, toutes les sources potentielles d'incertitude sont évaluées et propagées dans le cadre proposé en utilisant trois approches : le calcul analytique, la simulation de Monte-Carlo et la validation expérimentale sur des images synthétiques. Les différentes mises en œuvre et résultats ont permis de conclure sur les avantages et les inconvénients de chaque méthode. Ils prouvent également que le système développé répond aux attentes d'Airbus.

Enfin, le système conçu est validé sur des tests réels avec un A350-1000 du centre d'essais en vol d'Airbus. Ces expérimentations menées en conditions réelles montrent la pertinence de la solution proposée par rapport aux sources d'incertitude observées, et fournissent des résultats prometteurs.

Mots clés : Déformation d'Aile, Essais en Vol, Photogrammétrie, Ajustement de Faisceaux, Optimisation sous Contraintes, Limites Mécaniques, Propagation d'Incertitude.

Abstract — If you have ever been on an aircraft and looked at the window, you may have noticed the remarkable deformations of its wings. This observation actually conveys a lot of information about the aerodynamic efforts that are applied to the aircraft. Long before the first flight of an aircraft, manufacturers are able to predict its mechanical behavior in various scenarii depending for instance on the aircraft weight, speed or angle of attack, based on accurate theoretical models. As part of the aircraft certification procedure, these models have to be validated and refined through in-flight estimation of wing deformations. However, as the quality and accuracy of the wing models increase, the methods used to obtain the actual measurements should also evolve.

In this work, a new system is developed and evaluated to estimate the 3D shape of a wing in flight. To answer the new needs of dense mapping, precision, or frequency, while introducing no disturbance on the wing aerodynamic behavior, this study is focusing on the methods of non-contact 3D reconstruction. After performing a detailed study about state-of-the-art systems in this field, a photogrammetry approach using multiple cameras installed at the aircraft windows was retained, and a full algorithmic and hardware system was developed.

Similarly to most standard photogrammetry methods, the proposed approach is based on Bundle Adjustment (BA), a classical method that simultaneously estimates camera positions and surrounding 3D scene. BA is an iterative optimization algorithm that aims at minimizing a non-convex and non-linear cost function. Therefore, one cannot guarantee its convergence to a global minimum, and the choice of the initial conditions is crucial in practical applications. Consequently, the application of photogrammetry to 3D wing reconstruction in flight is a very challenging problem, due to strong installation constraints, and highly varying environment with vibrations, luminosity changes, potential reflections and shadows. To face these challenges, this work presents a new constrained BA, which uses prior knowledge resulting from wing mechanical limits beyond which the wing would break, and improves reconstruction results as demonstrated through realistic tests. In a second step, an in-depth study of error sources and reconstruction uncertainty is provided in order to guarantee the quality of the 3D estimation, as well as the possibility of having a better interpretation of reconstruction errors. To this aim, all potential sources of uncertainty are evaluated, and propagated through the proposed framework using three approaches: analytical calculation, Monte-Carlo simulation, and experimental validation on synthetic images. The different implementations and results allowed one to conclude on the advantages and disadvantages of each method. They also prove that the developed system meets the expectations of Airbus.

Finally, the designed system is validated on real tests with an A350-1000 of the flight test center in Airbus. These experimentations conducted in real conditions show the pertinence of the proposed solution with respect to the observed sources of uncertainty, and provide promising results.

Keywords: Wing Deformation, Flight Tests, Photogrammetry, Bundle adjustment, Optimization under Constraints, Mechanical Limits, Propagation of Uncertainty.

Airbus and TésA laboratory
Toulouse, France